Fatigue Characterization and Cyclic Plasticity Modeling of Magnesium Spot-Welds

by

Seyed Behzad Behravesh

A thesis

presented to the University of Waterloo

in fulfillment of the

thesis requirement for the degree of

Doctor of Philosophy

in

Mechanical Engineering

Waterloo, Ontario, Canada, 2013

AUTHOR'S DECLARATION

I hereby declare that I am the sole author of this thesis. This is a true copy of the thesis, including any required final revisions, as accepted by my examiners.

I understand that my thesis may be made electronically available to the public.

Seyed Behzad Behravesh

Abstract

The automotive industry is adopting lightweight materials to improve emissions and fuel economy. Magnesium (Mg) alloys are the lightest of engineering metals, but work is required to assess their structural strength, especially for spot-welded applications. In the present research, fatigue behavior of magnesium spot-welds was characterized and compared with steel and aluminum spot-welds. A fatigue model was proposed to predict the failure location and crack initiation life in magnesium structures.

The material under investigation, AZ31B-H24 Mg alloy, and its spot-welds were characterized from microstructural and mechanical points of view. Microstructure and hardness of the base metal (BM) and different regions in the spot-welds were studied. Monotonic testing of the BM demonstrated asymmetric hardening behavior under tension and compression. Under cyclic loading, the BM had an asymmetric hysteresis loop. Static behavior of spot-welds was studied with different specimen configurations. The effect of nugget size on the static peak load was similar to that of aluminum and less than steel. Cyclic behavior of magnesium spot-welds was measured using different specimen configurations, and the effect of geometrical factors on fatigue life was evaluated. Fatigue strength (in terms of load range) of magnesium spot-welds was similar to aluminum and less than steel. Crack initiation location and life as well as crack propagation path for different life ranges were compared.

A constitutive model was developed, implemented, and verified to model the asymmetric hardening behavior of wrought magnesium alloys under cyclic loading. The proposed phenomenological model is continuum-based and utilizes the Cazacu-Barlat asymmetric yield function along with an associated flow rule and a combined hardening rule. An algorithm for numerical implementation of the proposed model was developed. The numerical formulation was programmed into a user material subroutine to run with the commercial finite element software Abaqus/Standard. The proposed model was verified by solving two problems with available solutions.

A number of available fatigue models, as well as a new model proposed in this research were assessed by predicting fatigue life of magnesium spot-welds. One reference model from each of the following groups, fracture mechanics, structural stress, and local strain approaches, were implemented. The new model used a strain energy damage parameter. All models were evaluated by

comparing the predicted and experimental fatigue lives for different Mg spot-welded specimens. The effect of considering the asymmetric hardening behavior of wrought magnesium alloys on the accuracy of the fatigue life prediction was not significant for the available experimental data. This was attributed to the limited experimental data on spot-welded specimens.

The proposed material model and fatigue damage parameter were verified by simulating a real-life structure manufactured and fatigue tested by the US Automotive Materials Partnership. The structure was simulated under different experimental loading conditions. The results obtained from the proposed asymmetric model were compared with available symmetric simulation results and experimental data. The asymmetric material model along with the proposed damage parameter resulted in more accurate prediction of fatigue failure location and life.

Acknowledgements

First of all, I wish to praise and thank God for all His blessings. I would not have made any progress without His providence.

I would like to express my sincere gratitude to my supervisor, Professor Hamid Jahed, and my co-supervisors, Professor Steve Lambert and Professor Gregory Glinka, for their valuable supports and guidance.

I owe my deepest gratitude to my beloved parents and brothers for their unconditional love and inspiration throughout my education. I wish to remember my recently deceased father and two lovely brothers, Benyamin and Bahman; may God shower His blessings upon their souls. I would like to extend my appreciation to my parents-in-law for their sincere love and continuous supports. Special thanks to my dear wife, Roja, for her understanding, encouragement, and patience which made this research possible.

The financial support from AUTO21 and Automotive Partnership Canada is acknowledged. I am also grateful to General Motors for providing materials required for this research.

I am thankful to Tom Gawel, Andy Barber, Steve Hitchman, Martha Morales, and Richard Forgett for their technical supports. The collaboration of the resistance spot welding laboratory of the University of Waterloo, in particular Ray Liu and Tirdad Niknejad, for providing spot-weld specimens is appreciated.

I greatly appreciate my colleagues, Dr. Mohammad Noban, Arash Tajik, Dr. Amin Eshraghi, Dr. Morvarid Karimi, Dr. Jafar Al Bin Mousa, Elfaitori Ibrahim, Ali Roostaei, Bahareh Marzbanrad, and Mohammad Diab for their precious thoughts and discussions. I am especially thankful to Mi Chengji for his invaluable assistance.

Dedicated to the Leader of the Age, the ultimate savior of humankind,

who is promised to fill the earth with peace and justice,

as it has been filled with injustice and tyranny.

(May God hasten his reappearance)

Table of Contents

List of Figures

List of Tables

Nomenclature

$\pm$	Subscript denotes "signed"
$\boldsymbol{\alpha}$, α_{ij}	Back stress tensor for yield surface
$d\bar{\alpha}$	Size of back stress increment for yield surface
δ	Gap (distance between the current point on the yield surface and corresponding point on the bounding surface)
δ_{in}	Initial gap (distance between the most recent onset of yielding and the corresponding point on the bounding surface)
ε	Total Strain (for uniaxial loading)
$\boldsymbol{\varepsilon}$, ε_{ij}	Strain tensor
ε'_f	Fatigue ductility coefficient
$\bar{\varepsilon}^p$	Equivalent plastic strain
$\boldsymbol{\eta}$	Plastic flow direction
θ_d	Angle between two subsequent points on yield surface
θ_r	Reference angle
κ	Represents the size of yield surface
$\boldsymbol{\nu}$	Unit vector in the translation direction of yield surface
σ	Axial stress (for uniaxial loading)
$\boldsymbol{\sigma}$, σ_{ij}	Cauchy stress tensor
$\sigma_1, \sigma_2, \sigma_3$	Principal stresses
σ_{hyd}	Hydrostatic stress
σ'_f	Fatigue strength coefficient
$\bar{\sigma}$	Equivalent stress
φ	Consistency condition on yield surface
ω	Effective coupon width

$\mathbf{A}$, A_{ij}	Back stress tensor for bounding surface
$d\bar{A}$	Size of back stress increment for bounding surface
K	Represents the size of bounding surface
$\mathbf{\Sigma}$	Stress point on bounding surface corresponding to current point on yield surface
a	Subscript denotes amplitude
a	Crack length
b	Fatigue strength exponent
c	Fatigue ductility exponent
C	Material constant (representing the yield asymmetry)
$\boldsymbol{C^e}$	Elastic stiffness tensor
$\boldsymbol{C^{ep}}$	Elastic plastic (tangent) stiffness tensor
d	Nugget diameter
e	Superscript denotes elastic
E	Elastic modulus
E^{α}	Hardening moduli associated with the back stress of yield surface
E^{A}	Hardening moduli associated with the back stress of bounding surface
E^p	Plastic modulus
E^t	Tangent modulus
$f(\bullet)$	Yield surface equation (yield function)
$F(\bullet)$	Bounding surface equation
iso	Subscript denotes isotropic
J_2, J_3	Second and third invariants of deviatoric stress tensor
k	Superscript denotes iteration number for yield surface
K	Monotonic tensile strength coefficient
K_I, K_{II}, K_{III}	Stress intensity factor for mode I, II, or III loadings

K'	Cyclic strength coefficient
l	Superscript denotes iteration number for bounding surface
m	Subscript denotes “mean”
n	Subscript denotes increment number
n	Monotonic tensile strain hardening exponent
$\boldsymbol{n}$	Normal vector to yield surface
n'	Cyclic strain hardening exponent
N_f	Fatigue life
N_i	Crack initiation life
p	Superscript denotes plastic
ref	Subscript denotes the state in reference frame
R	Load ratio
R_a	Asymmetry ratio
R_s	Shrinkage ratio
s	Subscript denotes the status after shrinkage of yield surface
$\boldsymbol{S}$	Deviatoric stress tensor
S_y	Uniaxial yield strength (for symmetric materials under tension and compression)
S_y^c	Uniaxial yield strengths under compression
S_y^t	Uniaxial yield strengths under tension
t	Superscript denotes “total”
t	Sheet thickness
T	Superscript denotes the trial state
W	Strain energy

Chapter 1

Introduction

Magnesium alloys, owing to a very low density, have attracted significant attention in the automobile industry. For instance, magnesium sheet is being investigated as an alternative material for vehicle body parts. Automotive body components, which are mostly in form of sheet metal, are commonly joined together with resistance spot-welds. Service surveys show that a major proportion of structural durability issues in automobiles are related to spot-welds [1]. Thus, fatigue analysis of spot-welds is an essential part of the design process for the body structure. Wrought magnesium alloys exhibit unusual cyclic behavior and do not obey common material models. Therefore, fatigue analysis of magnesium structures is not a trivial task. The present research aims to reliably estimate fatigue failure location and fatigue crack initiation life in spot-welded structures made of magnesium. This chapter reviews the research motivations, objectives, and the thesis outline.

1.1 Motivation

Steel has been the prevailing material in the automotive industry since the 1920s [2]. Nevertheless, restricting standards and legislative requirements are forcing car manufacturers to reduce exhaust emissions and improve fuel efficiency. As a result, automobile weight has become one of the most critical criteria in design assessments. The need to reduce weight is responsible for the wide application of high strength steels in this industry. Another step taken since 1922 is the use of aluminum alloys [3]. Aluminum usage was 110 kg per car in 1996, and is predicted to reach 250 to 340 kg by 2015 [2]. For the same reason, interest in magnesium, with the lowest density among engineering metals (75% less than steel and 35% less than aluminum) has increased in the automobile industry. Volkswagen was the first car manufacturer to adopt magnesium [4]. Porsche in 1928 pioneered utilizing magnesium alloys in the engine block [5]. The trend in the average magnesium usage per car has been rapidly increasing from 3 kg in 2005 to 20 kg in 2010, and is projected to reach 50 kg in 2015 [5]. While magnesium has wide applications in automotive components such as casings, housings, and trim parts, its application to load bearing components is necessary to achieve its role as a major material in automotive manufacturing. It is therefore essential to examine the merits of these components made of magnesium alloys under both static and cyclic loads.

From the joining perspective, applicability of various welding techniques for automotive body parts has been studied mainly using steel [6,7] and aluminum [8,9]. With the new interest in magnesium in recent years, the feasibility and performance of different joining processes such as laser welding [10,11], electron beam welding [12,13], and friction stir welding [14,15] have been investigated on magnesium alloys. Nevertheless, resistance spot-welding is still the predominant joining technique in automobile body assembly lines [16], as it allows rapid and cost effective fabrication of complicated assemblies. A typical vehicle in North America contains about four to five thousand spot-welds [17]. However, service reports of automobiles show that a major proportion of

structural durability issues are related to spot-welds [1], which is due to the fact that spot-welds act as stress concentration sites, and are therefore more susceptible to fatigue failure. As a result, fatigue characterization of spot-welds as well as reliable prediction of the fatigue life has great significance.

Various models have been proposed over the past four decades to estimate the fatigue life of spot-welds. These models have targeted commonly used metals in the auto industry, *i.e.*, steel and aluminum, which exhibit isotropic and symmetric hardening behavior. Complex cyclic behavior of wrought magnesium alloys, such as yield asymmetry, is not incorporated in available models. Therefore, applicability of these models to magnesium spot-welds is questionable. As a result, developing a material model which closely follows the cyclic behavior of wrought magnesium alloys is required to provide a reliable basis for the fatigue modeling.

Recently, extensive investigations have been performed to promote magnesium application in automobile structural components. The Magnesium Front End Research and Development (MFERD) project was launched in 2006. A number of universities, industrial firms, and institutions from Canada, the United States and China are collaborating in this research. The feasibility of manufacturing the automobile front end structure from magnesium alloys is studied in the MFERD project. Fatigue and durability is one of the fundamental tasks in this project and has the goal of establishing a fatigue design methodology for magnesium structures. Participating institutions in the fatigue and durability task include the University of Waterloo and Ryerson University from Canada; Mississippi State University, Westmorland Corporation, General Motors, Chrysler, and Ford Motor Company from the United States; and the Institute of Metal Research (IMR) from China. The present research is a part of the fatigue and durability task of the MFERD project conducted at the University of Waterloo and aims to characterize magnesium spot-welds and develop a fatigue model to estimate fatigue crack initiation life.

1.2 Objectives

The ultimate goal in this study is to estimate fatigue crack initiation location and life in magnesium spot-welded structures. In what follows, the objectives are listed and briefly explained.

- **AZ31B Magnesium and Spot-Weld Characterization**

The mechanical behavior of AZ31B-H24 magnesium is studied under uniaxial monotonic tensile and compressive loading. Cyclic properties of this material are extracted through fully-reversed strain-control testing. Special features of the mechanical behavior are explained using knowledge of the magnesium microstructure and texture evolution. AZ31B spot-welds are also characterized from microstructural and mechanical perspectives. Static and fatigue behavior of spot-welds are studied and the different failure modes and the effects of welding parameters are discussed.

- **Constitutive Modeling of Wrought Mg Alloys**

Fatigue modeling of structures often requires a reliable finite element (FE) simulation. Proper material modeling is an essential component in FE modeling. Available material models in commercial FE software packages do not follow the unusual hardening behavior of wrought magnesium alloys. As a result, developing a constitutive cyclic plasticity model for magnesium alloys is an objective in this research.

- **Fatigue Modeling of Mg Spot-Welded Structures**

Predicting the fatigue failure location and fatigue crack initiation life in spot-welded structures made of magnesium is the main goal in the present study. Local stress/strain values are obtained from FE simulations which take advantage of the proposed material model. Total strain energy, *i.e.*, the

summation of plastic strain energy and positive elastic strain energy, is considered as a damage parameter for fatigue crack initiation.

- **Fatigue Model Verification**

To verify the proposed fatigue model, a structure with complex geometry and general loading and material combinations was tested as part of the overall MFERD project. This structure was assessed using the fatigue model developed in this research. The failure location and the fatigue life were used to evaluate the merits of the proposed model.

1.3 Thesis Overview

The present thesis contains three major parts: material characterization, constitutive modeling and fatigue modeling. The thesis overall structure is as follows:

Chapter 2 briefly presents background information about magnesium alloys and the spot-welding process. Literature regarding microstructural and mechanical properties of AZ31 magnesium alloy is reviewed. Available constitutive material models based on continuum mechanics approach are introduced. The most common fatigue models for life estimation of spot-welds are categorized and briefly described at the end of this chapter.

Chapter 3 introduces the material investigated and the different specimens adopted for testing the base metal and spot-welds. Experimental setup for material characterization is explained and the results including microstructural and mechanical properties are presented. Microstructure and hardness results for the base metal and different regions of the weld are presented and analyzed. Monotonic and cyclic test results are presented and the failure modes for spot-welded specimens are discussed. The effect of cyclic loading on the microstructure and fatigue crack initiation and

propagation are explained. Finally, the mechanical behavior of magnesium resistance spot-welds is compared with that of friction stir spot-welds.

Chapter 4 covers the theory, implementation, and verification of the cyclic plasticity model developed in this study for simulating the fatigue behavior of AZ31B. The three fundamental components in continuum plasticity, yield function, flow rule, and hardening rule, are introduced and the formulation for constitutive modeling is established. Numerical implementation of the plasticity model and the assumptions made are presented. The capability of the model to regenerate uniaxial cyclic behavior is demonstrated. Yield surface evolution for uniaxial and equi-biaxial loading is discussed. The results obtained from the proposed model are verified at the end of this chapter by comparison with available results in axisymmetric and pure bending problems.

Chapter 5 categorizes available fatigue models for spot-welds into three major groups. One of the most common fatigue models from each group is presented in detail. The selected models, those proposed by Swellam [18], Sheppard [19], and Pan [20], are assessed by predicting the fatigue life of magnesium spot-welds in the tensile-shear and cross-tension configurations. A new fatigue model is proposed for crack initiation using the plasticity model established in chapter 4. The effect of asymmetric material modeling is studied by comparing the predictions obtained from regular symmetric and proposed asymmetric material models.

Chapter 6 compares the simulation results with experimental data obtained from fatigue testing of a real-life automotive structure. The asymmetric material model developed herein and the proposed fatigue damage parameter were employed in the simulation. The asymmetric simulation was also compared with a symmetric simulation for different fatigue loading conditions. The predicted failure location and fatigue life are compared with experimental observations.

Finally, chapter 7 summarizes the research contributions, concluding remarks, and recommendations for future work.

Chapter 2

Background and Literature Review

This chapter presents background information about magnesium (Mg) alloys and the spot-welding process. Literature regarding properties of AZ31B magnesium alloy, constitutive material modeling based on continuum mechanics, and fatigue modeling of spot-welds are also reviewed in this chapter. Magnesium, the material investigated in this study, is introduced in terms of general micro- and macro-structural characteristics. Fundamental information about the resistance spot-welding process is presented. The special mechanical behavior of AZ31B magnesium alloy is reviewed and related to microstructural features of wrought Mg alloys. Available research regarding characterization of AZ31B spot-welds is presented. Different approaches for material modeling are introduced and continuum-based models are reviewed. The most common fatigue models for life estimation of spot-welds are briefly described at the end of this chapter.

2.1 Background

2.1.1 Magnesium

In the past, magnesium applications were mostly limited to the nuclear industry and the military. Magnesium was highly utilized in the First and Second World Wars. However, military usage decreased after the war, and Volkswagen was the main magnesium consumer [21,22]. Magnesium application in the automobile industry gradually diminished due to technical problems in achieving higher performance. In recent years, magnesium, with the lowest density among commercial engineering metals, has attracted more attention in the automobile industry to comply with ever restricting environmental standards [22].

Magnesium has found commercial application as a result of a series of beneficial properties. Magnesium, with a density of 1.738 gr/cm^3, roughly 1/4 that of steel and 2/3 that of aluminum, offers a superior stiffness-to-weight ratio among the common engineering metals [23]. Other advantages of magnesium and it's alloys include good castability, favorable machining behavior, weldability under controlled atmosphere, and availability [22,24].

Some poor properties, on the other hand, have limited magnesium's application. The weak points of magnesium include limited cold workability, low strength at elevated temperatures, high level of solidification shrinkage, and limited corrosion resistance [22,25]. Asymmetric mechanical behavior under tension and compression [24-26] can also be considered a disadvantage of wrought magnesium alloys from the modeling perspective. This unusual behavior arises due to uniformly oriented hexagonal crystals in wrought Mg alloys, but is not generally encountered in shaped castings as they have a random crystal orientation [24].

Although magnesium does not offer an outstanding combination of properties, it has been one of the most attractive materials over the last decade, especially where lightness is a critical design factor. Numerous automotive manufacturers, including Audi, Volkswagen, DaimlerChrysler, BMW, Toyota, Ford, GM, Hyundai, and Kia Motors, have adopted magnesium in their cars [23]. The trend in the average magnesium usage per car has been rapidly increasing from 3 kg in 2005 to 20 kg in 2010, and is projected to reach 50 kg in 2015 [5]. Almost all magnesium alloys being used in automobile parts are in the form of castings, and less than 2% is in the form of wrought alloys [5,27].

Magnesium is a hexagonal close-packed (HCP) metal, and this feature is responsible for many microstructural and mechanical characteristics. Because of the hexagonal lattice crystal structure, magnesium does not have enough basal slip systems at room temperature for uniform deformation [28-31]. Other possible non-basal slip systems are not activated below 225°C [30,32], which results in poor cold-formability. Twinning is an alternative mechanism for plastic deformation in HCP metals [29-33]. Pyramidal twinning on the $(10\bar{1}2)$ plane is the only operative twin system at low temperatures [30,32]. This twin system, which is usually called tension twinning, is favored in tension along the c-axis of the hexagonal crystal [25,26]. The primary slip planes as well as the pyramidal tension twin plane are shown in Figure 2.1.

Crystal rotation, anisotropy, and tension-compression asymmetry in stress-strain curves are other characteristics that can be interpreted using the HCP crystal structure. These features are predominant in wrought magnesium alloys which have strong crystallographic textures.

Wrought magnesium alloys are often manufactured through rolling, extrusion, or forging processes [26]. Hot/cold rolling changes the texture of magnesium sheet/plate, such that HCP crystals are mostly oriented with the c-axis perpendicular to the sheet surface [25-27]. Therefore, in-plane compression induces tension along the c-axis and may result in tension twin deformation.

Consequently, the yield strength is considerably lower under in-plane compression than under in-plane tension [32].

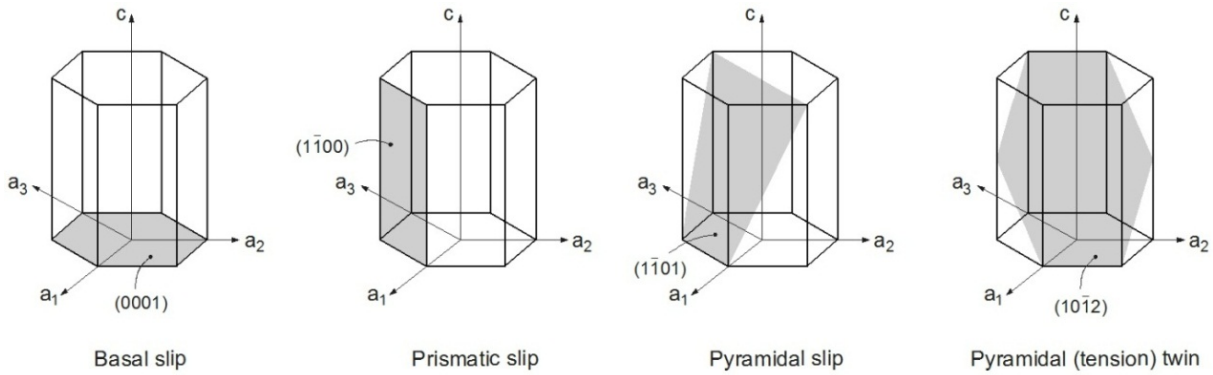

Figure 2.1: Predominant slip and twin planes in HCP metals [34]

According to the codification system proposed by the American Society for Testing Materials (ASTM) [35], magnesium alloys are designated by two letters which are followed by two integer numbers and a serial letter. The first two letters indicate the major alloying elements (A-aluminum, E-rare earths, K-zirconium, M-manganese, Z-zinc, *etc*.). The numbers represent the nominal weight percentages of the respective elements, rounded to the nearest whole number. The serial letter is arbitrarily chosen in alphabetical order to distinguish alloys with identical designations, and refers to the development sequence of the alloy. For instance, AZ31B designates the alloy Mg-3wt%Al-1wt%Zn which is the second alloy developed (after AZ31A) whose composition qualified for the assignment of the designation AZ31. Heat-treatment and work-hardening conditions are specified by a coding which follows the alloy designation. The heat-treatment coding consists of a letter (F, O, W, H, or T) which is followed by one or more numbers. For example, in AZ31B-H24 the suffix H24 indicates that AZ31B alloy was strain hardened (letter H), and then partially annealed (number 2) to half hard (number 4) [36].

2.1.2 Resistance Spot Welding

Resistance spot welding (RSW) is a joining process that makes a weld at the interface of two or more overlapping workpieces through the application of pressure and electric current by electrodes. The heat needed for welding is generated by the resistance of the workpieces against the welding current passing between electrodes through the workpieces. Welding current, which has a low voltage and a high amperage, is applied for a short time to heat the faying surfaces in a small area between electrodes, and form a circular fused nugget [37]. Electrodes are made hollow to allow for water-cooling, to maintain their performance for a long production life [38]. Figure 2.2 schematically illustrates the RSW process.

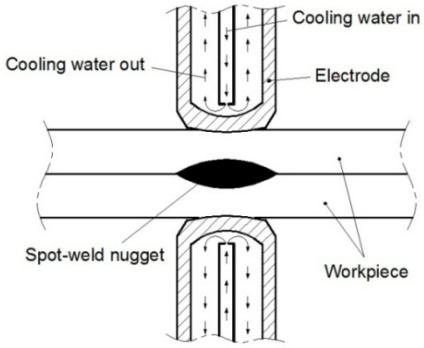

Figure 2.2: Resistance spot welding [39]

The RSW process was developed in 1898, but was not commercialized until the Second World War, due to limited power supply [38,40]. RSW has been widely used in joining sheet metal for automobile bodies since the 1950's [41]. This welding technique is now the predominant mode of fabrication in automotive production [17].

RSW process parameters include squeeze time, weld current, weld time and electrode force [25,40,42]. Squeeze time is the time interval between application of electrode force and passing welding current. Weld current is the amount of electrical current that flows through the workpieces. Weld time is the time during which the weld current passes, causing a spot-weld nugget to form. Electrode force is the amount of compressive load that the electrodes exert on the workpieces to ensure proper contact.

Alternative current (AC) and mid-frequency direct current (MFDC) are the two major power supplies for industrial RSW applications [43]. AC is the primary power supply for RSW in the automotive industry [44]. Low initial cost, inexpensive maintenance, and reliability are advantages of AC power supply [40,43]. The main shortcoming of RSW with AC power is the need for complex controls [40]. MFDC is a newer technology for RSW which is finding wider industrial applications. MFDC is especially favored for applications where higher welding current is required, such as welding aluminum [43]. Wide weld lobes and less electrode wear are among the advantages of MFDC over AC power supplies [45]; equipment cost and lower reliability are disadvantages of MFDC [44].

Magnesium and aluminum alloys, due to high electrical and thermal conductivity, require higher weld current than steel for RSW [46]. Therefore, the RSW equipment suitable for steel cannot be readily used for magnesium alloys. Nevertheless, RSW of Mg alloys may be accomplished with both AC and MFDC power supplies [25].

RSW operation must be performed such that standard welding qualification criteria are met. These specifications have been introduced in an AWS standard [47], and include minimum nugget size, shear strength, maximum electrode indentation, and lack of expulsion and cracking. To obtain Mg spot-welds with less porosity and expulsion, workpiece surfaces are chemically cleaned with chromic-sulphuric acid [25]. Weld current, weld time and electrode force have to be controlled carefully to obtain sound welds. As mentioned above, weld current for RSW of aluminum and magnesium alloys is significantly higher than that for RSW of steel [46]. Weld time in RSW of magnesium, in the range 2-4 cycles (1 cycle=1/60 second), has a major impact on nugget size and shear strength, but this effect saturates at higher weld times [48]. Also, increasing weld time beyond 10 cycles results in continuous electrode indentation [48]. Electrode force affects the quality of spot-welds by controlling the contact area and resistance [46]. Contact resistance is inversely proportional to the electrode force. Therefore, increasing the electrode force results in less contact resistance, which means higher weld current is required to achieve spot-welds with the same nugget size and strength [49].

2.2 Literature Review

This section reviews some studies related to the subjects covered in the present research. The section starts with a synopsis of available studies on characterization of AZ31B magnesium sheet, and its spot-welds, with the main focus on fatigue behavior. Available constitutive models based on continuum mechanics for wrought magnesium alloys are then reviewed. The most common fatigue models, which have been developed for life estimation of spot-welded structures, will be described briefly at the end of this section.

2.2.1 AZ31B Mg Alloy and Spot-Weld Characterization

2.2.1.1 AZ31B magnesium alloy characterization

Strict standards and regulations for reducing fuel consumption and exhaust emissions have driven a new interest in light-weight materials in the automobile industry. Owing to its very low density, magnesium has been under the spot light in the past decade. Wrought magnesium alloys, compared to alternative casting alloys, exhibit superior behavior under tensile [50] and cyclic loading [51]. However, magnesium's application in auto industry is dominated by cast alloys [27,52], due to poor cold formability of wrought alloys.

The limited cold formability of wrought magnesium alloys is attributed to the limited number of slip systems [52,53]. As shown in Figure 2.1, dislocation slip deformation in HCP crystals may occur on basal, prismatic, and pyramidal planes. However, slip deformation primarily happens in the basal plane at room temperature, as a result of lower critical resolved shear stress (CRSS). The Von Mises criterion states that five independent slip systems are required for arbitrary uniform deformation [54,55]. Slip deformation does not provide adequate independent slip systems in HCP metals at room

temperature. Kocks and Westlake [56] argued that five independent slip systems are not necessary for homogeneous deformation of HCP metals, and another deformation mechanism, called twinning, may be activated to provide the required deformation systems. Twin deformation is dominantly activated through extension along the c-axis of magnesium HCP crystal, or compression parallel to the basal plane [57-60]. The twin CRSS is twice that of basal slip, while the CRSS for prismatic and pyramidal slip is about two orders of magnitude higher than that of basal slip for pure magnesium [52]. Twinned HCP crystals experience reorientation, such that the c-axis after twinning lies mostly in the original basal plane [59,61,62].

AZ31B magnesium sheet, similar to other wrought magnesium alloys, has a strong texture [63,64]. The rolling process reorients HCP crystals such that the basal plane is aligned parallel to the sheet surface [64]. Therefore, tension normal to the sheet surface and in-plane compression induce extension along the c-axis and may activate twin deformation. Nevertheless, since the rolling process does not produce sheets with a perfect texture, some inhomogeneities in crystals orientation exist. As a result, even in-plane tension may activate twin deformation in a limited number of grains, which are not aligned to the primary basal texture [52]. The CRSS for slip is three times that for twinning according to X-ray diffraction measurements, and the CRSS for prismatic slip is one to five times that of basal slip for AZ31B [52].

Wrought magnesium alloys exhibit distinct yielding and hardening behavior under in-plane tension and compression. Post yielding behavior of magnesium sheets under in-plane tension is similar to BCC and FCC engineering metals, *e.g.*, steel and aluminum, due to the slip deformation mechanism. The tensile curve has a concave-down shape with a continuously decreasing strain hardening rate. However, the yield strength of rolled magnesium alloys under compression is significantly less than that under tension [64-66]. Post-yielding stress-strain behavior under in-plane compression has an unusual concave-up appearance. Minimal strain hardening is observed for small plastic strains due to the activation of twin deformation [67]. Strain hardening gradually increases and

saturates by exhaustion of twin deformation. The flow curve is then followed by a behavior very similar to the hardening under in-plane tension [64]. Therefore, slip is believed to dominate the plastic deformation under large plastic strains [52]. At elevated temperatures, non-basal slip systems are easily activated and twinning is overwhelmed under in-plane compression, which results in a regular, non-inflected hardening curve [52,64].

Directional behavior, often referred to as anisotropy, has been observed in AZ31B sheet [65,66,68]. AZ31B shows higher yield strength, ultimate strength, and ductility in the transverse direction (TD) than in the rolling direction (RD) under monotonic tensile and compressive loading [66]. This behavior is attributed to stronger basal texture in the TD, which makes basal slip harder in this direction [52,66]. The strong texture also causes activation of non-basal slip systems in the TD, which are hard to activate in the RD, and makes the sheet more ductile in the TD [52]. Therefore, necking is observed in the TD [66], but brittle fracture occurs in the RD under monotonic tensile loading [52,66]. The overall shape of the stress-strain response in the normal-to-sheet direction (ND) under tension is the same as that in the RD and the TD under compression, due to activation of twin deformation [68]. AZ31B sheet under compression has a much higher flow stress in the ND but very low ductility, because basal and prismatic slip systems cannot accommodate plastic deformation along the c-axis [68].

Besides slip and twinning, untwinning is another mode of plastic deformation in HCP metals. Untwinning may happen in material crystals which have already undergone twin deformation, and eliminates or narrows twin bands [52,62]. Untwinning causes crystal reorientation by approximately 90°, such that crystals that have experienced reorientation during twinning deformation rotate back to their original orientation [61,62]. Untwinning, having the same nature as twinning, results in a concave-up hardening behavior [68]. However, untwinning is activated easier than twinning because nucleation is not required or happens more easily [52,62]. As a result, the elastic region during in-plane tension following compression is smaller than that for in-plane compression. During

untwinning, AZ31 shows little hardening after yielding as the accumulated twin deformation is recovered [69]. After exhaustion of untwinning, basal slip initially dominates [52], and then harder non-basal slip systems or compression twin systems are activated, and strain hardening rapidly increases [62,69].

Cyclic loading causes twinning and untwinning in consecutive reversals. Wu et al. [68] investigated AZ31B sheet under cyclic loading and explained fatigue characteristics using microstructural features. According to this work, texture measurement demonstrates that twin deformation accumulated during compressive loading is not fully recovered in subsequent tension reversal. Therefore, the volume fraction of twins continuously increases over cycles. Analyzing subsequent hysteresis loops shows that AZ31B sheet exhibits cyclic hardening behavior during compression and cyclic softening during the tension reversal [66,68]. Accumulation of twin deformation during cyclic loading demands activation of harder deformation systems in compression reversals, which results in cyclic hardening under compression [68]. On the other hand, the inflection point in the tension reversal is postponed to higher strain and post-untwinning hardening is delayed. Consequently, cyclic softening is observed in AZ31B at the end of tension reversal [68]. Strain-controlled cyclic testing by Lv et al. [66] shows that the stress amplitude is higher and plastic strain amplitude is lower in the TD than they are in the RD. Stabilized hysteresis plastic energy is higher in the RD than the TD, which causes superior fatigue performance in the TD [66].

The Bauschinger effect [70] is a common phenomenon in metals observed under cyclic loading, particularly in the low cycle fatigue regime. The Bauschinger effect states that strain hardening in forward loading reduces the yield strength in reverse loading. Dislocation pileups at grain boundaries and internal stress between dislocations are responsible for the Bauschinger effect [29,71,72]. Yielding under forward loading causes movement of dislocations and their pileup at barriers such as grain boundaries, and other dislocations [72]. Dislocations interact with repulsive forces which must be overcome to continue plastic deformation [29,73]. Plastic deformation in unloading and reloading

happens at lower yield stress because the dislocations' internal stress is in the same direction as the applied stress [29,73]. In materials where twinning is a significant deformation mechanism, twin bands act as hard barriers and dislocations may pileup at twin boundaries, which results in a larger Bauschinger effect than in materials with only slip deformation [73]. Begum et al. [74] and Lin et al. [69] characterized AZ31 under cyclic loading and reported that the Bauschinger effect was more pronounced at high strain amplitudes. Upon unloading reversal, *i.e.*, compression following tension, the Bauschinger effect is evident at the onset of yielding in compression. During reloading reversals, *i.e.*, tension following compression, the Bauschinger effect is much more significant due to the existence of twin bands, such that the material yields even before the applied stress becomes positive [62,69].

2.2.1.2 AZ31B spot-welding

Resistance spot welding is the predominant joining technique in automobile body assembly lines [16]. Owing to the new interest in magnesium in the automotive industry, many studies have been performed on the application of resistance spot-welding process to magnesium alloys.

Studies regarding RSW of magnesium alloys can be categorized into two major groups: Mg-to-Mg similar joints, and Mg to other metal (dissimilar) joints. Investigations of Mg-to-Mg RSW similar joints deal with different aspects of weld characterization, *e.g.*, effect of surface condition on RSW strength [75], effect of welding conditions on microstructure and mechanical properties of spot-welds [76,77], nugget growth simulation [78], *etc*. Work on magnesium RSW dissimilar joints have mainly focused on Mg-to-steel and Mg-to-aluminum, as they are the dominant metals in automobile body fabrication [79,80]. According to the scope of the present study, reviewed literatures are limited to those investigating effects of RSW parameters on AZ31-to-AZ31 joints.

For the goal of magnesium application in automobile body parts, a number of researchers have studied microstructural features of AZ31 spot-welds and effects of welding parameters on the microstructure. Sun et al. in 2007 [81] observed that the fusion zone (FZ) in AZ31 spot-welds

contains two distinct microstructure. FZ has cellular dendritic structure at the boundary, and equiaxed dendritic structure in the center. This finding was later confirmed by Lang et al. [76,82], Xiao et al. [83], and Babu et al. [84]. Increasing weld current results in coarser cellular and equiaxed dendrites. This observation was explained using cooling rates, which decrease by increasing the welding current or heat input [76]. Xiao et al. [85] reported that the width of the cellular dendritic region is controlled by Al_8Mn_5 intermetallic particle size, *i.e.*, coarser Al_8Mn_5 particle size tends to narrow the cellular dendritic zone. In addition to Al_8Mn_5 [83,85], $Al_{12}Mg_{17}$ second-phase particles were detected inside the FZ of AZ31 spot-welds [76,84,85]. Electrode force within the range 1.5-3.5 kN has minimal effect on the FZ microstructure. However, excessive electrode force (4.5 kN) changes microstructure at the nugget core from equiaxed dendritic structure to equiaxed grains [76]. Some pores were observed inside the FZ by Babu et al. [84], the formation of which was attributed to interaction of molten magnesium with air and moisture in a surface oxide film at the interface. Work by Sun et al. [81] and Lang et al. [82] showed that AZ31 magnesium alloy is highly susceptible to solidification cracking in the FZ. Low melting point interdendritic region along with tensile stress during cooling is responsible for solidification cracking [81,82]. These studies state that susceptibility of solidification cracking rises with increasing heat input, *i.e.*, increasing welding current or time. The FZ is surrounded by heat affected zone (HAZ), the microstructure of which is granular with coarser grains compared to those in unaffected base metal (BM) [81,84]. "*Liquation cracking*" happens in the HAZ at the vicinity of the FZ [82]. Similar to solidification cracking, a low melting point intergranular region and tensile stresses induced during cooling, are responsible for liquation cracking [82].

Hardness is often measured in welds to study effects of welding process on probable strength discontinuities in the BM and weld region, *i.e.*, HAZ and FZ. Hardness measurement for RSW is performed on a diagonal traverse across the weld cross-section using micro-indentation hardness (Vickers or Knoop) instruments [86]. Liu et al. [87] showed that a small hardness under-matching exists in the FZ of AZ31 spot-welds as compared to the BM. Reduction of dislocation density in the FZ was identified as the reason for lower hardness values inside the nugget. In contrast, the work by Babu et al. [84] showed that hardness within the weld region is significantly less than that in the BM.

Dendritic structure and large grains were identified as responsible factors for lower hardness in the FZ and HAZ, respectively.

Effects of welding parameters on static strength and failure modes have been studied by a number of researchers. Lang et al. [76] found through experiments that increasing weld time up to 16 cycles continuously enlarges nugget diameter and enhances ultimate tensile-shear load. Work by Sun et al. [81] and Lang et al. [76] demonstrate that increasing weld current up to 23 kA (for a constant welding time) increases nugget size and improves ultimate tensile-shear load. However, static strength diminishes at welding currents higher than 23 kA, even though the nugget is still enlarged [76]. Liu et al. in 2010 [87] investigated the effect of FZ microstructure on static strength of AZ31 spot-welds. They found that improving the static strength of RSW requires narrow cellular dendritic structure with short primary dendrite arms rather than wide cellular dendritic zone with long primary arms [87]. Two failure modes are commonly observed under monotonic tensile-shear loading: interfacial and button-pullout, depending on welding current. Low welding current results in interfacial failure, and high welding current causes button-pullout failure [76,81]. Nevertheless, static tensile-shear testing on RSW specimens with large coupon thickness of 3 mm resulted in only interfacial failure [84]. This observation suggests that increasing sheet thickness tends to shift the failure in magnesium spot-welds to the interfacial mode, which has been observed for steel spot-welds [88].

Published research available regarding fatigue characterization of RSW of AZ31 are limited to a very few studies. Xiao et al. in 2011 [83] observed only two modes of failure: interfacial failure in LCF, and coupon failure in HCF. When failure happens in the interfacial mode, fine FZ microstructure results in superior fatigue resistance as compared to coarse microstructure [83].

To the best of author's knowledge there has been no published research on fatigue modeling of magnesium spot-welds.

2.2.2 Constitutive Modeling

Modeling the plastic behavior of materials is a crucial part of elastic-plastic simulations. Approaches to describe plasticity of materials may be divided into two basic groups: crystal plasticity and continuum plasticity. Crystal plasticity models explicitly account for crystal orientations, possible slip and twinning deformation systems, critical resolved shear stresses for activating deformation systems, and interaction between slip and twinning systems. Crystal plasticity models capture anisotropy of materials by updating the initial texture employing a suitable model [89]. Crystal plasticity models can be implemented into a finite element (FE) code to predict the polycrystalline aggregate behavior [90]. However, such FE simulations demand very intensive calculations which limit application of this approach in real-life problems. Literature regarding crystal plasticity is not reviewed because this approach was not followed in this study.

Continuum plasticity is an alternative approach which is computationally more efficient and suitable for more complex problems. Continuum plasticity models require three fundamental components: flow rule, yield function, and hardening rule.

The flow rule determines the components or the direction of the plastic strain or the plastic strain increment. The flow rule is one of the consequences of Drucker's postulate [91] for material stability. Associated and non-associated flow rules are the two common flow rules [92]. An associated flow rule assumes that the plastic strain increment vector is normal to the yield surface at the current point in stress-space, and is often adopted for engineering metals [92,93]. A non-associated flow rule assumes that the plastic strain increment vector is normal to the plastic potential surface, and is often applied to geo-materials such as soil, rock, and concrete [92,93]. Flow rules are explained in more detail in Chapter 4.

The yield function is a function of stress components and specifies the shape of the yield locus in stress-space under multi-axial loading. Several yield criteria have been proposed for different engineering materials since the 1850s. The yield functions developed by Tresca in 1864 [94], von Mises in 1913 [95], and Drucker in 1948 [96] are among the first and most well-known formulations for isotropic materials. Hill in 1948 [97] proposed a quadratic yield criterion for anisotropic materials by generalizing the Mises yield function. Later experimental evidence indicated that quadratic yield surfaces cannot follow the yielding behavior of polycrystalline BCC and FCC metals [98]. The development of a non-quadratic isotropic yield function by Hosford in 1972 [99] was an attempt at a more successful description of the yield surface for these materials. Since then, several non-quadratic anisotropic criteria were developed: by Hill in 1990 [100], Barlat et al. in 1997 [101], Cazacu et al. in 2003 [102], *etc*. However, these models targeted metals with cubic microstructure, and therefore were not able to account for tension-compression yield asymmetry. Hosford in 1966 [103] modified the Hill's [97] criterion to describe tension-compression yield asymmetry. Nevertheless, this function was only successful for metals with minor yield asymmetry such as titanium [104]. Cazacu et al. in 2004 [104] modified Drucker's [96] criterion, which includes both J_2 and J_3 invariants of the Cauchy stress deviator. This yield function was the first macroscopic criterion that accounts for both anisotropy and yield asymmetry of HCP metals. Comparing the yield loci predictions with available data for titanium [104] and magnesium [105] indicates that this yield criterion can accurately capture yielding behavior of these metals. In 2006, Cazacu et al. [106] proposed another yield function to describe anisotropy and tension-compression yield asymmetry, the validity of which was confirmed by a number of studies [89].

The hardening rule dictates how the yield surface evolves during plastic deformation. Isotropic and kinematic hardening models are the two basic hardening rules. Isotropic hardening assumes that a yield surface uniformly expands during plastic deformation, without any change in the yield surface origin [107]. Isotropic hardening properly models materials' behavior under monotonic loading, but

not under non-proportional loading or where reverse loading is involved [108]. In contrast, kinematic hardening assumes that a yield surface only translates, with no change in shape and size. Since it accounts for the Bauschinger effect, kinematic hardening is often preferred where a materials' behavior under reverse loading is of interest [70]. Prager in 1956 [109] proposed the simplest form of the linear kinematic hardening rule. The back-stress increment in Prager's model is proportional to the plastic strain increment vector. A drawback of this hardening rule is that uniaxial loading results in multi-axial translation of the yield surface. This consequence of Prager's rule implies that during uniaxial loading, materials soften or harden in lateral directions, which is not supported by experimental results [93]. To overcome deficiencies of Prager's hardening rule, Ziegler in 1959 [110] proposed a model that assumes the yield surface translates in the radial direction. Prager's and Ziegler's hardening models may capture the Bauschinger effect [70], but not transient behavior [111].

Several constitutive models have been developed for nonlinear hardening materials, which can be classified into: single surface, multi-surface and two-surface plasticity models. Armstrong and Frederick (A-F) in 1966 [112] added a term to Prager's model to recall back-stress. Chaboche in 1986 [113] generalized A-F's modification by adding multiple back-stress recall terms to better describe the ratcheting effect. A multi-surface family of models was introduced by Mroz in 1967 [114], which involve multiple yield surfaces with Prager's linear kinematic hardening rule between each two subsequent yield surfaces. A shortcoming of the Mroz model is that yield surfaces may intersect under non-proportional loading. To resolve this issue, Garud in 1981 [115] modified the Mroz model. Two-surface models were proposed by Krieg in 1975 [116] and Dafalias and Popov in 1976 [117]. Two-surface constitutive models use two yield surfaces with continuous updating of the hardening between the two surfaces. The original two-surface models were modified by a number of researchers; for instance, Hassan in 1994 [118] proposed a two-surface plasticity model which accounts for cyclic ratcheting behavior. Advancements in cyclic plasticity have been reviewed in detail by Chaboche in 2008 [119].

Although extensive studies have been performed regarding constitutive modeling of metals under cyclic loading, only a few published works are available for materials with asymmetric hardening behavior, such as magnesium. Most of the continuum-based constitutive models developed for magnesium have been intended for sheet forming applications. Therefore, formulations were derived using the plane-stress state assumption, which remarkably limits the applicability of these models. Li et al. in 2006 [108,120] proposed the first phenomenological constitutive models for wrought magnesium alloys. To simplify the formulation and numerical implementation, von Mises isotropic yield criterion was adopted and a plane-stress state was considered in this model. A non-zero initial back-stress was assumed to describe anisotropy and yield asymmetry. A combination of isotropic and kinematic hardening rules was adopted to formulate evolution of the yield surface. The model was able to regenerate the unusual hardening behavior of magnesium under uniaxial compression and uniaxial tension following compression. The plastic deformation mechanism was modeled by considering reorientation of grains during twinning and untwinning. The constitutive model was verified by simulating a simple shear test and comparing with experimental results.

Kim et al. in 2008 [121] developed a constitutive model for AZ31 magnesium sheet at room temperature. Plane-stress was assumed, as this model has intended for magnesium sheet metal forming. The yield criterion proposed by Cazacu et al. in 2006 [106] was adopted. Due to the asymmetric hardening behavior, two different isotropic hardening laws were employed for tension and compression. The constitutive model was verified by simulating a three-point bending test. A deficiency of this model is that it does not account for the Bauschinger effect, because back-stress evolution is not considered in the hardening rule.

Lee et al. in 2008 [90] developed a phenomenological continuum plasticity model which captures both anisotropy and asymmetry of AZ31B magnesium sheet. The modified Drucker-Prager's yield criterion [122] was adopted assuming plane-stress, along with isotropic-kinematic hardening rule. The original two-surface model was extended to include the three plastic deformation

mechanisms: slip, twinning, and untwinning. It was shown that the model was able to regenerate material behavior under uniaxial loading paths; however, no model verification was presented. A shortcoming of this model is that the Drucker-Prager's yield function is pressure dependent, and is applicable to porous media, not HCP metals which are essentially pressure insensitive [104].

Nixon et al. in 2010 [89] proposed a continuum based constitutive model for high purity α-titanium. The yield function proposed by Cazacu et al. in 2004 [104] in generalized form for anisotropic materials was adopted in conjunction with the anisotropic hardening model developed by Plunkett et al. in 2006 [123]. According to this hardening rule, coefficients of anisotropy as well as the size of the yield surface are updated in each increment. However, the yield surface center is assumed to be fixed at the origin. The model output was compared with experimental data under uniaxial loading, but the model was not verified using a more general load case. A drawback of this model is that the hardening rule does not account for back-stress evolution. Consequently, this model is not applicable to problems where reverse loading is involved, *e.g.* cyclic plasticity.

2.2.3 Fatigue Modeling of Spot-Welded Structures

Numerous models have been developed for predicting fatigue life of spot-welds, and verified mostly for steel spot-welds. These models can be categorized into three major groups: fracture mechanics, structural stress, and local strain approaches.

The spot-weld in some studies is considered as a sharp notch, and is treated as a crack [124-126]. The fatigue models based on fracture mechanics consider a measure of stress intensity factor (SIF) or J-integral as the damage parameter and relate this parameter to the fatigue life or the crack growth rate. Crack initiation life is usually assumed to be insignificant in these models. Pook in 1975 [127] derived formulations for mode I and II stress intensity factors for tensile-shear spot welds, assuming that the notch at the nugget edge is an initial crack. Stress intensities were calculated for the initial state, neglecting specimen rotation and crack growth. Contributions of the mode II SIF were ignored in this model, and the range of mode I SIF, ΔK_I, was introduced as a fatigue damage parameter. Neglecting fatigue crack initiation life, Paris' equation was employed to relate fatigue crack growth rate to SIF range, and this was integrated to predict total life. A drawback of this model is that the formulations are based on a through-nugget cracking assumption, while experiments have shown that base metal cracking is the common failure mode for tensile-shear specimens. Also, a limitation of Pook's formulation is that it is not applicable to spot-weld problems under a general load case. The applicability is restricted to spot welds in tensile-shear configuration with the ratio $r/t \leq 5$, where r is the spot-weld nugget radius and t is the sheet thickness.

Swellam in 1992 [18] developed a fatigue model for spot-welds based on the fracture mechanics approach, combining the effect of mode I and mode II SIFs. This model considered spot-welds under a general load case, and found forces and moments at the spot-weld center from static equilibrium of a coupon. The loads at the spot-weld, including axial load, shear load, and bending moment, were obtained from hand calculations for simple specimens, or from linear FE analysis for complex

structures. SIF formulations developed by Tada et al. [128] for two half spaces joined by a circular region were adopted. Normal and shear SIFs were related through a function to an equivalent SIF, which was used with Paris' equation to obtain fatigue life. Because SIFs were assumed to be independent of crack length, an explicit equation was derived between equivalent SIF and the fatigue life. Although this model does not theoretically have any applicability limitation, it fails to predict contributing loads and moments for some loading configurations, such as cross-tension. Moreover, a through-nugget crack is assumed in this model.

Newman in 1998 [129] developed a closed form equation for fatigue life estimation of spot-welds under the tensile-shear load case. Formulations proposed by Pook [127] for mode I and II SIFs were employed and combined to obtain an equivalent mode I SIF on the plane of maximum principal stress. A number of assumptions were made to generate a closed form solution: SIFs were assumed to be constant and independent of crack length, crack was assumed planar, the ratio of specimen width-to-nugget radius was greater than 5, and the average stress on the nugget was less than 80% of the yield strength of the base metal. This model is based on Pook's formulation and assumes through-nugget cracking, and considers the nugget edge as the crack initiation point, which is not supported by experimental observations.

Since the late 1980's, a number of models have related the fatigue life of spot-welds to structural stress. Structural stress is a linearly distributed stress over the thickness, obtained by neglecting the effect of any stress concentration. The structural stress is usually calculated by superposing the effects of different forces and moments, which are obtained from linear elastic FE simulations. For FE modeling of spot-welded structures, the sheets and spot-welds are modeled by shell and beam elements, respectively. The structural stress approach, due to its flexibility, is widely employed in industry, including the automobile industry [130]. However, some weak points are inherent in fatigue models based on this approach. A serious shortcoming with this approach is that the notch effect at the spot-weld edge is ignored [130].

The models proposed by Radaj [131], Rupp [132], and Sheppard [133] are among the most frequently used models based on the structural stress approach. Radaj in 1989 [131] proposed the concept of structural stress. Assuming that the spot-weld is an ideal crack-like slit, SIFs for mode I, II and III load cases were related to nominal structural stresses. SIFs were combined through an equation to obtain an equivalent SIF, which was used for fatigue life estimation. Radaj in 1990 [1] presented formulations for structural stresses in terms of forces and moments, which were element nodal forces at the node shared between the spot-weld (beam element) and the considered plate (shell element). A drawback of this model, similar to the fracture mechanics approach, is that the fatigue crack is assumed to be through the nugget. Also, SIFs are assumed constant during the course of crack propagation.

Rupp et al. in 1995 [132] employed theories of beams, sheets and plates to develop a structural stress definition for spot-welds. Forces and moments (membrane, transverse and normal forces, as well as two out-of-plane bending moments) were obtained at the nugget center from a FE analysis. Through-nugget cracking and through-plate cracking were considered as possible failure modes in spot-welded structures. The beam theory was used to find structural stresses for through-nugget failure, and knowing that the nugget has a brittle structure, the maximum normal stress criterion was used as a fatigue damage parameter. Sheet and plate theory was employed to obtain structural stresses for through-plate failure, and the equivalent von Mises stress was used as the damage driving factor. Depending on whether the representative stress in the nugget or plate was higher, failure was predicted to happen in the corresponding mode. An advantage of this model is that not only the fatigue life, but also the mode of failure is predicted. A weak point of this model is it only considers resultant loads in the nugget and therefore the effect of self-equilibrating forces on structural stresses are missing.

Sheppard et al. in 1992 [134] developed a model to predict fatigue crack initiation life for spot-welds based on the structural stress concept. The structural stress definition in this model only

accounted for membrane load and bending moment. Structural stress range was obtained on neighboring elements to the spot-weld at the node shared with a spot-weld beam element on both sheets. The maximum structural stress range was converted to actual elastic-plastic stress and strain ranges using Neuber's rule at the spot-weld edge. The stress concentration factor was obtained using an equation proposed for tensile-shear specimens. The Smith-Watson-Topper relationship [135] was employed to find fatigue initiation life in terms of actual stress and strain ranges.

Sheppard in 1993 [19] extended the application of the structural stress to estimate fatigue crack propagation life. Considering only mode I effects, the SIF range was obtained in terms of structural stresses due to membrane load and bending moment. An explicit equation was derived between structural stress range and fatigue crack propagation life through Paris' equation and a number of assumptions. Structural stress definition was later modified in 1996 to take the effect of normal (cupping) force into account [133]. Some common problems with structural stress-based models were resolved in this model. For instance, crack initiation and propagation phenomena were explicitly included, and the SIF for mode I loading was not assumed constant during crack propagation. However, effects of modes II and III loadings in crack propagation were still ignored. There was no comprehensive formulation for calculating stress concentration factors under a general load case. Furthermore, similar to other models based on the structural stress approach, effects of material anisotropy and yield asymmetry were not taken into account.

Some studies, in contrast to the fracture mechanics approach, consider a spot-weld as a blunt notch with a finite radius. Therefore, a detailed FE model with a fine mesh in the vicinity of the spot-weld is required. The fatigue life in these models is usually related to a measure of local stress/strain at the spot-weld edge. Local stress/strain values are calculated from an elastic-plastic FE simulation, or from an elastic solution along with a variant of Neuber's rule [136]. An advantage of this approach is that the effect of the spot-weld notch is well described. Also, cyclic characteristics of materials, *e.g.*, anisotropy and hardening asymmetry, may be accounted for. On the other hand, a number of

drawbacks are also present. For instance, crack propagation is not considered in local notch models. Moreover, intensive FE calculations restrict applicability of this approach for real-life problems. The most commonly referenced models in this group were developed by Oh [137] and Pan [20]. Oh in 1982 [137] obtained stress/strain results from linear elastic FE analysis. The elastic solution in the region around the spot-weld nugget was then transferred to an elastic-plastic solution using Neuber's rule. These estimated stress and strain values were then related to total fatigue life through Morrow's rule [138]. This model is computationally more efficient but less accurate than elastic-plastic FE simulation. Also, stress concentration factor was calculated based on a two-dimensional representation of the spot-weld.

Pan in 2000 [139] demonstrated that Sheppard's structural stress model was not successful for spot-welds with dissimilar thicknesses. Therefore, Pan [20,139] proposed a local strain model for such cases. Local stress and strain values at the spot-weld edge were directly obtained from three-dimensional elastic-plastic FE simulations. Nonlinear geometry and material properties were included in the FE analysis. Because the HAZ of the spot-weld contains a gradient of material properties from BM to FZ, this region was split into several subzones with corresponding nonlinear properties, if information was available. The location where maximum principal strain occurred at the end of the first reversal was selected as the hot spot. Cyclic principal strain range was calculated as the difference between principal strain values at the hot spot at the end of the first and second reversals. Cyclic principal strain range was considered as the fatigue damage parameter and was related to total fatigue life. Although this approach does not provide a justifiable description for crack propagation, a better correlation was achieved with this model for spot-welds with dissimilar thicknesses than Sheppard's structural stress model [20].

Chapter 3

Experimental Work

This chapter introduces the material investigated and the specimens adopted for the range of tests considered. Material characterization was performed from both microstructural and mechanical points of view. Microstructure and hardness results regarding the base metal and different regions of the weld are presented and analyzed. Monotonic and cyclic test results are demonstrated and the specimen failure modes are discussed. The effect of cyclic loading on microstructure and fatigue crack initiation and propagation are explained. Finally, the mechanical behavior of resistance spot-welds is compared with that of friction stir spot-welds. A part of this chapter has been published in a paper entitled: “Characterization of magnesium spot welds under tensile and cyclic loadings”.

3.1 Material and Specimens

3.1.1 Material

The material investigated in this research was AZ31B-H24 hot-rolled magnesium sheet. The sheet was provided by Magnesium Elektron of North America (MENA) with the dimension 20" × 48", in 2 mm and 4 mm thicknesses. The sheet is produced by rolling the direct-chill casted ingots. The chemical composition of the sheet is listed in Table 3.1.

Table 3.1: Chemical composition of AZ31B-H24 magnesium sheet

Composition	Al	Zn	Mn	Mg
Weight %	2.73	0.915	0.375	Bal.

3.1.2 Base Metal Specimens

This research focuses on fatigue behavior of spot-welded AZ31B-H24 sheet. As a result, the specimens for tensile and fatigue tests of the base metal were flat.

Three different flat specimen geometries were used for mechanical characterization of the AZ31B-H24 sheet. Dog-bone shape specimens and laminated blocks were adopted for monotonic testing, and sub-size dog-bone shape specimens were utilized for fatigue testing.

The most common geometries for flat specimen testing are based on the American Society for Testing and Materials (ASTM) standard [140,141]. These specimens are straight throughout the reduced section. Monotonic tensile and especially cyclic testing on standard specimens shows that many of them fail under the extensometer knife edge, or even outside the gage length, due to the uniform stress distribution all along the reduced section. Therefore, the specimen geometry shown in Figure 3.1 was employed for tensile testing of the base metal. The main feature of this design is that the reduced section has a continuous curvature, which provides the minimum cross-section at the

middle of the cross-section while maintaining a near-uniform stress distribution within the gauge length. This geometry has been proposed by Professor T. Topper at the University of Waterloo in an unpublished study. Monotonic tensile specimens were machined from 2 mm-thick sheets; all 10 specimens tested failed inside the gauge length.

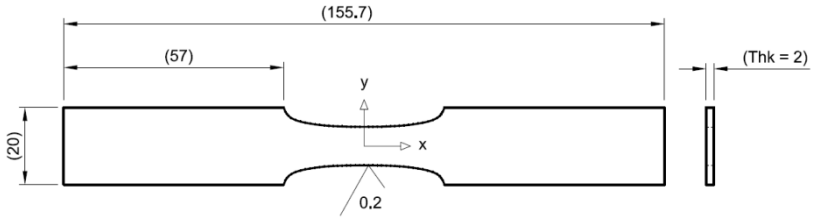

x [mm]	y [mm]
0.00	5.00
1.14	5.00
2.28	5.01
3.42	5.02
4.56	5.04
5.70	5.07
6.85	5.11
8.00	5.17
9.15	5.25
10.33	5.33
11.51	5.45
12.72	5.61

x [mm]	y [mm]
13.95	5.81
15.23	6.05
16.53	6.35
17.80	6.74
18.91	7.28
19.60	7.84
20.00	8.29
20.40	8.89
20.85	10.00
77.85	10.00
77.85	0.00

Notes

1. All dimensions are in (mm) except the surface roughness which is in micro-meter.
2. Curvature of the reduced section is determined by the coordinates shown in the table.
3. Axes x and y are axes of symmetry.

Figure 3.1: Specimen geometry for monotonic tensile testing of AZ31B-H24

Monotonic compression testing of the base metal was first examined using a geometry similar to the tensile specimens. The only difference was that the compression specimens were prepared from 4 mm-thick sheet to avoid bucking. The first compression test revealed a clear buckling at the beginning of the test. In the next attempt, the compression test was performed on a sub-size specimen which was essentially the same as the tensile specimen, scaled down by the factor of 0.4; it was machined from a 4 mm-thick sheet. This geometry was chosen to provide a square cross-section (4×4 mm^2) in the middle of the gauge length to eliminate the preferred buckling axis. The new design improved the buckling instability threshold significantly. However, the specimen still buckled before reaching the ultimate compressive stress. The next type of compression specimen used was a laminated block. Because of unavailability of AZ31B-H24 sheets with higher thickness, two strips were cut to the rough size of 16×8.5×4 mm^3, glued together, and finally machined to the exact size according to Figure 3.2.

The laminated block specimens could successfully withstand the compressive load to the ultimate compressive stress without buckling or delamination. The monotonic compression test setup will be introduced later, in section 3.3.1.1.

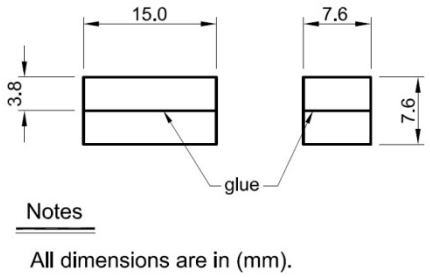

Figure 3.2: Specimen geometry for monotonic compression testing

Fatigue testing of the base metal was performed on sub-size specimens to prevent buckling during compressive reversals. For the same reason, the specimens were machined from a sheet with 4 mm thickness. Figure 3.3 illustrates the fatigue specimen geometry.

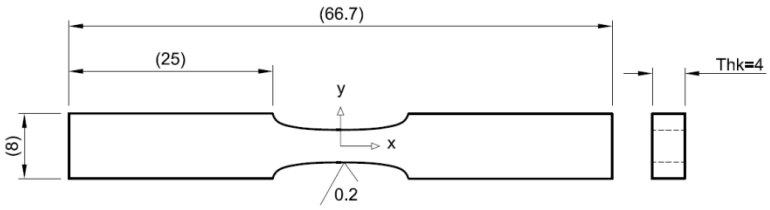

x [mm]	y [mm]
0.00	2.00
0.46	2.00
0.91	2.00
1.37	2.01
1.83	2.02
2.28	2.03
2.74	2.05
3.20	2.07
3.67	2.10
4.13	2.14
4.61	2.18
5.09	2.25

x [mm]	y [mm]
5.59	2.32
6.10	2.42
6.62	2.54
7.13	2.70
7.57	2.91
7.85	3.14
8.01	3.32
8.17	3.56
8.35	4.00
33.35	4.00
33.35	0.00

Notes

1. All dimensions are in (mm) except the surface roughness which is in micro-meter.
2. Curvature of the reduced section is determined by the coordinates shown in the table.
3. Axes x and y are axes of symmetry.

Figure 3.3: Specimen geometry for fatigue testing

Fully-reverse fatigue testing was accomplished on sub-size specimens up to 2% strain amplitude.

3.1.3 Spot-Welded Specimens

Spot-welds in real-life structures are exposed to various modes of loading. As a result, successful fatigue modeling of spot-welds requires fatigue test results from specimens with different configurations to include the spot-weld behavior under various loadings. Typical spot-welded specimens are shown in Figure 3.4.

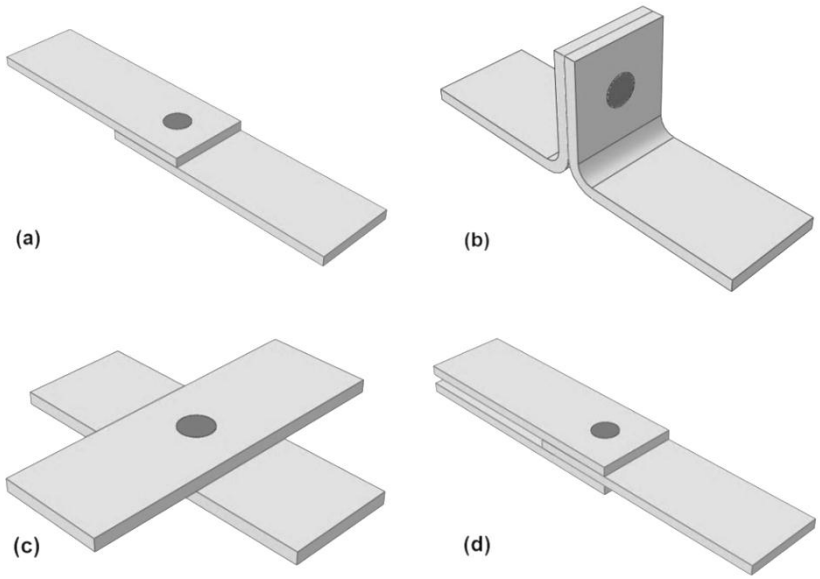

Figure 3.4: Typical spot-welded specimens (a) tensile-shear (b) coach-peel (c) cross-tension (d) pure-shear

Tensile-shear and coach-peel are the most common specimens in the literature [142-144], mainly because no extra test setup or fixture is required. An attempt at preparing a coach-peel specimen was not successful in this research, because fabricating the bent coupons from AZ31B sheets was not feasible. The fact that magnesium has limited formability at room temperature is responsible for this behavior [145]. Bending magnesium coupons at elevated temperature was tried by the resistance spot-welding group at the University of Waterloo but failed even at 250°C. Consequently, the cross-tension (CT) design was used in this research as an alternative to the coach-peel specimen, along with the tensile-shear (TS) design.

Two different designs for the TS specimens, with different coupon widths and gripping distances, were employed in this study. TS specimen geometries are displayed in Figure 3.5.

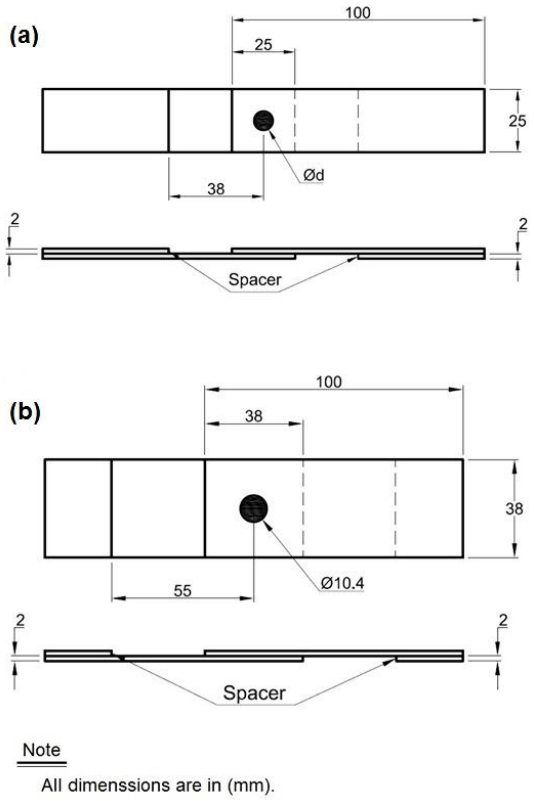

Figure 3.5: Tensile-shear spot-welded specimen geometries: (a) standard (b) wide

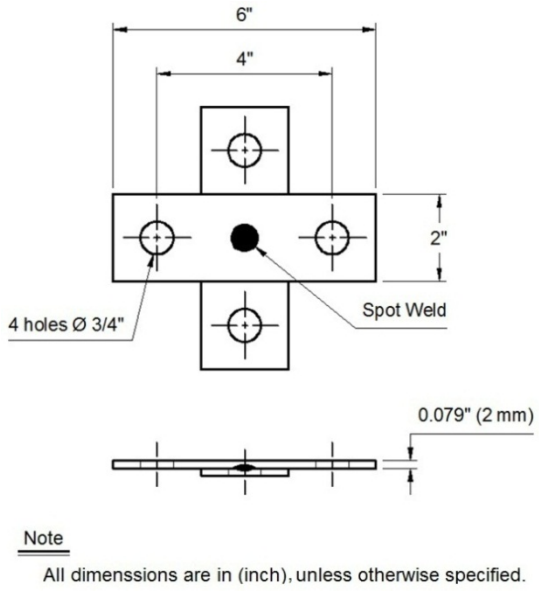

Figure 3.6: Cross-tension spot-welded specimen geometry

The design of the narrow TS specimen, Figure 3.5(a), is according to the American Welding Society (AWS) standard [47] and resistance welding manual [146]. The wide TS specimen geometry, Figure 3.5(b), is more common in the literature. To compensate for the coupons offset and prevent initial bending of the specimens, two spacers with the same thickness as the plate were attached to the ends of the TS specimens.

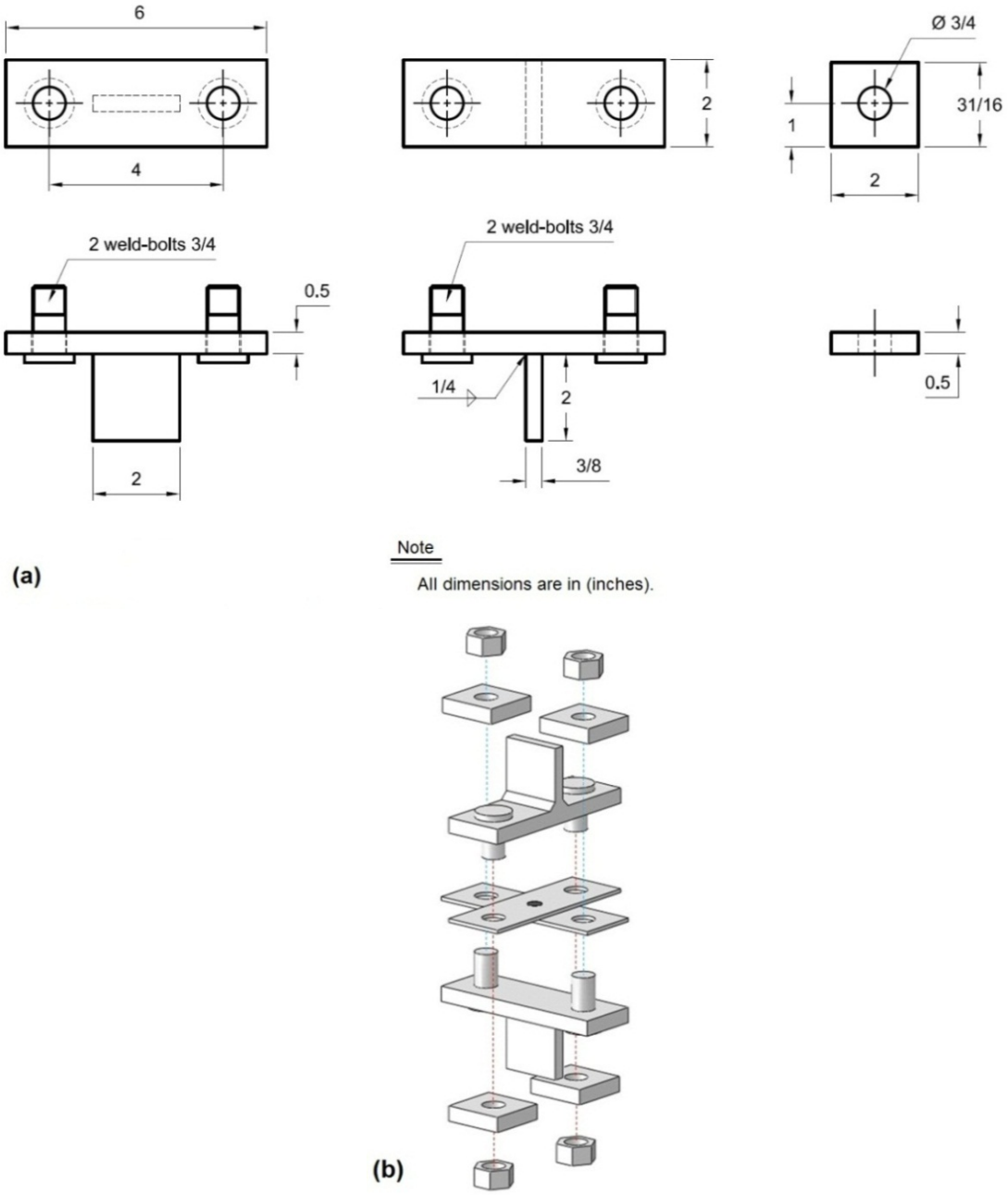

Figure 3.7: Cross-tension specimen (a) testing fixture (b) test setup exploded view

Figure 3.6 illustrates the design of the CT specimens, which is in accordance with the resistance spot welding manual [146]. Testing CT specimen requires a fixture to adapt the specimens to standard tensile testing machines, as shown in Figure 3.7.

Spot-welded specimens were prepared by Ray Liu and Tirdad Niknejad in the resistance spot-welding laboratory at the University of Waterloo. Coupons were cut along the sheet rolling direction and the surfaces were cleaned with chromic acid (2.5 gr CrO_3 + 100 ml H_2O) before welding, to obtain spot-welds with less porosity and expulsion [75].

Seven sets of spot-welded specimens in TS and CT configurations were prepared with an AC spot-welding machine. Six out of seven sets of spot-weld specimens tested were in the TS configuration. Each set consisted of 30 specimens. Different welding parameters were used to achieve different spot-weld nugget diameters. Table 3.2 summarizes the specifications of the specimens and the coding. Nugget sizes were measured after monotonic testing as the average diameters of the bonding area, along and perpendicular to the loading direction.

Table 3.2: Spot-welded specimens coding and process parameters

Specimen set	Configuration	Welding current (kA)	Welding time (cycle [c])	Electrode force (kN)	Avg. nugget size (mm)
A	TS [a]	26	10	4	8.2 (0.7) [d]
B	TS	28	8	4	8.6 (0.4)
C	TS	30	8	4	9.5 (0.1)
D	TS	32	8	4	9.8 (0.1)
E	TS	34	8	4	10.4 (0.2)
F	TS-W [b]	34	8	4	10.4 (0.2)
G	CT	34	8	4	10.4 (0.2)

[a] Standard size tensile-shear, Figure 3.5(a)
[b] Wide tensile-shear, Figure 3.5(b)
[c] 1 cycle = 1/60 sec (Power frequency = 60Hz)
[d] values in parentheses are standard deviations.

The quality of spot-welds after preparation of some specimens from each set was evaluated according to the standard welding qualification criteria, described in the AWS standard [47].

3.2 Microstructural Characterization

As a part of this research, the base metal, *i.e.*, AZ31B-H24, and different regions of the spot-weld were characterized from a microstructural point of view to obtain a better understanding of the fatigue behavior of magnesium spot-welds, and how it relates to microstructural features. Metallographic observations and hardness measurement results are presented and discussed in this section.

3.2.1 Microstructure

A number of specimens from sets A, C, and E were used to prepare metallographic samples for studying the effect of welding parameters and cyclic loading on the microstructure and hardness in the base metal (BM) and the weld region. These specimens were sectioned slightly offset from the nugget centerline, along the loading direction. The samples were then mounted, ground, and polished to the nugget centerline and etched with a solution of 4.2 gr picric acid, 10 ml acetic acid, 70 ml ethanol, and 10 ml distilled water.

Figure 3.8 shows the microstructure of the BM in the rolling and transverse directions (RD and TD).

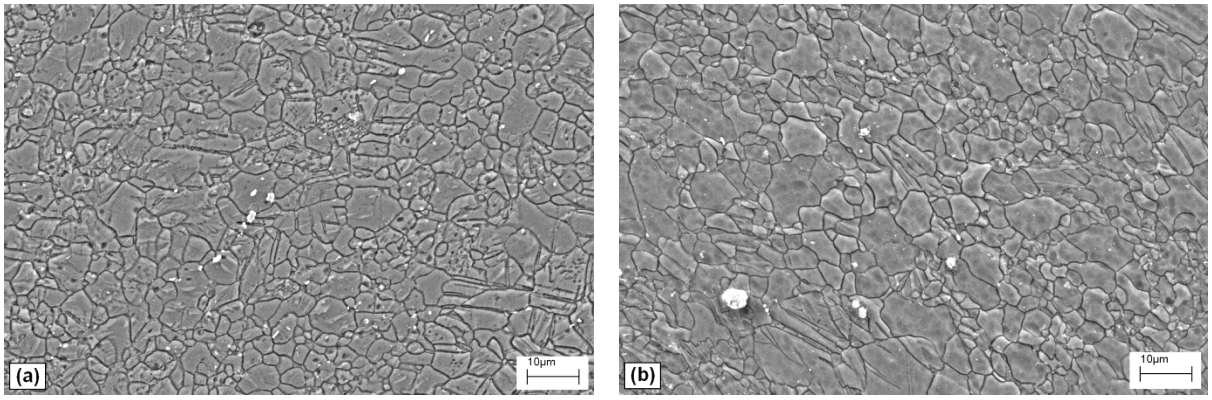

Figure 3.8: Microstructure of the base metal (a) in RD (b) in TD

It can be seen that grains were equiaxed with approximately the same average grain size of 5 μm in both RD and TD. Grains were not elongated in the rolling direction as a result of recrystallization phenomenon during the annealing process after rolling of the AZ31B-H24 sheet.

The microstructure in AZ31B magnesium spot-welds consisted of a heat affected zone (HAZ), partially melted zone (PMZ), and fusion zone (FZ). Figure 3.9 shows a quarter of a spot-weld, illustrating these regions.

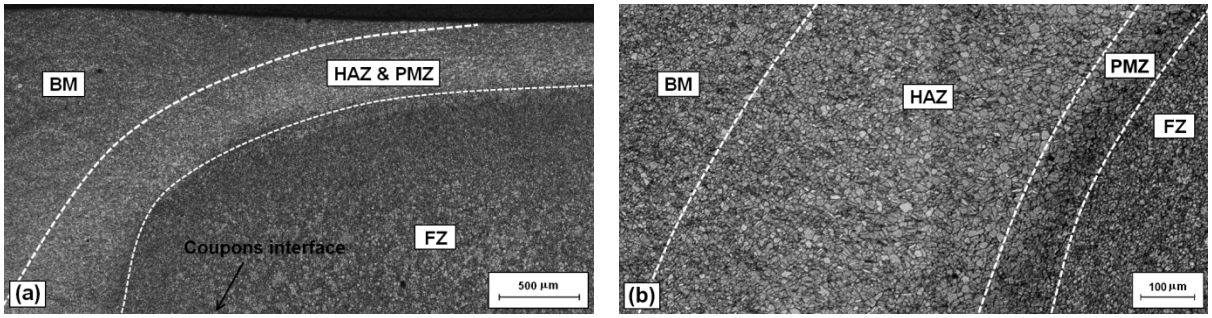

Figure 3.9: Different zones in AZ31B spot-welds (a) low magnification (b) high magnification

The heat affected zone is the region where the temperature is high enough to change the microstructure, *i.e.*, recrystallization, but not sufficient for melting. Figure 3.10(a) displays the microstructure of the HAZ with a grain size gradient, *i.e.*, 6-10 μm, increasing toward the PMZ boundary.

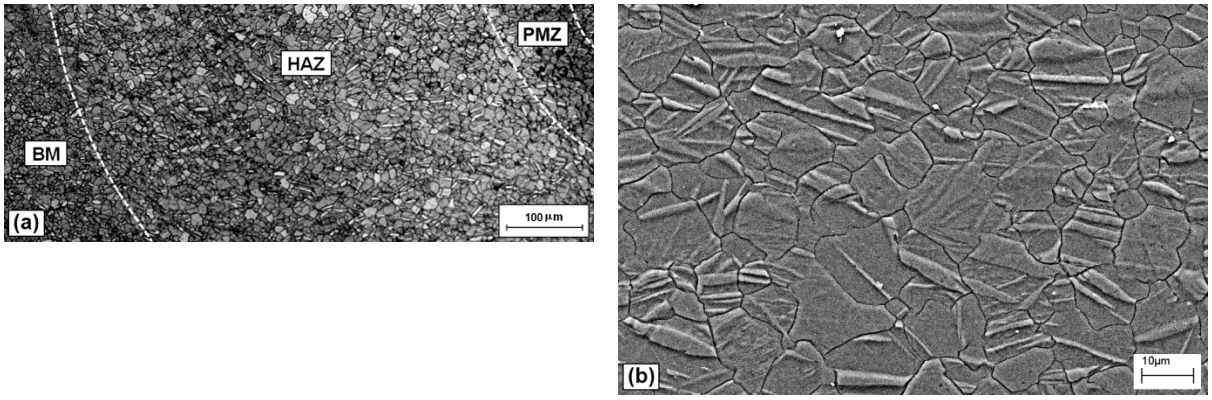

Figure 3.10: Microstructure of HAZ in AZ31B spot-welds (a) low magnification (b) high magnification

The reason is that the region in the HAZ close to the PMZ has a higher annealing temperature and time, compared with the region neighboring the BM. Also, considering liquation does not occur

in the HAZ, even in grain boundaries with a lower melting point than grains, intermetallic particles are not expected to form in this region. Figure 3.10(b) shows an SEM image from the HAZ without any indication of intermetallics. Another microstructural feature is that the twin band density is remarkably higher in the HAZ than in the BM. Highly twinned recrystallized region has already been observed in AZ31 welds [147].

The partially melted zone is the region surrounding the FZ in which liquation may happen locally during the welding process. The microstructure in the PMZ is shown in Figure 3.11. The peak temperature in the PMZ of AZ31 is between the solidus and liquidus temperatures, and therefore grain boundaries due to higher aluminum content and lower melting point may liquate. During solidification, because of a high cooling rate, the aluminum content does not have enough time to make a homogeneous solid solution in the α-matrix. Therefore intermetallics ($Al_{12}Mg_{17}$) are formed as the second phase in the grain boundaries of PMZ, as can be seen in Figure 3.11(b).

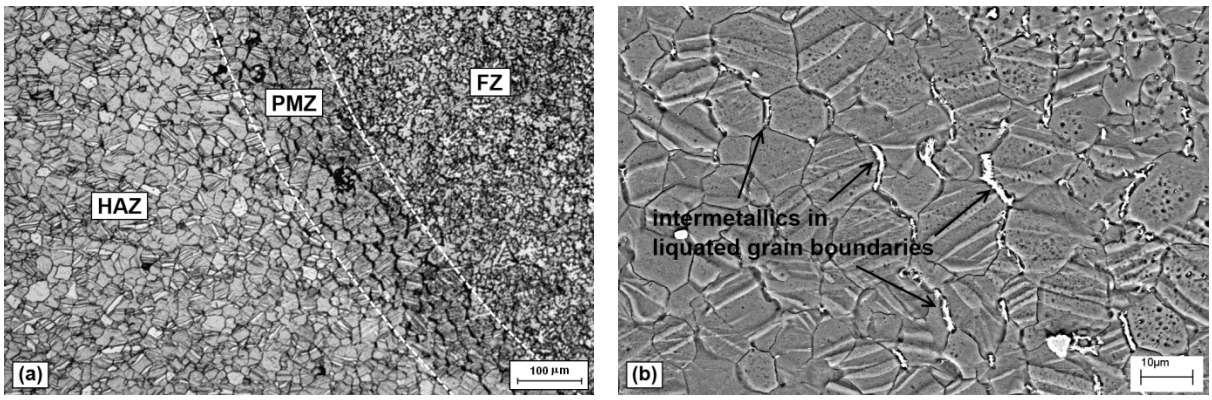

Figure 3.11: Microstructure of PMZ in AZ31B spot-welds (a) low magnification (b) high magnification

The fusion zone is the region which experiences complete liquation during welding. Figure 3.12 displays representative microstructures in the FZ. Porosity, as shown in Figure 3.12(a), existed in the FZ and increasing the welding current raised the chance of this developing, as well as the size of the porosity. Porosity may weaken spot-welds under loading conditions that cause failure in the nugget, *i.e.*, monotonic and high cyclic loading, which will be discussed later in sections 3.3.1.2 and 3.3.2.2. According to Figure 3.12(b), center of the FZ in AZ31B spot-welds has an equiaxed dendritic structure.

Intermetallic particles during solidification are pushed away from dendrites and gather in interdendritic regions, which are shown as light-etching regions in the SEM image of the FZ, Figure 3.12(b).

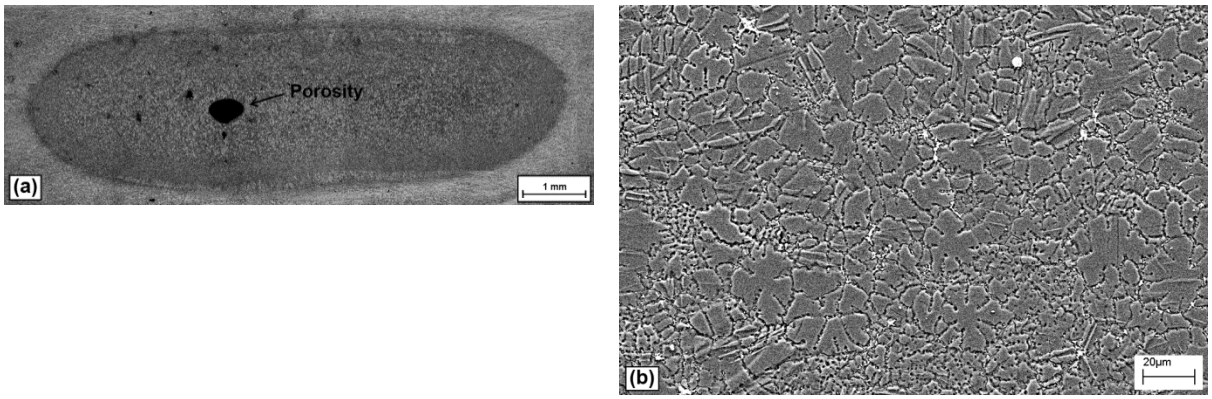

Figure 3.12: Microstructure of FZ (a) overall (b) equiaxed dendrites in FZ-core

3.2.2 Hardness

Hardness testing was performed on the cross-section of spot-welds in a plane parallel to the rolling direction. The micro-indentation Vickers test was chosen due to availability of the testing machine and micro-sized indenter, which makes it possible to measure the hardness distribution in the BM and different regions of the welded area. The test was conducted according to ASTM E384-99 [148], at room temperature with a 100 gr indentation load and a 15 sec holding time.

Figure 3.13(a) illustrates a schematic of the spot-weld cross-section with small dots representing the indentation path. Indentations were performed on a diagonal trajectory according to the AWS D8.9M standard [86].

The polished and etched metallographic samples from the spot-welded specimen sets A, C, and E were employed for the micro-indentation hardness testing. The hardness distributions are shown in Figure 3.13(b). To compare the hardness profiles for different nugget sizes, hardness values were plotted versus the ratio of the distance from the nugget center to the indentation point (d), to the distance from the nugget center to the FZ boundary (d_{FZ}), as shown in Figure 3.13(a). As can be seen,

the hardness profile and hence the strength of the weld region is largely independent of the welding parameters.

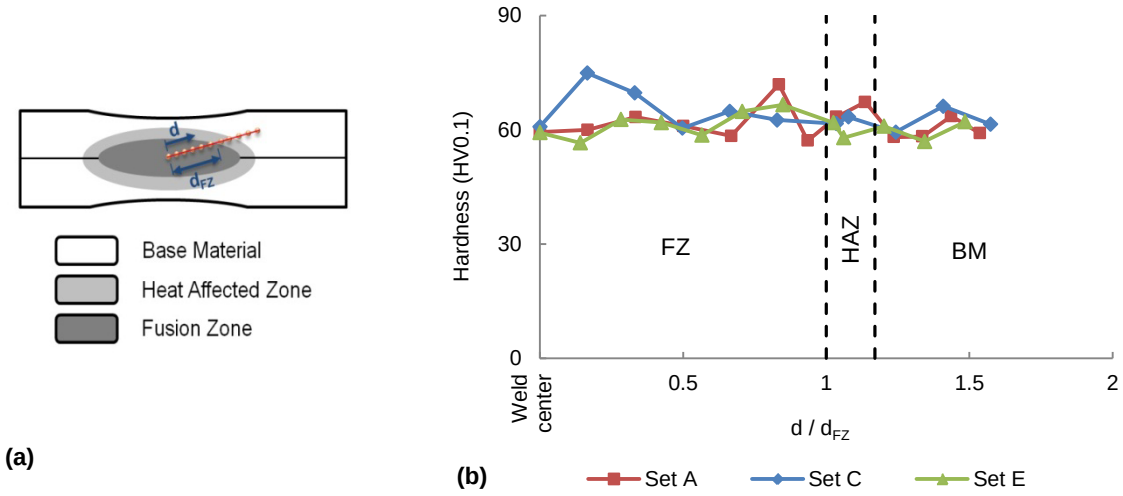

Figure 3.13: Micro-indentation Vickers hardness test (a) indentation path and (b) hardness profile for specimen sets A, C, and E

The profiles in this graph show that the hardness of AZ31B-H24 magnesium spot-welds in the BM and the weld area are almost the same. With dissimilar microstructures in the different zones, two phenomena are likely acting to counteract one another with respect to the hardness. Increasing the grain/dendrite size from the BM to the FZ tends to decrease the hardness. On the other hand, intermetallics present in the PMZ and FZ, and twin bands in the HAZ, increase the hardness. A study by Liu et al. [87] shows slightly lower hardness in the FZ than the BM, but Babu et al. [84] observed major hardness drop in the weld region.

The uniform hardness distribution observed in the present research is in contrast to what has been reported for friction stir welds (FSW) and laser beam welds (LBW) of AZ31B-H24, both of which result in lower hardness in the weld region than the BM [10,149].

On the other hand, RSW of steel and aluminum results in a non-uniform hardness distribution. Hardness in the FZ of steel spot-welds is higher than the BM [149], while it is lower in the FZ of aluminum spot-welds, compared with the BM [150].

3.3 Mechanical Characterization

A number of studies have been conducted regarding the mechanical characterization of AZ31B magnesium sheet in recent years [52,59,68]. However, published works available on the fatigue characterization of magnesium spot-welds are very limited [83]. As a part of this research, monotonic and fatigue testing was performed to characterize the mechanical behavior of the base metal and the spot-welds. These tests were conducted at room temperature on an Instron 8874 testing machine with ±25 kN axial force capacity and ±100 N.m torque capacity. The experimental results are presented and discussed in this section.

3.3.1 Monotonic Behavior

3.3.1.1 Base metal

A. Tension test

Monotonic tension tests were performed on the specimen shown in Figure 3.1. Engineering strain was measured using an Instron extensometer with 12.5 mm gauge length and ±5 mm travel. Five specimens were tested in each of the rolling and transverse directions. Tests were performed in strain-control mode with a strain rate 10^{-3} sec^{-1}. Figure 3.14 illustrates the typical monotonic engineering stress-strain curve.

It is known that the rolling process changes the orientation of magnesium crystals such that the c-axis is along the sheet normal, *i.e.*, the basal planes of the HCP crystals are parallel to the sheet surface [27]. Therefore, in-plane tensile loading of magnesium sheets induces compression along the c-axis of the HCP crystals, which does not activate the twin deformation [56,151]. As a result,

dislocation-slip is the predominant plastic deformation mechanism, and the hardening behavior in both RD and TD are concave-down (Figure 3.14), which is typical for metals.

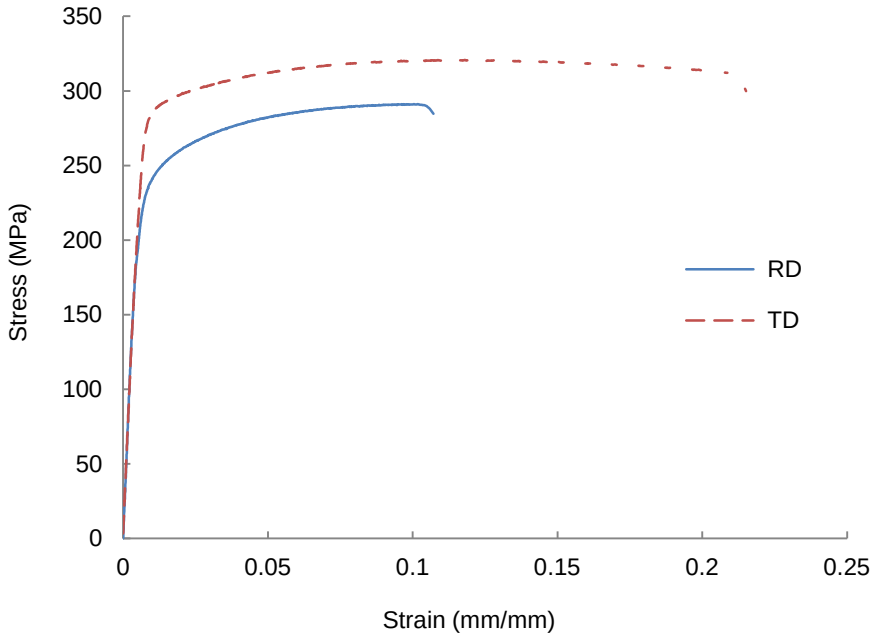

Figure 3.14: Typical monotonic tensile stress-strain curves for AZ31B-H24

Optical microscopy shows only a limited number of narrow twin bands after in-plane uniaxial tension [52]. These twins are generated under tensile stress, because even in textured sheets, the c-axis in some grains may be aligned with the loading direction [152].

Figure 3.14 shows the in-plane anisotropy of AZ31B-H24 sheet at room-temperature. This phenomenon, including higher flow stress in TD, has been reported by several researchers [52,63,66,153,154]. Higher strength in TD compared with the RD is attributed to a higher spread of basal poles in RD [63,66]. However, anisotropy decreases with annealing; for instance AZ31B in the O-tempered condition exhibits less strength variation in the different directions [153].

Table 3.3 lists the tensile properties of AZ31B-H24 magnesium alloy in RD and TD, including the coefficients for a power-law hardening model, *i.e.*, the Ramberg-Osgood equation. The monotonic tensile properties are in good agreement with earlier measurements [154].

Table 3.3: Average monotonic tensile properties for AZ31B-H24 in RD and TD

Direction	0.2% offset yield strength (MPa)	Ultimate tensile strength (MPa)	Elongation (%)	K [b] (MPa)	n [b]
RD	224 (3.5) [a]	292 (0.6)	14 (3.0)	347	0.067
TD	281 (0.4)	320 (0.5)	22 (2.6)	348	0.035

[a] values in parentheses are standard deviations.

[b] Ramberg-Osgood coefficient, $\varepsilon = \frac{\sigma}{E} + \left(\frac{\sigma}{K}\right)^{\frac{1}{n}}$

Another feature in the monotonic tensile properties of AZ31B-H24 is a very low strain hardening in both the RD and TD. Strain hardening behavior is controlled by grain size and dislocation density. Decreasing the grain size results in increasing the yield strength and decreasing the hardening capacity [155]. AZ31B sheet in the O-tempered condition has higher strain hardening than in the H24 condition [63], because it is fully annealed and grain sizes are larger. On the other hand, an increase in the dislocation density increases dislocation interactions, which induces higher strain hardening [155,156].

Ductility also shows a significant difference between the RD and TD, according to Table 3.3. This might be related to a different basal texture, *i.e.*, stronger texture in TD may cause activation of more slip systems and higher ductility than for the RD [66]. AZ31B magnesium sheet exhibits significant ductility of 14-25% at room temperature; nevertheless, it offers poor cold-formability. Limited formability of AZ31B sheet could be partially attributed to the low strain hardening, because strain hardening is known to be one of the main factors governing plastic instability of metals [63].

The elastic modulus and Poisson's ratio for AZ31B from most studies are 45 GPa and 0.35, respectively [24,52,157-159]. The same Poisson's ratio is used in this research; however, the elastic modulus was 43 GPa according to measurements in the current work.

B. Compression test

Monotonic compression tests were performed on specimens with the design shown in Figure 3.2. Strain was measured with an Instron extensometer with 10 mm gauge length and ±1 mm of travel. Three specimens were tested in each of the RD, 45° and TD. Tests were performed in strain-control mode with a strain rate 10^{-3} sec^{-1}. As discussed in section 3.1.2, a non-regular specimen design was utilized for compression testing, to tackle the bucking problem. As a result, a test setup was required to adapt the specimen to the testing machine. Figure 3.15 shows the setup used in this research.

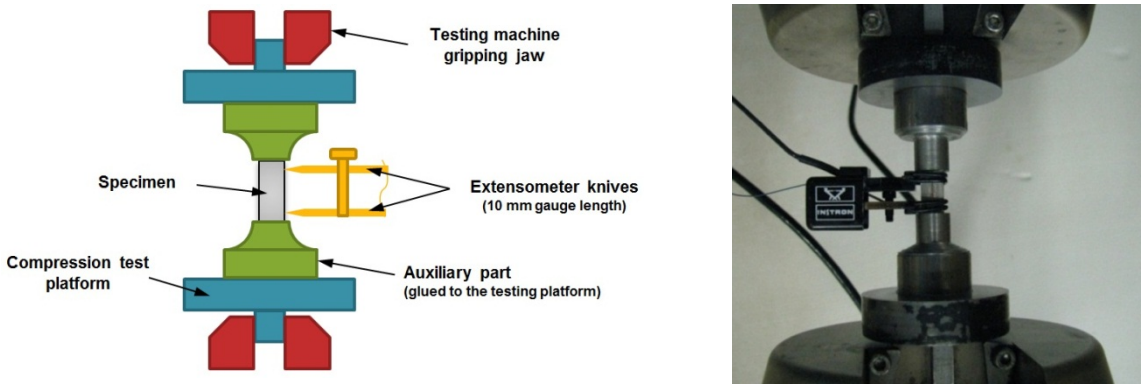

Figure 3.15: Monotonic compression test setup

Figure 3.16 illustrates typical monotonic compressive stress-strain curves for specimens machined along different orientations.

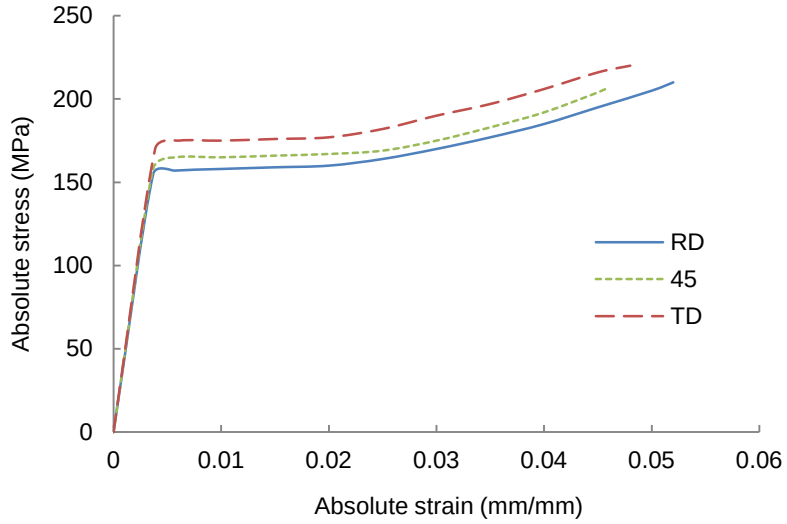

Figure 3.16: Typical monotonic compressive stress-strain curves for AZ31B-H24

The in-plane compressive loading of magnesium sheets generates tension along the c-axis of the magnesium crystals, which activates twin deformation at low stresses [56,151], before the slip mechanism is activated. As a result, twinning is the prevailing plastic deformation mechanism for compressive loading in the RD and TD, and the hardening behavior is concave-up (Figure 3.16), which is not common in metals with cubic crystal structures.

Table 3.4 presents the compressive properties of AZ31B-H24 magnesium alloy for different orientations. Power-law equations cannot properly model the hardening behavior under compressive loading because of the concave-up trend of the flow curve. The monotonic compressive yield strengths are in good agreement with earlier measurements [66].

Table 3.4: Average monotonic comrpessive properties for AZ31B-H24 in RD, 45°, and TD

Direction	0.2% offset yield strength (MPa)	Ultimate Compressive strength (MPa)	Deformation (%)
RD	162 (2.8) [a]	211 (2.7)	5.2 (0.1)
45°	167 (3.5)	213 (5.5)	4.8 (0.3)
TD	181 (0.9)	223 (1.6)	4.6 (0.2)

[a] values in parentheses are standard deviations.

The tension-compression asymmetry in AZ31B-H24 at room-temperature is obvious according to Table 3.3 and Table 3.4.

Figure 3.16 shows the in-plane anisotropy of AZ31B-H24 sheet under compressive load at room-temperature. The difference in hardening behavior between the RD and TD has been reported in a number of studies [52,66,154]. Similar to tensile behavior, the higher flow stress in the TD as compared to the RD is attributed to the difference in basal texture [66].

Figure 3.14 and Figure 3.16 show the in-plane anisotropy of AZ31B-H24 sheet under tension and compression, as discussed earlier in this section. Nevertheless, it is much less evident when compared to the AZ31B extrusion (Figure 3.17). In addition, a study by Lou et al. [52] showed that the in-plane anisotropy of AZ31B-H24 under several reversals is insignificant at room temperature.

Therefore, to simplify the implementation of the cyclic plasticity model, the anisotropy in AZ31B sheet was neglected.

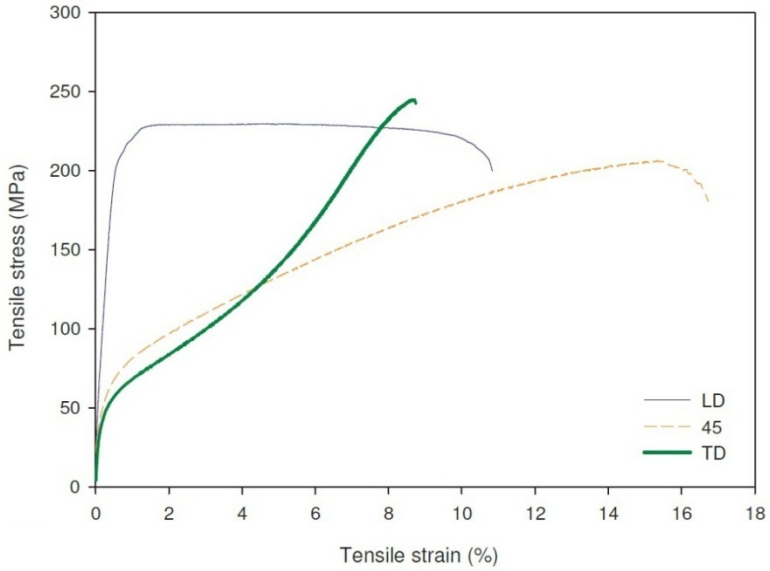

Figure 3.17: Monotonic tensile stress-strain curves for AZ31B extrusion at different directions [3]

The effect of tension-compression asymmetry, which is a key feature of wrought magnesium alloys, is considered in the material modeling sections in the next chapter.

3.3.1.2 Spot-welds

Monotonic testing was performed to evaluate the load-carrying capacity of magnesium spot-welds in tensile–shear (TS) and cross-tension (CT) configurations under static loading. These tests were run in displacement-control mode, with a cross-head displacement rate of 1 mm/min at room temperature. The failure mode and the load and displacement histories were recorded in each test.

Five specimens from each set listed in Table 3.2 were tested and the results are summarized in Table 3.5.

Table 3.5: Average ultimate loads from different spot-welds

	Set A	Set B	Set C	Set D	Set E	Set F	Set G
Ultimate load (kN)	5.12 (0.22)[a]	5.73 (0.3)	6.67 (0.16)	7.15 (0.10)	7.75 (0.35)	7.62 (0.05)	4.16 (0.50)

[a] values in parentheses are standard deviations.

Considering Table 3.2 and Table 3.5, it can be concluded that the ultimate load in TS specimens is enhanced by increasing nugget size. The size of the nugget is controlled by welding current; increasing which enlarges the spot-weld nugget and increases the ultimate load. Considering the minimal effect of process parameters on hardness in the FZ, Figure 3.13(b), increasing the ultimate load with welding current is attributed solely to the different nugget sizes.

As displayed in Figure 3.18, the test results show that there is a linear relationship between the ultimate load and the nugget diameter of magnesium TS specimens within the investigated range of nugget diameter.

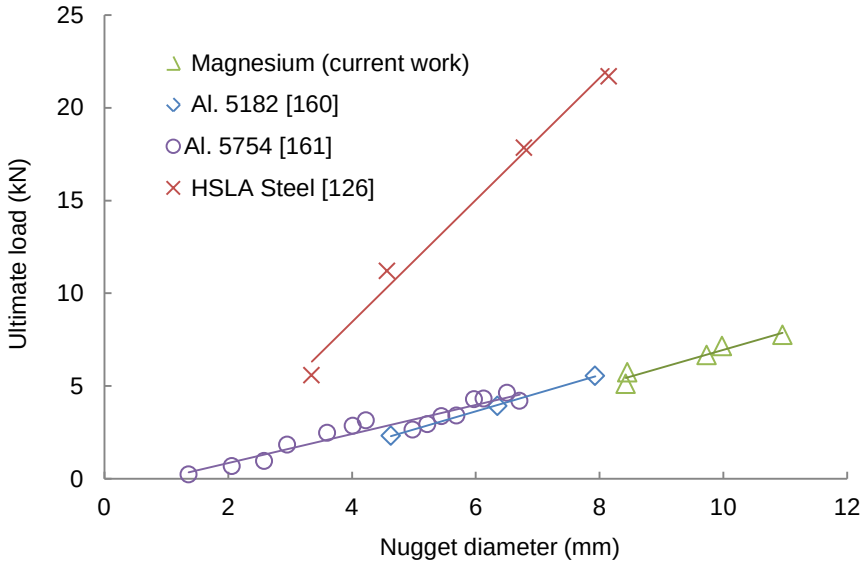

Figure 3.18: Effect of nugget diameter on ultimate load in TS specimens

The same correlation has already been reported in the literature for aluminum [160,161] and steel [126]. An interesting point is that the trend line slope is 1 kN/mm for both magnesium and aluminum spot-welds, and is 3 kN/mm for high strength low alloy (HSLA) steel spot-welds. It should be mentioned that the sensitivity of the weld strength to nugget size for low carbon steel is very close to magnesium and aluminum [162].

Monotonic loading yields two failure modes for the TS, and two different modes for the CT specimens. "*Interfacial*" failure is the predominant mode of rupture for TS specimens; 28 out of 30 TS specimens failed in this mode. As shown in Figure 3.19(a), interfacial failure occurs through the nugget at the interface. Another mode of failure is "*partially-interfacial*", in which the failure starts in the interfacial mode and continues through the coupon thickness and leaves a button on one coupon and a hole on the other, Figure 3.19(b). This mode of failure was observed in 2 out of 30 TS specimens. "*Button-pullout*" is the common failure mode for CT specimens, as 3 out of 5 CT specimens failed in this mode. Button-pullout is a failure mode in which one coupon tears around the HAZ, resulting in a plug on one coupon and a hole on the other coupon, but unlike partially-interfacial failure, there is no nugget shear-off in this mode. Figure 3.19(c) illustrates a specimen fractured in this mode. "*Coupon*" failure occurred in 2 out of 5 CT specimens. In this mode of failure, one coupon fails adjacent to the nugget, as shown in Figure 3.19(d).

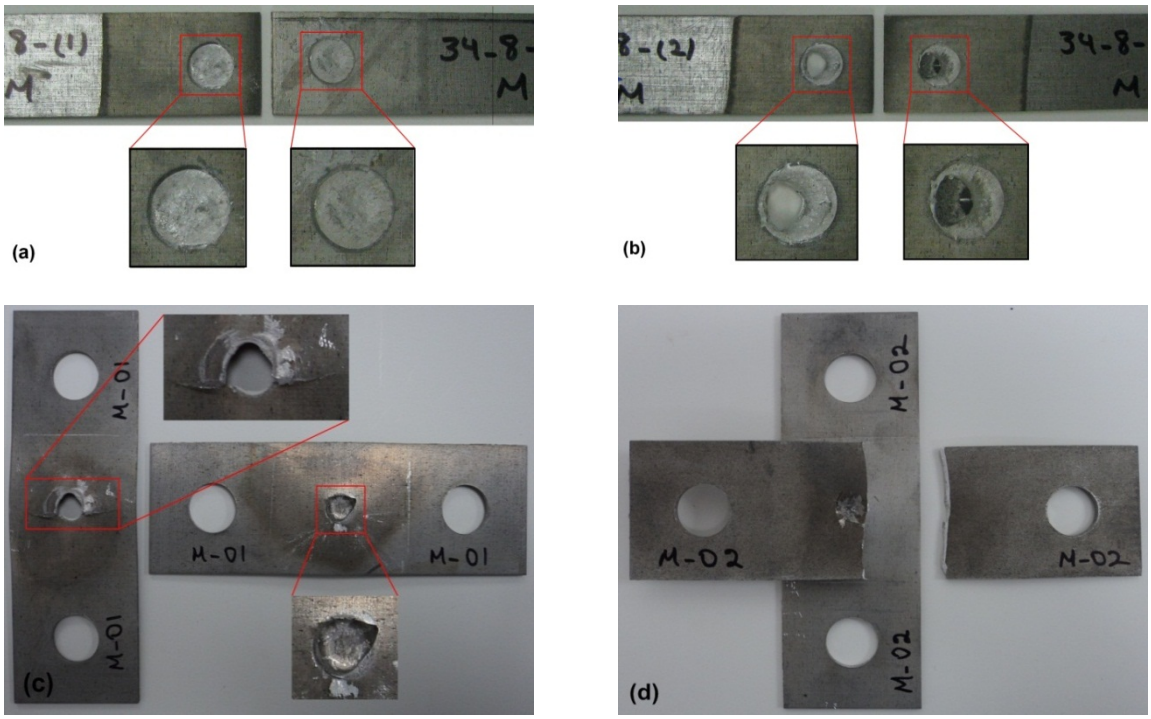

Figure 3.19: Failure modes in spot-welded specimens under monotonic loading
(a) interfacial failure in TS specimens (b) partially-interfacial failure in TS specimens
(c) button-pullout failure in CT specimens (d) coupon failure in CT specimens

It is worth noting that a recent study shows that magnesium TS specimens with a nugget diameter larger than 10.5 mm fail in the button-pullout mode [75]; however, that research also reports that button-pullout failure mode correlates with a drop in ultimate load. Therefore, obtaining a larger nugget size does not ensure an optimized welding process, from a practical point of view.

Regarding the TS specimens, aluminum spot-welds might fail in interfacial [160,161,163], partially-interfacial [160,161], or button-pullout [160,161] modes depending on the welding process parameters. Aluminum spot-welds with larger nugget sizes tend to fail in the button-pullout mode [161,163]; nevertheless, the specimens which fail in this mode show a decrease in the ultimate load. Therefore, similar to magnesium TS specimens, interfacial failure is the most favorable mode in aluminum spot-welds in terms of ultimate static load, provided that the nugget size is sufficiently large. For steel spot-welds, button-pullout is the most common failure mode in well-prepared TS specimens under monotonic loading [41,160].

Aluminum and steel spot-welds in the CT configuration fail only in button-pullout mode, regardless of the nugget size [41,160]. Dissimilar failure modes in magnesium CT specimens can be attributed to different stress distributions. Having button-pullout as the only failure mode in steel and aluminum CT specimens indicates that the shear stress around the nugget is dominant, while coupon and button-pullout failures in magnesium CT specimens suggests that the tensile stress in coupons, due to more significant bending deformation, is comparable to the shear stress around the nugget. Secondary cracks along coupon width and around nugget are evidences for the competitive failure modes. The balance between the tensile and shear stresses is mainly a function of geometrical factors, including the nugget diameter, sheet thickness, and coupon width [164].

Figure 3.20 compares the ultimate tensile-shear load in AZ31 magnesium alloy with spot-welds of aluminum alloys [160,161,165] and steel alloys [142,166,167]. The aluminum and steel alloys shown in this figure are commonly used or competitive alloys in the automotive industry. The

ultimate load values for aluminum and steel spot-welds were selected from the literature with the $d/\sqrt{t}$ ratio (d: nugget diameter, t: sheet thickness) close to that for magnesium spot-weld (set A). This ratio was inferred from the AWS D8.9M standard [86] and is often used as the equivalence criterion when comparing different spot-welds [160,168]. The label above each column includes the corresponding $d/\sqrt{t}$ ratio and the ultimate tensile strength for the base metal (UTS).

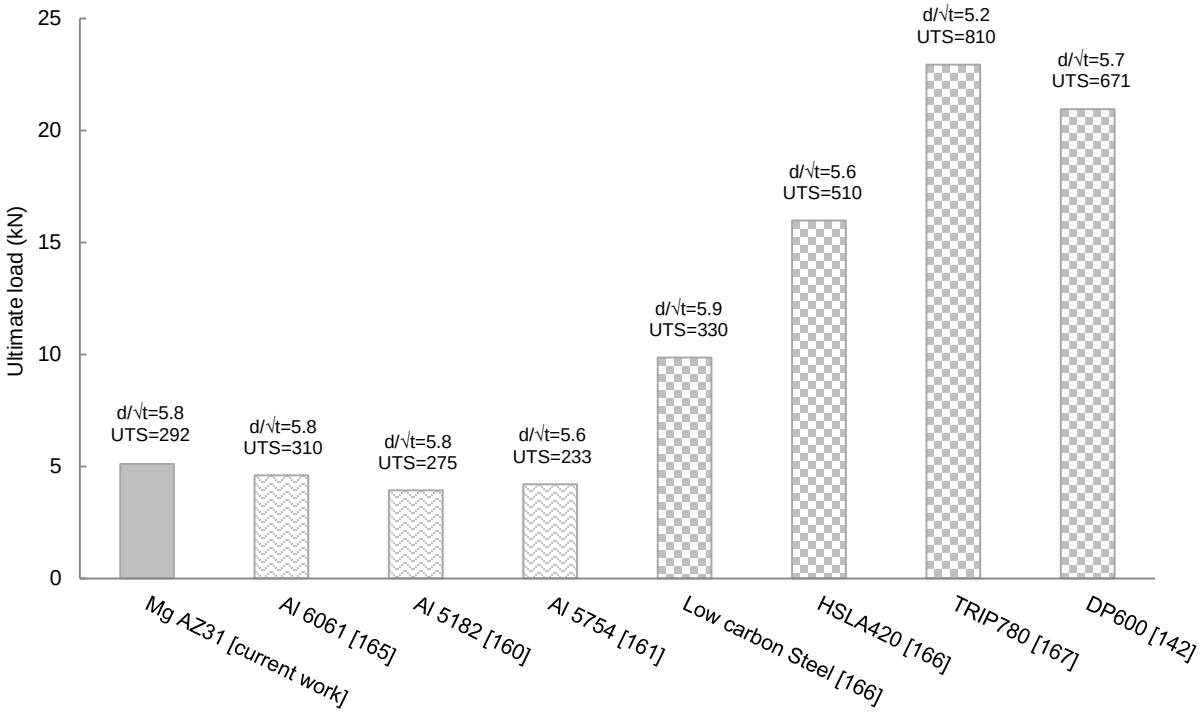

Figure 3.20: Comparison between ultimate load in magnesium, aluminum [160,161,165] and steel [142,166,167] tensile-shear spot-welds (d/√t and UTS values are in √mm and MPa, respectively)

This figure shows that the load carrying capacity of magnesium spot-welds is comparable with and slightly superior to aluminum spot-welds. With similar UTS of magnesium and aluminum alloys, the uniform hardness distribution in magnesium spot-welds and strength under-matching in aluminum spot-welds (as discussed in section 3.2.2) may contribute to the somewhat higher static load of magnesium spot-welds. This figure also includes the ultimate load for spot-welds of a low carbon steel [166] and three high strength steel alloys, *i.e.*, HSLA420 [166], TRIP780 [167], and DP600 [142]. According to this graph steel spot-welds exhibit significantly higher overload capacity than TS

spot-welds of magnesium and aluminum. This is mainly attributed to higher UTS and strength over-matching in the weld area of steel alloys. Similarly, the larger peaks loads for high strength steel alloys than low carbon steel is related to higher UTS.

3.3.2 Cyclic Behavior

3.3.2.1 Base metal

Fatigue testing was conducted on the specimen shown in Figure 3.3. Engineering strain was measured using an Epsilon extensometer with 6 mm gauge length and ±0.8 mm travel. Fatigue testing was performed in strain-control mode for approximately 10^4 cycles, and then stopped and switched to load-control mode, since the load response had stabilized. The main reason for controlling the load is to increase the frequency. The testing frequency was 0.1-0.15 Hz and 3-10 Hz for strain- and load-control testing, respectively. The tests were run in the fully reversed loading condition, *i.e.*, the strain ratio was -1. Tests were stopped if the life exceeded 10^7 cycles, and considered a run-out. Another criterion for stopping the test in the strain-control mode was 50% load drop. Seventeen specimens were tested at different strain amplitudes. Figure 3.21 illustrates the second and half-life hysteresis loops for different strain amplitudes.

Figure 3.21 reveals a number of features regarding the cyclic behavior of AZ31B-H24. First of all, comparing the second and the half-life hysteresis indicates that the material shows a minor cyclic hardening behavior, in terms of tensile or compressive peak stresses. Also, narrower hysteresis loops for stabilized cycle than the second cycle confirms that the material exhibits a slight cyclic hardening behavior. Fatigue of AZ31B extrusion [169,170] showed a more noticeable cyclic hardening behavior. The minor cyclic hardening behavior in compression reversals will be discussed later in this section.

Dissimilar peak stresses in tension and compression, even though the strain amplitude is symmetric, is a cyclic attribute of AZ31B sheet. This feature becomes more noticeable when plasticity prevails.

The unusual asymmetric shape of the hysteresis loop is pronounced, especially at higher strain amplitudes. The same observation was made for AZ31B sheet [52,65,66], AZ31B extrusion [3,170], and other wrought magnesium alloys [62,171]. The hysteresis asymmetry in AZ31B extrusions is remarkably more evident than for AZ31B sheet, which is expected since there is more drastic asymmetry under monotonic loading.

Another cyclic feature is that in the loading reversal, *i.e.*, from compression to tension, there is a distinct point where the slope of the hardening curve starts increasing. This point hereafter is referred to as the "*inflection point*". Similar to other asymmetric cyclic features, the inflection point is more distinguishable at high strain amplitudes. This inflection point did not appear on the unloading curve in this study, even at the highest strain amplitude. However, experimental results for very large strain amplitudes, *e.g.*, 3.5%, reveal an inflection point on the unloading reversal [52].

To interpret these observations, the deformation mechanisms must be analyzed. Metals with a HCP crystal structure, including magnesium, have fewer slip systems than metals with a cubic crystal structure. However, twinning is another deformation mechanism that can be activated in HCP structures if tension is applied along the c-axis of HCP crystals.

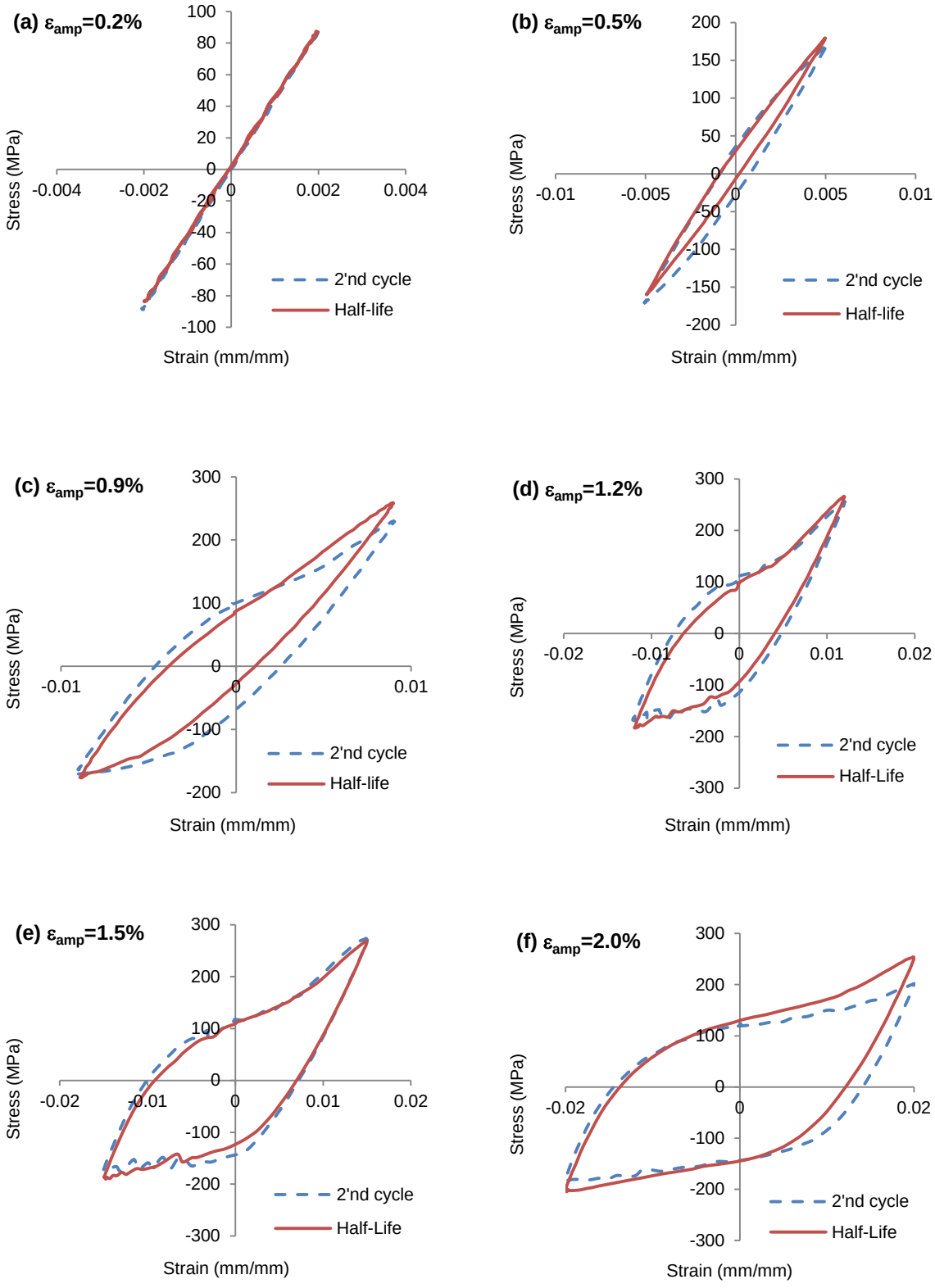

Figure 3.21: Second and half-life hysteresis loops at different total strain amplitudes

The crystals in wrought Mg alloys have a preferred orientation. As mentioned before, AZ31B sheet due to the rolling process have a crystal structure oriented such that the basal planes are predominantly parallel to the sheet surface. As a result, in-plane tensile loading can induce contraction along the c-axis and the twin system is not activated. Conversely, applying compression along the sheet extends the c-axis and triggers the twin deformation at low stress [52]. Twinning results in an approximately 90° rotation in crystal orientation [52,62]. Therefore, the twinned crystals are prone to untwin during reloading under subsequent tension [61]. In other words, twin bands may disappear or become narrower under reloading, and can reappear under unloading [62]. As a result, twinning and untwinning occur alternately in cyclic loading [151]. Another important behavior is that untwinning deformation may start happening immediately after reloading from a compression reversal. In other words, twinned crystals may untwin even under external compressive in-plane stress [62], due to twin interactions.

Considering the deformation mechanisms, one can justify the asymmetric cyclic behavior. Early yielding in compression is attributed to the easily activated tension twin as the dominant mechanism for plastic deformation, which changes the c-axis orientation to the loading direction.

Subsequent in-plane tension produces the reloading flow curve with a reversed yielding more gradual than for the compression yielding, such that the elastic part is hardly distinguishable. The reloading flow curve consists of two distinct sections separated from each other at the inflection point. In the first section, the tensile stress causes an extension along the c-axes of the rotated crystals, activating the untwinning process. As indicated earlier, during reversed loading, the grains that rotated on the compression reversal reorient back to their initial unloaded orientations. Therefore, the continuous decrease in the hardening slope of the first section is an indication of untwinning saturation. In other words, at the inflection point the twin deformation is almost recovered. In the second section of the flow curve, *i.e.*, after the inflection point, the hardening rate rapidly increases.

Wu et al. [62] found that basal slip is hard to activate after untwinning is exhausted; therefore non-basal slip or compression twin mechanisms, are activated, which results in a high hardening rate.

Stabilized hysteresis loops, illustrated in Figure 3.21, especially at high strain amplitudes, reveal that the inflection point is located approximately at the same strain amplitude as the yield point in compression. Therefore, it can be concluded that the strain range needed for untwinning is almost equal to the strain range during twin deformation.

According to Figure 3.21, the absolute value of the compression peak stress in the half-life cycles is higher than that in the second cycle, demonstrating a minor cyclic hardening behavior. The reason could be that the twinned grains in the compression reversal are not fully untwinned in the subsequent tension reversal, and hence residual twinned grains accumulate during cycling [62]. Interaction between increasing twin bands is responsible for cyclic hardening in compression reversals.

Figure 3.22 displays the stabilized half-life hysteresis loops obtained from fatigue tests at different strain amplitudes.

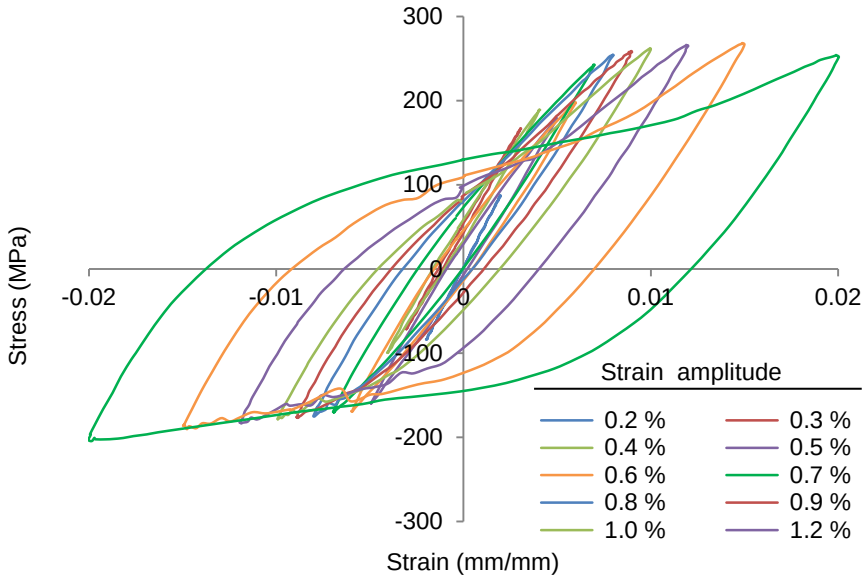

Figure 3.22: Stabilized hysteresis loops for different strain amplitudes

Comparing this graph with the stabilized hysteresis loops for AZ31B extrusion confirms that the cyclic asymmetry behavior, in terms of dissimilar plastic strain energy in tension and compression as well as the mean stress, is much less pronounced in AZ31B-H24.

Cyclic properties of metals are usually obtained by fitting the Ramberg-Osgood equation:

$$\varepsilon = \frac{\sigma}{E} + \left(\frac{\sigma}{K'}\right)^{n'} \tag{3.1}$$

to the peak stresses of the stabilized hysteresis loops. Similar to monotonic compression behavior, stabilized cyclic behavior of AZ31B under compression does not obey power-law equations. Therefore, Ramberg-Osgood equation was only fitted to tension peak points. The cyclic properties achieved in the rolling direction are listed in Table 3.6.

Table 3.6: Cyclic properties of AZ31B-H24 in rolling direction

	Cyclic strength coefficient K' (MPa)	Cyclic strain hardening exponent n'
Tension	383	0.070

A strain-life curve obtained from fatigue testing is illustrated in Figure 3.23.

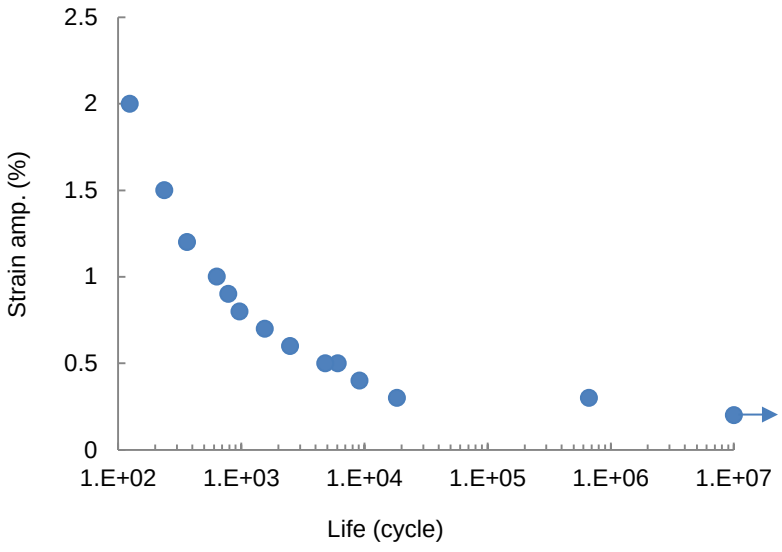

Figure 3.23: Strain-life curve for AZ31B-H24 in rolling direction

This figure shows a sharp knee at a life of 2×10^4 cycles, and the endurance limit is at a strain amplitude of 0.2%, which are very similar to AZ31B extrusions [3]. Another aspect of the strain-life curve is a kink at a strain amplitude of 0.5% and a life of 6×10^3 cycles. According to Figure 3.21, the kink corresponds to the strain amplitude above which the cyclic hysteresis loop becomes asymmetric, *i.e.*, twin and untwin deformations become evident. The same behavior has been recently reported for AZ31B extrusion [172].

Although the kink separates the strain-life curve into two parts, a single Manson-Coffin equation:

$$\varepsilon_a = \frac{\Delta\varepsilon}{2} = \frac{\sigma'_f}{E}\left(2N_f\right)^b + \varepsilon'_f\left(2N_f\right)^c \tag{3.2}$$

can successfully capture the experimental data points. In this equation, E the is elastic modulus, N_f is fatigue life, σ'_f is fatigue strength coefficient, b is fatigue strength exponent, ε'_f is fatigue ductility coefficient, and c is fatigue ductility exponent. To obtain the Manson-Coffin parameters, total strain amplitude, ε_a, measured in experiments was divided into elastic and plastic strain amplitudes,

$$\varepsilon_a^e = \frac{\sigma_a}{E} \quad , \tag{3.3}$$
$$\varepsilon_a^p = \varepsilon_a - \varepsilon_a^e \quad ,$$

where, ε_a^e is elastic strain amplitude, ε_a^p is plastic strain amplitude, and σ_a is the stabilized stress amplitude. Then, the first and second terms on the right-hand side of equation (3.2) were fitted separately to the elastic and plastic strain amplitudes, respectively. Figure 3.24 illustrates the curve fitting to the elastic and plastic components of strain amplitude.

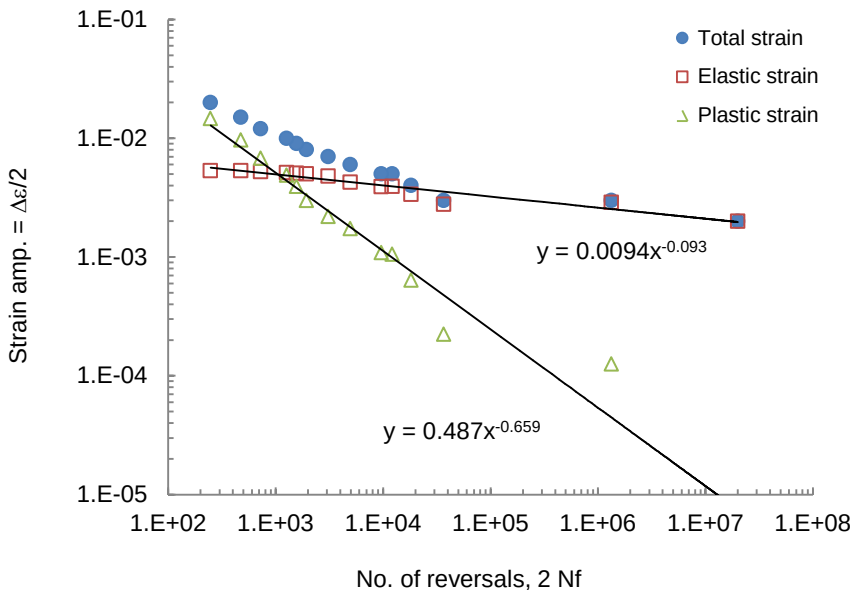

Figure 3.24: Determination of Manson-Coffin parameters

The Manson-Coffin parameters are presented in Table 3.7.

Table 3.7: Manson-Coffin parameters for AZ31B-H24 in rolling direction

σ'_f (MPa)	b	ε'_f	c
405	-0.093	0.487	-0.659

The Manson-Coffin coefficients obtained in this research are not in good agreement with previous studies by Wu et al. [68], and Lv et al. [66]. The difference could be attributed to dissimilar sheet fabrication process and different tempering conditions.

3.3.2.2 Spot-welds

Fatigue testing of spot-welded specimens was performed at room temperature, on the specimens shown in Figure 3.5 and Figure 3.6. The tests were conducted in load-control mode with the load ratio, R=0.2; except for the specimen set F, Figure 3.5(b), for which R= 0.1. The testing frequency was 1-30 Hz, depending on the load level. Tests stopped after a life of 10^7 cycles, which was considered a run-out.

A. Load-life experimental results

The fatigue life experimental data are shown in Figure 3.25. The load-life curves shown in these figures were obtained from a bi-linear regression fit using log–log scale, Figure 3.25(a). Comparing the load-life curves corresponding to TS specimens, *i.e.*, sets A, C, and E, reveals that enlarging the nugget size slightly enhances the fatigue strength.

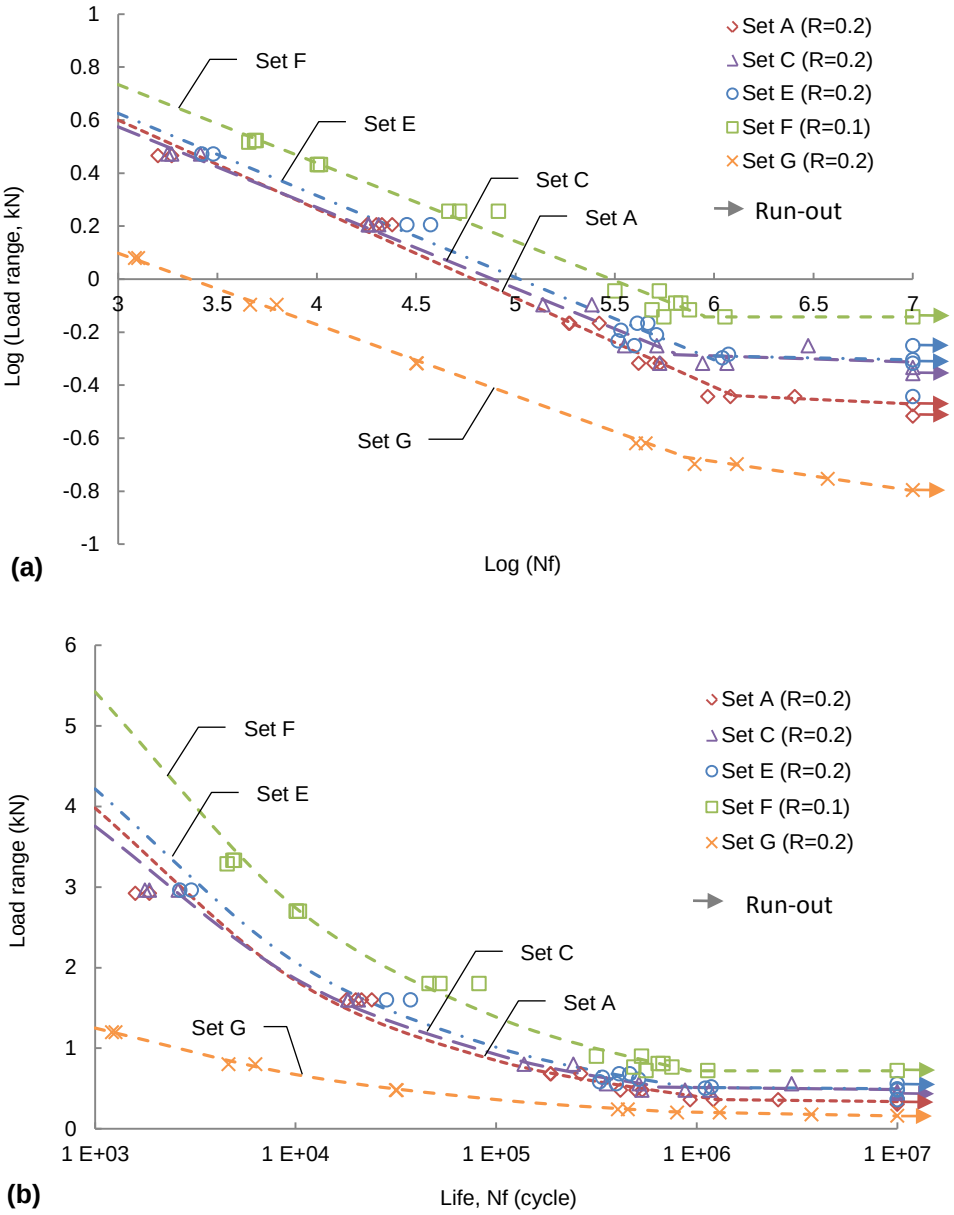

Figure 3.25: Load-life experimental data for spot-welded specimens

Comparison between sets A-E and set F indicates that increasing the coupon width and decreasing the mean load improve the fatigue strength in LCF, and this effect gradually diminishes in HCF. Fatigue test results on CT specimens, *i.e.*, set G, show a remarkable drop in fatigue strength, as compared to TS and TS-W specimens, with the same nugget size, *i.e.*, sets E and F. This observation demonstrates that normal cyclic loading of spot-welds is more destructive than shear dominated loading. The endurance limit is 0.34 kN, 0.44 kN, 0.48 kN, 0.72 kN, and 0.16 kN for sets A, C, E, F, and G, respectively. Similar effects have been reported for steel [126] and aluminum [160]. However, recent research reported that increasing the nugget size resulted in decreasing the fatigue strength of spot-welds in AISI304 stainless steel [173]. Lower fatigue strength at larger nugget diameter can be explained by increasing size of porosities and chance of expulsion at higher weld time and welding current which are required for obtaining larger spot-welds.

Figure 3.26 compares fatigue strengths (in terms of load range) for magnesium, aluminum [174,175] and steel [142,143] spot-welds in TS configuration.

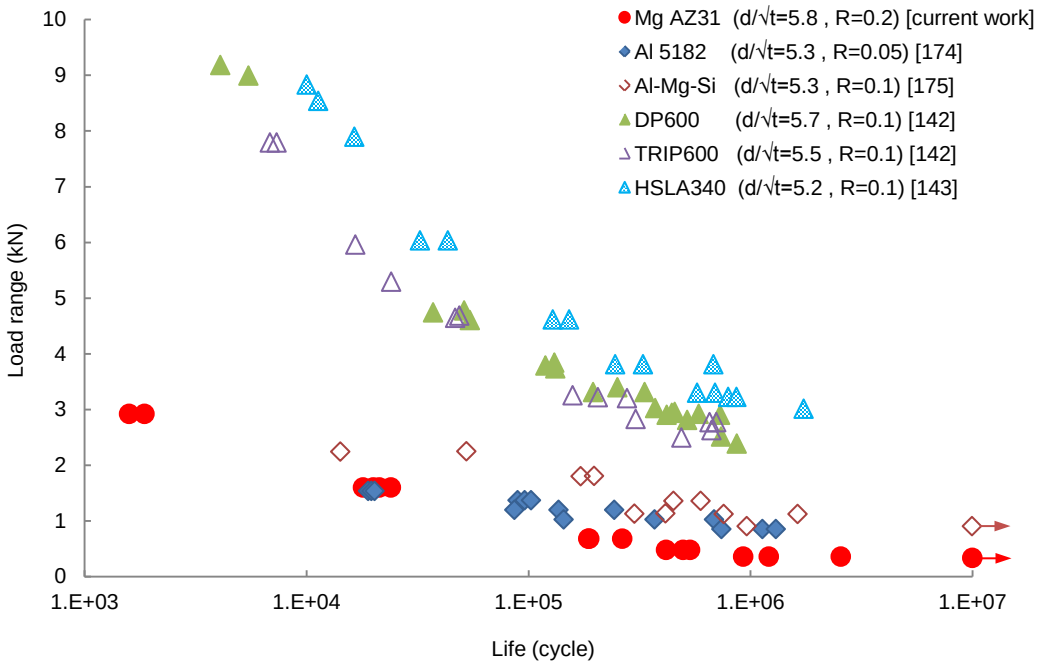

Figure 3.26: Comparison between fatigue performance of magnesium, aluminum [174,175] and steel [142,143] spot-welds in TS configuration (d/√t values are in √mm)

The load-life data for aluminum and steel alloys was obtained from the literature so that the $d/\sqrt{t}$ ratio and R-ratio are close to those for magnesium spot-welds (set A). This figure demonstrates that spot-welds of high strength steel alloys (DP600, TRIP600, and HSLA340) have significantly higher fatigue strength in LCF and HCF than magnesium and aluminum spot-welds. The large difference within LCF can be attributed to different modes of failure (fatigue failure modes for Mg spot-welds will be discussed in the next section). Magnesium and aluminum [175] spot-welds fail in interfacial mode, while steel spot-welds fail from the HAZ [142], due to the high strength in the FZ. In HCF regime, coupon failure is the common mode of failure for all the alloys; therefore, the distance between fatigue strengths is diminished. Superior fatigue strength of steel spot-welds in HCF can be related to higher strength in the HAZ. Aluminum alloys (Al5182 and Al-Mg-Si) and AZ31 Mg alloy exhibit overall comparable fatigue strength; aluminum spot-welds have higher strength within HCF and magnesium spot-welds are expected to perform superior in LCF, due to higher static peak load (Figure 3.20).

B. Failure modes

The TS spot-welded specimens failed in three different failure modes under cyclic loading: interfacial, partially-interfacial, and coupon failures.

In the interfacial failure mode, Figure 3.27(a), a crack initiated from the nugget edge in the load-bearing side of the nugget and along the loading direction. The crack then propagated through the nugget until complete separation of coupons, while the crack also grew through the coupon thickness. Therefore, the fatigue strength in this mode of failure depends mainly on the size and strength of the nugget. This failure mode was observed only when a very high cyclic load was applied.

Coupon failure, shown in Figure 3.27(c), is the most common mode of failure in TS specimens. In this failure mode, a crack started either from the BM–HAZ interface or from the BM, with an offset from the nugget edge, depending on the load level. This issue will be discussed in detail in

section 3.4.3. The crack in this mode then propagated through the coupon thickness and extended perpendicular to the loading direction, until the coupons were separated. Fatigue life is therefore independent of nugget strength, but rather depends on cyclic loading level and dimensional parameters, such as sheet thickness. Coupon failure was observed at lower loads, in the intermediate and high cycle regimes.

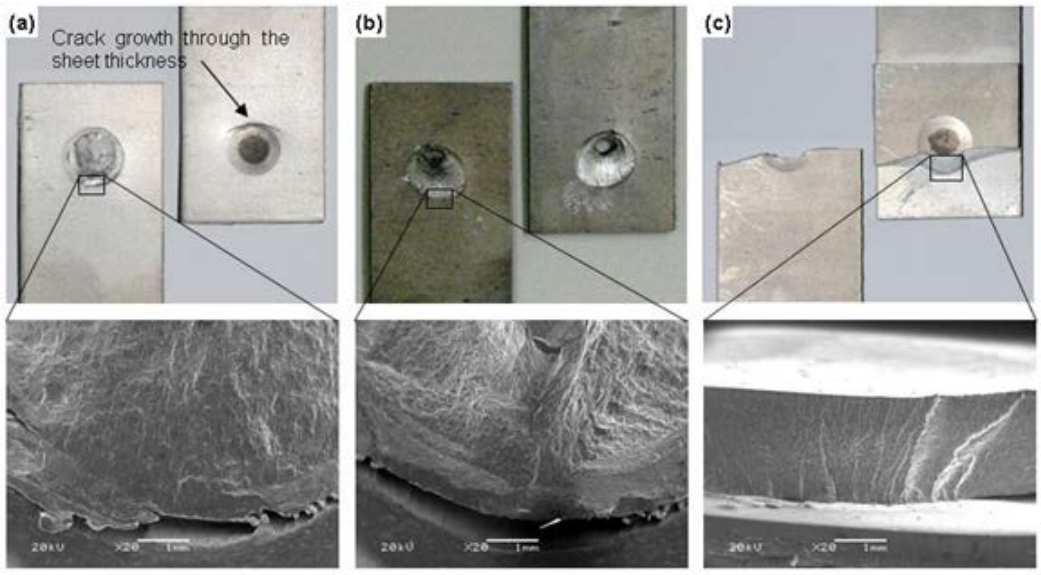

Figure 3.27: Failure modes in TS specimens under cyclic loading
(a) interfacial (b) partially-interfacial (c) coupon failure

Partially-interfacial failure was a rare mode of failure under cyclic loading, and occurred only as a transition between interfacial and coupon failures. Cracks in this mode, as shown in Figure 3.27(b), nucleated from the same location as for interfacial failure, and grew first inside the nugget and then through the sheet thickness, following the bonding area. It can be seen that, similar to interfacial failure, there was another crack in this mode through the thickness, which was not as critical as the main crack. This mode of failure was observed in a narrow region between very low and low cycle regimes, *i.e.*, when fatigue life was between 3×10^3 and 10^4 cycles.

The CT spot-weld specimens failed only in button-pullout mode under cyclic loading, as shown in Figure 3.28. The fatigue crack in this failure mode started from the nugget edge, on the gripping sides of one coupon, and propagated through the sheet thickness, following the FZ and around the

nugget. The spot-weld nugget was left on one coupon and a hole on the other after the coupons were separated. The specimens that failed within LCF exhibited button-pullout failure in both coupons, Figure 3.28(a). However, the CT specimens that failed in HCF showed button-pullout on a single coupon, Figure 3.28(b).

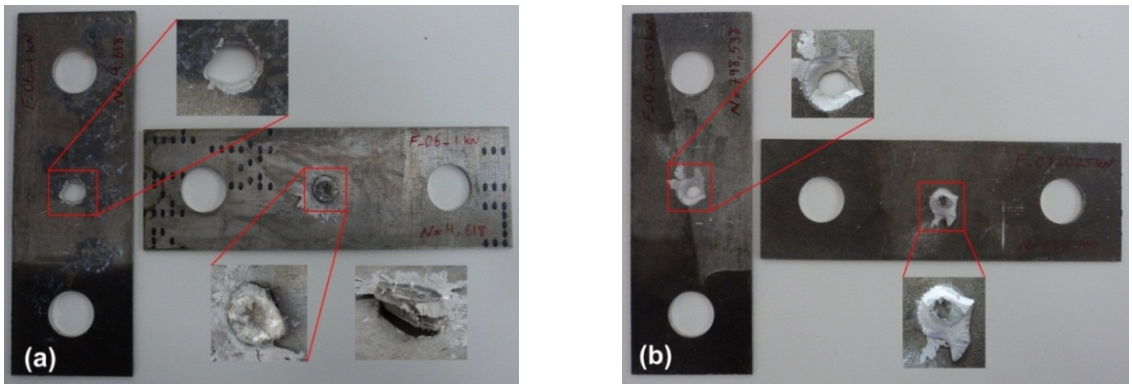

Figure 3.28: Fatigue failure modes in CT specimens
(a) P_{max}=1 kN, life=4,618 cycle ; (b) P_{max}=0.25 kN, life=798,538 cycle

The different failure modes in the TS specimens under cyclic loading can be described in terms of crack propagation as related to the applied load. As shown in Figure 3.29, "*n-plane*" and "*t-plane*" are defined normal and tangent to coupon interface, respectively.

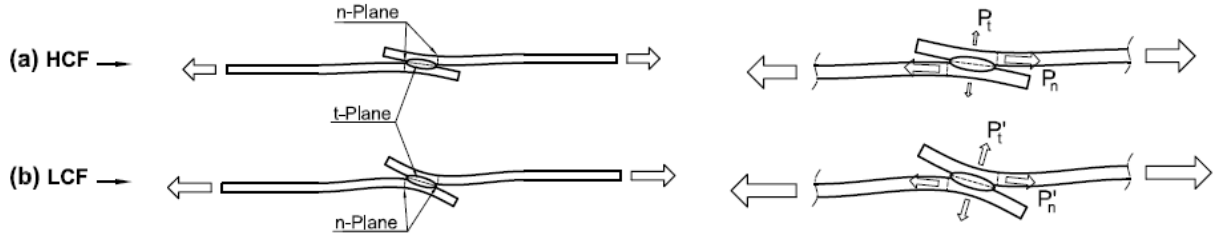

Figure 3.29: Tensile–shear specimen (a) under low load/in high cycle regime and (b) under high load/in low cycle regime.

The mode I SIF is usually considered as the main factor controlling crack growth rate for TS spot-welds [19,127]. Therefore, the load components on the t- and n-planes can be considered as major parameters determining crack propagation rates. In HCF, where a small load is cyclically applied to the specimen, Figure 3.29(a), the component of load on the n-plane, P_n, dominates and the mode I (opening mode) stress intensity factor (SIF) is larger on this plane. Therefore, the crack

propagates faster on the n-plane. Under high cyclic loads, however, bending is more appreciable and the load component on the t-plane (P'_t) becomes comparable to that on the n-plane (P'_n). Therefore, the stress intensity factors corresponding to these two planes are similar and the cracks grow with similar rates. As the applied load is increased, the chance of interfacial failure rises, which can be seen in Figure 3.27(a). At lower loads, where the stress intensities are of the same magnitude, mixed mode failure on both the t- and n-planes may occur, Figure 3.27(b).

The through-thickness cracks in the interfacial and partially interfacial failure modes are supporting evidence for this interpretation. At very high loads, where the specimen fails in the first loading reversal, *i.e.*, static tests, due to severe bending in coupons, failure happens on the t-plane without a crack on the n-plane (see Figure 3.19).

C. Crack initiation life

Most metals, including magnesium and its alloys, are known as polycrystalline materials, *i.e.*, they are composed of numerous arranged crystals (grains). Several grains are oriented such that slip susceptible planes within those grains are along the maximum shear stress planes. Shear stress may develop parallel planes which tend to move relative to each other. Slip plastic deformation happens when a plane slides against adjacent planes within a grain [176]. As they are the weakest, surface grains are more prone to slip plastic deformation, which produces a micro-crack within a grain [177]. Slip occurs under monotonic and cyclic loadings. Figure 3.30(a) represents coarse slip deformation under static loading in which slip happens on a limited number of planes. For the case of uniaxial loading, maximum shear stress planes make an angle of 45° with the loading direction and slip takes place at about this angle. Figure 3.30(b) displays fine slip deformation under fatigue loading which forms extrusion/intrusion pairs. This is because the slip deformation which happens in a cyclic loading reversal is not recovered when loading is reversed; rather, reverse slip occurs in adjacent planes [177]. Figure 3.30(c) illustrates progressive development of the extrusion/intrusion pairs. As

shown in this figure, cyclic loading may cause coarse slip which gradually becomes finer by activating slip deformation on nearby planes which results in formation of extrusions and intrusions at the surface. Slip plane intrusions are stress concentration sites from where surface fatigue cracks may initiate [176]. Because slip takes place within a grain, fatigue crack initiation is a transgranular rather than an intergranular phenomenon [177]. Surface finish, residual stress and environmental conditions are key factors controlling the resistance to fatigue crack initiation [177].

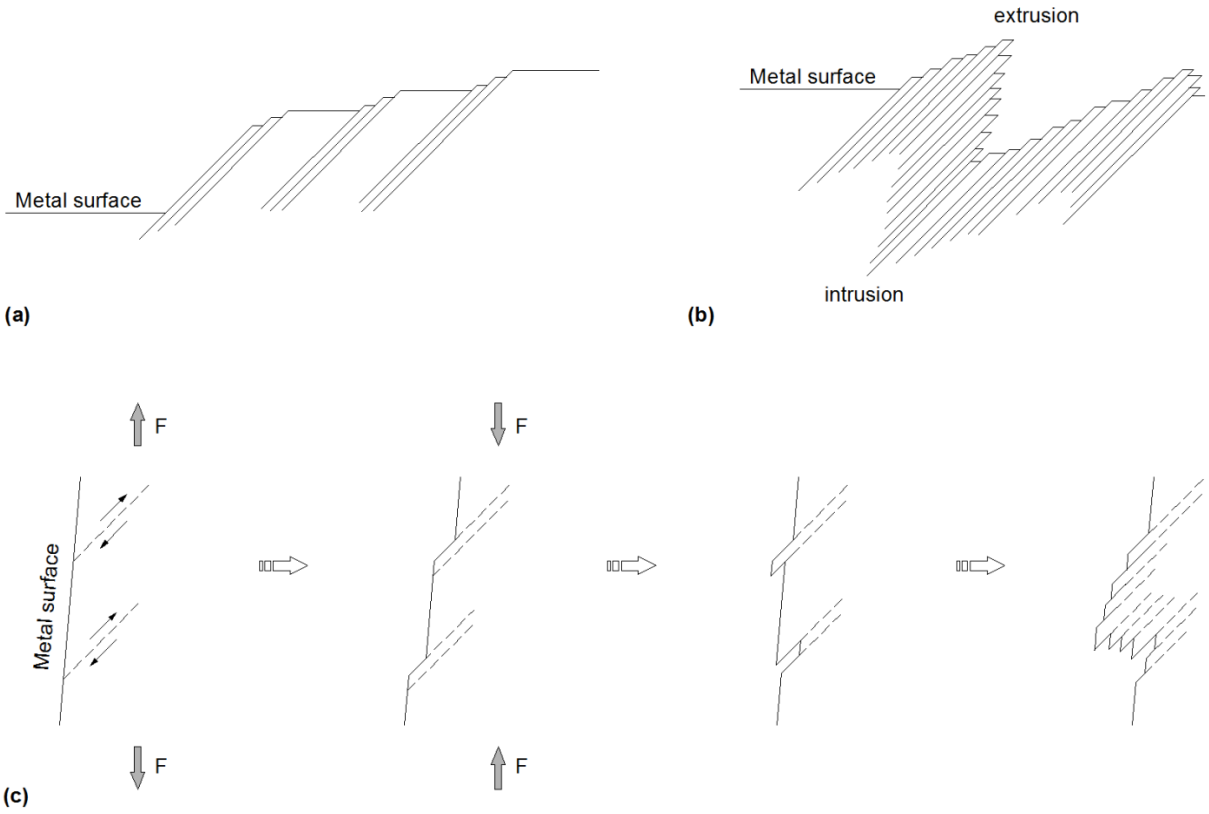

Figure 3.30: Slip deformation at metal surface (a) under monotonic loading (b) under cyclic loading (c) slip progression under cyclic loading [176]

From a practical aspect, there is not a unique definition for the fatigue crack initiation. This inconsistency is more evident for welded specimens/structures, especially RSW in which the crack initiation location is not visible. Crack initiation in some studies is assumed when the crack reaches the length of 0.25 mm [134,178] or 18% of the sheet thickness [18]. Crack initiation is related to compliance in some other researches [168,179]. Fatigue crack initiation in the current research is

considered as 5% increase in non-dimensional compliance [180]. Non-dimensional compliance is defined [180] as

$$E\delta_{amp}t/P_{amp} \quad , \tag{3.4}$$

where E is the elastic modulus, t is sheet thickness, δ_{amp} is displacement amplitude, and P_{amp} is load amplitude. Therefore, to obtain crack initiation life for a specimen, compliance should be calculated for the entire test and plotted versus loading cycles. Figure 3.31 schematically represents the compliance curve and how the fatigue crack initiation life is measured.

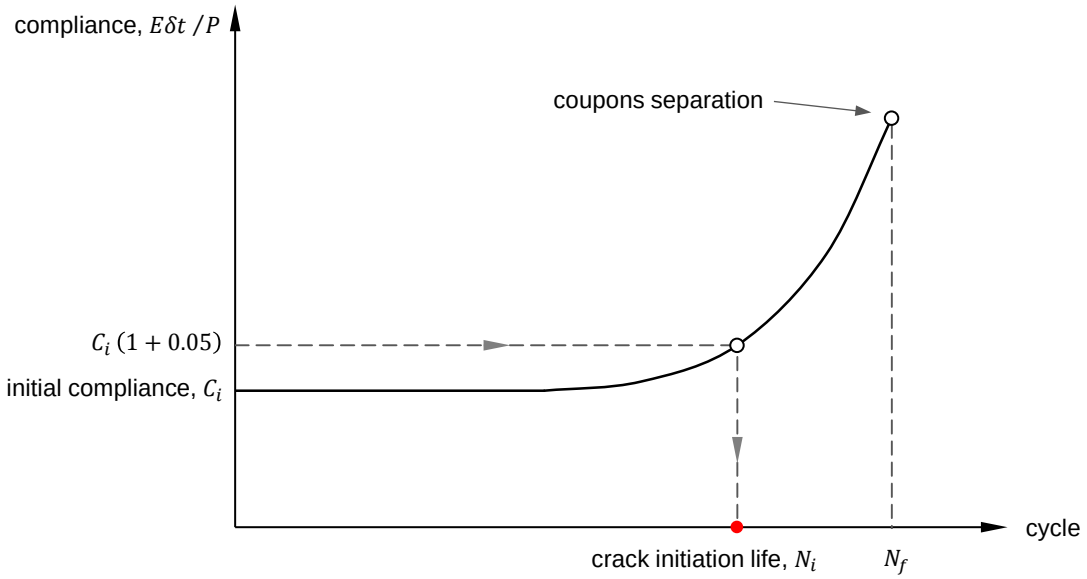

Figure 3.31: Illustration of calculating the fatigue crack initiation life

This method was applied to all the experimental points shown in Figure 3.25, and the graph was re-plotted in terms of fatigue crack initiation life, as displayed in Figure 3.32.

Comparing Figure 3.25(b) and Figure 3.32 reveals that the trends are approximately the same for a certain specimen set in the range where (initiation) life is greater than one million cycles. This implies that crack initiation constitutes a major portion of the total life in HCF. For shorter lives, the trends in the load-initiation life graph are steeper than those in the load- life graph. This observation indicates that a significant fraction of the total life is devoted to crack propagation within low and moderate cycle fatigue.

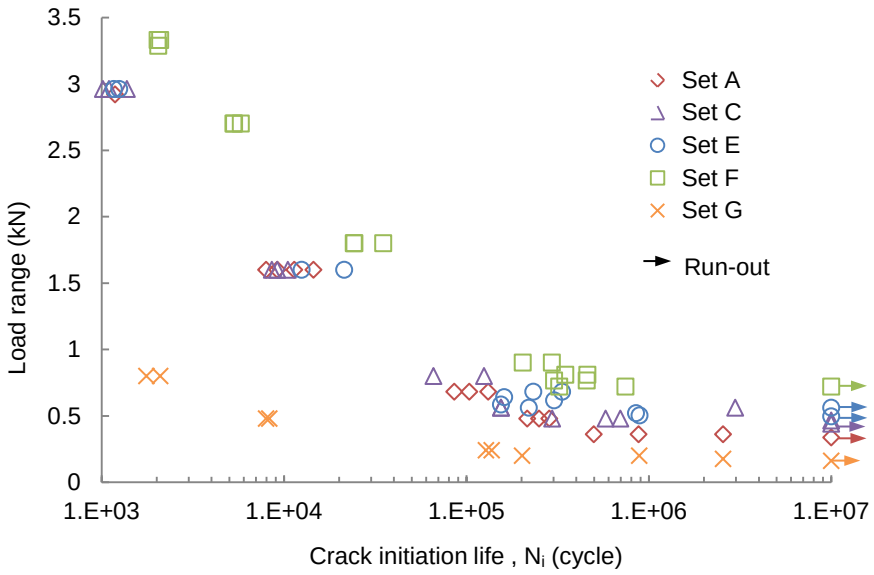

Figure 3.32: Fatigue experimental results in terms of crack initiation life

The results for the crack initiation life were normalized by the total life to demonstrate the contribution of crack initiation over different ranges of the fatigue life. Figure 3.33 illustrates the results for various RSW specimen sets.

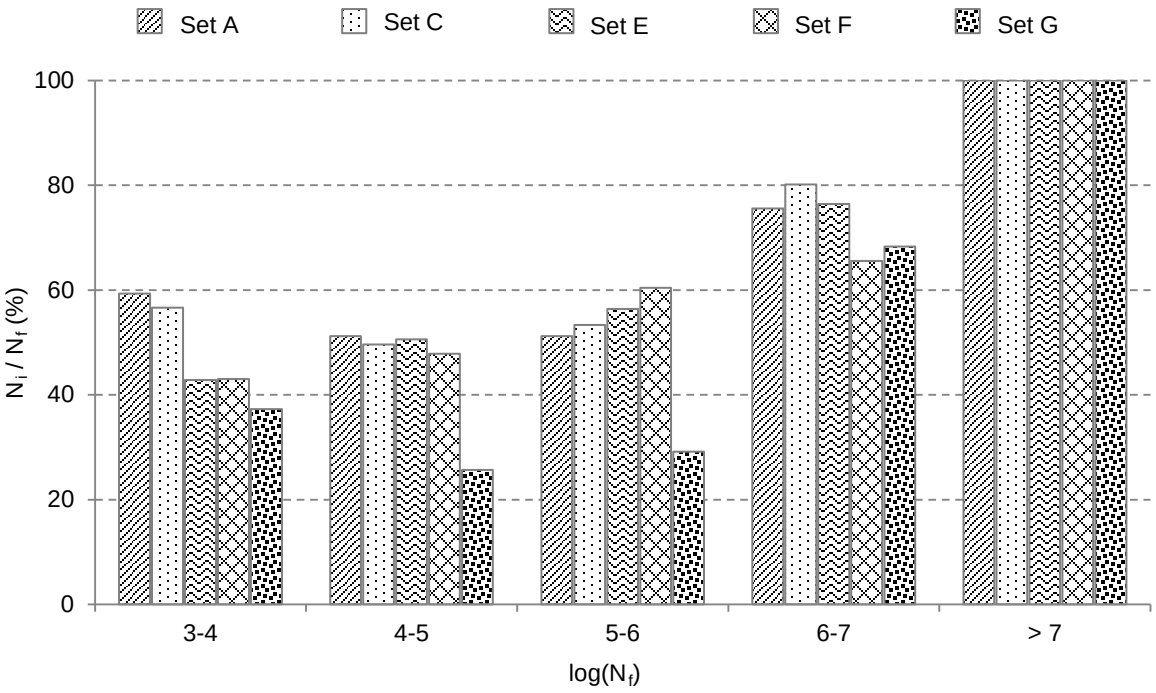

Figure 3.33: Crack initiation life portion for different RSW specimens

This graph shows that for $N_f < 10^6$ cycles crack initiation life for magnesium spot-welds in TS configuration (sets A to F) and CT configuration (set G) is around 50% and 30% of the total life, respectively. This fraction increases at higher lives such that for run-out tests, *i.e.*, $N_f > 10^7$ cycles, the crack initiation life is equal to total interrupted life for all spot-weld specimens investigated.

3.4 Cyclic Loading Effects

Three specimen sets (A, C, and E) were chosen to study the effect of cyclic loading. A number of specimens from these sets were analyzed before and after cyclic loading. The results are presented and discussed in the following sections.

3.4.1 Microstructure

Figure 3.34 shows the microstructures of the BM, HAZ and FZ on samples which failed in LCF and HCF.

Comparing these microstructures with Figure 3.8, Figure 3.10 and Figure 3.12 reveals that cyclic loading does not have a significant effect on microstructural features of the BM and the weld region. In particular, the HAZ, which is identified as the most critical spot through finite element simulations to be presented in Chapter 5, does not show a significant change in twin band volume fraction, before or after cyclic loading. This observation confirms that twin deformation in unloading reversals is almost fully recovered in subsequent reloading reversals. It is worth noting that the HAZ does not have the same texture as the BM, as a result of recrystallization; therefore, weaker texture is expected inside the HAZ. Consequently, each loading reversal may cause twinning in some grains and untwinning in some others. The same observation has been reported for AZ31B sheet [52], and ZK60A extrusions for Mg alloys [62].

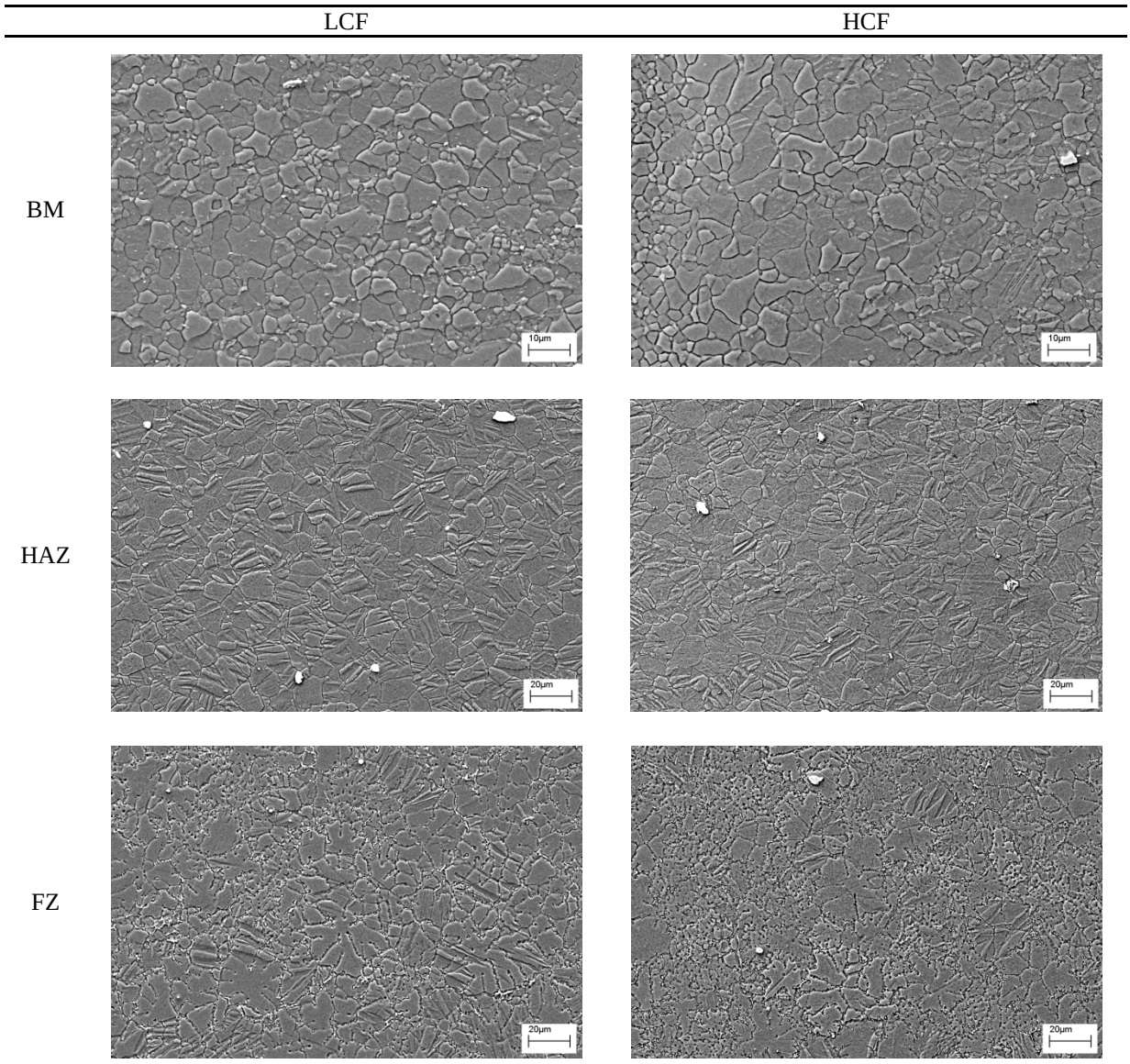

Figure 3.34: Cyclic loading effects on microstructures

3.4.2 Hardness

The graphs in Figure 3.35 compare the hardness profiles for specimens in sets A, C and E under three loading conditions, *i.e.*, before loading and after failure in LCF or HCF. Hardness tests in all cases were performed from the weld center to the BM on one side. “BL” in the graph legend denotes the “before loading” condition.

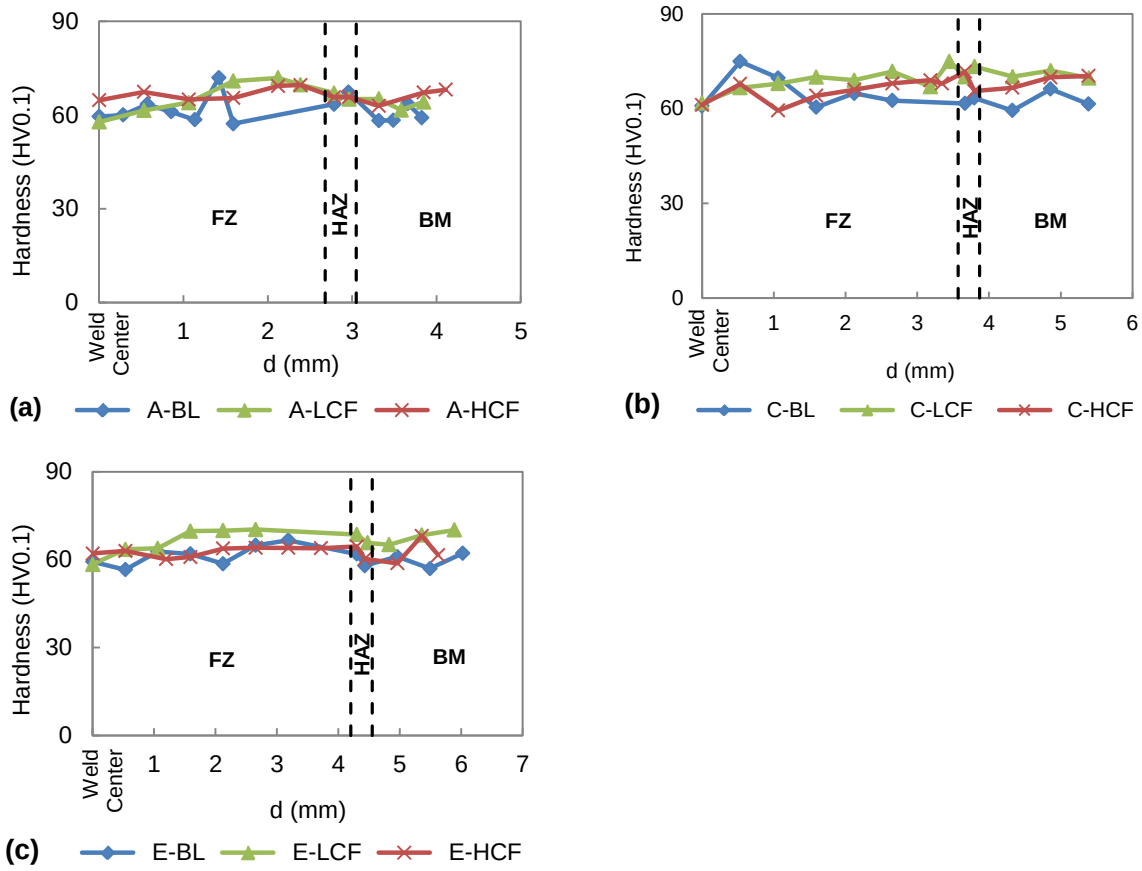

Figure 3.35: Effect of cyclcic loading on hardness profiles (a) set A (b) set C and (c) set E

The profiles in this figure show that hardness does not appreciably vary before and after cyclic loading, which agrees with the insignificant effect of cyclic loading on the microstructure. Therefore, it is expected that the BM and the weld area do not show cyclic softening or hardening behavior. This is similar to advanced high strength steel (AHSS) spot-welds, but is in contrast to HSLA steel spot-welds, which show cyclic softening behavior in the weld region under high cyclic loads [142].

3.4.3 Crack Initiation and Propagation

Along with the goal of characterizing the fatigue behavior of Mg spot-welds, the effect of cyclic loading on the fatigue crack initiation point was investigated. As shown in Figure 3.36, the distance between the nugget edge and the crack initiation site, “L”, is considered as the comparison criterion,

as it is independent of nugget diameter and represents the location of maximum local strain from the bond region.

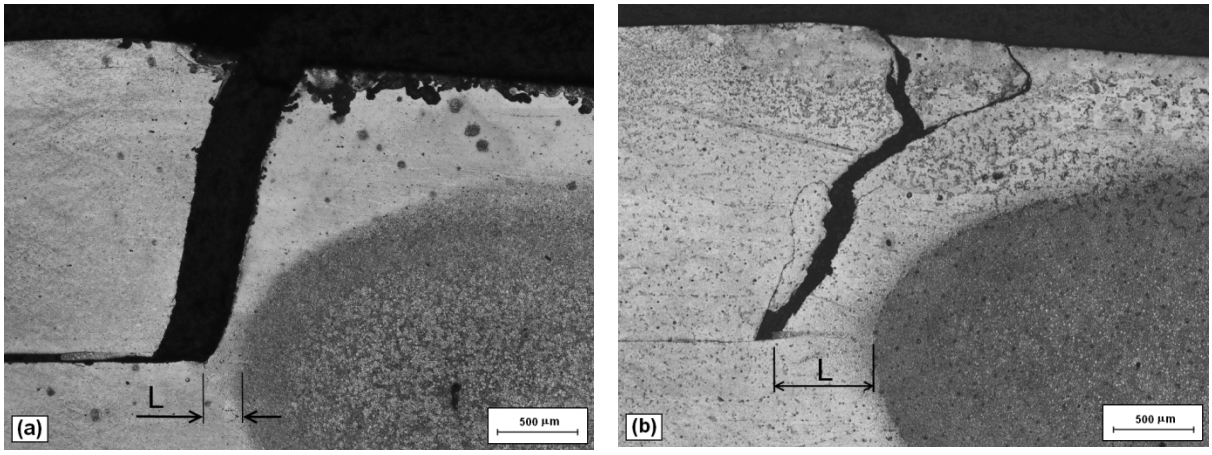

Figure 3.36: Crack initiation point (a) in LCF (b) in HCF

The distance L was measured in various specimens from sets A, C, and E, and the results are summarized in Figure 3.37. This graph shows that in the three specimen sets under investigation, crack initiation is closer to the nugget edge in LCF, and as the cyclic load decreases, cracks initiate farther from the nugget. The same observations have been reported for steel spot-welds [1,142].

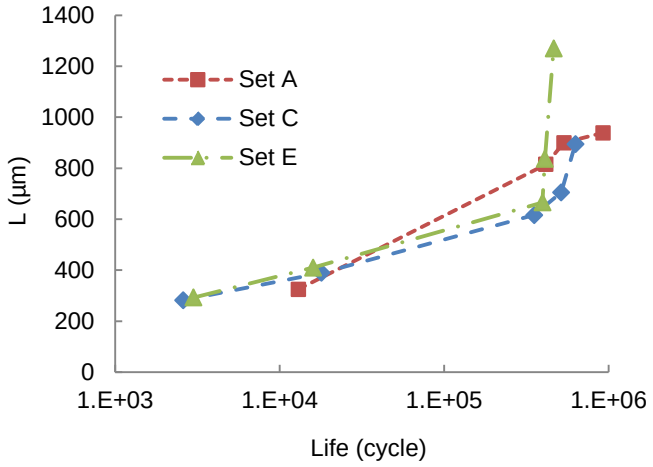

Figure 3.37: Distance between crack initiation point and nugget edge

Cracks in all specimens which failed in LCF nucleated inside the HAZ or at the interface of the HAZ and BM, while in specimens which failed in HCF, cracks initiated in the BM. One of the reasons why nugget size has less pronounced effect on fatigue resistance in HCF (see Figure 3.25) is

that the cracks initiated far from the FZ and therefore nugget size did not have as much of an effect on the stress field at the crack nucleation site.

In terms of fatigue crack propagation, the crack length was measured on the cross-section passing through the center of the spot-welds in different specimens, under low and high cyclic loads. Studying the spot-weld cross-section reveals that there are two cracks on most samples, one on each coupon, on the load bearing side of the weld. In failed specimens, the crack which caused separation in the specimen is referred to as the "primary crack" and the other crack, which is on the opposite side of the weld, is called the "secondary crack". Figure 3.38 shows the primary and secondary cracks in two specimens in set C, under different cyclic loading conditions.

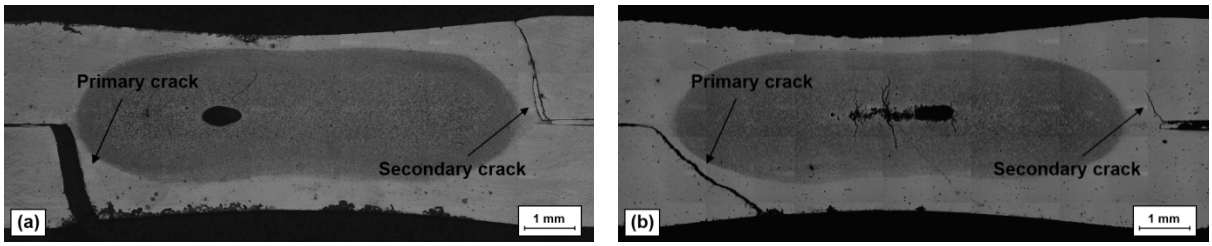

Figure 3.38: crack propagation in specimens in set C (a) in LCF and (b) in HCF

Figure 3.38 illustrates that in LCF the secondary crack has propagated through the whole coupon thickness, while in the high cycle regime it only propagated a portion of the sheet thickness. Table 3.8 summarizes the crack propagation length in the three sets under investigation.

Table 3.8: Fatigue crack propagation under high and low cyclic loads

Specimen	Loading condition	Crack propagation
Set A	LCF	Cracks on both sides; SC[a] length =t[b]
	HCF	Cracks on both sides; SC length = 0.8t
	Run-out	No crack
Set C	LCF	Cracks on both sides; SC length =t
	HCF	Cracks on both sides; SC length = 0.3t
	Run-out	No crack
Set E	LCF	Cracks on both sides; SC length =t
	HCF	Crack on one side
	Run-out	No crack

[a] SC: Secondary Crack
[b] t: sheet thickness

In specimens which did not fail, *i.e.*, run-out specimens, no crack was initiated on either side, suggesting that the crack initiation life is a significant portion of the total fatigue life for spot-welds in

HCF, which supports the finding reported in section 3.3.2.2. Also, this is in agreement with work by McMahon and Smith [181].

In terms of primary crack propagation, there is a dependence between the propagation path and cyclic loading amplitude. The primary crack under high cyclic loads, as shown in Figure 3.39(a), grows through the coupon thickness normal to the sheet surface and follows the nugget's circular shape in the plane of the sheet, and finally extends through the coupon width perpendicular to the loading direction.

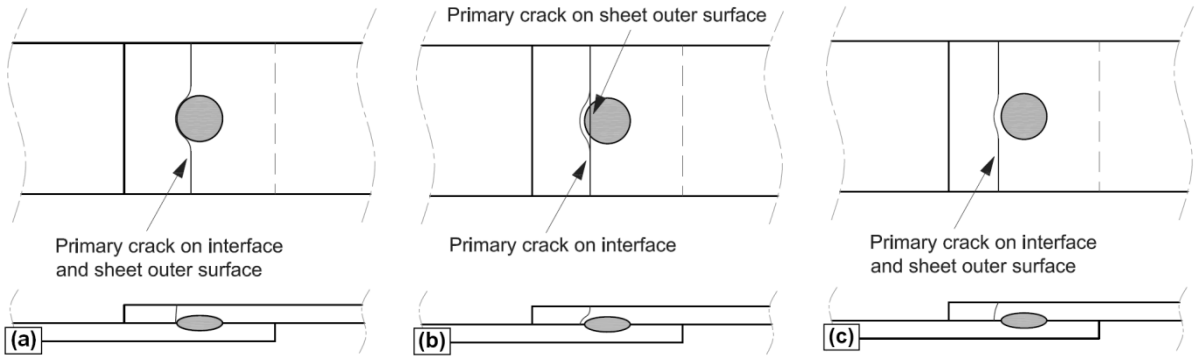

Figure 3.39: Primary crack propagation path under (a) high load, (b) intermediate load, and (c) low load

Figure 3.39(b) shows the crack propagation path under lower loads, *i.e.*, the intermediate cycle regime. This was similar to the path under high loads, except that along the thickness the crack tended toward the nugget and did not follow the nugget shape as much in the plane of the sheet. For loads just above the endurance limit, *i.e.*, lives more than 5×10^5 cycles, as shown in Figure 3.39(c), crack growth through the thickness was on a curved path and then propagated along the coupon width, almost along a straight line, with an offset from the nugget.

3.5 Discussion: Resistance Spot *vs.* Friction Stir Spot-Weld

As a part of the fatigue task of the MFERD project, a multinational round-robin experimental program was planned between four separate universities and institutes from Canada, China, and the United States for fatigue testing of friction stir spot-weld (FSSW) specimens. University of Waterloo (UW), Ryerson University (RU), Institute of Material Research (IMR), and Mississippi State University (MSU) participated in this program. Each university was provided with eight specimens by Hitachi America Ltd. Research & Development with the geometry shown in Figure 3.40.

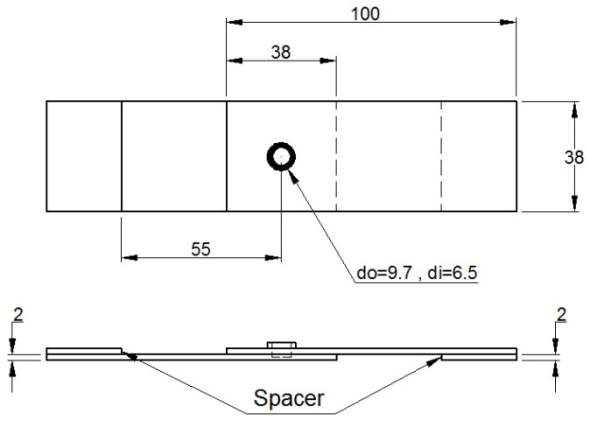

Figure 3.40: FSSW specimen geometry

In addition to the FSSW testing, UW (the current research) performed the same tests on resistance spot-weld (RSW) specimens, to compare the performance of these two welding processes for Mg sheets. The RSW specimen testing was conducted on the specimen Set F, Figure 3.5(b), and the results were presented earlier in this chapter.

The FSSW process parameters included a spindle speed of 750 rpm, a plunging speed of 20 mm/min, a shoulder plunge depth 0.1 mm, and a holding time of 2.5 sec. Comparing Figure 3.40 with Figure 3.5(b), the geometry of FSSW and RSW specimens was the same, except the nugget size, as a result of the different nature of the welding processes.

Monotonic testing on FSSW specimens was performed with the same conditions as RSW specimens, mentioned in section 3.3.1.2. Two FSSW specimens were tested at Waterloo and the load and displacement histories, as well as the failure mode, were recorded. Table 3.9 compares the monotonic ultimate load for FSSW and RSW specimens.

Table 3.9: Monotonic test results for FSSW and RSW specimens

	Avg. ultimate load (kN)	Std. Dev.
FSSW	4.66	0.01
RSW	7.62	0.05

According to this table, there is a noticeable difference between the static ultimate loads. Considering that FSSW and RSW specimens both failed at the interface, the difference was mainly attributed to the bonded area. Although the outer diameter of the bonded area in FSSW specimens (9.7 mm) was very close to the nugget diameter in RSW specimens (10.4 mm), the effective bonded area for FSSW is much less than that for RSW (40 mm^2 for FSSW and 85 mm^2 for RSW), due to the tool hole inside the FSSW. In addition, the two welding processes likely result in different strengths in the FZ; this can contribute to the different monotonic ultimate loads.

Similar to RSW specimens, FSSW specimens failed in the interfacial mode under monotonic loading. Figure 3.41 displays a fractured FSSW specimen under monotonic loading.

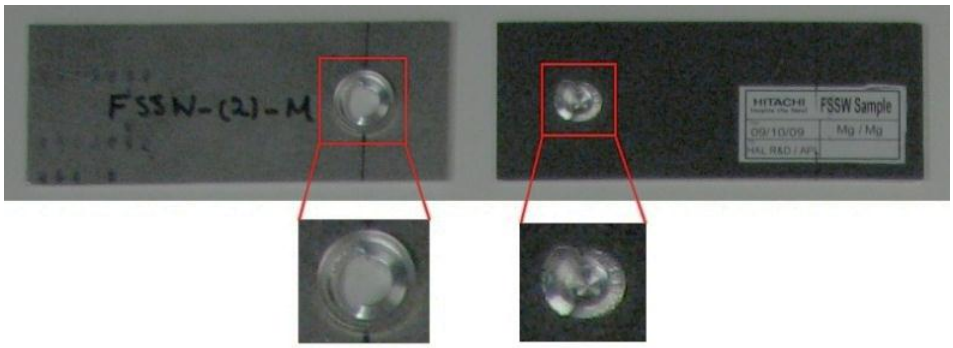

Figure 3.41: Failure mode in FSSW under monotonic loading

Fatigue testing was performed at a load ratio, R=0.1, for two load levels, P_{max}= 1 kN and 3 kN, with a loading frequency of 5 Hz. Each University conducted fatigue tests on six specimens, three at

each load level. Figure 3.42 compares the load-life results obtained from fatigue testing of FSSW and RSW specimens.

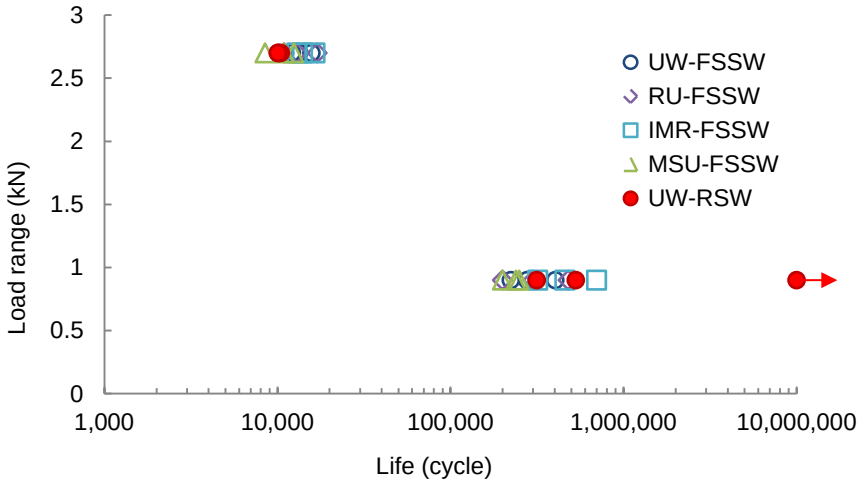

Figure 3.42: Load-life experimental data for FSSW and RSW specimens

Fatigue lives at the higher load (LCF) are very similar for the two welds. At the lower load (HCF), RSW exhibits slightly superior performance. Having a run-out test for RSW at P_{max}=1 kN indicates that the endurance limit is very close to this load level.

Figure 3.43 illustrates the failure modes in FSSW and RSW specimens under low and high cyclic loads. FSSW specimens failed in the coupon under low cyclic load, and in the interfacial mode under high cyclic load. Coupon failure was the only mode of failure for RSW specimens.

Max. Load	FSSW	RSW
1 kN		
3 kN		

Figure 3.43: Fatigue failure modes in FSSW and RSW specimens

With the same failure modes in HCF, the superior performance of RSW specimens can be attributed to a larger outer nugget diameter for RSW specimens, which results in more stiffness, less coupon bending, and less normal stress in the coupons.

3.6 Summary

Material characterization was performed from microstructural and mechanical points of view. The material under investigation was AZ31B-H24 Mg alloy. Several spot-welds with different configurations and nugget sizes were studied.

Microstructure and hardness testing was performed on the BM and different regions in the spot-welds. It was shown that grains are equiaxed within the BM as a result of post-rolling heat treatment. The average grain size in the BM was 5 μm along both the RD and the TD. The HAZ possessed a gradient in grain size from 6 to 10 μm, which increased toward the FZ due to higher annealing temperatures and time. The PMZ was identified as the interfacial region between the HAZ and FZ. The main feature associated with the PMZ was liquation and intermetallic formation at grain boundaries as a result of higher aluminum content. The core of the FZ had an equiaxed dendritic microstructure with intermetallics gathered at interdendritic regions. Hardness profiles were generated for different spot-welds through micro-indentation Vickers hardness testing. The results revealed that magnesium spot-welds, in contrast to steel and aluminum spot-welds, had a substantially uniform hardness distribution.

Monotonic testing was conducted on the BM and spot-welded specimens. Monotonic testing of the BM demonstrated asymmetric hardening behavior under tension and compression, which was attributed to the textured microstructure of wrought magnesium alloys. Hardening behavior of AZ31B under uniaxial in-plane tension was concave-down, *i.e.*, could be modeled with power-law equation, as a result of the slip deformation mode. However, the flow curve under uniaxial in-plane compression had a concave-up shape, due to twinning plastic deformation. Monotonic testing of the BM in RD and TD showed in-plane anisotropy. Monotonic testing was also performed on spot-welded specimens in the TS and CT configurations. Interfacial and partially-interfacial were the failure modes for the TS specimens, and button-pullout and coupon failure were the modes of failure for CT specimens. Similar to spot-welds of steel and aluminum, a linear relationship was found between ultimate tensile shear load and nugget diameter for magnesium spot-welds.

Fatigue testing was conducted on the BM in the RD in fully-reversed strain-control conditions. An unusual asymmetric shape of the hysteresis loop was the key feature of the cyclic behavior, which was more pronounced at high strain amplitudes. The inflection point on the reloading curve, *i.e.*, tension following compression, became distinguishable at high strain amplitudes due to saturation of untwinning deformation. An increase in hardening rate after the inflection point was related to the activation of non-basal slip or compression twin mechanisms of plastic deformation.

Fatigue testing of different spot-weld specimens showed that enlarging the nugget size slightly enhanced the fatigue strength in LCF, but this effect becomes less pronounced in HCF. It was also demonstrated that increasing the coupon width and decreasing the mean load improved the fatigue strength in LCF, but this effect gradually diminished in HCF. Fatigue test results on CT specimens showed a remarkable drop in fatigue strength, as compared to TS specimens with the same nugget size. Fatigue failure modes in TS spot-weld specimens include interfacial, partially-interfacial, and coupon failure, while the CT spot-weld specimens failed only in the button-pullout mode under cyclic loading.

Fatigue crack initiation behavior was studied for spot-welded specimens. Crack initiation life was calculated for all experimental data points. The criterion for crack initiation in the current research was a 5% increase in non-dimensional compliance. It was shown that, for the cases that total fatigue life was less than one million cycles, crack initiation lives for TS and CT spot-welded specimens was around 50% and 30% of the total life, respectively. This fraction increased at higher lives, such that for run-out tests, the crack initiation life was equal to the interrupted life for all spot-welded specimens investigated. Fatigue crack initiation location depended on the load level. Under high cyclic loading, cracks initiated close to the nugget edge; decreasing the cyclic load caused the cracks to initiate farther from the nugget. In run-out specimens, no crack was detected; this observation supported the conclusion that the crack initiation life was a significant portion of the total fatigue life of spot welds in the high cycle regime.

Chapter 4

Cyclic Plasticity Modeling of AZ31B

As discussed in the previous chapter, wrought magnesium alloys in general, and AZ31B sheet in particular, deform with dissimilar plastic deformation mechanisms under different loading conditions, which causes non-regular mechanical behavior. As a result, these materials do not follow the well-known material models implemented in commercial finite element packages. Therefore, a successful elastic-plastic FE simulation of wrought Mg structures requires developing a user material model which can properly simulate the material behavior. Because the final aim in this research is to model the fatigue behavior of Mg structures, cyclic plasticity theory needs to be employed in the material modeling. This chapter covers the theory, formulation, and implementation of a cyclic plasticity-based constitutive model for simulating the fatigue behavior of AZ31B. The model is verified at the end of this chapter.

4.1 Constitutive Modeling of AZ31B

4.1.1 Introduction

Stress analysis of structures under a small load can be accomplished employing theory of elasticity, *i.e.*, the assumption of linear-elastic material behavior. This assumption implies that the deformation or strain is fully recovered upon load removal. However, higher loads result in permanent deformation, indicating that the stress-strain relationship is no longer linear. Therefore, a realistic general solution requires application of the theory of plasticity through an elastic-plastic analysis.

There are two main approaches in the theory of plasticity: total deformation, and incremental plasticity. The total deformation approach has a simple formulation, but the drawback is that plastic strain components are obtained from the final values of stress components, regardless of stress history. Therefore, this approach is solely applicable to proportional loading. Incremental plasticity, however, relates increments of strains to stresses; hence it depends on load history. Incremental plasticity is a more promising approach for non-proportional (including cyclic) loading. However, more complex formulation and implementation are involved in this approach.

The theory of plasticity, regardless of the approach, includes three fundamental components: yield criterion or function, flow rule, and hardening rule. Yield criterion is a function of stress components, and specifies when initial yielding occurs. Flow rule determines the components or direction of plastic strain or plastic strain increment. Hardening rule dictates how the yield surface evolves during plastic loading. These concepts are explained in more details in the following sections.

4.1.2 Yield Function

4.1.2.1 Introduction

The yield function defines the elastic limit of a material under general stress states. For the simple case of uniaxial loading, the yield function is reduced to a value, *i.e.*, a *point* on the uniaxial stress-strain curve. Under biaxial loading, the yield function is represented as a *curve* in two-dimensional stress space, and in the case of multi-axial loading a *surface* defines the yield boundary, which is also called the yield surface. The majority of experimental results on metals show that hydrostatic tensile and compressive stresses do not change the yield surface [92,182]. Therefore, yield surfaces have cylindrical or prismatic shapes oriented along the hydrostatic stress axis ($\sigma_1 = \sigma_2 = \sigma_3$). However, a number of geo-materials such as soil, rock and concrete exhibit hydrostatic pressure dependence [182].

The most well-known yield functions, including Tresca, von Mises, coulomb-Mohr, and Drucker-Prager, are briefly introduced in following sections. A newly-developed asymmetric yield function, Cazacu-Barlat, is also explained.

4.1.2.2 Tresca

Henri Tresca in 1864 [94] proposed the first yield criterion for metals under multi-axial loading. This yield criterion states that yielding begins when the maximum shear stress reaches the shear stress at the yield point in a uniaxial tensile test. The Tresca yield criterion in terms of principal stresses can be stated as

$$max\left(\frac{1}{2}|\sigma_1 - \sigma_2| \ , \ \frac{1}{2}|\sigma_2 - \sigma_3| \ , \ \frac{1}{2}|\sigma_3 - \sigma_1|\right) = \frac{S_y}{2} \tag{4.1}$$

where σ_1 , σ_2, σ_3 are principal stresses, and S_y is the uniaxial yield strength. Tresca yield surface for plane-stress state, $\sigma_3 = 0$, is shown in Figure 4.1. This figure shows that the Tresca yield criterion assumes symmetric yield stresses under tension and compression.

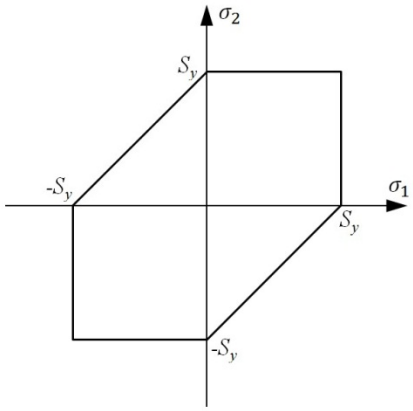

Figure 4.1: Tresca yield surface for plane-stress state

The Tresca yield surface in the three-dimensional principal stress space is a hexagonal prism oriented along hydrostatic axis with infinite length, as shown in Figure 4.2(b). This means that the Tresca yield criterion is pressure-independent, and applicable to metals.

4.1.2.3 von Mises

Richard E. von Mises in 1913 [95] developed the most common yield criterion for ductile materials. This yield criterion predicts that yielding begins when the distortion energy per unit volume reaches the distortion energy per unit volume in a uniaxial tensile test at the yield point [183]. The von Mises yield criterion in terms of principal stresses can be expressed as

$$\sqrt{1/2\ [(\sigma_1 - \sigma_2)^2 + (\sigma_2 - \sigma_3)^2 + (\sigma_3 - \sigma_1)^2]} = S_y \quad . \tag{4.2}$$

The von Mises yield surface for plane-stress state is illustrated in Figure 4.2(a) and compared with the Tresca yield surface. This figure shows that the von Mises yield function is applicable to materials with symmetric yielding under tension and compression. This figure also demonstrates that the Tresca yield criterion is more conservative as compared to the von Mises.

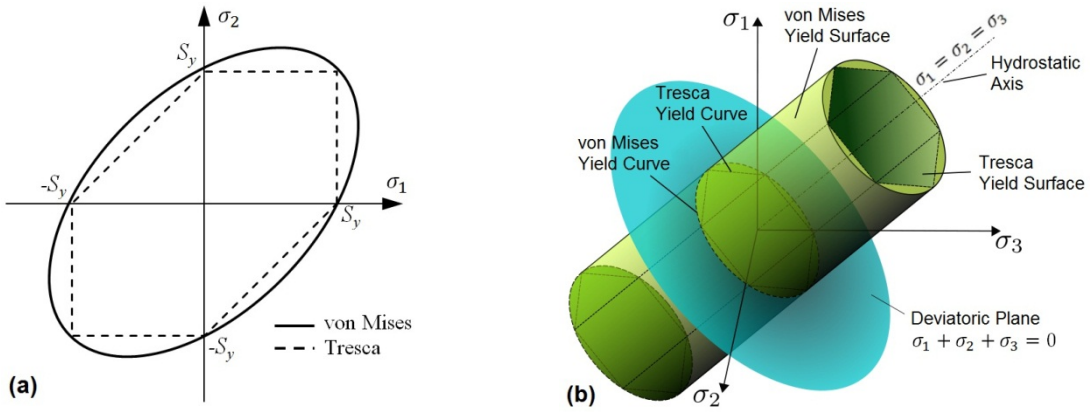

Figure 4.2: von Mises and Tresca yield surfaces (a) two-dimensional space (b) three-dimensional space [184]

Figure 4.2(b) compares the von Mises and Tresca yield surfaces in three-dimensional principal stress space. This figure illustrates that, similar to the Tresca, the von Mises yield surface is pressure-independent.

4.1.2.4 Coulomb-Mohr

The Coulomb-Mohr yield criterion, similar to the Tresca criterion, is based on the maximum shear stress. It can be mathematically expressed as

$$\frac{m+1}{2} max[|\sigma_1 - \sigma_2| + K(\sigma_1 + \sigma_2),\ |\sigma_2 - \sigma_3| + K(\sigma_2 + \sigma_3), |\sigma_3 - \sigma_1| + K(\sigma_3 + \sigma_1)] = S_y^c \quad (4.3)$$

where $m = \frac{S_y^c}{S_y^t}$, $K = \frac{m-1}{m+1}$, and S_y^t and S_y^c are uniaxial yield strengths under tension and compression, respectively.

The Coulomb-Mohr criterion is essentially a generalized form of the Teresa criterion, because it considers asymmetric yielding under tension and compression, Figure 4.3(a). Moreover, the Coulomb-Mohr criterion assumes that the critical value for shear stress changes with hydrostatic stress ($\sigma_{hyd} = 1/3 \sum_{i=1}^{3} \sigma_{ii}$). Therefore, the Coulomb-Mohr criterion is pressure-dependent, and has a conical prism shape in three-dimensional stress space with a hexagonal cross-section, as shown in Figure 4.3(b).

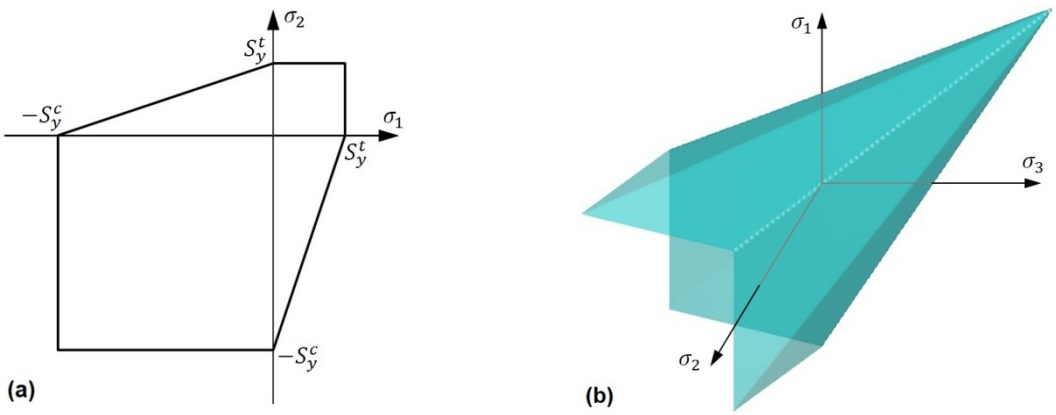

Figure 4.3: Coulomb-Mohr yield surface in (a) two-dimensional space (plane-stress state) (b) three-dimensional space [184]

This yield function is mostly used to model geo-materials, for which the yielding behavior is pressure-dependent.

4.1.2.5 Drucker-Prager

The Drucker-Prager yield function is based on distortion energy, and is a modification of the von Mises criterion. This yield function in terms of principal stresses is stated as

$$\left(\frac{m-1}{2}\right)(\sigma_1+\sigma_2+\sigma_3)+\left(\frac{m+1}{2}\right)\sqrt{\frac{(\sigma_1-\sigma_2)^2+(\sigma_2-\sigma_3)^2+(\sigma_3-\sigma_1)^2}{2}}=S_y^c \tag{4.4}$$

where $m=\frac{S_y^c}{S_y^t}$.

Figure 4.4(a) compares the Drucker-Prager and Coulomb-Mohr yield criteria. It can be seen that the Drucker-Prager yield criterion, similar to Coulomb-Mohr, can model materials with asymmetric yielding in tension and compression. Equation (4.4) and it's graphical illustration in Figure 4.4(b) indicate that the Drucker-Prager yield criterion depends on hydrostatic stress. Therefore, it is not applicable to the majority of metals which exhibit pressure-independent yielding behavior.

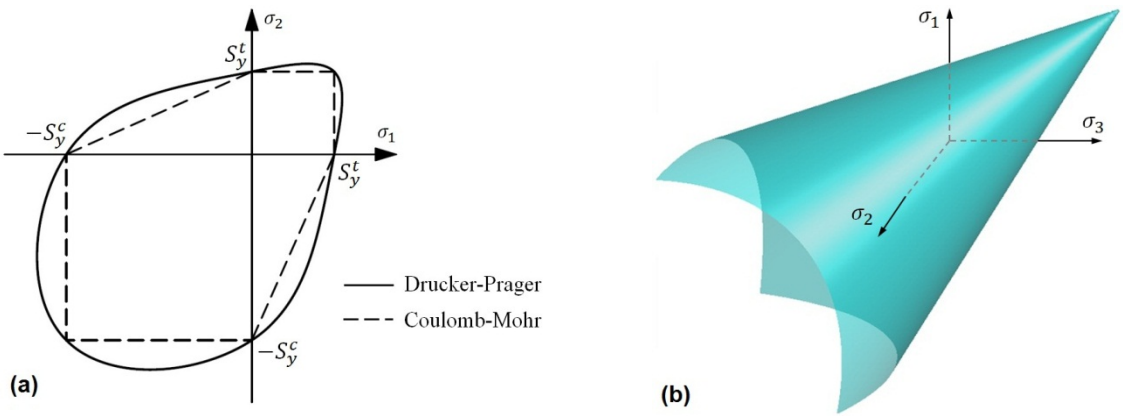

Figure 4.4: Drucker-Prager and Coulomb-Mohr yield surfaces in (a) plane-stress state (b) three-dimensional space [184]

4.1.2.6 Cazacu-Barlat

Cazacu and Barlat in 2004 [104] proposed the first macroscopic asymmetric yield criterion for pressure-independent materials, which is a generalized form of the von Mises yield criterion. This yield function for isotropic materials is of the form

$$f = (J_2)^{3/2} - C\,J_3 \tag{4.5}$$

where $J_2 = \frac{1}{2}tr(\boldsymbol{S}^2)$ and $J_3 = \frac{1}{3}tr(\boldsymbol{S}^3)$ are the second and third invariants of deviatoric stress tensor $\boldsymbol{S}$, respectively[1]. Deviatoric stress is obtained by subtracting hydrostatic stress from the Cauchy stress tensor, $S_{ij} = \sigma_{ij} - \sigma_{hyd}\,\delta_{ij}$, where δ_{ij} is the Kronecker delta. The symbol tr stands for the trace operator, $tr(\boldsymbol{A}) = \sum_{k=1}^{3} A_{kk}$. Parameter C is a material constant, representing the yielding asymmetry, and is obtained from

$$C = \frac{3\sqrt{3}}{2} \cdot \frac{\left(S_y^{t\,3} - S_y^{c\,3}\right)}{\left(S_y^{t\,3} + S_y^{c\,3}\right)} \tag{4.6}$$

For materials with symmetric yielding, *i.e.*, $S_y^t = S_y^c$ or $C = 0$ the Cazacu-Barlat yield criterion reduces to the von Mises yield criterion. To ensure convexity of the yield surface, the parameter C has

[1] Regular and bold symbols in this thesis represent scalar and tensorial variables, respectively.

to be within the range: $C \in \left[-3\sqrt{3}/2\ ,\ 3\sqrt{3}/4\right]$. The concept of convexity will be explained later in section 4.1.3.2. Figure 4.5 illustrates the effect of parameter C on the shape of the yield surface.

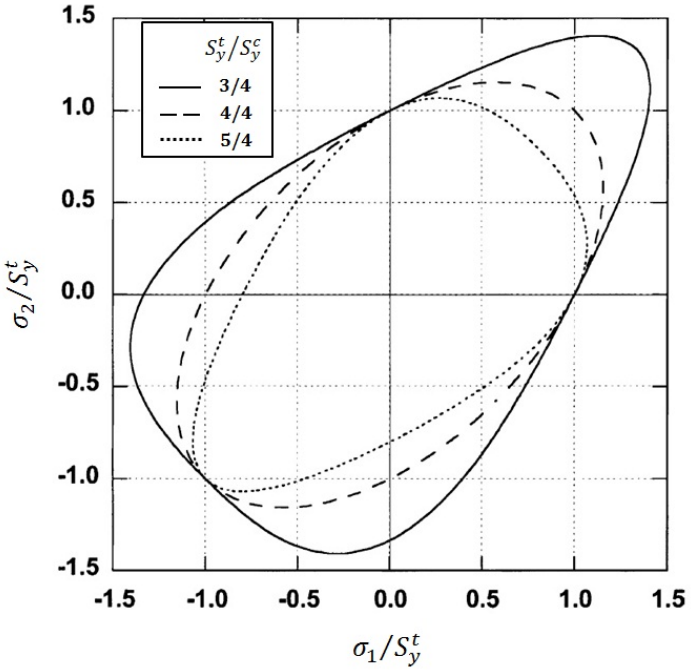

Figure 4.5: Cazacu-Barlat yield criterion for plane-stress state [104]

The equivalent stress corresponding to this yield function is given by

$$\bar{\sigma} = A\left[(J_2)^{3/2} - C\,J_3\right]^{\frac{1}{3}} \tag{4.7}$$

where A is a parameter that is found such that the equivalent stress, $\bar{\sigma}$, is equal to the stress under uniaxial tensile loading. For isotropic materials, $A = 3\left(3^{3/2} - 2c\right)^{-1/3}$.

The Cazacu-Barlat yield criterion was adopted in this research, because it considers yielding asymmetry and is hydrostatic stress-independent. A more general form of this yield criterion has been developed by Cazacu and Barlat for anisotropic materials [104], however, it is not presented in this section, because anisotropy of AZ31B sheet is neglected for cyclic behavior in this research, as discussed in the previous chapter.

4.1.3 Flow Rule

The flow rule in theories of plasticity determines how the material deforms after reaching the yield surface. In other words, it specifies the components of plastic strain or plastic strain increment. The majority of plasticity models assume that the plastic strain vector is normal to a surface, called the plastic potential. Plastic potential may or may not be the same as the yield surface (this will be explained in section 4.1.3.2). This division results in associated and non-associated flow rules. These flow rules will be described in more detail in this section, with more emphasis on the associated flow rule, which was employed in the current research. First, Drucker's stability postulate will be explained briefly as the basis for the associated flow rule.

4.1.3.1 Drucker's stability postulate

Let us consider an element of a material, loaded from the elastic region (point A_0) to the elastic-plastic region (point A_2), and unloaded to the same stress point (point A_3), as shown in Figure 4.6. Point A_1 corresponds to the yield point before loading.

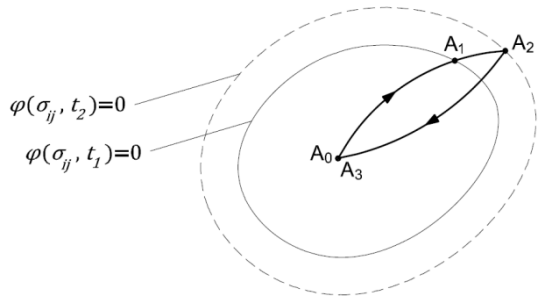

Figure 4.6: Loading and unloading in stress space [92]

Assuming an infinitesimal plastic strain ($d\varepsilon^p$) during loading, the plastic work per unit volume in this cycle is

$$dW^p = \oint \sigma . d\varepsilon^p . \tag{4.8}$$

Drucker's stability postulate states that a material is stable if for any arbitrary start point (A_0), located inside the elastic region, the plastic work is positive. Figure 4.7 illustrates this loading cycle on the uniaxial stress-strain curve for stable and unstable materials.

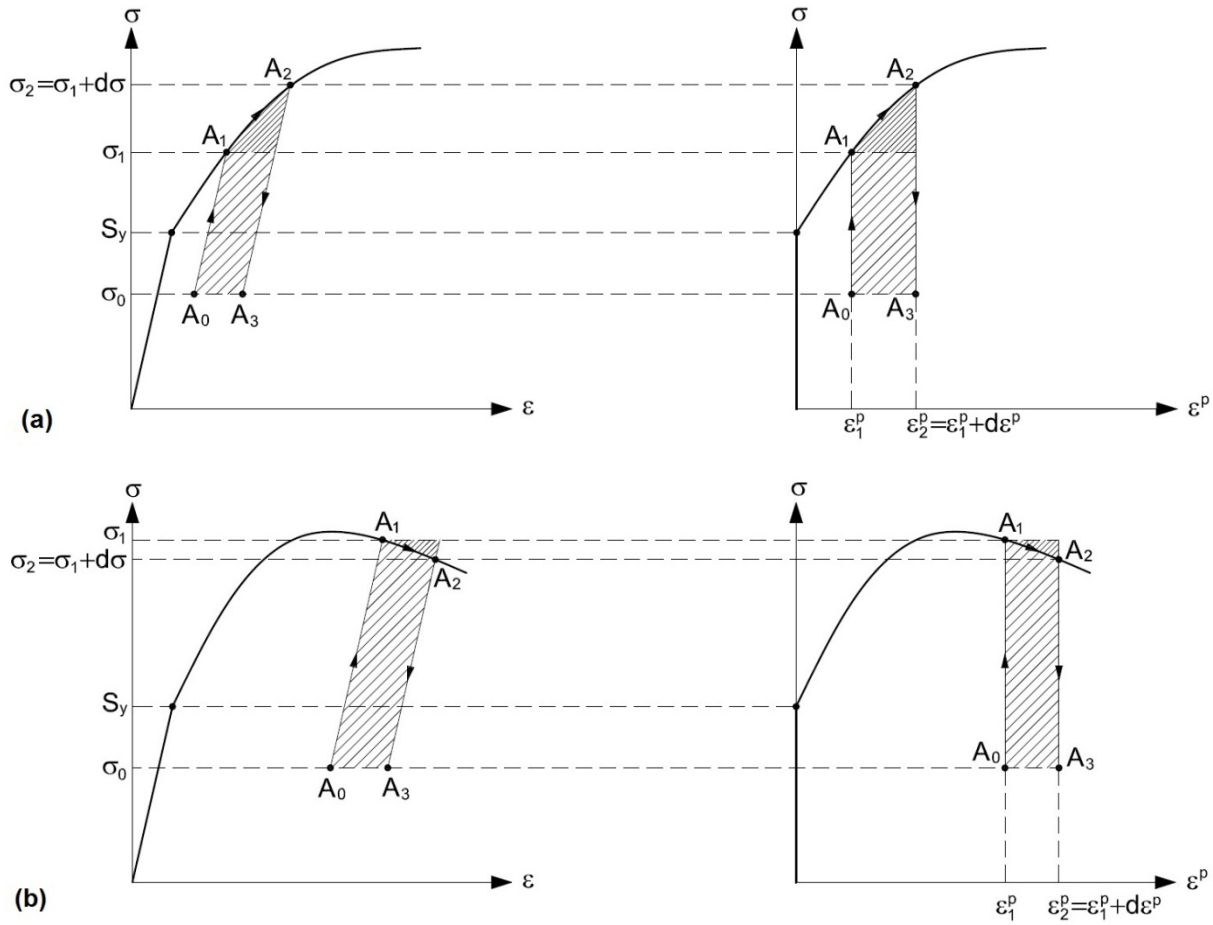

Figure 4.7: Drucker's postulate illustration for (a) stable material (b) unstable material [92]

According to Figure 4.7, Drucker's stability postulate for uniaxial loading may be expressed as

$$dW^p = (\sigma_1 - \sigma_0)d\varepsilon^p + \frac{1}{2}d\sigma d\varepsilon^p \ > 0\ , \tag{4.9}$$

or for general loading may be written as

$$dW^p = (\boldsymbol{\sigma}_1 - \boldsymbol{\sigma}_0)\ d\boldsymbol{\varepsilon}^p + \frac{1}{2}d\boldsymbol{\sigma}\ d\boldsymbol{\varepsilon}^p \ > 0\ . \tag{4.10}$$

To satisfy the above inequality, both terms in equation (4.10) have to be positive. Two basic concepts in the theory of plasticity are consequences of the Drucker's postulate. Classification of flow rules into associated and non-associated is based on these concepts. The implications of the Drucker's postulate are described in the next section.

4.1.3.2 Associated vs. Non-associated flow rule

According to Drucker's postulate, two conditions have to be satisfied to establish the stability of a material

$$(\boldsymbol{\sigma}_1 - \boldsymbol{\sigma}_0)\, d\boldsymbol{\varepsilon}^p > 0\,, \qquad d\boldsymbol{\sigma}\, d\boldsymbol{\varepsilon}^p > 0\,. \tag{4.11}$$

The first condition implies that any arbitrary vector $(\boldsymbol{\sigma}_1 - \boldsymbol{\sigma}_0)$ and plastic strain increment vector $(d\boldsymbol{\varepsilon}^p)$ have to make an acute angle. According to Figure 4.8, this condition results in "*convexity*" of the yield surface.

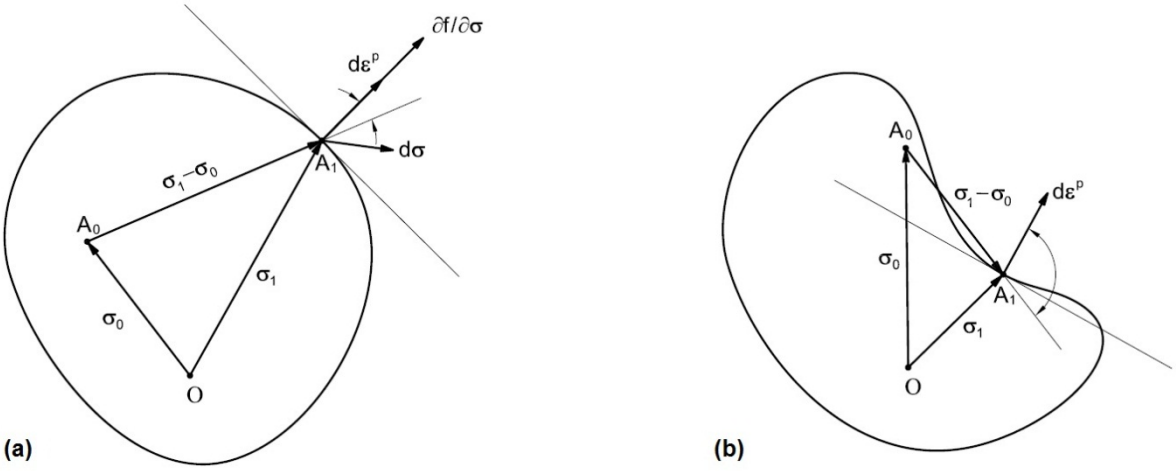

Figure 4.8: Drucker's postulate conclusions (a) convex yield surface (b) concave yield surface [92]

The second condition means that the angle between the stress increment vector $(d\boldsymbol{\sigma})$ and plastic strain increment vector $(d\boldsymbol{\varepsilon}^p)$ must be acute. The stress increment vector for plastic loading may have any direction, as long as it lies outside the current yield surface. Therefore, the plastic strain

increment vector has to be perpendicular to the yield surface, *i.e.*, parallel to the yield surface gradient vector, as shown in Figure 4.8(a). This implication of Drucker's criterion is the so-called "*normality rule*".

The concept of "*plastic potential*" was developed by Mises in 1928 [54]. Plastic potential, $g(\sigma_{ij})$, is a function of stress components, and the plastic strain increment vector is proportional to the gradient of this function. Therefore, the relationship between plastic strain components and stress components, *i.e.*, the "*flow rule*" is

$$d\varepsilon_{ij}^{p} = d\lambda \frac{\partial g(\sigma_{ij})}{\partial \sigma_{ij}} \quad . \tag{4.12}$$

where $d\lambda$ is a scalar, usually called the "*plastic multiplier*". If the plastic potential is the same as the yield function, the flow rule will be associated with the yield criterion. The flow rule in this case is a so-called "*associated flow rule*", and may be expressed as

$$d\varepsilon_{ij}^{p} = d\lambda \frac{\partial f(\sigma_{ij})}{\partial \sigma_{ij}} \quad . \tag{4.13}$$

If the plastic potential is different from the yield function, the flow rule is called a "*non-associated flow rule*". A non-associated flow rule is usually applied to materials that have pressure-dependent yielding behavior, such as geo-materials [92,185]. Considering that magnesium is a pressure-independent material [104], an associated flow rule was adopted in this study. The flow rule associated with the Cazacu-Barlat yield function is derived in appendix A.

4.1.4 Hardening Rule

While the yield function defines the initial yield surface, the hardening rule governs the yield surface change during plastic deformation. Hardening rules often assume that the change in yield surface is limited to translation and/or expansion, without any change in the yield surface shape and

orientation. The effect of the hardening rule on elastic-plastic solution is significant for problems involving complex loading such as non-proportional loading, unloading, and cyclic loading. The most common hardening rules are *isotropic hardening*, *kinematic hardening*, and *combined hardening*. These hardening rules are described in the following sections.

4.1.4.1 Isotropic hardening

As the simplest work-hardening model, the isotropic hardening rule assumes that materials harden uniformly in all directions during plastic deformation. In other words, the initial yield surface solely evolves by expansion, without any distortion or translation. Therefore an isotropic material remains isotropic after plastic deformation. The isotropic hardening rule can be written in the following general form

$$f(\boldsymbol{\sigma}) = \kappa(\bar{\varepsilon}^p) \quad \text{or} \quad f(\sigma_{ij}) = \kappa(\bar{\varepsilon}^p)\,, \tag{4.14}$$

where $\kappa > 0$ represents the size of the yield surface, and is a function of the *equivalent plastic strain*, $\bar{\varepsilon}^p$. Equivalent plastic strain is the summation of equivalent plastic strain increments, *i.e.*, $\bar{\varepsilon}^p = \int d\bar{\varepsilon}^p$, which may be related to plastic strain increments, $d\varepsilon_{ij}^p$, through the normality rule.

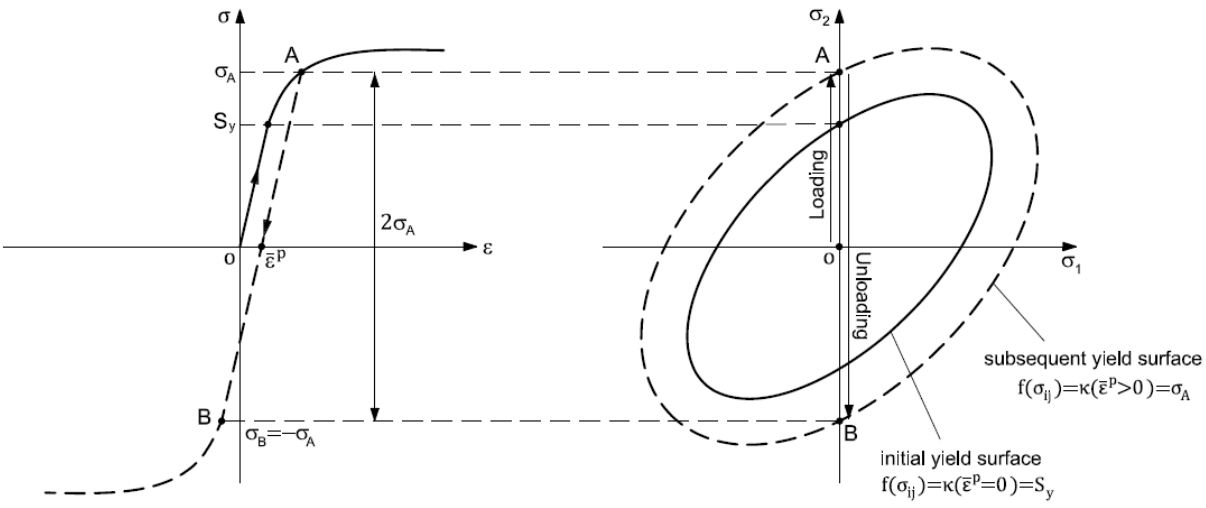

Figure 4.9: Yield surface evolution and reverse yielding under uniaxial loading for isotropic hardening

Figure 4.9 shows the evolution of the yield surface for the von Mises yield function. This figure also shows the predicted onset of yielding in unloading, point B, for the uniaxial tension-compression case. As can be seen in this figure, the isotropic hardening rule predicts symmetric yielding in reverse yielding, and does not account for the Bauschinger effect. The Bauschinger effect refers to a special behavior of materials, when yielding in one direction reduces the yield strength in the opposite direction, which is observed in most structural materials [182]. Therefore, isotropic hardening is not a suitable hardening rule for problems dealing with unloading or cyclic loading.

4.1.4.2 Kinematic hardening

The kinematic hardening rule models the evolution of the yield surface by a rigid body translation in stress space, without changing the size and shape of the yield surface. This hardening rule was proposed to account for the Bauschinger effect. Figure 4.10 shows the evolution of the yield surface for the von Mises yield function under uniaxial loading.

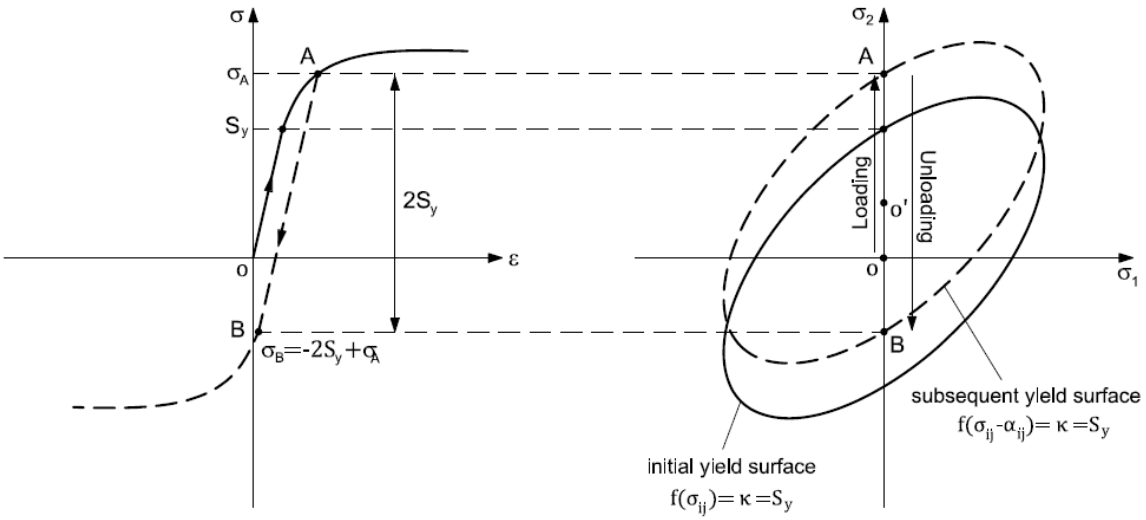

Figure 4.10: Yield surface evolution and reverse yielding under uniaxial loading for kinematic hardening

If the initial yield surface is defined as $f(\sigma_{ij}) = \kappa$, the subsequent yield surface will be

$$f(\boldsymbol{\sigma} - \boldsymbol{\alpha}) = \kappa \quad , \quad f(\sigma_{ij} - \alpha_{ij}) = \kappa \, , \tag{4.15}$$

where $\boldsymbol{\alpha}$ is a tensor representing the center of the yield surface, usually called the *"back stress"*, or *"shift tensor"*. The Parameter κ, which determines the size of the yield surface, is constant in this model, while $\boldsymbol{\alpha}$ evolves during plastic deformation. Therefore, a kinematic hardening model must include a strategy to define the evolution of the back stress. In what follows, two of the most popular models for back-stress evolution are introduced.

A. Prager's rule

Prager in 1955 [186] developed a model for evolution of the back stress, $\boldsymbol{\alpha}$, in which the yield surface translates along the plastic strain increment tensor, $d\boldsymbol{\varepsilon}^p$, or normal to the yield surface at the loading point. The constitutive equation for this hardening rule is of the form

$$d\alpha_{ij} = \xi d\varepsilon_{ij}^{p} \quad , \tag{4.16}$$

where ξ is a scalar. Prager's hardening rule for uniaxial loading is illustrated in Figure 4.11 for the von Mises yield function.

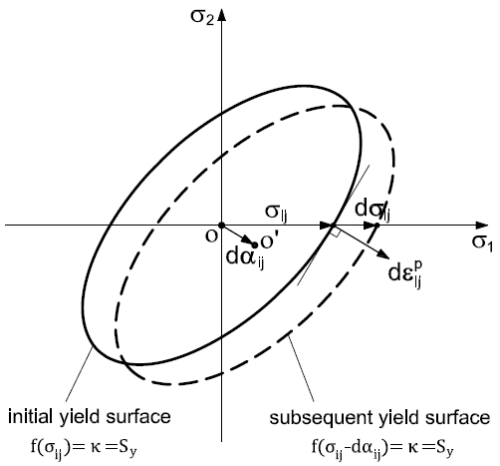

Figure 4.11: Prager's kinematic hardening rule for uniaxial tension

A drawback of this hardening rule is that uniaxial loading results in a multi-axial translation of the yield surface, due to the fact that the plastic strain increment tensor, $d\varepsilon_{ij}^{p}$, has three non-zero normal components under uniaxial loading, *i.e.*, $d\varepsilon_{22}^{p} = d\varepsilon_{33}^{p} = -\frac{1}{2}d\varepsilon_{11}^{p}$ for loading in the 1-direction. This consequence of Prager's rule implies that, during uniaxial loading, materials soften or harden in lateral directions, which is not supported by experimental results [93].

B. Zielger's rule

To overcome deficiencies in Prager's hardening rule, Shield and Ziegler in 1958 [187] proposed a model which assumes that the yield surface translates in the radial direction. This model is expressed as

$$d\alpha_{ij} = d\mu(\sigma_{ij} - \alpha_{ij}) \quad , \tag{4.17}$$

in which $d\mu$ is a positive scalar. Figure 4.12 shows the evolution of back stress according to Ziegler's rule for uniaxial and biaxial loading.

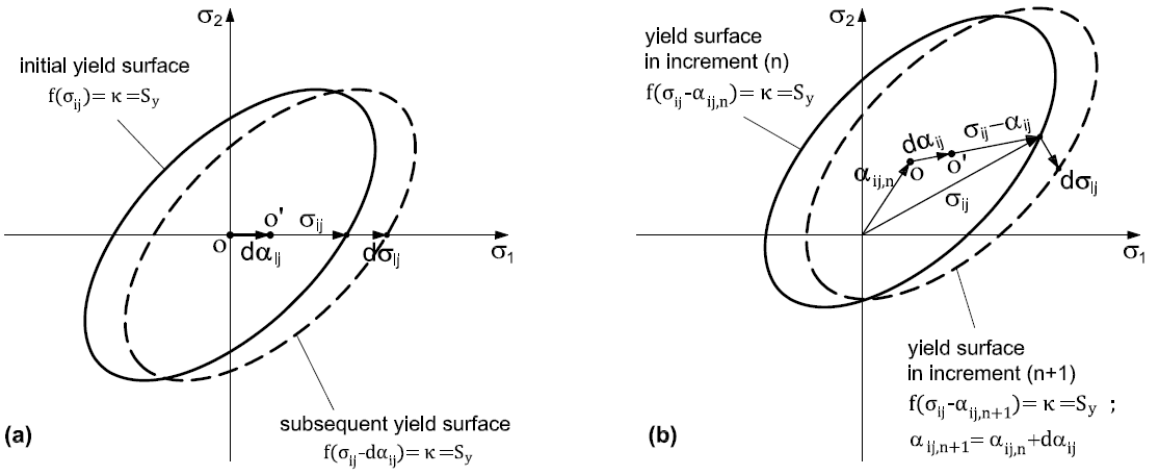

Figure 4.12: Ziegler's hardening rule (a) uniaxial loading (b) biaxial loading

As can be seen in Figure 4.12(a), the yield surface using Ziegler's rule translates only in the loading direction under uniaxial loading.

4.1.4.3 Combined hardening

Conventional isotropic and linear kinematic hardening models successfully represent hardening behavior of materials under proportional loading. However, the hardening behavior under complex loading paths, *e.g.*, cyclic loading, is not reasonably explained by these hardening rules. As a result, realistic modeling of engineering materials under cyclic loading has attracted many researchers' attention in recent years [93]. A number of constitutive models were developed to address this need

during the past five decades. Single-surface model proposed by Armstrong and Frederick [112], multi-surface model proposed by Mroz [114], and two-surface model developed by Dafalias and Popov [117] are among the major attempts toward this goal. The single-surface model produces nonlinear hardening behavior by adding a term to Prager's linear kinematic hardening rule. The multi-surface model involves multiple yield surfaces with Prager's linear kinematic hardening rule between each two subsequent yield surfaces. Therefore, the predicted flow curve is piecewise linear. In contrast, the two-surface model employs two yield surfaces with continuous updating the hardening between the two surfaces.

The hardening rule often adopted in the two-surface model is a combination of isotropic and kinematic hardening, so-called "combined hardening". This means that the yield surface both expands and translates during plastic deformation. Therefore, two hardening parameters (α_{ij} and $\bar{\varepsilon}^p$) are involved in this hardening model. The combined hardening rule can be formulated as

$$f\left(\sigma_{ij} - \alpha_{ij}\right) = \kappa(\bar{\varepsilon}^p) \ . \tag{4.18}$$

Yield surface evolution based on the combined hardening rule is illustrated in Figure 4.13, for the von Mises yield function in two-dimensional principal stress space. Translation of the yield surface is according to Ziegler's rule in this figure.

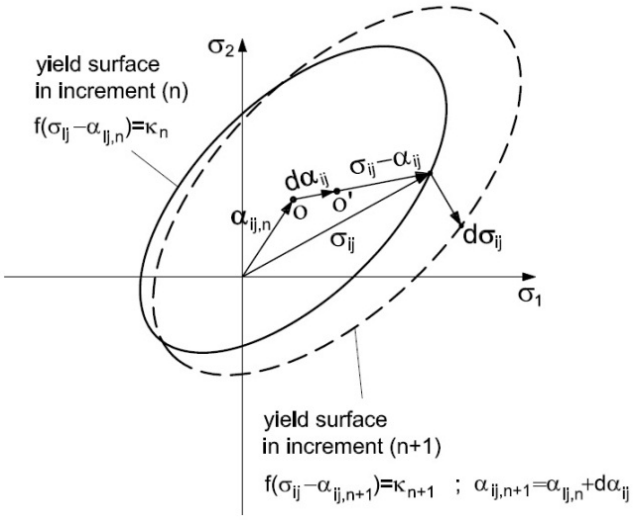

Figure 4.13: Combined hardening rule

As presented in chapter 3, AZ31B magnesium sheet exhibits complicated cyclic hardening behavior, which cannot be modeled by either isotropic or kinematic hardening rules. Hence, a nonlinear hardening rule is essential to reasonably model the complex hardening behavior. The two-surface constitutive model with a combined hardening rule was adopted in the current research as it provides smooth hardening behavior, and less complexity is involved in the implementation. The two-surface plasticity model is presented in the next section.

4.1.5 Two-Surface Plasticity

Dafalias and Popov in 1976 [117] proposed a constitutive plasticity model to represent the uniaxial cyclic stress-strain curve. As mentioned above, this model uses only two yield surfaces and introduces an algorithm for continuous updating of the plastic modulus.

To describe a stress-strain curve, the slope of the curve is needed at the current point, for which stress or strain is also known (depending on whether a stress- or strain-control approach is being used). According to relationship between different uniaxial moduli

$$\frac{1}{E^t} = \frac{1}{E} + \frac{1}{E^p} \quad , \tag{4.19}$$

the slope of a stress-strain curve at a particular point, *i.e.*, tangent modulus (E^t), is determined by knowing the constant elastic modulus (E) and the slope of the uniaxial stress-plastic strain curve, *i.e.*, plastic modulus (E^p). Hence, plastic modulus has a prominent role in obtaining the correct stress-strain curve. Because plastic modulus changes during inelastic loading, it should be a function of some variables related to plastic deformation, the so called plastic internal variables.

Dafalias and Popov investigated experimental results on grade 60 steel under random cyclic loading, Figure 4.14, and noticed the three following features,

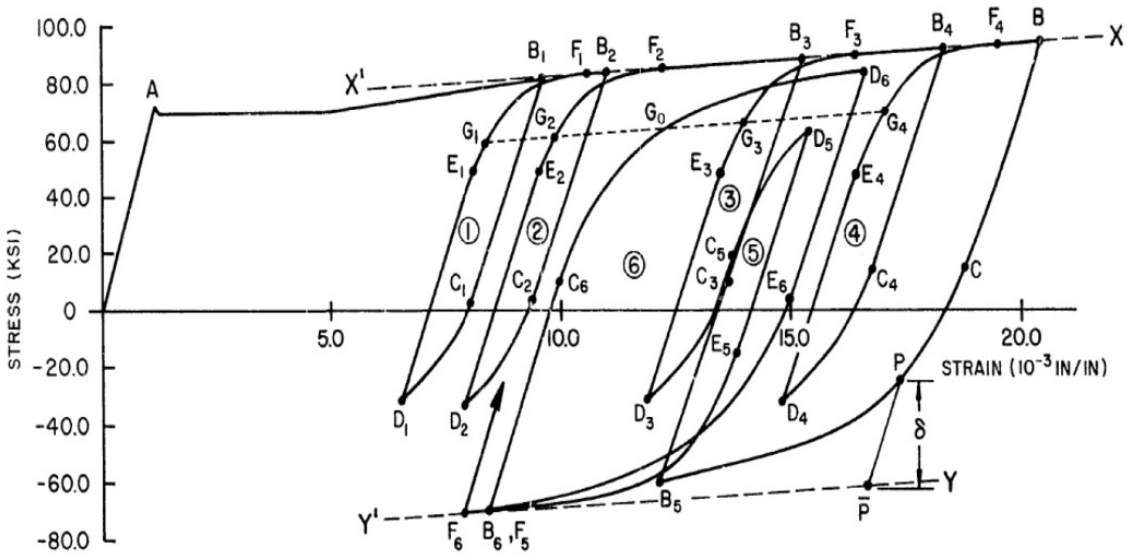

Figure 4.14: Experimental hysteresis loops for random cyclic loading [117]

1. Stress-strain curves, regardless of previous plastic deformation history, converge to two curves, *i.e.*, XX' and YY' in tension and compression, respectively. This implies that a bounding surface exists. Since the bounding curves do not have to be straight lines, the bounding slope may change with plastic straining. Therefore, plastic strain is one of the plastic internal variables.
2. Points with the same distance to the bounding curves have the same slope. For instance, points G_1 to G_4 with the same distance to XX' bounding line have the same slope. This suggests that the distance between the loading and bounding surface is a determining factor for the slope, and is one of the plastic internal variables.
3. Although point G_0 is located at the same distance to the XX' bounding line as G_1 and G_4, the slope is quite different at this point. This could be related to the most recent yield point, which in the case of G_1 to G_4 is E_1 to E_4, with almost the same distance to the bounding line. However, the yield point for G_0 is C_6, with a noticeably larger distance to the bounding line. This means that the distance between the most recent yield point and the bounding line should be considered as another plastic internal variable.

These observations establish the bases for the two-surface plasticity model, and result in the following definition for the plastic modulus

$$E^p = E^p(\bar{\varepsilon}^p, \delta, \delta_{in}) \quad , \tag{4.20}$$

where δ is the distance between the current point on the loading surface and the corresponding point on the bounding surface, hereafter referred to as the "*gap*", and δ_{in} is the distance between the most recent onset of yielding and the corresponding point on the bounding surface, usually referred to as the "*initial gap*". The initial gap has to be updated each time reversed yielding happens. The plastic modulus has upper and lower limit values as follows

$$\delta \to \delta_{in} \quad , \quad E^p \to \infty \quad , \tag{4.21}$$

$$\delta \to 0 \quad , \quad E^p = \overline{E^p}(\bar{\varepsilon}^p) \quad , \tag{4.22}$$

where $\overline{E^p}$ is the plastic modulus on the bounding line. Figure 4.15(a) shows the parameters introduced in the two-surface model in stress-plastic strain space for uniaxial loading. E^α and E^{A} are hardening moduli associated with the back stress of the loading surface (α) and the back stress of the bounding surface (A), respectively, and are defined as follows for uniaxial loading

$$E^\alpha = \frac{d\alpha}{d\varepsilon^p} \quad , \tag{4.23}$$

$$E^{\mathrm{A}} = \frac{d\mathrm{A}}{d\varepsilon^p} \quad . \tag{4.24}$$

Figure 4.15(b) illustrates the two-surface model in principal stress space (sectioned by the π-plane) for the von Mises yield function. The deviatoric plane or π-plane ($\sigma_1 + \sigma_2 + \sigma_3 = 0$) is the plane normal to the hydrostatic axis ($\sigma_1 = \sigma_2 = \sigma_3$).

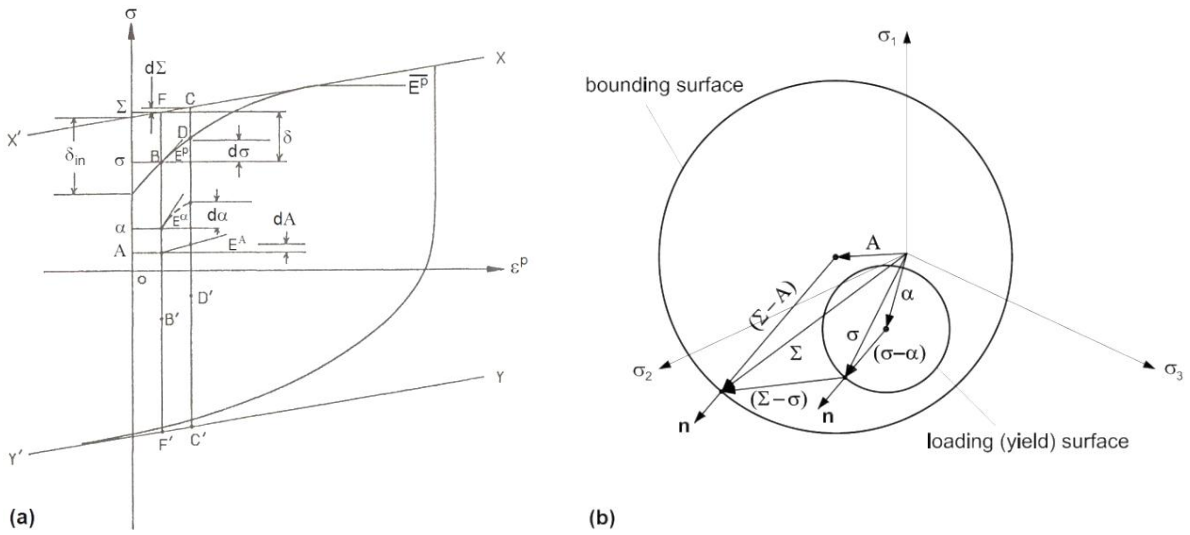

Figure 4.15: Illustration of the two-surface model parameters (a) for uniaxial loading [93] (b) for von-Mises yield function on π-plane

Before dealing with constitutive equations, one of the basic assumptions in incremental plasticity should be introduced. This assumption is called "*consistency*", and was defined by Prager [188].

The consistency condition indicates that the stress point or stress state has to remain on the active yield surface in stress space during plastic deformation. To explain the mathematical indication of this condition, the combined hardening model, equation (4.18), is considered. An infinitesimal stress increment ($d\boldsymbol{\sigma}$) during plastic deformation results in changes of hardening parameters to $d\boldsymbol{\alpha}$ and $d\bar{\varepsilon}^p$. To satisfy the consistency condition, equation (4.18) has to hold in the new state

$$f(\boldsymbol{\sigma} + \boldsymbol{d\sigma} - \boldsymbol{\alpha} - \boldsymbol{d\alpha}) - \kappa(\bar{\varepsilon}^p + d\bar{\varepsilon}^p) = 0 \quad . \tag{4.25}$$

This equation can be expanded as

$$f(\boldsymbol{\sigma} + \boldsymbol{d\sigma} - \boldsymbol{\alpha} - \boldsymbol{d\alpha}) - \kappa(\bar{\varepsilon}^p + d\bar{\varepsilon}^p) = \tag{4.26}$$
$$f(\boldsymbol{\sigma} - \boldsymbol{\alpha}) - \kappa(\bar{\varepsilon}^p) + \frac{\partial f(\boldsymbol{\sigma}-\boldsymbol{\alpha})}{\partial(\boldsymbol{\sigma}-\boldsymbol{\alpha})} : d\boldsymbol{\sigma} - \frac{\partial f(\boldsymbol{\sigma}-\boldsymbol{\alpha})}{\partial(\boldsymbol{\sigma}-\boldsymbol{\alpha})} : d\boldsymbol{\alpha} - \frac{d\kappa}{d\bar{\varepsilon}^p} d\bar{\varepsilon}^p = 0 \quad .$$

Operator ":" denotes the inner product of two vectors.

Comparing equations (4.18) and (4.26) results in

$$\frac{\partial f(\boldsymbol{\sigma}-\boldsymbol{\alpha})}{\partial(\boldsymbol{\sigma}-\boldsymbol{\alpha})}:d\boldsymbol{\sigma}-\frac{\partial f(\boldsymbol{\sigma}-\boldsymbol{\alpha})}{\partial(\boldsymbol{\sigma}-\boldsymbol{\alpha})}:d\boldsymbol{\alpha}-\frac{d\kappa}{d\bar{\varepsilon}^{p}}d\bar{\varepsilon}^{p}=0 \quad . \tag{4.27}$$

Equation (4.27) is often referred to as the *consistency condition*.

The equations governing a plasticity problem are derived in the following sections for stress- and strain-control problems, separately.

4.1.5.1 Constitutive equations for stress-control problems

Stress-control problems are those in which all variables from the previous increment are known, as well as the stress increment for the current increment. The variables to be found include elastic and plastic strain increments, and back-stress increments for loading and bounding surfaces, which make the current increment fully determined.

To obtain the constitutive equations, the following forms are considered for the yield and bounding surfaces with combined isotropic-kinematic hardening

$$f(\boldsymbol{\sigma}-\boldsymbol{\alpha})-\kappa(\bar{\varepsilon}^{p})=0 \quad , \tag{4.28}$$

$$F(\boldsymbol{\Sigma}-\mathbf{A})-\mathrm{K}(\bar{\varepsilon}^{p})=0 \quad , \tag{4.29}$$

where $\boldsymbol{\sigma}$ is the stress state on the loading surface, f. Variables α and A, and κ and K are centers and sizes of loading and bounding surfaces, respectively. $\boldsymbol{\Sigma}$ is the stress point on the bounding surface, F, corresponding to $\boldsymbol{\sigma}$ on the loading surface. A reasonable method to obtain $\boldsymbol{\Sigma}$ is finding a point on the bounding surface with the same normal vector as the loading surface at the current stress point ($\boldsymbol{\sigma}$), which means

$$\lambda\frac{\partial f}{\partial\boldsymbol{\sigma}}=\Lambda\frac{\partial F}{\partial\boldsymbol{\Sigma}} \quad , \tag{4.30}$$

Where λ and Λ are scalar factors.

The multi-axial plastic modulus (K^p), similar to the uniaxial plastic modulus (E^p), has the following form

$$K^p = K^p(\bar{\varepsilon}^p, \delta, \delta_{in}) \quad . \tag{4.31}$$

To ensure that the loading and bounding surfaces do not intercept each other, the translation vector must be defined such that the surfaces meet at points with the same normal vectors. Therefore, as shown in Figure 4.15(b), the relative translation of loading and bounding surfaces should be

$$d\mathbf{A} - d\boldsymbol{\alpha} = -d\mu\,(\boldsymbol{\Sigma} - \boldsymbol{\sigma}) \quad , \tag{4.32}$$

in which $d\mu$ is a scalar. Back stress evolution of the yield surface may follow any of Prager's, Ziegler's or another flow rule. The following back-stress evolution law was proposed by Khan et al. [93]

$$d\boldsymbol{\alpha} = \frac{K_{\boldsymbol{\alpha}}}{K^p}\frac{(\boldsymbol{n}:d\boldsymbol{\sigma})}{\boldsymbol{n}:\boldsymbol{\nu}}\boldsymbol{\nu} \quad , \tag{4.33}$$

where $K_{\boldsymbol{\alpha}}$ is the hardening modulus of $\boldsymbol{\alpha}$, and $\boldsymbol{\nu}$ is a unit vector in the translation direction of the yield surface. Substituting $d\boldsymbol{\alpha}$ from equation (4.33) into the consistency condition, equation (4.27), after some manipulations results in

$$K_{\boldsymbol{\alpha}} = K^p\left[1 - \frac{(d\kappa/d\bar{\varepsilon}^p)d\bar{\varepsilon}^p}{(\partial f/\partial\boldsymbol{\sigma}:\partial f/\partial\boldsymbol{\sigma})^{1/2}(\boldsymbol{n}:d\boldsymbol{\sigma})}\right] \quad , \tag{4.34}$$

where $\boldsymbol{n}$ is the unit normal vector to the yield surface

$$\boldsymbol{n} = \frac{(\partial f/\partial\boldsymbol{\sigma})}{(\partial f/\partial\boldsymbol{\sigma}:\partial f/\partial\boldsymbol{\sigma})^{1/2}} \quad . \tag{4.35}$$

Similarly, the consistency condition on the bounding surface yields

$$\frac{\partial F(\boldsymbol{\Sigma}-\mathbf{A})}{\partial(\boldsymbol{\Sigma}-\mathbf{A})}:d\boldsymbol{\Sigma} - \frac{\partial F(\boldsymbol{\Sigma}-\mathbf{A})}{\partial(\boldsymbol{\Sigma}-\mathbf{A})}:d\mathbf{A} - \frac{d\mathrm{K}}{d\bar{\varepsilon}^p}d\bar{\varepsilon}^p = 0 \quad . \tag{4.36}$$

The multiplier $d\mu$ is obtained by substituting $d\mathbf{A}$ from equation (4.32) into equation (4.36) and rearranging

$$d\mu = \frac{\partial F(\boldsymbol{\Sigma}-\mathbf{A})/\partial(\boldsymbol{\Sigma}-\mathbf{A}):d\boldsymbol{\alpha}+(d\mathrm{K}/d\bar{\varepsilon}^p)d\bar{\varepsilon}^p-\partial F(\boldsymbol{\Sigma}-\mathbf{A})/\partial(\boldsymbol{\Sigma}-\mathbf{A}):d\boldsymbol{\Sigma}}{\partial F(\boldsymbol{\Sigma}-\mathbf{A})/\partial(\boldsymbol{\Sigma}-\mathbf{A}):(\boldsymbol{\Sigma}-\boldsymbol{\sigma})} \quad . \tag{4.37}$$

Back stress increments for the yielding and bounding surfaces are found by substituting equation (4.34) into equation (4.33), and equation (4.37) into equation (4.32), respectively.

Infinitesimal strain increment can be divided into elastic and plastic strain increments (additive decomposition law)

$$d\boldsymbol{\varepsilon} = d\boldsymbol{\varepsilon}^e + d\boldsymbol{\varepsilon}^p \quad , \tag{4.38}$$

in which the elastic strain increment ($d\boldsymbol{\varepsilon}^e$) is found from

$$d\boldsymbol{\varepsilon}^e = \boldsymbol{C}^{e^{-1}}: d\boldsymbol{\sigma} \quad , \tag{4.39}$$

where $\boldsymbol{C}^e$ is the elastic stiffness tensor. The plastic strain increment ($d\boldsymbol{\varepsilon}^p$) is obtained from the associated flow rule [93]

$$d\boldsymbol{\varepsilon}^p = \frac{1}{K^p}(\boldsymbol{n}: d\boldsymbol{\sigma})\boldsymbol{n} \quad . \tag{4.40}$$

The multi-axial plastic modulus function, $K^p(\bar{\varepsilon}^p, \delta, \delta_{in})$, is defined using experimental results. The function proposed by Dafalias and Popov [117] for uniaxial plastic modulus is

$$E^p(\bar{\varepsilon}^p, \delta, \delta_{in}) = \overline{E^p}(\bar{\varepsilon}^p) + \frac{a}{1+br^m}\left(\frac{\delta}{\delta_{in}-\delta}\right) \tag{4.41}$$

where a, b, m are material constants to be found from experiments, and $r = \delta_{in}/\sigma_r$ in which σ_r is a reference stress. The equivalent plastic strain ($\bar{\varepsilon}^p$) and gap (δ) are updated in each increment, and the initial gap (δ_{in}) is updated after each reverse yielding.

4.1.5.2 Constitutive equations for strain-control problems

Strain-control problems are those in which the total strain increment for the current increment is known, and the variables to determine are elastic and plastic portions of the total strain increment, the stress increment, as well as back-stress increments for loading and bounding surfaces. The following are the constitutive equations required to obtain the unknown variables.

Loading and bounding surfaces have the same equations as those for stress-control problems, *i.e.*, equations (4.28) and (4.29). The consistency condition for the loading surface is given by equation (4.27).

The plastic work equivalence principle states that the plastic work increment, dW^p, is

$$dW^p = \boldsymbol{\sigma}: d\boldsymbol{\varepsilon}^p = (\boldsymbol{\sigma} - \boldsymbol{\alpha}): d\boldsymbol{\varepsilon}^p + \boldsymbol{\alpha}: d\boldsymbol{\varepsilon}^p = \bar{\sigma}\, d\bar{\varepsilon}^p \quad , \tag{4.42}$$

where $\bar{\sigma}$ is the equivalent stress corresponding to the yield function. According to the modified plastic work equivalence relationship [111]

$$dW_{iso}^p = (\boldsymbol{\sigma} - \boldsymbol{\alpha}): d\boldsymbol{\varepsilon}^p = \bar{\sigma}_{iso} d\bar{\varepsilon}^p \tag{4.43}$$

where $\bar{\sigma}_{iso}$ is the equivalent value for isotropic stress, $\bar{\sigma}_{iso} = f(\boldsymbol{\sigma} - \boldsymbol{\alpha})$. According to the loading surface equation, the isotropic equivalent stress is $\bar{\sigma}_{iso} = \kappa(\bar{\varepsilon}^p)$, which leads to

$$d\bar{\varepsilon}^p = \frac{(\boldsymbol{\sigma}-\boldsymbol{\alpha})}{\kappa(\bar{\varepsilon}^p)}: d\boldsymbol{\varepsilon}^p \quad . \tag{4.44}$$

Therefore, the consistency condition can be rewritten as

$$\frac{\partial f(\boldsymbol{\sigma}-\boldsymbol{\alpha})}{\partial(\boldsymbol{\sigma}-\boldsymbol{\alpha})}: d\boldsymbol{\sigma} - \frac{\partial f(\boldsymbol{\sigma}-\boldsymbol{\alpha})}{\partial(\boldsymbol{\sigma}-\boldsymbol{\alpha})}: d\boldsymbol{\alpha} - \frac{dk}{d\bar{\varepsilon}^p}\frac{(\boldsymbol{\sigma}-\boldsymbol{\alpha})}{\kappa}: d\boldsymbol{\varepsilon}^p = 0 \quad . \tag{4.45}$$

Similar to equation (4.33), back stress evolution may obey any hardening rule, or in general be in an arbitrary direction $\boldsymbol{\nu}$

$$d\boldsymbol{\alpha} = d\psi\, \boldsymbol{\nu} \tag{4.46}$$

where, $d\psi$ is a scalar. The magnitude of the back-stress increment is determined by substituting the back-stress increment in the yield function, f [111]. For first order homogeneous yield functions[1]

$$f(d\boldsymbol{\alpha}) = f(d\psi\, \boldsymbol{\nu}) = d\psi f(\boldsymbol{\nu}) = d\bar{\alpha} \ . \tag{4.47}$$

Therefore,

$$d\boldsymbol{\alpha} = \frac{d\bar{\alpha}}{f(\boldsymbol{\nu})}\, \boldsymbol{\nu} = \left(\frac{d\bar{\alpha}}{d\bar{\varepsilon}^p}\, d\bar{\varepsilon}^p\right)\frac{\boldsymbol{\nu}}{f(\boldsymbol{\nu})} \ , \tag{4.48}$$

where the multiplier, $d\bar{\alpha}$, describing the size of the back-stress increment, is considered as the back-stress increment in the reference stress state, which is often assumed uniaxial tension. Using the normality rule, the increment of the plastic strain tensor for a first order homogenous yield function can be related to the equivalent plastic strain increment, $d\bar{\varepsilon}^p$ [122]

$$d\boldsymbol{\varepsilon}^p = d\bar{\varepsilon}^p\, \frac{\partial f(\boldsymbol{\sigma}-\boldsymbol{\alpha})}{\partial(\boldsymbol{\sigma}-\boldsymbol{\alpha})} \ . \tag{4.49}$$

Substituting equations (4.49) and (4.48) into equation (4.45) yields

$$d\bar{\varepsilon}^p = \frac{\partial f(\boldsymbol{\sigma}-\boldsymbol{\alpha})/\partial(\boldsymbol{\sigma}-\boldsymbol{\alpha}) : \boldsymbol{C^e} : d\boldsymbol{\varepsilon} - (d\bar{\alpha})/f(\boldsymbol{\nu})\, \partial f(\boldsymbol{\sigma}-\boldsymbol{\alpha})/\partial(\boldsymbol{\sigma}-\boldsymbol{\alpha}) : \boldsymbol{\nu}}{\partial f(\boldsymbol{\sigma}-\boldsymbol{\alpha})/\partial(\boldsymbol{\sigma}-\boldsymbol{\alpha}) : \boldsymbol{C^e} : \partial f(\boldsymbol{\sigma}-\boldsymbol{\alpha})/\partial(\boldsymbol{\sigma}-\boldsymbol{\alpha}) + d\kappa/(d\bar{\varepsilon}^p)\ (\boldsymbol{\sigma}-\boldsymbol{\alpha})/\kappa : \partial f(\boldsymbol{\sigma}-\boldsymbol{\alpha})/\partial(\boldsymbol{\sigma}-\boldsymbol{\alpha})} \ . \tag{4.50}$$

Substituting equation (4.49) into equation (4.44) yields

$$\frac{\partial f(\boldsymbol{\sigma}-\boldsymbol{\alpha})}{\partial(\boldsymbol{\sigma}-\boldsymbol{\alpha})} = \frac{\kappa}{(\boldsymbol{\sigma}-\boldsymbol{\alpha})} \ . \tag{4.51}$$

[1] A yield function, $f(\sigma)$, is a homogeneous function of order m if: $f(\sigma) - \bar{\sigma}^m = 0$.

Using equation (4.51), equation (4.50) is reduced to

$$d\bar{\varepsilon}^p = \frac{\partial f(\boldsymbol{\sigma}-\boldsymbol{\alpha})/\partial(\boldsymbol{\sigma}-\boldsymbol{\alpha}):\boldsymbol{C}^e:d\boldsymbol{\varepsilon}-(d\bar{\alpha})/f(\boldsymbol{\nu})\,\partial f(\boldsymbol{\sigma}-\boldsymbol{\alpha})/\partial(\boldsymbol{\sigma}-\boldsymbol{\alpha}):\boldsymbol{\nu}}{\partial f(\boldsymbol{\sigma}-\boldsymbol{\alpha})/\partial(\boldsymbol{\sigma}-\boldsymbol{\alpha}):\boldsymbol{C}^e:\partial f(\boldsymbol{\sigma}-\boldsymbol{\alpha})/\partial(\boldsymbol{\sigma}-\boldsymbol{\alpha})+d\kappa/(d\bar{\varepsilon}^p)} \quad . \tag{4.52}$$

For Ziegler's flow rule, where $\boldsymbol{\nu} = \frac{(\boldsymbol{\sigma}-\boldsymbol{\alpha})}{\|\boldsymbol{\sigma}-\boldsymbol{\alpha}\|}$, the equivalent plastic strain increment may be obtained from

$$d\bar{\varepsilon}^p = \frac{\partial f(\boldsymbol{\sigma}-\boldsymbol{\alpha})/\partial(\boldsymbol{\sigma}-\boldsymbol{\alpha}):\boldsymbol{C}^e:d\boldsymbol{\varepsilon}-d\bar{\alpha}}{\partial f(\boldsymbol{\sigma}-\boldsymbol{\alpha})/\partial(\boldsymbol{\sigma}-\boldsymbol{\alpha}):\boldsymbol{C}^e:\partial f(\boldsymbol{\sigma}-\boldsymbol{\alpha})/\partial(\boldsymbol{\sigma}-\boldsymbol{\alpha})+d\kappa/(d\bar{\varepsilon}^p)} \quad . \tag{4.53}$$

Now, the plastic strain increment ($d\boldsymbol{\varepsilon}^p$) is found by substituting equation (4.53) back into equation (4.49), and using the additive decomposition law, equation (4.38), the elastic strain increment ($d\boldsymbol{\varepsilon}^e$) is calculated. Then, the stress increment is determined from

$$d\boldsymbol{\sigma} = \boldsymbol{C}^e : d\boldsymbol{\varepsilon}^e \quad . \tag{4.54}$$

Loading and bounding surfaces are often assumed to have the same shape. The stress state on the bounding surface corresponding to the stress point on the loading surface is found such that the normal vectors are in the same direction. This can be stated as

$$\boldsymbol{\Sigma} - \mathbf{A} = \frac{\mathrm{K}}{\kappa}\,(\boldsymbol{\sigma} - \boldsymbol{\alpha}) \quad . \tag{4.55}$$

To assure that the loading and bounding surfaces meet each other at the current stress state, the relative translation of the two surfaces should be along the vector connecting the current stress point on the loading surface to the corresponding point on the bounding surface, $(\boldsymbol{\Sigma} - \boldsymbol{\sigma})$, which means [111]

$$d\mathbf{A} - d\boldsymbol{\alpha} = -d\mu\,(\boldsymbol{\Sigma} - \boldsymbol{\sigma}) \quad \text{or} \quad d\mathbf{A} = d\boldsymbol{\alpha} - d\mu\,(\boldsymbol{\Sigma} - \boldsymbol{\sigma}) = d\mathbf{A}_1 + d\mathbf{A}_2\,. \tag{4.56}$$

Similar to equation (4.48), the second term can be written as

$$d\mathbf{A}_2 = -d\mu\,(\boldsymbol{\Sigma} - \boldsymbol{\sigma}) = \frac{d\bar{A}_2(\bar{\varepsilon}^p)}{f(\boldsymbol{\Sigma}-\boldsymbol{\sigma})}\,(\boldsymbol{\Sigma} - \boldsymbol{\sigma}) \quad , \tag{4.57}$$

where $d\bar{A}_2 = f(d\mathbf{A}_2)$. The scalar $d\bar{A}_2(\bar{\varepsilon}^p)$ can be considered as the back-stress increment of the bounding surface in the corresponding reference stress state.

It is noteworthy that, for the sake of simplicity, the bounding surface was assumed stationary in this research. In other words, for the bounding surface, no evolution was considered for size and back-stress

$$\mathrm{K}(\bar{\varepsilon}^p) = \mathrm{K}(\bar{\varepsilon}^p = 0) \quad , \tag{4.58}$$

$$\mathbf{A} = 0 \quad ; \quad d\mathbf{A} = 0 \quad . \tag{4.59}$$

The bounding surface was considered large enough (as observed from experimental hardening behavior), to ensure that the loading and bounding surfaces do not intersect. The size of the bounding surface was assumed to be K =500 MPa in this study. Nonetheless, constitutive equations derived in this section, as well as numerical implementation in the next section, include bounding surface evolution to maintain generality and completeness of the plasticity model.

Besides the yield function, flow rule, and hardening rule which are the common components in plasticity constitutive models, some additional phenomena need to be explained for cyclic plasticity modeling. *Reverse yielding* and the *Bauschinger effect* are two essential constituents of cyclic plasticity models, and are described in following sections.

4.1.6 Reverse Yielding

One of the elements of cyclic plasticity modeling is a criterion for distinguishing the loading and unloading reversals. This is especially important for materials with asymmetric hardening behavior, because this rule allows the model to follow the appropriate hardening curve. The criterion proposed by Lee et al. [111] was adopted in this research. According to this criterion, reverse yielding occurs if the angle between two subsequent points on the yield surface, θ_d, is greater than a predefined reference angle, θ_r. Figure 4.16 illustrates the reverse yielding criterion on a typical Cazacu-Barlat yield function.

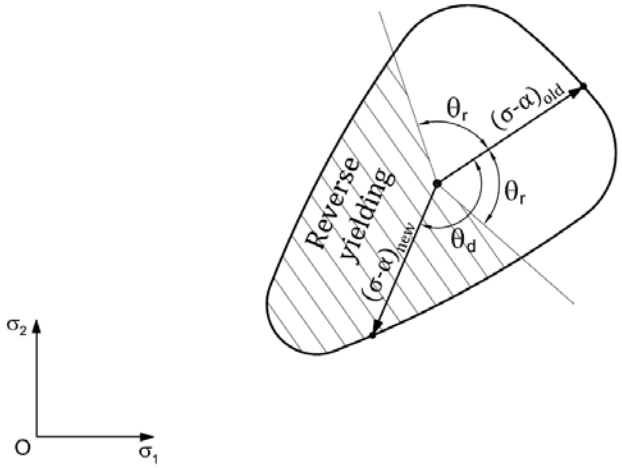

Figure 4.16: Reverse yielding criterion

The angle between two subsequent points on the yield surface, θ_d, is obtained from

$$\theta_d = \cos^{-1}(\boldsymbol{d}_{old} : \boldsymbol{d}_{new}) = \cos^{-1}\left(\frac{\boldsymbol{\sigma}-\boldsymbol{\alpha}}{[(\boldsymbol{\sigma}-\boldsymbol{\alpha}):(\boldsymbol{\sigma}-\boldsymbol{\alpha})]^{1/2}}\Big|_{old} : \frac{\boldsymbol{\sigma}-\boldsymbol{\alpha}}{[(\boldsymbol{\sigma}-\boldsymbol{\alpha}):(\boldsymbol{\sigma}-\boldsymbol{\alpha})]^{1/2}}\Big|_{new}\right) \quad . \tag{4.60}$$

where $\boldsymbol{d}_{old}$ and $\boldsymbol{d}_{new}$ are normal vectors along $(\boldsymbol{\sigma}-\boldsymbol{\alpha})_{old}$ and $(\boldsymbol{\sigma}-\boldsymbol{\alpha})_{new}$, respectively. The reference angle $\theta_r = \pi/2$ was used in this study.

To model the hardening behavior of the material used in this study, AZ31B-H24, the procedure below was followed.

Stabilized hardening curves for loading and unloading reversals under different strain amplitudes were generated through uniaxial cyclic testing, and the results were presented in chapter 3. During the incremental solution of a problem, for the first time that yielding occurs, tension/compression reversal was determined according to the sign of the hydrostatic stress, such that for positive or negative value of the hydrostatic stress, tension or compression reversal was assumed, respectively, and the proper hardening curve was followed. For subsequent elastic-plastic increments, the angle θ_d was calculated with respect to the most recent point on the yield surface using equation (4.60). For $\theta_d < \theta_r = \pi/2$, the previous hardening curve was maintained and if $\theta_d > \theta_r$, the hardening curve was updated. If the reversed yielding criterion was met, *i.e.*, $\theta_d > \theta_r$, the tension and compression reversals were changed to compression and tension reversals, respectively. The initial gap, δ_{in}, was updated each time that reverse yielding occurred.

4.1.7 Bauschinger Effect

Metals are known to exhibit the Bauschinger effect, which refers to lower yield strength after reversed plastic loading. The Bauschinger effect has been attributed to different mechanisms: residual stresses induced in forward loading or internal stresses from interactions between dislocations [72,189], or dislocation concentrations at grain boundaries [71]. The Bauschinger effect in metals with cubic crystal structure, which results in symmetric hardening behavior, is the same for tension-compression and compression-tension loading sequences [90].

Hardening behavior of AZ31B-H24 under monotonic and cyclic loading was discussed in the previous chapter. Asymmetric yielding, hardening behavior, and initial yield surface of wrought magnesium alloys are schematically shown in Figure 4.17. As shown in this figure, when AZ31B is loaded but before reaching the initial yield point, the yield surface size or elastic region size is ERS_0. Experiments show that if a material is unloaded after elastic-plastic tension, the elastic region, ERS_1, is smaller than the initial yield surface size. This feature may be considered as the regular

Bauschinger effect. However, unlike symmetric metals, the Bauschinger effect in AZ31B is stronger for compression-tension than that for tension-compression. In other words, if AZ31B is plastically loaded under compression and then loaded in the reverse direction, the yield surface size ERS_2 is not only smaller than ERS_0, but also smaller than ERS_1 for the same plastic strain ($ERS_2 < ERS_1 < ERS_0$).

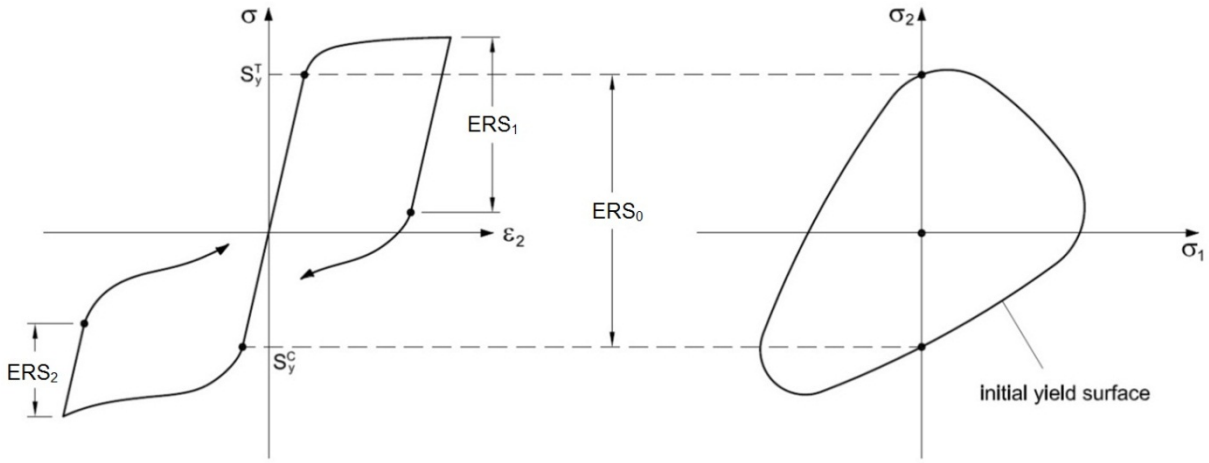

Figure 4.17: Sudden change in elastic region size after reverse yielding

Similar behavior has already been reported for AZ31B and ZK60A magnesium alloys [52,62]. The asymmetric Bauschinger effect in twinning and untwinning can be attributed to different activation stresses. Partridge in 1965 [190] reported that less activation stress is required for untwinning as compared to that for twinning. This is related to nucleation which happens in twinning, but does not occur or easily occurs in untwinning [52]. This observation shows that separate adjustments are needed for the abrupt change in the yield surface size when the material starts to deform plastically under tension and compression. One should note that the Bauschinger effect herein refers to the change in the yield surface size under cyclic loading at the onset of yielding in each reversal. Therefore, tensile and compressive curves in Figure 4.17 represent stabilized cyclic curves.

The Bauschinger effect, due to instant softening, causes an immediate change in back-stress. Figure 4.18 illustrates the effect of sudden yield surface shrinkage on back-stress. As shown in this

figure, the center of the yield surface instantly changes from o to o' once the stress state reaches the yield surface (point A).

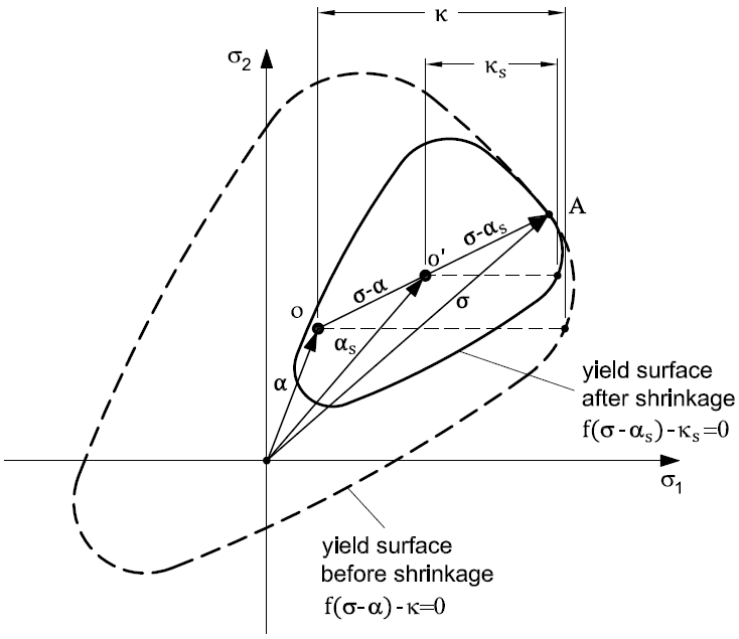

Figure 4.18: Yield surface shrinkage and back-stress change due to the Bauschinger effect

Because the yield surface after shrinkage maintains its shape and is tangent to the yield surface before shrinkage, the updated back-stress is obtained from

$$\boldsymbol{\alpha_s} = \boldsymbol{\sigma} - \frac{\kappa_s}{\kappa}(\boldsymbol{\sigma} - \boldsymbol{\alpha}) \quad , \tag{4.61}$$

where, $\boldsymbol{\alpha_s}$ and κ_s are the back-stress and the size of the yield surface after reverse yielding, respectively.

4.1.8 Numerical Implementation

Numerical implementation of the plasticity model and the assumptions made in this research are presented in this section. The numerical outputs are compared with the experimental results for uniaxial loading. The evolution of the yield surface during a full cycle is presented and discussed for uniaxial and equi-biaxial loading.

4.1.8.1 Numerical formulation and algorithm

The numerical algorithm proposed by Lee et al. [111] was modified and adopted in this study. The numerical formulation was implemented into a user material (UMAT) subroutine to run with the commercial finite element program Abaqus/Standard [191]. Because the total strain increment is passed by Abaqus/Standard to UMAT subroutines, the strain-control formulations were employed for the numerical implementation.

The purpose of the numerical formulation is to obtain the unknown variables in the current increment using the known variables. The known variables at the beginning of each increment are total strain increment for the current increment, as well as stress and strain tensors and state variables from the previous increment. State variables include but are not limited to elastic and plastic strain, and back stress tensors. The unknown variables are elastic and plastic strains, and stress and back-stress tensors for the loading and bounding surfaces. Stabilized cyclic hardening curves corresponding to different strain amplitudes are also known in terms of equivalent plastic strain from experiments. Hardening curves for other strain amplitudes are obtained by linear interpolation. All variables in the strain-control approach can be related solely to the increment of equivalent plastic strain. Therefore, the equivalent plastic strain increment is determined first by solving the consistency condition. According to the consistency condition, the stress point remains on the updated yield surface after a plastically loading increment, which means for the current increment we have

$$\varphi = f(\boldsymbol{\sigma}_{n+1} - \boldsymbol{\alpha}_{n+1}) - \kappa\left(\bar{\varepsilon}^{p}_{n+1}\right) = 0 \quad , \tag{4.62}$$

where the subscript $(n+1)$ represents the increment number.

First, assuming that the current increment is elastic, an elastic trial stress is calculated for the given total strain increment, $\Delta\boldsymbol{\varepsilon}$, while the other variables remain unchanged

$$\boldsymbol{\sigma}_{n+1}^{T} = \boldsymbol{\sigma}_n + \boldsymbol{C^e}.\Delta\boldsymbol{\varepsilon} \quad ; \quad \boldsymbol{\alpha}_{n+1}^{T} = \boldsymbol{\alpha}_n \quad ; \quad \bar{\varepsilon}_{n+1}^{p,T} = \bar{\varepsilon}_n^{p} \quad ; \qquad (4.63)$$
$$\boldsymbol{\Sigma}_{n+1}^{T} = \boldsymbol{\Sigma}_n \quad ; \quad \mathbf{A}_{n+1}^{T} = \mathbf{A}_n$$

in which the superscript T denotes a trial state. The assumption of an elastic increment is then evaluated against the yield condition

$$\varphi_{n+1}^{T} = f(\boldsymbol{\sigma}_{n+1}^{T} - \boldsymbol{\alpha}_{n+1}^{T}) - \kappa\left(\bar{\varepsilon}_{n+1}^{p,T}\right) \quad . \qquad (4.64)$$

For $\varphi \leq 0$, the stress state is inside or on the yield surface, and the elastic solution is valid. Hence, the true values of the variables for the current increment are equal to the trial states. Otherwise, for $\varphi > 0$, an elastic-plastic solution is required, and the trial values must be corrected. The elastic-plastic solution is an iterative procedure, and is initialized as

$$k = 1 \quad ; \quad \boldsymbol{\sigma}_{n+1}^{(k=1)} = \boldsymbol{\sigma}_{n+1}^{T} \quad ; \quad \boldsymbol{\alpha}_{n+1}^{(k=1)} = \boldsymbol{\alpha}_{n+1}^{T} \quad ; \quad \Delta\bar{\varepsilon}_{n+1}^{p(k=1)} = \Delta\bar{\varepsilon}_0^{p} \qquad (4.65)$$
$$\bar{\varepsilon}_{n+1}^{p,(k=1)} = \bar{\varepsilon}_{n+1}^{p,T} \quad .$$

where the superscript k stands for iteration number, and $\Delta\bar{\varepsilon}_0^{p}$ is an arbitrary initial value for equivalent plastic strain increment.

Equivalent plastic strain is obtained for the k'th iteration from

$$\bar{\varepsilon}_{n+1}^{p(k)} = \bar{\varepsilon}_n^{p} + \Delta\bar{\varepsilon}_{n+1}^{p(k)} \quad . \qquad (4.66)$$

The reverse yielding criterion is evaluated. If $\theta_d > \theta_r$, reverse yielding happens and initial gap and hardening curves are updated. Otherwise, the same hardening curve as the previous increment is followed.

Flow (plastic strain increment) direction is calculated according to the associated flow rule

$$\boldsymbol{\eta} = \frac{\partial f(\boldsymbol{\sigma}-\boldsymbol{\alpha})}{\partial(\boldsymbol{\sigma}-\boldsymbol{\alpha})}\Big|_{\boldsymbol{\sigma}_{n+1}^{(k-1)}-\boldsymbol{\alpha}_{n+1}^{(k-1)}} \quad , \qquad (4.67)$$

and plastic strain increment tensor and Cauchy stress tensor are updated

$$\Delta\boldsymbol{\varepsilon}_{n+1}^{p(k)} = \Delta\bar{\varepsilon}_{n+1}^{p(k)}\,\boldsymbol{\eta} \quad , \tag{4.68}$$

$$\begin{aligned}\boldsymbol{\sigma}_{n+1}^{(k)} &= \boldsymbol{\sigma}_n + \boldsymbol{C^e}\!:\Delta\boldsymbol{\varepsilon}_{n+1}^{e(k)} = \boldsymbol{\sigma}_n + \boldsymbol{C^e}\!:\left(\Delta\boldsymbol{\varepsilon}_{n+1} - \Delta\boldsymbol{\varepsilon}_{n+1}^{p(k)}\right) = \\ &= \boldsymbol{\sigma}_{n+1}^{T} - \boldsymbol{C^e}\!:\Delta\boldsymbol{\varepsilon}_{n+1}^{p(k)} = \boldsymbol{\sigma}_{n+1}^{T} - \Delta\bar{\varepsilon}_{n+1}^{p(k)}\boldsymbol{C^e}\!:\frac{\partial f(\boldsymbol{\sigma}-\boldsymbol{\alpha})}{\partial(\boldsymbol{\sigma}-\boldsymbol{\alpha})}\Big|_{\boldsymbol{\sigma}_{n+1}^{(k-1)}-\boldsymbol{\alpha}_{n+1}^{(k-1)}}\end{aligned} \tag{4.69}$$

According to equation (4.48)

$$\boldsymbol{\alpha}_{n+1}^{(k)} = \boldsymbol{\alpha}_n + \Delta\bar{\alpha}\left(\Delta\bar{\varepsilon}_{n+1}^{p(k)}\right)\frac{\boldsymbol{\sigma}_n-\boldsymbol{\alpha}_n}{f(\boldsymbol{\sigma}_n-\boldsymbol{\alpha}_n)} \quad . \tag{4.70}$$

$\Delta\bar{\alpha}\left(\Delta\bar{\varepsilon}_{n+1}^{p(k)}\right)$ is considered as the back-stress increment in the corresponding reference stress state (uniaxial loading)

$$\Delta\bar{\alpha}\left(\Delta\bar{\varepsilon}_{n+1}^{p(k)}\right) = \Delta\alpha_{ref}\left(\Delta\bar{\varepsilon}_{n+1}^{p(k)}\right) \quad . \tag{4.71}$$

Figure 4.19 illustrates the stress state and back-stress evolution in the actual and reference frames.

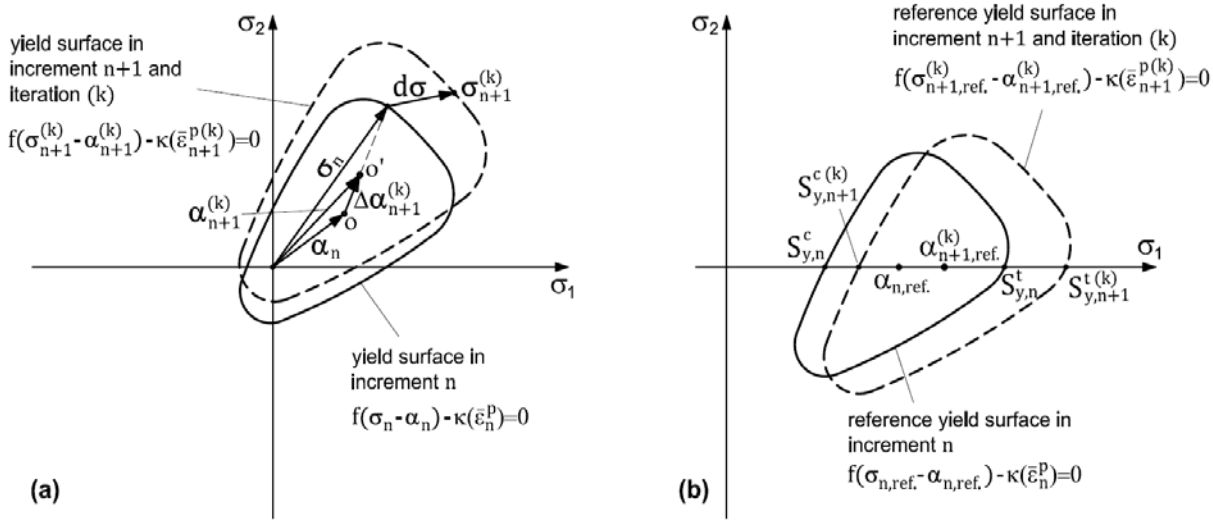

Figure 4.19: Back-stress evolution in (a) actual stress state (b) reference stress state

The *asymmetry ratio*, R_a, which represents tension-compression yield asymmetry, is defined according to the initial yield strengths,

$$R_a = S_y^t / S_y^c \quad , \tag{4.72}$$

where S_y^t and S_y^c are initial yield strengths under tension and compression, respectively. It should be mentioned that S_y^t and S_y^c for cyclic plasticity modeling are obtained from uniaxial stabilized cyclic curves, rather than from uniaxial monotonic curves. In the current work, it is assumed that the yield surface maintains its shape during plastic deformation; therefore, the R_a obtained from the initial state is applicable to the entire solution. In the reference frame, Figure 4.19(b), we have

$$R_a = \frac{S_{y,n+1}^{t\,(k)} - \alpha_{n+1,ref}^{(k)}}{\alpha_{n+1,ref}^{(k)} - S_{y,n+1}^{c\,(k)}} \qquad \text{or} \qquad \alpha_{n+1,ref}^{(k)} = \frac{S_{y,n+1}^{t\,(k)} + R_a\, S_{y,n+1}^{c\,(k)}}{R_a + 1} \quad , \tag{4.73}$$

where $\alpha_{n+1,ref}^{(k)}$ is the back-stress in the reference frame, and $S_{y,n+1}^{t\,(k)}$ and $S_{y,n+1}^{c\,(k)}$ are tensile and compressive yield strengths in the reference frame, which are obtained from appropriate hardening curves knowing $\bar{\varepsilon}_{n+1}^{p(k)}$.

The back-stress increment in the reference frame is determined by

$$\Delta\alpha_{ref}\left(\Delta\bar{\varepsilon}_{n+1}^{p(k)}\right) = \alpha_{n+1,ref}^{(k)} - \alpha_{n,ref} \quad , \tag{4.74}$$

and the back-stress tensor in the actual frame is updated using equation (4.70).

In case of reverse yielding, a bisecting technique is employed to account for the Bauschinger effect. In other words, if the current load increment is associated with the onset of yielding in the reverse direction, the increment is split into two sub-increments. The first segment accounts for movement of the stress point from inside the active yield surface to the yield surface. Instant changes in the yield surface size and back-stress are accounted for in this portion of the increment.

Back-stress after the yield surface shrinkage, $\boldsymbol{\alpha}_s$, is obtained from

$$\boldsymbol{\sigma}_{s,iso} = (\boldsymbol{\sigma}_n - \boldsymbol{\alpha}_n)\frac{\kappa(\bar{\varepsilon}_n^p)}{f(\boldsymbol{\sigma}_n - \boldsymbol{\alpha}_n)} \tag{4.75}$$

$$R_s = \frac{S_{y,n+1}^t - S_{y,n+1}^c}{S_{y,n}^t - S_{y,n}^c} \tag{4.76}$$

$$\boldsymbol{\alpha}_s = \boldsymbol{\alpha}_n + (1 - R_s)\boldsymbol{\sigma}_{s,iso} \tag{4.77}$$

where $\boldsymbol{\sigma}_{s,iso}$ is isotropic stress when the stress point reached the yield surface. R_s is *shrinkage ratio* which represents ratio of the yield surface size after the shrinkage to that before the shrinkage.

The second sub-increment considers gradual evolution of the yield surface and back-stress as a regular plastic increment.

The yield surface size is updated according to the reference frame

$$\kappa\left(\bar{\varepsilon}_{n+1}^{p(k)}\right) = S_{y,n+1}^{t\,(k)} - \alpha_{n+1,ref}^{(k)} \quad . \tag{4.78}$$

The consistency condition is examined in each iteration, after updating the stress, back-stress and the yield surface size

$$\varphi_{n+1}^{(k)} = f\left(\boldsymbol{\sigma}_{n+1}^{(k)} - \boldsymbol{\alpha}_{n+1}^{(k)}\right) - \kappa\left(\bar{\varepsilon}_{n+1}^{p,(k)}\right) \quad . \tag{4.79}$$

The residual value obtained, $\left|\varphi_{n+1}^{(k)}\right|$, is compared with a predefined acceptable tolerance for distance between the current stress state and the active yield surface. A tolerance, $Tol = 10^{-6}$, was considered in the current work. If $\left|\varphi_{n+1}^{(k)}\right| < Tol$ the consistency condition is satisfied, *i.e.*, the stress state is close enough to the yield surface. Thus, variables obtained in the k'th iteration are considered to be the elastic-plastic results for the current increment. Otherwise, the solution has to continue until the stress state converges to the yield surface. To continue with the iterative solution, $\Delta\bar{\varepsilon}_{n+1}^p$ must be updated for the next iteration, as all variables are functions of the equivalent plastic strain. Substituting

equations (4.69) and (4.70) into equation (4.79) results in a nonlinear equation in terms of $\Delta\bar{\varepsilon}^p_{n+1}$. Linearization of this equation for the Newton-Raphson method yields

$$\delta(\Delta\bar{\varepsilon}^p)^{(k+1)}_{n+1} = -\varphi^{(k)}_{n+1} \Big/ \left(\frac{\partial\varphi_{n+1}}{\partial\Delta\bar{\varepsilon}^p_{n+1}}\right)^{(k)} \quad . \tag{4.80}$$

According to equation (4.79) and using the chain rule we have

$$\frac{\partial\varphi_{n+1}}{\partial\Delta\bar{\varepsilon}^p_{n+1}} = \frac{\partial\varphi_{n+1}}{\partial\boldsymbol{\sigma}_{n+1}}\frac{\partial\boldsymbol{\sigma}_{n+1}}{\partial\Delta\bar{\varepsilon}^p_{n+1}} + \frac{\partial\varphi_{n+1}}{\partial\boldsymbol{\alpha}_{n+1}}\frac{\partial\boldsymbol{\alpha}_{n+1}}{\partial\Delta\bar{\varepsilon}^p_{n+1}} + \frac{\partial\varphi_{n+1}}{\partial\kappa_{n+1}}\frac{\partial\kappa_{n+1}}{\partial\Delta\bar{\varepsilon}^p_{n+1}} \quad . \tag{4.81}$$

Because all terms in this equation correspond to the k^{th} iteration, the superscripts (k) are not shown. The terms $\frac{\partial\boldsymbol{\sigma}_{n+1}}{\partial\Delta\bar{\varepsilon}^p_{n+1}}$ and $\frac{\partial\boldsymbol{\alpha}_{n+1}}{\partial\Delta\bar{\varepsilon}^p_{n+1}}$ in equation (4.81) are obtained from equations (4.69) and (4.70), respectively:

$$\frac{\partial\boldsymbol{\sigma}_{n+1}}{\partial\Delta\bar{\varepsilon}^p_{n+1}} = -\boldsymbol{C^e}\!:\!\frac{\partial f(\boldsymbol{\sigma}_{n+1}-\boldsymbol{\alpha}_{n+1})}{\partial(\boldsymbol{\sigma}_{n+1}-\boldsymbol{\alpha}_{n+1})} \quad , \tag{4.82}$$

$$\frac{\partial\boldsymbol{\alpha}_{n+1}}{\partial\Delta\bar{\varepsilon}^p_{n+1}} = \frac{\partial\Delta\bar{\alpha}(\Delta\bar{\varepsilon}^p_{n+1})}{\partial\Delta\bar{\varepsilon}^p_{n+1}}\frac{\boldsymbol{\sigma}_n-\boldsymbol{\alpha}_n}{f(\boldsymbol{\sigma}_n-\boldsymbol{\alpha}_n)} \quad . \tag{4.83}$$

Other terms are determined using equation (4.79)

$$\frac{\partial\varphi_{n+1}}{\partial\boldsymbol{\sigma}_{n+1}} = -\frac{\partial\varphi_{n+1}}{\partial\boldsymbol{\alpha}_{n+1}} = \frac{\partial f(\boldsymbol{\sigma}_{n+1}-\boldsymbol{\alpha}_{n+1})}{\partial(\boldsymbol{\sigma}_{n+1}-\boldsymbol{\alpha}_{n+1})} \quad , \tag{4.84}$$

$$\frac{\partial\varphi_{n+1}}{\partial\kappa_{n+1}} = -1 \quad . \tag{4.85}$$

After finding $\delta(\Delta\bar{\varepsilon}^p)^{(k+1)}_{n+1}$ from equation (4.80), the equivalent plastic strain increment is updated

$$\Delta\bar{\varepsilon}^{p,(k+1)}_{n+1} = \Delta\bar{\varepsilon}^{p,(k)}_{n+1} + \delta(\Delta\bar{\varepsilon}^p)^{(k+1)}_{n+1} \quad . \tag{4.86}$$

Now that all variables for the loading surface ($\boldsymbol{\sigma}_{n+1}$, $\boldsymbol{\alpha}_{n+1}$, $\Delta\bar{\varepsilon}^p_{n+1}$) are updated, the consistency condition, equation (4.79), is evaluated for iteration $(k+1)$ and this loop continues until the consistency condition is satisfied.

After finding the variables on the loading surface for the current increment, the solution procedure continues, to obtain the corresponding stress point, $\boldsymbol{\Sigma}$, and back-stress, $\mathbf{A}$, on the bounding surface. According to equations (4.55), (4.56), and (4.57) we have

$$\boldsymbol{\Sigma}_{n+1}^{(l)} - \mathbf{A}_{n+1}^{(l)} = \frac{\mathrm{K}\left(\Delta\bar{\varepsilon}_{n+1}^{p}\right)}{\kappa\left(\Delta\bar{\varepsilon}_{n+1}^{p}\right)}\left(\boldsymbol{\sigma}_{n+1} - \boldsymbol{\alpha}_{n+1}\right) \quad , \tag{4.87}$$

$$\mathbf{A}_{n+1}^{(l)} = \mathbf{A}_n + \Delta\boldsymbol{\alpha}_{n+1} - \Delta\bar{\mathrm{A}}_2\left(\Delta\bar{\varepsilon}_{n+1}^{p}\right)\frac{\left(\boldsymbol{\Sigma}_{n+1}^{(l)} - \boldsymbol{\sigma}_{n+1}\right)}{f\left(\boldsymbol{\Sigma}_{n+1}^{(l)} - \boldsymbol{\sigma}_{n+1}\right)} \quad , \tag{4.88}$$

where, the superscript l represents iteration number. Similar to the back-stress increment for the loading surface, $\Delta\bar{\mathrm{A}}_2 = \Delta\mathrm{A}_{2,ref}$.

Simultaneous solution of equations (4.87) and (4.88) for $\boldsymbol{\Sigma}_{n+1}^{(l)}$ yields

$$\boldsymbol{\Pi}_{n+1}^{(l)} = \boldsymbol{\Sigma}_{n+1}^{(l)} - \frac{\mathrm{K}\left(\Delta\bar{\varepsilon}_{n+1}^{p}\right)}{\kappa\left(\Delta\bar{\varepsilon}_{n+1}^{p}\right)}\left(\boldsymbol{\sigma}_{n+1} - \boldsymbol{\alpha}_{n+1}\right) - \mathbf{A}_n - \Delta\boldsymbol{\alpha}_{n+1} + \Delta\bar{\mathrm{A}}_2\left(\Delta\bar{\varepsilon}_{n+1}^{p}\right)\frac{\left(\boldsymbol{\Sigma}_{n+1}^{(l)} - \boldsymbol{\sigma}_{n+1}\right)}{f\left(\boldsymbol{\Sigma}_{n+1}^{(l)} - \boldsymbol{\sigma}_{n+1}\right)} = 0 \quad . \tag{4.89}$$

Linearization of equation (4.89) gives

$$\delta\boldsymbol{\Sigma}_{n+1}^{(l+1)} = -\boldsymbol{\Pi}_{n+1}^{(l)} \Big/ \left(\frac{\partial\boldsymbol{\Pi}_{n+1}}{\partial\boldsymbol{\Sigma}_{n+1}}\right)^{(l)} \quad , \tag{4.90}$$

where the partial derivative $\frac{\partial\boldsymbol{\Pi}_{n+1}}{\partial\boldsymbol{\Sigma}_{n+1}}$ for the l^{th} iteration is obtained from

$$\frac{\partial\boldsymbol{\Pi}_{n+1}}{\partial\boldsymbol{\Sigma}_{n+1}} = \boldsymbol{I} + \frac{\Delta\bar{\mathrm{A}}_2\left(\Delta\bar{\varepsilon}_{n+1}^{p}\right)}{f\left(\boldsymbol{\Sigma}_{n+1} - \boldsymbol{\sigma}_{n+1}\right)}\boldsymbol{I} - \frac{\Delta\bar{\mathrm{A}}_2\left(\Delta\bar{\varepsilon}_{n+1}^{p}\right)}{f^2\left(\boldsymbol{\Sigma}_{n+1} - \boldsymbol{\sigma}_{n+1}\right)}\left(\boldsymbol{\Sigma}_{n+1} - \boldsymbol{\sigma}_{n+1}\right) \otimes \frac{\partial f\left(\boldsymbol{\Sigma}_{n+1} - \boldsymbol{\sigma}_{n+1}\right)}{\partial\boldsymbol{\Sigma}_{n+1}} \quad , \tag{4.91}$$

where $\boldsymbol{I}$ is the identity vector, and the operator $\otimes$ represents the cross product of two vectors. Thus, the variation of the stress state on the bounding surface is obtained from equation (4.90), and then the stress state on the bounding surface is updated for the next iteration

$$\boldsymbol{\Sigma}_{n+1}^{(l+1)} = \boldsymbol{\Sigma}_{n+1}^{(l)} + \delta\boldsymbol{\Sigma}_{n+1}^{(l+1)} \quad . \tag{4.92}$$

The iterative solution continues until $\left\|\boldsymbol{\Pi}_{n+1}^{(l)}\right\| < Tol$ is satisfied. After obtaining the converged result for $\boldsymbol{\Sigma}_{n+1}$, back-stress of the bounding surface is updated using equation (4.88).

Finally, elastic-plastic stiffness tensor, $\boldsymbol{C^{ep}}$, is updated according to the work by Nixon et al. [89] with an adjustment due to the isotropic behavior assumption

$$\boldsymbol{C^{ep}} = \begin{cases} \boldsymbol{C^e} & \text{if } \Delta\bar{\varepsilon}^p = 0 \\ \boldsymbol{C^e} - \frac{\boldsymbol{C^e}:\boldsymbol{\eta}\otimes\boldsymbol{C^e}:\boldsymbol{\eta}}{\boldsymbol{\eta}:\boldsymbol{C^e}:\boldsymbol{\eta}+h} & \text{if } \Delta\bar{\varepsilon}^p > 0 \end{cases} \quad . \tag{4.93}$$

where $h = \frac{\Delta S_y^t(\bar{\varepsilon}^p)}{\Delta\bar{\varepsilon}^p}$ is the slope of the hardening curve.

The flowchart for the numerical implementation is shown in Appendix B.

It should be emphasized that, despite some similarities between the plasticity model proposed in this study and the works by Lee et al. [90,111], a number of modifications were implemented in this work.

- Lee et al. [111] employed a yield function which was developed originally for aluminum and is not capable of modeling asymmetric yielding [192]. Lee et al. [90] later proposed another two-surface plasticity model in which an asymmetric, but pressure-dependent, yield function was utilized. Furthermore, the yield functions in both were simplified for a plane-stress state, as the plastic models were intended to simulate sheet metal forming. The yield function employed in this study is asymmetric and pressure independent, and was not simplified for plane-stress problems. Although the current study deals with sheet metals, the stress state for which is often assumed plane-stress, the stress state at the spot-weld nugget edge, which is the point of interest, is very close to plane-strain.

- The work by Lee et al. [90] considers anisotropy for AZ31B. However, experiments demonstrate that although anisotropy exists in AZ31B sheet, it is not significant under subsequent reversals [52]. Therefore, AZ31B-H24 was assumed to be isotropic under cyclic loading for the sake of simplicity in the present work.
- The hardening model employed by Lee et al. [90] assumes that the isotropic to kinematic hardening ratio is constant. However, this ratio in the current work is updated in each increment according to experimental results.
- In this research, back-stress updating for the loading and bounding surfaces is performed according to the back-stress evolution in the reference stress state. The Bauschinger effect and instant back-stress change at the beginning of reverse yielding were accounted for using a bisecting technique. The back-stress updating procedure is not clearly explained in the work of Lee et al. [90].

4.1.8.2 Stress-strain solution and yield surface evolution

The two-surface plasticity model introduced in this chapter was implemented in a user material (UMAT) subroutine to run with a commercial finite element program, Abaqus/standard. A simple FE model was generated to validate the formulation and implementation of the plasticity model. The FE model included a single eight-node linear brick element. The model was run under different loading scenarios in uniaxial and equi-biaxial conditions. The graphs in Figure 4.20 compare the experimental results with the stress-strain output obtained from the FE simulations using the UMAT. This figure demonstrates that the material model implemented in the UMAT follows the material behavior very well under different loading modes, *i.e.*, tension, compression, tension-compression (TC), and tension-compression-tension (TCT) with different strain amplitudes. Because replicating Lee's model required considerable time, the results obtained from the proposed cyclic plasticity model were not compared to Lee's model. Furthermore, as mentioned earlier, Lee's model is based on plane-stress assumption and is not applicable to spot-weld problems with plane-strain conditions.

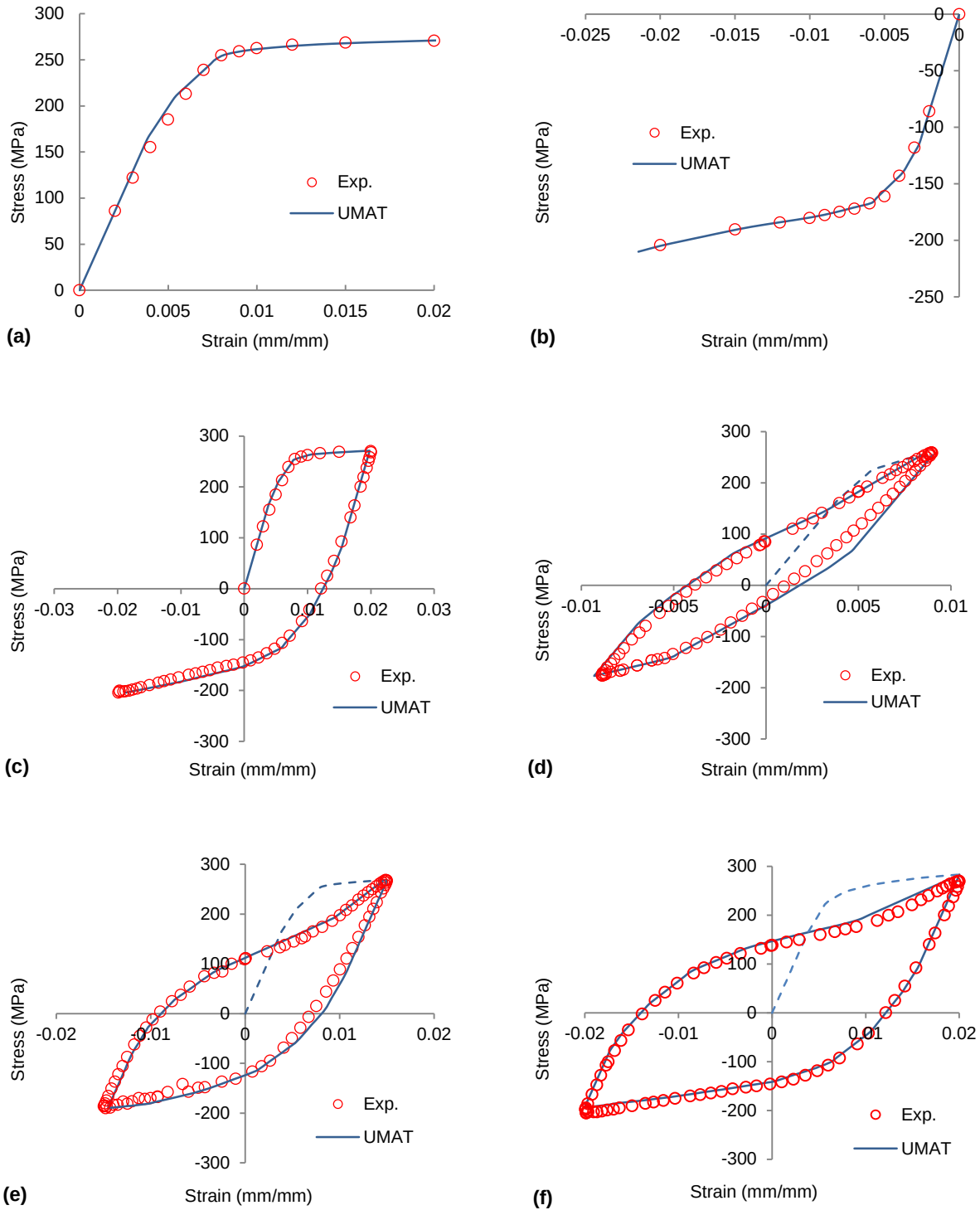

Figure 4.20: Stress-Strain response for (a) tension, (b) compression, (c) TC (d) TCT, $\varepsilon_{amp} = 0.9\%$, (e) TCT, $\varepsilon_{amp} = 1.5\%$, (f) TCT, $\varepsilon_{amp} = 2.0\%$

Figure 4.21 illustrates the evolution of the yield surface for uniaxial loading at different points during loading, unloading, and reloading, as shown in Figure 4.21(a). The initial yield surface is shown in Figure 4.21(b); it is asymmetric but the yield surface center is at the origin of the coordinate system in the stress space. The center of the yield surfaces in Figure 4.21 are shown with a "×" symbol. The yield surface remains unchanged during elastic loading, from point ① to ② in Figure 4.21(a). The yield surface at the beginning of tensile yielding, point ②, is illustrated in Figure 4.21(*c*), and compared with the initial yield surface. The new yield surface is tangent to the previous yield surface at the current stress point in stress space. The center of the yield surface has moved along the σ_1 axis, *i.e.*, the $(\boldsymbol{\sigma} - \boldsymbol{\alpha})$ direction, as a result of uniaxial loading in the 1-direction. The sudden change in back-stress is due to the instant yield surface shrinkage, which happens at the beginning of twin deformation. Although the loading path has not yet reversed, the yield surface contracts to accommodate early yielding in unloading. Figure 4.21(d) demonstrates the yield surface at the end of the loading reversal, point ③. This figure exhibits gradual movement of the yield surface along the loading direction. The yield surface also expands slightly to account for the change in elastic region size. Figure 4.21(e) illustrates the yield surface at the onset of yielding in compression. During unloading, from point ③ to point ④, the stress point moves from the right end of the yield surface to the left end, on a horizontal line passing through the center of the yield surface ③. Yield surface contraction happens at point ④ where the stress point reaches the active yield surface in the compression side. The new yield surface ④ is tangent to the previous yield surface at the current stress state, and the back-stress changes immediately to satisfy the tangency and shrinkage conditions. This contraction accounts for the Bauschinger effect for tension following compression. Figure 4.21(f) shows the yield surface corresponding to end of unloading reversal, point ⑤. The yield surface continues to move toward the compression side, and expands simultaneously.

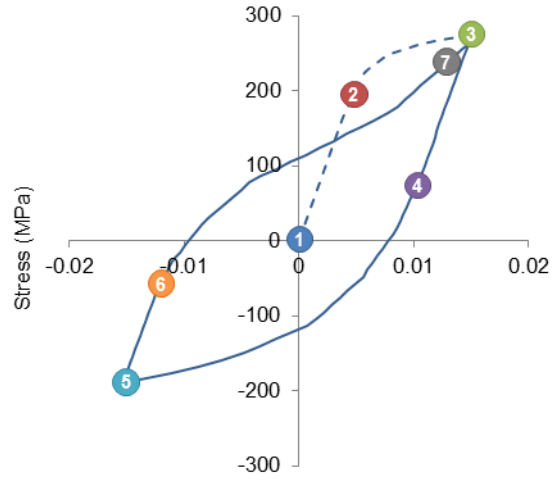
300
200
100
0
-100
-200
-300
-0.02
-0.01
0
0.01
0.02
Stress (MPa)
Strain (mm/mm)
1
2
3
4
5
6
7

(a)

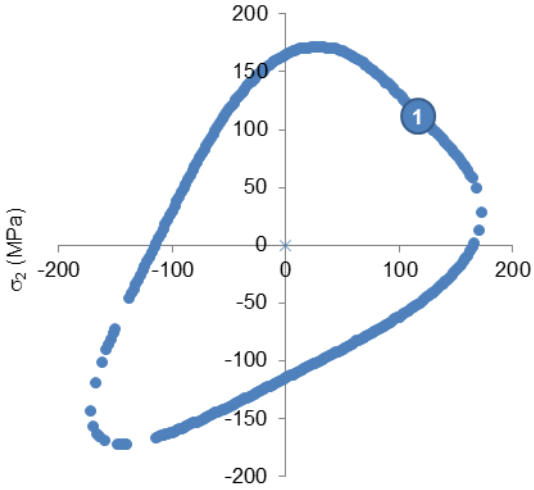
200
150
100
50
0
-50
-100
-150
-200
-200
-100
0
100
200
σ2 (MPa)
σ1 (MPa)
1

(b)

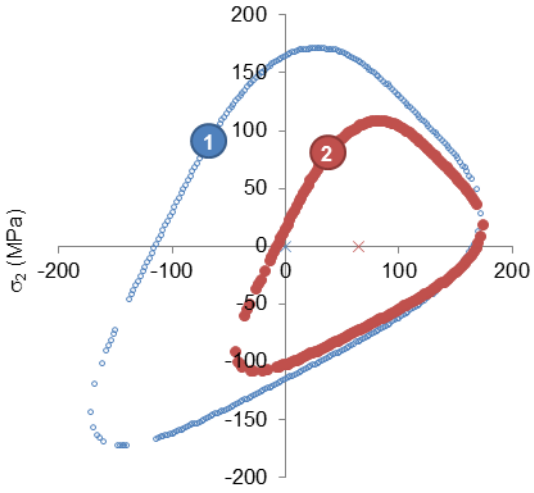
200
150
100
50
0
-50
-100
-150
-200
-200
-100
0
100
200
σ2 (MPa)
σ1 (MPa)
1
2

(c)

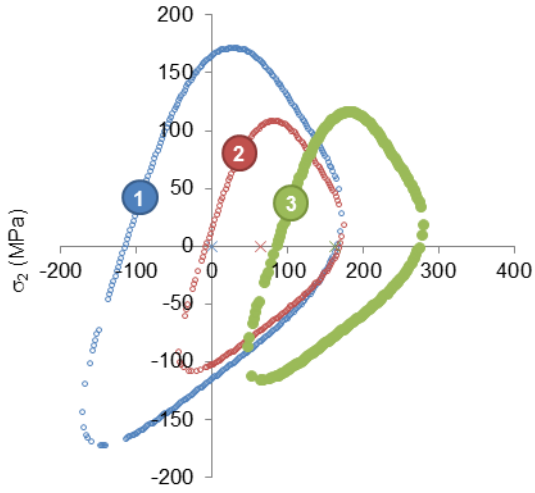
200
150
100
50
0
-50
-100
-150
-200
-200
-100
0
100
200
300
400
σ2 (MPa)
σ1 (MPa)
1
2
3

(d)

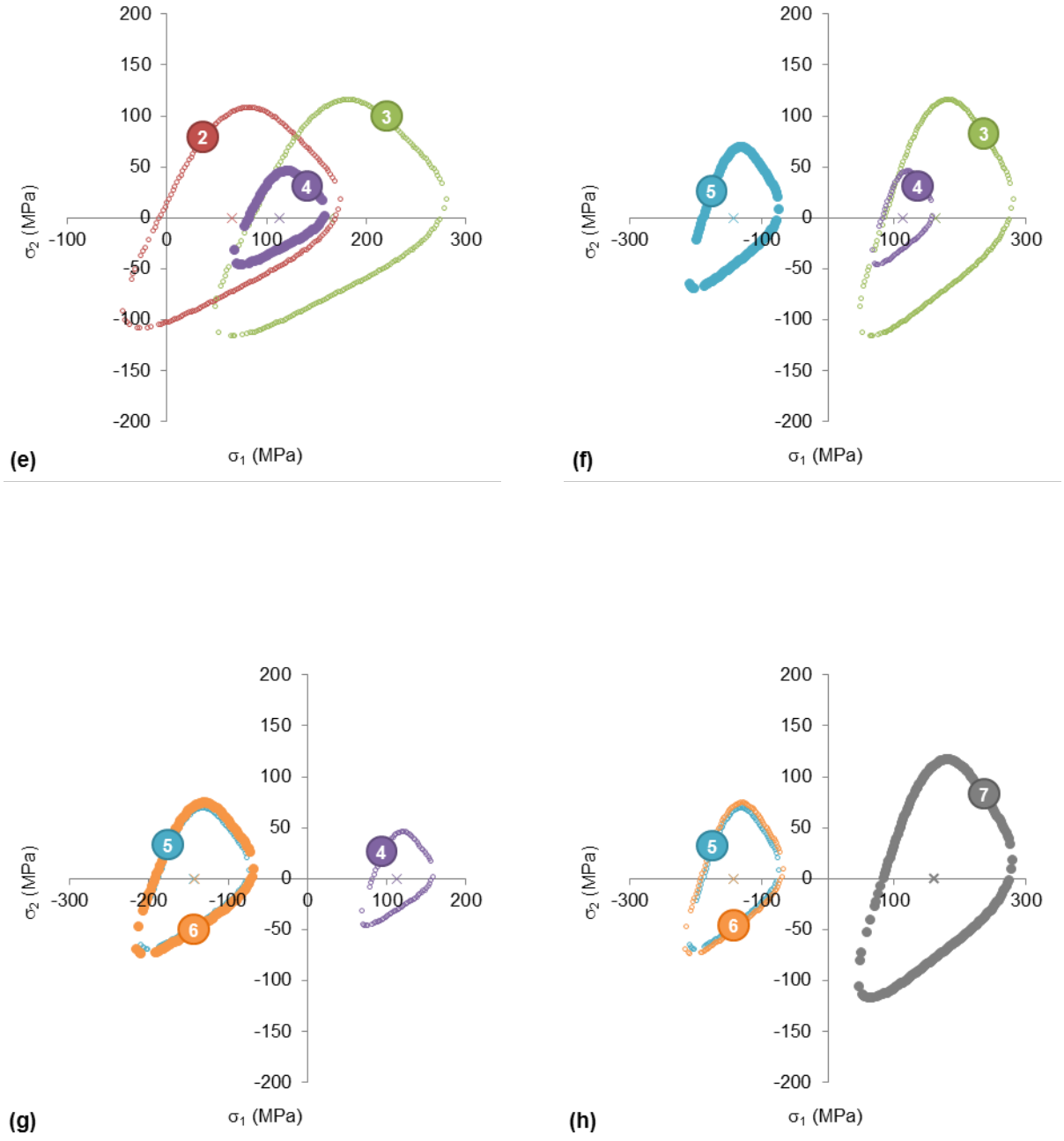

Figure 4.21: Yield surface evolution for uniaxial loading, TCT, $\varepsilon_{amp} = 1.5\%$

The yield surface at the beginning of untwinning, point ⑥, is depicted in Figure 4.21(g). According to this figure the yield surface maintains its size and position, which means tension following compression does not soften the material. Finally, Figure 4.21(h) represents the yield surface at the end of reloading, point ⑦. This figure shows a gradual movement of the yield surface in the opposite direction, *i.e.*, toward tension. The change in the yield surface size (isotropic hardening) for tension following compression is more significant than that for compression after tension. A similar trend in yield surface evolution will be followed for subsequent cycles.

To examine the UMAT output under multi-axial loading, equi-biaxial loading of a single element was considered. Equi-biaxial loading in this study refers to the same axial stress histories in two orthogonal directions without any phase difference. The graphs in Figure 4.22 illustrate the yield surface evolution for equi-biaxial loading. Comparing this figure with Figure 4.21 reveals that the trends in yield surface evolution are similar in uniaxial and biaxial loading, in terms of expansion and contraction of the yield surface. The yield surface contracts and the back-stress changes abruptly at the onset of yielding under tension and compression. Expansion of the yield surface occurs gradually during plastic deformation in the same reversal. The main difference between the yield surface evolutions for uniaxial and biaxial loading is the movement direction of the yield surface. The back-stress, according to the Ziegler's hardening law, evolves in the isotropic stress direction, *i.e.*, $(\boldsymbol{\sigma} - \boldsymbol{\alpha})$. In the case of uniaxial loading, back-stress has only one non-zero component, while for equi-biaxial loading two equal, non-zero back-stress components are generated in the same directions as the principal stresses.

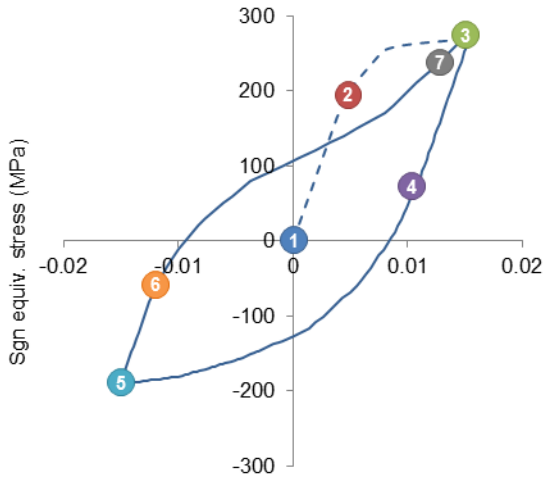
Sgn equiv. stress (MPa)
Sgn strain (mm/mm)
300
200
100
0
-100
-200
-300
-0.02
-0.01
0
0.01
0.02
1
2
3
4
5
6
7

(a)

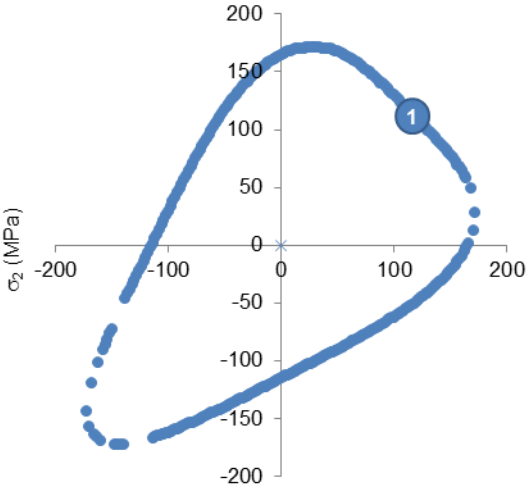
σ2 (MPa)
σ1 (MPa)
200
150
100
50
0
-50
-100
-150
-200
-200
-100
0
100
200
1

(b)

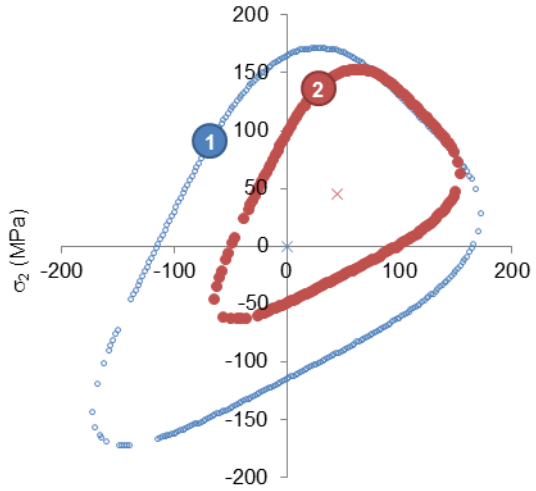
σ2 (MPa)
σ1 (MPa)
200
150
100
50
0
-50
-100
-150
-200
-200
-100
0
100
200
1
2

(c)

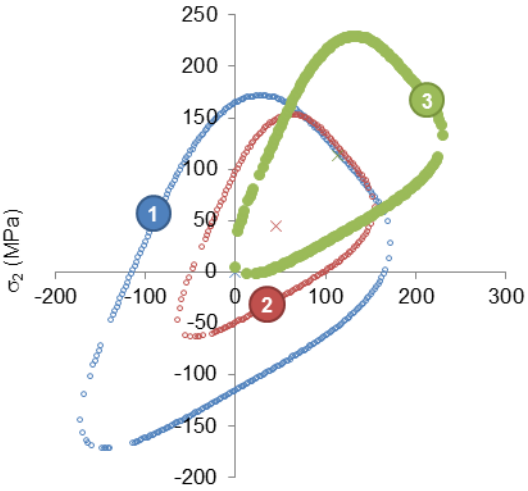
σ2 (MPa)
σ1 (MPa)
250
200
150
100
50
0
-50
-100
-150
-200
-200
-100
0
100
200
300
1
2
3

(d)

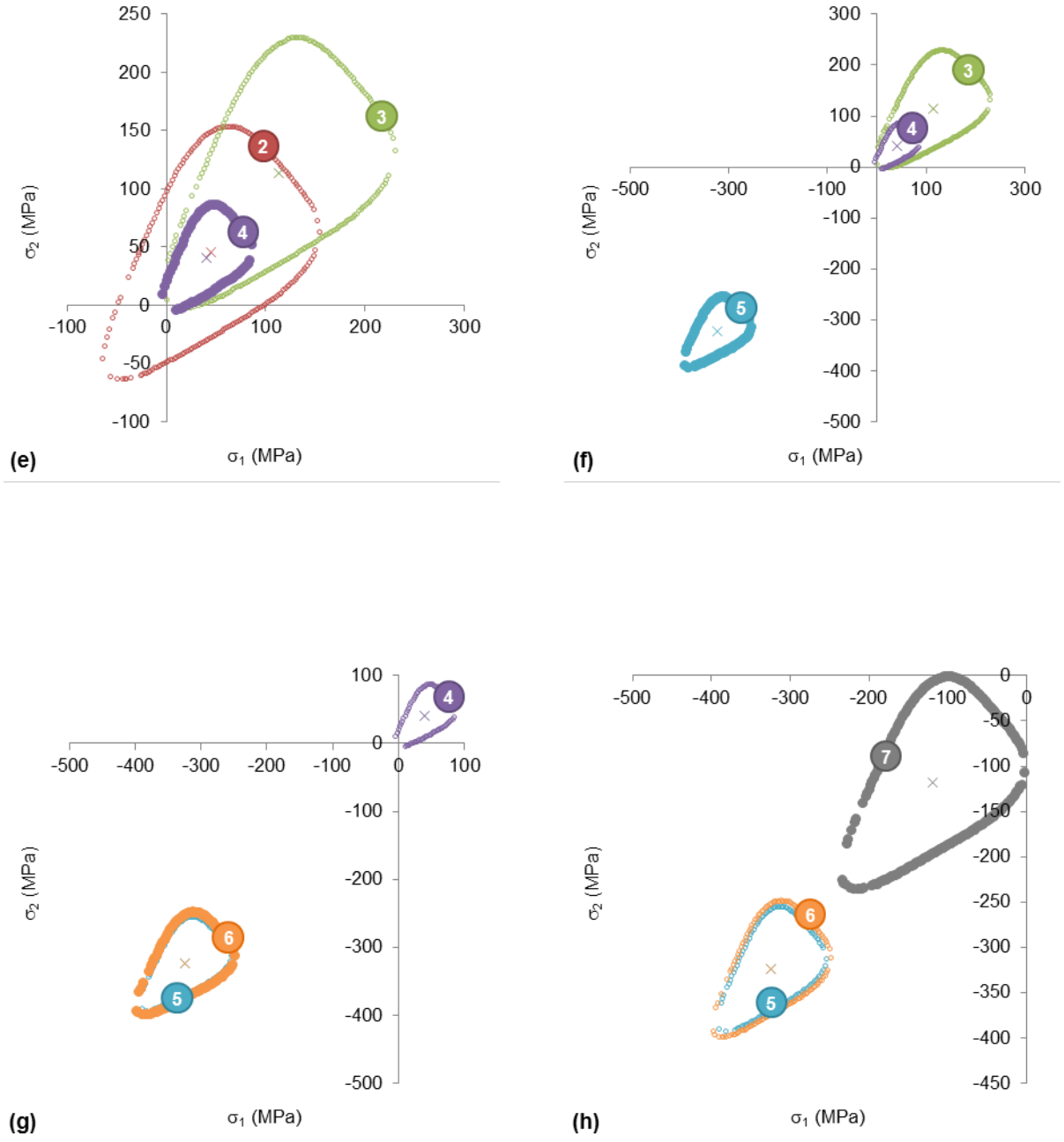

Figure 4.22: Yield surface evolution for equi-biaxial loading, TCT, $\varepsilon_{amp} = 1.5\%$

It is noteworthy that since the graphs in Figure 4.20 and Figure 4.21(a) correspond to uniaxial loading, the horizontal and vertical axes refer to uniaxial total strain and uniaxial stress, respectively. However, for the case of multi-axial loading, Figure 4.22(a), to plot the hysteresis loop and to calculate the hysteresis energy, horizontal and vertical axes represent "*signed total strain*" and "*signed equivalent stress*", respectively. The signed equivalent stress, $\bar{\sigma}_{\pm}$, is defined such that it regenerates the uniaxial stress, σ_{11}, during the course of loading, unloading, and reloading for the case of uniaxial loading. Signed equivalent stress in the current study is defined as

$$\bar{\sigma}_{\pm} = \begin{cases} \alpha_{ref} + f(\boldsymbol{\sigma} - \boldsymbol{\alpha}) & if \quad \sigma_{iso,hyd} > 0 \\ \alpha_{ref} - f(\boldsymbol{\sigma} - \boldsymbol{\alpha})/R_a & if \quad \sigma_{iso,hyd} < 0 \end{cases} , \tag{4.94}$$

where $\sigma_{iso,hyd} = 1/3\ tr\,(\boldsymbol{\sigma} - \boldsymbol{\alpha})$ is the hydrostatic part of the isotropic stress tensor. Signed total strain, $\varepsilon_{\pm}$, is defined to distinguish between different loading reversals, and is considered as

$$\varepsilon_{\pm} = \varepsilon_{\pm}^{e} + \bar{\varepsilon}_{\pm}^{p} \ , \tag{4.95}$$

$$\varepsilon_{\pm}^{e} = \bar{\sigma}_{\pm} / E \ , \tag{4.96}$$

$$\bar{\varepsilon}_{\pm,n+1}^{p} = \begin{cases} \bar{\varepsilon}_{\pm,n}^{p} + \Delta\bar{\varepsilon}_{n+1}^{p} & if\ tension\ reversal \\ \bar{\varepsilon}_{\pm,n}^{p} - \Delta\bar{\varepsilon}_{n+1}^{p} & if\ compression\ reversal \end{cases} . \tag{4.97}$$

Signed equivalent stress and signed equivalent plastic strain are stored as state variables in the UMAT.

4.2 Model Verification

The cyclic plasticity model, presented in this chapter and implemented in a UMAT, was verified before applying to the problem of interest. The stress-strain results presented in section 4.1.8.2 demonstrated that the UMAT can regenerate the material behavior. Model verification is usually performed by solving a real-life problem involving higher degree of complexity for which experimental results are available. However, component testing was not conducted in this study due to fabrication and fixturing complexities. Moreover, no experimental results were available from cyclic testing of a component made from the same AZ31B-H24 magnesium sheet. Therefore, a one-dimensional problem and a two-dimensional problem with available solutions [193,194] were solved using the UMAT. The available solutions, which were used as a benchmark, are based on a method called "*variable material property*" (VMP) [195]. The VMP method is based on total deformation plasticity approach and generates inelastic solution using the linear elastic solution through an iterative procedure [195]. The accuracy of this method has been verified by comparison with experimental measurements [196]. Results obtained from the VMP method and FE simulation using the UMAT are compared and discussed in this section.

4.2.1 1-D Verification

A cantilever beam problem under pure bending was considered for one-dimensional verification, Figure 4.23.

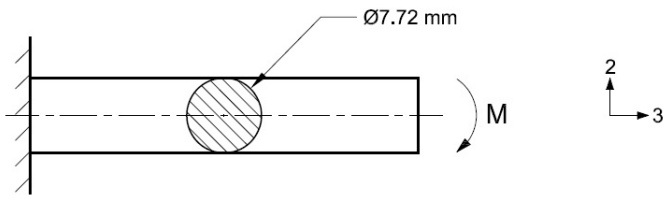

Figure 4.23: Illustration of the cantilever beam problem under pure bending

The beam has a circular cross-section with diameter 7.72 mm and is long enough to avoid end effects. The beam is assumed to be made from AZ31B-H24 with elastic properties E= 43 GPa and ν= 0.35. Stabilized cyclic curves, presented in chapter 3, were used for the tension and compression hardening behavior.

A half of the beam was considered for FE modeling, taking advantage of symmetry about the vertical-longitudinal plane, Figure 4.24. Eight-node linear brick elements with reduced integration were utilized in the FE model. Elements were gradually refined toward the center of the beam cross-section for a more accurate calculation of the neutral axis (N.A) location. The neutral axis of a beam under bending is the axis in the cross-section on which the normal stress is zero.

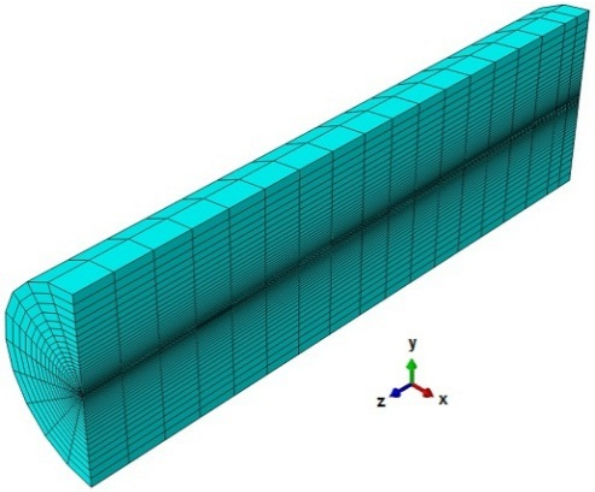

Figure 4.24: FE model for cantilever beam under bending

Asymmetric material behavior under tension and compression results in movement of the N.A. Normal stress, σ_{33}, was calculated along the vertical diameter of the cylinder beam in the middle of the beam to avoid end effects.

Figure 4.25(a) shows the distribution of normal stress for different applied moments, obtained from the UMAT. As can be seen in this graph, the N.A deviates from the center toward the tensile side of the beam cross-section due to earlier yielding in compression. This chart also demonstrates that the offset from the N.A to the center of the beam cross-section increases with increasing moment.

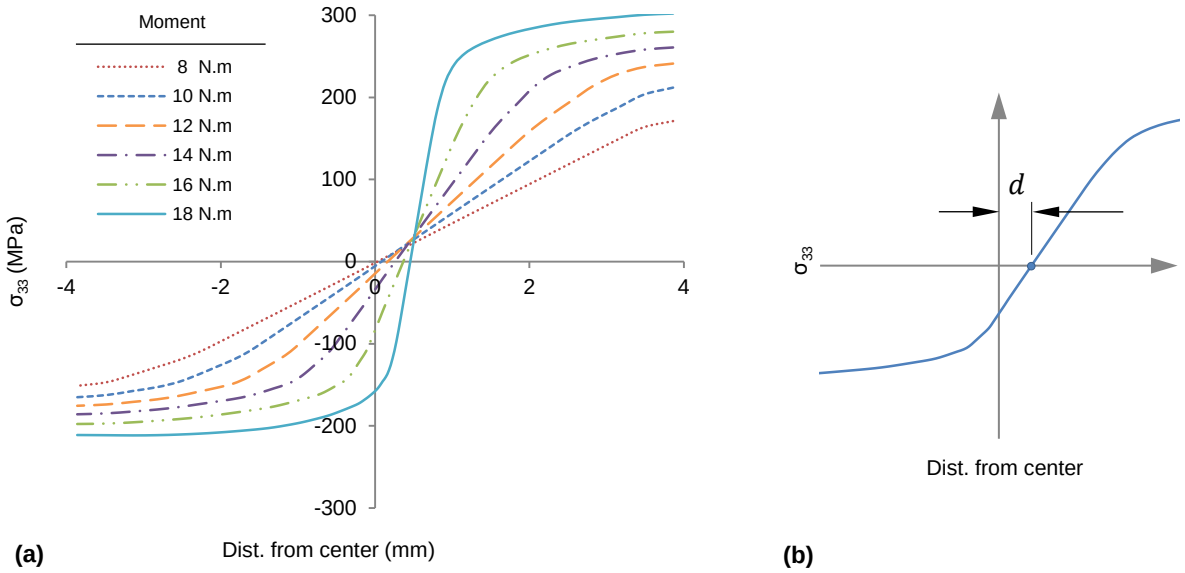

Figure 4.25: (a) stress distribution for different moments (b) illustration of N.A offset from the center

Figure 4.25(b) represents this offset schematically, and denotes it as "d". The distance d was calculated from the UMAT and compared with available results from the VMP method [193] for different bending moments. The results are shown in Table 4.1.

Table 4.1: Comparison of N.A offset between VMP [193] and UMAT

	Applied moment (N.m)					
	8	10	12	14	16	18
d_{VMP} (mm) [193]	0.046	0.090	0.166	0.263	0.371	0.461
d_{UMAT} (mm)	0.030	0.082	0.162	0.259	0.365	0.455
Difference (%)	35.5	9.4	2.4	1.7	1.6	1.3

This table shows that the difference between UMAT and VMP is significant for low bending moments, but continuously diminishes with increasing applied moment. For low bending moments, which result in limited plasticity, a slight difference in stress calculation and mesh size may cause a significant change in N.A offset. However, plastic deformation dominates under high bending moments, resulting in minimal sensitivity to numerical calculation factors.

UMAT verification was also performed for unloading of the beam. To this end, a 16 N.m bending moment was applied to the beam and then removed. Figure 4.26 compares the available

VMP results [193] with UMAT solution in terms of normal stress profiles after loading and unloading.

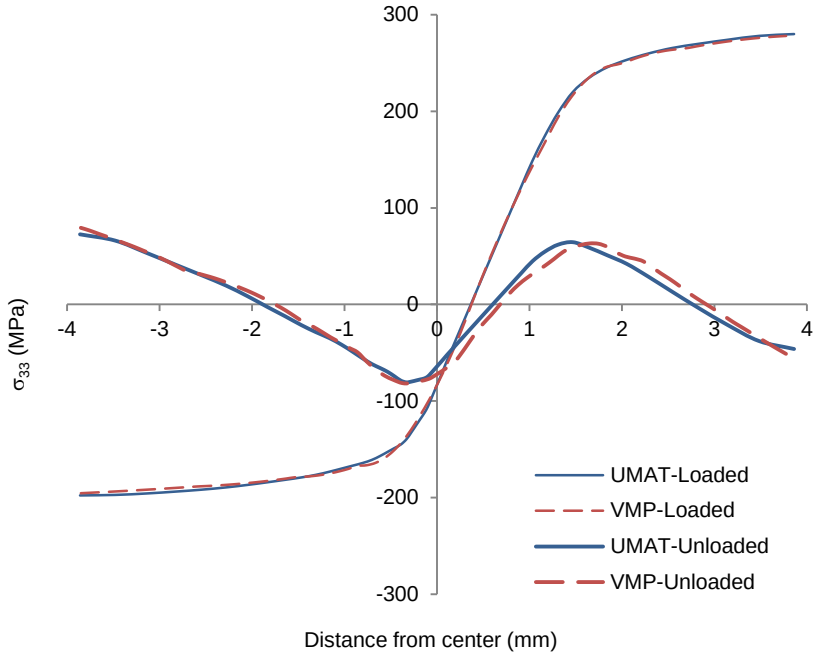

Figure 4.26: Stress distribution after loading and unloading the cantilever beam from VMP [193] and UMAT

According to this diagram, stress and residual stress results agree very well throughout the beam cross-section.

4.2.2 2-D Verification

A pressurized cylinder with a large wall-thickness and fixed-ends, Figure 4.27, was analyzed using the UMAT, and the results were compared with an available VMP solution [194] to provide two-dimensional verification. The inner and outer diameters equal 44 mm and 203.4 mm, respectively.

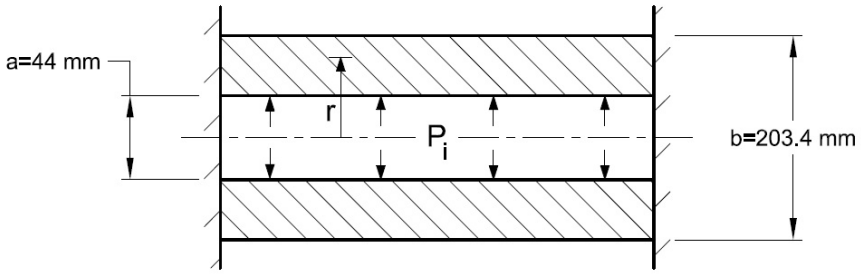

Figure 4.27: Schematic illustration of plane-strain pressurized cylinder problem

The cylinder is assumed to be made from a magnesium alloy with mechanical properties shown in Figure 4.28.

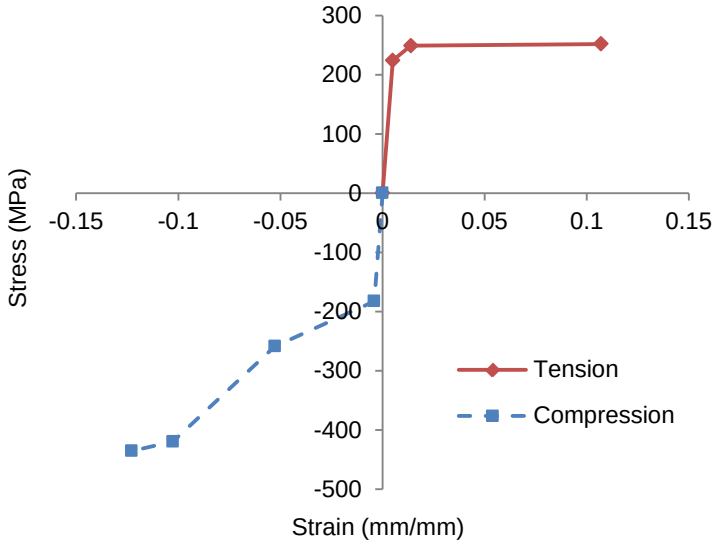

Figure 4.28: Material properties for the pressurized cylinder

A three dimensional FE model was generated for the UMAT solution. Because the problem is axisymmetric, only a narrow sector of the cross-section, with a 5° including angle was considered for FE modeling. The FE model is shown in Figure 4.29. Twenty-node quadratic brick elements were employed for FE modeling.

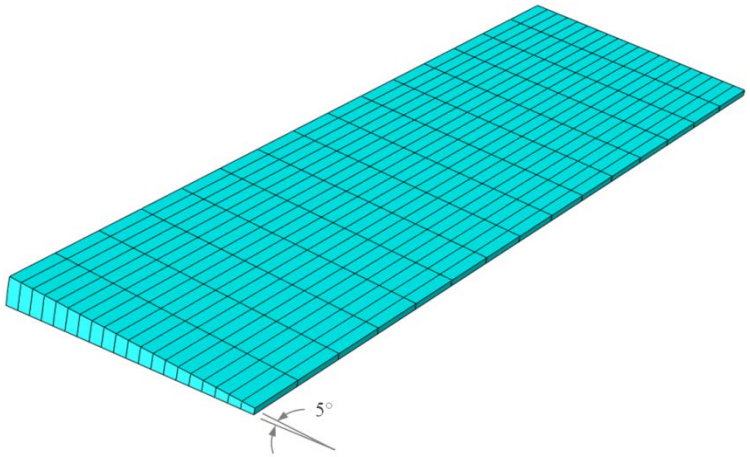

Figure 4.29: 3D FE model for the pressurized cylinder

Figure 4.30 compares the stress results in the hoop, radial, and longitudinal directions under two different internal pressures, *i.e.*, P_i=250 MPa or 350 MPa. Stress responses indicate that a portion of the wall-thickness from the inner radius is in the elastic-plastic region, while the outer regions are still elastic. The radius at which the hoop stress starts descending, or at which the longitudinal stress begins to plateau, corresponds to the plastic radius of the cylinder. In these cases, plastic deformation occurs over nearly 30% or 75% of the cylinder wall-thickness, for P_i=250 MPa or 350 MPa, respectively. The plastic radii estimated using the UMAT and VMP approaches are in good agreement. The hoop stress distributions over the cylinder wall thickness are reasonably close. The hoop stress in the plastic zone from the UMAT for P_i=250 MPa is somewhat larger than that from the VMP, and is smaller in the elastic zone. One of the reasons for the difference is dissimilar hardening curves. In the VMP method, the hardening curve associated with an element is the average of the tensile and compressive hardening curves based on the hydrostatic stress. However, the UMAT follows either the tensile or compressive hardening curve according to the sign of the hydrostatic isotropic stress.

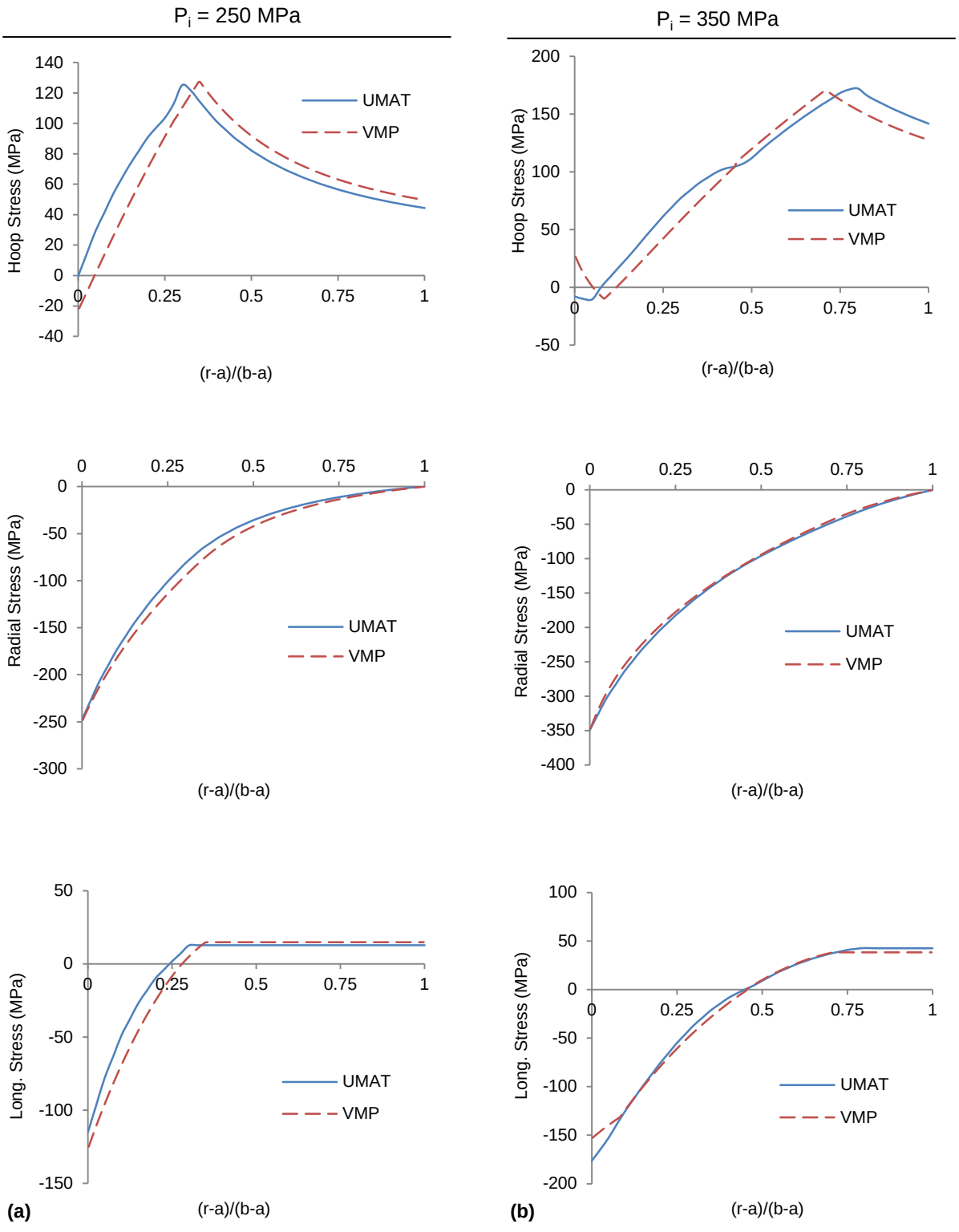

Figure 4.30: Pressurized cylinder solution by VMP [194] and UMAT (a) for P_i=250MPa (b) for P_i=350 MPa

This feature causes a kink in the Hoop stress results from the UMAT, which is minor for P_i=250 MPa at (r-a)/(b-a)≈0.25 but becomes more evident for P_i=350 MPa at (r-a)/(b-a)≈0.42. The turning point in this curve represents the radius at which the sign of the hydrostatic isotropic stress has changed. Another factor that contributes to the difference between the hoop stress results arises due to the distinct natures of the VMP and UMAT approaches. Although it is an iterative method, the VMP method uses total deformation theory of plasticity, while incremental theory of plasticity is implemented in the UMAT. Therefore, in the VMP solution, internal pressure is applied all at once and diagonal components of the stress tensor for each element in the last iteration determine the hardening curve of that element. However, in the UMAT solution, pressure is applied incrementally and the hardening curve that an integration point follows might change during the course of loading, depending on the stress tensor for that increment. Radial stresses are in overall very good agreement throughout the thickness. Longitudinal stress distributions are well matched in the elastic region. The difference in the elastic-plastic region can be attributed to the same reasons as already discussed for the hoop stress.

4.3 Summary

In this chapter, a constitutive model was developed, implemented, and verified to model the asymmetric hardening behavior of wrought magnesium alloys under cyclic loading. The proposed phenomenological model was based on continuum theory of plasticity with the incremental approach. The Cazacu-Barlat yield function along with associated flow rule and a combined hardening model were used in this model. The Cazacu-Barlat yield criterion was adopted as it considers the yielding asymmetry and is hydrostatic stress independent. Because anisotropy of AZ31B sheet was neglected, a simplified form of this yield criterion for isotropic materials was employed. Considering that magnesium is a pressure-independent material, an associated flow rule was utilized and formulations for the flow rule associated with the Cazacu-Barlat yield function were derived for a general stress state. A combined isotropic-kinematic hardening model was adopted because AZ31B magnesium sheet exhibited complicated hardening behavior under cyclic loading, which could not be modeled by isotropic or kinematic hardening models alone. Translation of the yield surface was governed according to Ziegler's hardening rule. To identify the proper reversal and hardening rule during cyclic loading, a criterion was considered for reverse yielding. According to this criterion, reverse yielding occurs if the angle between two subsequent points on the yield surface is greater than a predefined reference angle. An adjustment for abrupt change of back-stress and size of the yield surface was introduced at the onset of reverse yielding. The algorithm for numerical implementation of the proposed mode was presented. The numerical formulation was implemented into a user material (UMAT) subroutine to run with the commercial finite element program Abaqus/Standard. Different uniaxial and biaxial loading scenarios were simulated in Abaqus in conjunction with the UMAT. Stress-strain results obtained from the FE simulations were compared with experimental results. It was demonstrated that the material model implemented in the UMAT followed the experimental material behavior under different loading conditions, *i.e.*, tension, compression, tension-compression,

and tension-compression-tension for different strain amplitudes. Evolution of the yield surface during the course of loading, unloading, and reloading was presented and discussed for uniaxial and biaxial load cases. To verify the material model, one-dimensional and two-dimensional problems with available solutions were solved using the UMAT. The available solutions, which were used as a benchmark, are based on a method called variable material property (VMP). The results obtained from the UMAT and VMP methods showed good agreement for both problems.

Chapter 5

Fatigue Modeling

Resistance spot-welding (RSW) has been widely used as a joining process in the automotive industry, and is currently the predominant joining technique in the automotive body assembly line [16]. A typical vehicle in North America contains about four to five thousand spot-welds [17].

On the other hand, service reports of automobiles show that a major portion of structural durability issues are related to spot-welds [1], which is due to the fact that spot-welds act as stress concentration sites, and are therefore more susceptible to fatigue failure. As a result, a reliable fatigue life prediction method is crucial for durability and safety design of automobiles.

Several fatigue models have been proposed for spot-welds, and verified mostly for steel spot-welds. A number of the most common fatigue models are introduced in this chapter, and are employed for predicting the fatigue life of magnesium spot-welds. A fatigue model is proposed at the end of this chapter based on the plasticity model developed in chapter 4.

5.1 Fatigue Modeling of Spot-Welds

Numerous models have been developed for predicting the fatigue life of spot-welds. These models can be categorized into three major groups: fracture mechanics, structural stress, and local strain approaches. An introduction to these approaches is given in the following sections, and the most well-known fatigue models from each approach are explained.

5.1.1 Fracture Mechanics Approach

Until the 1970s, the fatigue strength of spot-welds was represented by specimen-dependent quantities, such as load amplitude. Therefore, specimen-level fatigue test results were not directly transferable to a component, or even to a specimen with a different geometry. The fracture mechanics approach was one of the first solutions proposed to resolve this issue.

In the past four decades, several researchers have considered the spot-weld as a crack-like slit based on some experimental observations and simplifications [124-126,197]. The RSW process, as introduced earlier, produces a circular joint between two or more sheets, with a notch at the spot-weld edge. Figure 5.1 displays the edge notch in steel and magnesium spot-welds. Because the notch radius is small compared to the sheet dimensions, the spot-weld in some studies is considered a sharp notch. Therefore, the spot-weld is treated as a circular region surrounded by a pre-existing crack.

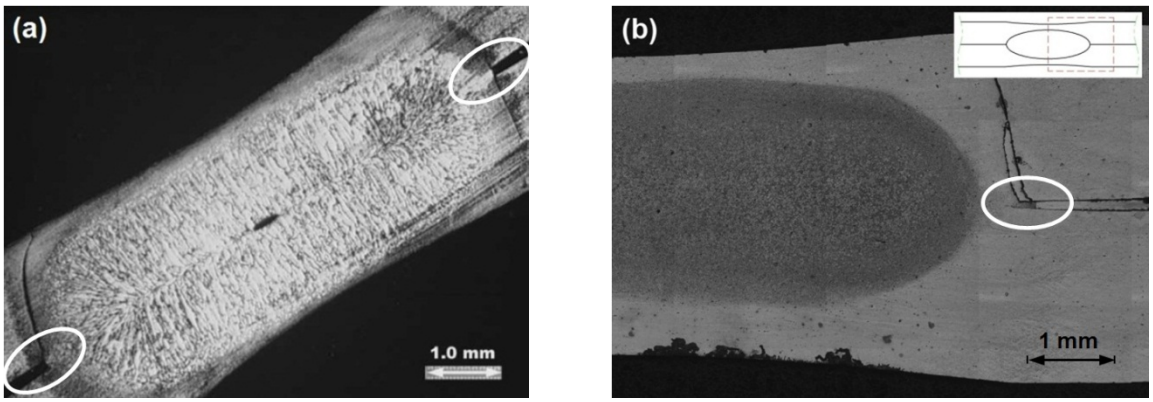

Figure 5.1: Spot-weld edge notch (a) in a steel spot-weld [20] (b) in a magnesium spot-weld

Fatigue failure, in general, consists of fatigue crack initiation and crack propagation processes. For the case of smooth specimens and blunt notched components, where the crack initiation process dominates, fatigue life is closely related to the material strength [198]. However, fatigue life in sharp notched and cracked components is controlled by crack propagation and is insensitive to material strength [199]. Experimental results for steel spot-welds demonstrate that the base metal strength has an insignificant effect on the fatigue life [126,198]. These observations support the idea that spot-welds are crack-like flaws, and fracture mechanics is the appropriate approach for fatigue modeling.

The fracture mechanics approach considers a measure of stress intensity factor (SIF) or J-integral as the fatigue damage parameter, and relates this parameter to the fatigue life or the crack growth rate. Pook [127], Swellam et al. [18], and Wang et al. [200] proposed different methods for calculating the SIF or J-integral range for spot-welds. The well-known Paris' equation,

$$\frac{da}{dN} = C\ (\Delta K)^m \quad , \tag{5.1}$$

is used in these models to estimate fatigue life, in which a is the crack length, N is the fatigue life, ΔK is the equivalent mode I SIF range ($\Delta K = \Delta K_{I_{eq}}$), and C and m are material constants. The fatigue crack propagation direction in all of these models is assumed to be through the coupons interface. Also, the SIF is assumed constant, *i.e.*, independent of the crack length, which is based on the work by Cooper et al. [201]. Therefore, an explicit equation may be derived between equivalent SIF range and fatigue life,

$$\Delta K_{I_{eq}} = A\ (N)^{-b} \quad , \tag{5.2}$$

where A and b are material constants.

Pook in 1975 [202] was the first researcher who applied linear elastic fracture mechanics (LEFM) to spot-welds, and derived a formulation for modes I and II SIFs for tensile-shear specimens.

Employing plate theory and using the average shear stress over the nugget cross-section, Pook developed the following equations for SIFs at the centerline of tensile-shear specimens:

$$K_I = \frac{F}{(d/2)^{3/2}} \left[0.341 \left(\frac{d}{t}\right)^{0.397}\right] \quad , \tag{5.3}$$

$$K_{II} = \frac{F}{(d/2)^{3/2}} \left[0.282 + 0.162 \left(\frac{d}{t}\right)^{0.710}\right] \quad , \tag{5.4}$$

where K_I and K_{II} are modes I and II SIFs, F is the applied load on tensile-shear specimen, d is the nugget diameter, and t is the sheet thickness. Pook considered the mode I SIF range, ΔK_I, for fatigue life estimation, by neglecting the mode II SIF contribution [127]. A drawback of this model is that the effect of crack growth on SIFs is ignored. Also, Pook's formulation is not applicable to spot-weld problems under a general load case, *i.e.*, a spot-welded structure; applicability is restricted to spot-welds in the tensile-shear configuration with a ratio $d/t \leq 10$.

Newman [129] later adopted Pook's formulation to develop a fatigue model for spot-welds under tensile-shear loading. According to Tada et al. [128], the principal stress plane, which is assumed to be the initial crack growth direction, is obtained by solving the following equation,

$$K_I \sin\theta_0 = -K_{II}(3\cos\theta_0 - 1) \quad , \tag{5.5}$$

in which K_I and K_{II} are obtained from equations (5.3) and (5.4), and θ_0 is the direction of initial crack propagation with respect to the coupons interfacial plane. Equivalent mode I SIF range, $\Delta K_{I_{eq}}$, on the plane of principal stress is considered as the crack driving force,

$$\Delta K_{I_{eq}} = \frac{\Delta K_I}{4}\left[3\cos\frac{\theta_0}{2} + \cos\frac{3\theta_0}{2}\right] - \frac{\Delta K_{II}}{4}\left[3\sin\frac{\theta_0}{2} + 3\sin\frac{3\theta_0}{2}\right] \quad . \tag{5.6}$$

A number of assumptions were made in this model: SIFs are assumed to be independent of crack length, the crack is planar, and the ratio of specimen width to nugget radius is greater than 5. Similar to Pook's model, this model is only applicable to tensile-shear spot-welds.

Wang et al. in 1991 [200] used the J-integral to correlate with the fatigue life of coach-peel spot-weld specimens. The J-integral in this work was calculated from a linear elastic FE analysis. The maximum J-integral range at the periphery of the spot-weld was used for fatigue life estimation through an equation similar to equation (5.2). This method is applicable to any loading condition and takes the effect of modes I, II, and III into account. However, the complexities involved in FE model preparation and the intensive calculations restrict the applicability of this method for real-life problems.

Swellam in 1992 [18] developed a fatigue model for spot-welds under a general loading. This model considers spot-welds under an arbitrary load, and finds forces and moments at the spot-weld center from static equilibrium of a coupon. The SIF formulations developed by Tada et al. [128] were adopted in this model. Equivalent SIF range, which is defined in terms of the SIF ranges due to axial and shear forces and bending moment, was used in Paris' equation to obtain the fatigue life. The main advantage of this model is that it is applicable to any spot-weld specimen or structure, due to the simplicity of the calculations. A shortcoming of this model is that the crack is assumed to be in the interfacial plane, which is often not a valid assumption, as will be discussed later in this section. Moreover, SIFs are calculated for the initial configuration, and the effect of crack propagation is neglected. This model is explained in more detail in section 5.2.1.

Zhang in 1997 [203] argued that Pook's formulations were based on average shear stress in the nugget, which did not directly contribute in the SIFs at the spot-weld edge. Analytical relationships for SIFs and the J-integral were derived in this work utilizing normal and shear stresses in the sheet at the point of interest. Normal and shear stresses are normally obtained from FE analyses. For the special case of tensile-shear specimens, the SIF formulations were simplified in terms of the applied load,

$$K_I = \frac{\sqrt{3}F}{2\pi d\sqrt{t}} \quad , \tag{5.7}$$

$$K_{II} = \frac{2F}{\pi d\sqrt{t}} \quad . \tag{5.8}$$

The equivalent stress intensity factor range, ΔK_{eq}, including the effect of both modes I and II SIFs, is considered in this model as the damage parameter,

$$\Delta K_{eq} = \sqrt{\Delta K_I^2 + \Delta K_{II}^2} \quad . \tag{5.9}$$

Although Zhang resolved some of the disadvantages associated with Pook's formulation, this model still assumes the crack is on the coupons faying surface, rather than through the sheet thickness.

Regardless of the fatigue model, the fracture mechanics approach in general has a number of advantages and drawbacks. The main advantage of this approach is that the crack propagation process may be closely followed. A drawback of this approach is that the nugget edge is considered as a crack and therefore crack initiation life is assumed insignificant, which is not supported by experimental observations and analysis. The work by Swellam et al. [18] shows that crack initiation life in spot-welds of a low carbon steel overwhelms the crack propagation life in the high cycle fatigue regime, *i.e.*, $N_f > 10^5$ cycles. McMahon et al. [178] demonstrated that up to 55% of the total fatigue life of spot-welds can be consumed by crack initiation. This ratio in the work by Sheppard et al. [134] is 30%. Crack initiation life is the number of cycles required for the crack to reach a length of 18% of the sheet thickness in Swellam's work [18], and 0.25 mm in the studies by McMahon et al. and Sheppard et al. [134,178]. Another deficiency associated with the fracture mechanics approach is that the formulations are based on the assumption that the crack is along the faying surface; according to experiments, through-thickness cracking is the more common fatigue failure mode for tensile-shear specimens [126,142,160,204]. Moreover, in contrast to the assumption in this approach, primary cracks in some cases do not initiate from the nugget edge [139]; similar results were obtained in the current study (chapter 3).

5.1.2 Structural Stress Approach

Since 1989, a number of fatigue models have been developed for spot-welds based on the structural stress concept. Structural stress is a linearly distributed stress over the thickness by neglecting the effect of stress concentration. Structural stress reflects the forces and moments at the spot-weld center or edge, and theoretically may be defined in the plate or nugget depending on the mode of failure. Therefore, structural stress has been considered as the factor which directly or indirectly controls the fatigue failure. Structural stress is usually calculated by superposing the effects of different forces and moments, obtained from linear elastic FE simulations. To suit this approach, the sheets and spot-welds in the FE model are represented by shell and beam elements, respectively. The structural stress approach, as opposed to many fracture mechanics-based models, often provides enough flexibility to be applicable to different specimens and structures. Therefore, these models are widely employed in industry, including the automobile industry [130]. However, some weak points are also associated with this approach. A serious shortcoming is that the notch effect at the spot-weld edge is ignored [130].

Radaj in 1989 [131] proposed the concept of structural stress for fatigue assessment of spot-welds. Adopting the structural stress concept and assuming that the spot-weld is an ideal crack-like slit, the following equations were proposed to obtain SIFs at the spot-weld edge (which is assumed to be the crack tip),

$$K_I = \left[0.144\left(\sigma_{ti} - \sigma_{to} + \sigma_{bi} - \sigma_{bo}\right) + 1.115\left(\tau_t^{\perp} - \tau_b^{\perp}\right)\right]\sqrt{t} \quad , \tag{5.10}$$

$$K_{II} = \left[0.25\left(\sigma_{ti} - \sigma_{bi}\right) + 0.275\left(\tau_t^{\perp} + \tau_b^{\perp}\right)\right]\sqrt{t} \quad , \tag{5.11}$$

$$K_{III} = 0.707\left(\tau_{ti}^{\parallel} - \tau_{bi}^{\parallel}\right)\sqrt{t} \quad , \tag{5.12}$$

where σ and τ are nominal normal and shear structural stresses, respectively. Subscripts t and b represent top and bottom sheets, subscripts i and o stand for inner and outer surface, and superscripts

∥ and ⊥ represent in-plane and out-of-plane (transverse) shear stresses, respectively. Radaj in 1990 [1] presented formulations for nominal structural stresses in terms of forces and moments for spot-welded specimens. The forces and bending moments were obtained from FE analysis, and were the element nodal forces at the node shared between the spot-weld (beam element) and the plate (shell element). A drawback of this model, similar to the fracture mechanics approach, is that the fatigue crack is assumed to be through the nugget. Also, SIFs are assumed constant during the course of crack propagation.

Rupp et al. in 1995 [132] employed beam and plate theories to develop structural stress formulations for spot-welds. Forces and moments (membrane, transverse and normal forces, as well as two out-of-plane bending moments) were obtained at the nugget center from FE analysis (the torsional moment was neglected). Through-nugget cracking and through-plate cracking were considered as possible failure modes.

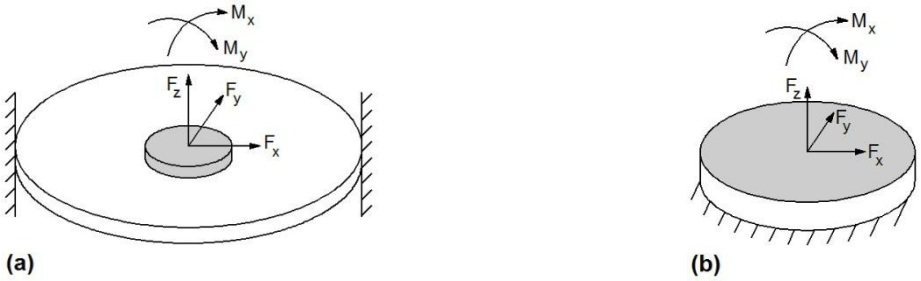

Figure 5.2: Rupp's model illustration (a) plate theory for sheet failure (b) beam theory for nugget failure [132]

The theory of sheet and plate, Figure 5.2(a), was employed to obtain structural stresses for through-plate failure,

$$\sigma_{r,max} = F_{x,y}/\pi dt \quad , \tag{5.13}$$

$$\sigma_{r,max} = K\ 1.744\ F_z/t^2 \quad , \tag{5.14}$$

$$\sigma_{r,max} = K\ 1.872\ M_{x,y}/dt^2 \quad , \tag{5.15}$$

where $K = 0.6\sqrt{t}$ is an empirical stress correction factor for tension and bending terms.

Equivalent von Mises stress was calculated in plates around the nugget periphery at different angles; the maximum value was considered as the fatigue damage parameter in plates.

For through-nugget failure, the beam bending theory was used to find the structural stress from resultant forces at the nugget center, as shown in Figure 5.2(b). The expressions for calculating structural stress at the nugget are

$$\sigma_n = 4\,F_z/\pi d^2 \quad , \tag{5.16}$$

$$\sigma_{b,max} = 32\,M_{x,y}/\pi d^3 \quad , \tag{5.17}$$

$$\tau_{max} = 16\,F_{x,y}/3\pi d^2 \quad . \tag{5.18}$$

Knowing that the nugget has a brittle structure, the maximum normal stress criterion was used as the fatigue damage parameter. Depending on whether the representative stress in the nugget or plate is higher, failure is predicted to happen in the corresponding mode. An advantage of Rupp's model is that not only the fatigue life, but also the mode of failure is predicted. A weak point of this model is that only resultant loads in nugget are considered and therefore the effect of self-equilibrating forces on structural stresses is missing. Also, it is assumed that the fatigue failure process is controlled by a measure of stress, which is not justifiable for cracked specimens and structures. Moreover, a reliable prediction of crack initiation location and life requires accounting for spot-weld edge notch radius which is suppressed in this method.

Sheppard et al. in 1992 [134] developed a model to predict fatigue crack initiation life for spot-welds based on the structural stress concept. The structural stress definition in this model only accounted for membrane load and bending moment. The structural stress range was obtained on neighboring elements of the spot-weld at the node shared with the spot-weld beam element on both sheets. Maximum structural stress range was converted to actual elastic-plastic stress and strain ranges at the spot-weld edge using Neuber's rule. The stress concentration factor was obtained using an equation developed by them for tensile-shear specimens. The Smith-Watson-Topper relationship

[135] was employed to find the fatigue initiation life in terms of actual stress and strain ranges. Sheppard in 1993 [19] extended the application of structural stress to include fatigue crack propagation. Considering only mode I effects, the SIF range was obtained in terms of structural stresses due to membrane load and bending moment. Paris' equation was employed to find fatigue crack propagation life from the maximum structural stress range. The structural stress relationship was later modified in 1996 to include the effect of forces normal to the sheet, *i.e.*, the "cupping force" [133]. Some common problems with structural stress-based models were resolved in this model. For instance, crack initiation and propagation phenomena were explicitly accounted for, and the mode I SIF was not assumed constant during crack propagation. However, the effects of modes II and III loading during crack propagation were ignored. There is no comprehensive formulation for calculating the stress concentration factor for spot-welds; this is a challenge in the application of Neuber's rule under a general load case. Furthermore, similar to other models based on the structural stress approach, effects of material anisotropy and yield asymmetry were not taken into account. This model is explained in more detail in section 5.2.2.

5.1.3 Local Strain Approach

Some studies, in contrast to the fracture mechanics approach, consider a spot-weld as a blunt notch with a finite radius. Therefore, a detailed FE model with a fine mesh at the vicinity of the spot-weld is required. A measure of local strain at the spot-weld edge is often assumed to control fatigue failure in this approach. Local stress/strain values are calculated from an elastic-plastic FE simulation, or from an elastic solution along with a variant of Neuber's rule [136]. An advantage of this approach is that the effect of the spot-weld notch is considered. Also, cyclic characteristics of materials, *e.g.*, anisotropy and hardening asymmetry, may be accounted for. On the other hand, crack propagation is not considered in local notch models. Moreover, complexities of FE model preparation, as well as

intensive FE calculations, restrict the applicability of this approach for real-life problems. The most commonly referenced models in this group have been developed by Oh [137] and Pan [20].

Oh in 1982 [137] obtained stress/strain results from a linear elastic FE analysis. The elastic solution in the region around the spot-weld nugget was then transferred to actual elastic-plastic results using Neuber's rule. The stress concentration factor in this model was calculated analytically based on a two dimensional representation of tensile-shear specimens. For the sake of simplicity, shear stress was assumed uniformly distributed over the nugget cross-section. Actual stress and strain values were then related to total fatigue life through Morrow's formulation [138]. A deficiency of this model is that the effect of coupon bending on stress concentration factor is neglected. Even with this simplification, the expression given for the stress concentration factor is only applicable to tensile-shear spot-welds.

Pan in 2000 [139] demonstrated that Sheppard's structural stress model was not successful for spot-welds between sheets with dissimilar thicknesses. Pan [20,139] proposed a local strain model for such cases. Local stress and strain values at the spot-weld edge were obtained directly from three-dimensional elastic-plastic FE simulations. Nonlinear geometry and material properties were included in the FE analyses. Because the HAZ of spot-welds contains gradients in material properties from the BM to FZ, this region was split into several subzones with corresponding nonlinear properties, if the information was available. The location where maximum principal strain occurred at the end of the first reversal was selected as the hot-spot. Cyclic principal strain range was considered as the fatigue damage parameter. The cyclic principal strain range was calculated as the difference between principal strain values at the end of the first and second reversals at the hot-spot. A shortcoming of this model is that it does not provide a reasonable description of crack propagation. However, a better correlation was achieved employing this model for spot-welds with dissimilar thicknesses than Sheppard's structural stress model [20]. An extended description of Pan's model is presented in section 5.2.3.

5.2 Fatigue Model Evaluation

One fatigue model from each category was selected to evaluate predictions for magnesium spot-welds. Swellam's fracture mechanics model was chosen for assessment because its applicability is not limited to any particular specimen geometry, in contrast to most fatigue models in this category. Sheppard's structural stress model was used since the assumption used in this model, *i.e.*, plate cracking rather than nugget cracking, better explains the fatigue failure in magnesium spot-welds. The notch model proposed by Pan was used as it directly and more accurately accounts for spot-weld notch effects, and the stress concentration factor is not required in this model. The selected models are explained in detail and assessed in the following sections.

5.2.1 Swellam's Model

5.2.1.1 Introduction

Swellam et al. in 1992 [18] proposed a fatigue model for predicting crack propagation life for spot-welds based on the fracture mechanics approach. In this model, the effects of modes I and II loading were taken into account. The spot-weld was considered under a general applied load, F, as shown in Figure 5.3.

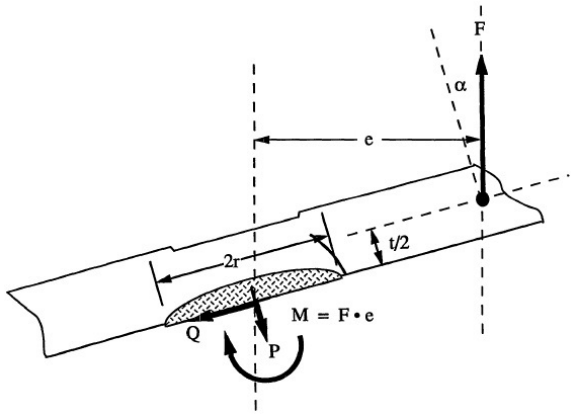

Figure 5.3: Resolving a general applied load, F, at the center of the spot-weld [18]

Resultant forces and moments, including axial load, P, shear load, Q, and bending moment, M, at the spot-weld center, were found from static equilibrium of a coupon. The stress intensity factors developed by Tada et al. [128] for two half spaces joined by a circular region were used in this study,

$$K_I = K_{axial} + K_{moment} = \frac{P}{2r\sqrt{\pi r}} + \frac{3M}{2r^2\sqrt{\pi r}} \quad , \tag{5.19}$$

$$K_{II} = K_{shear} = \frac{Q}{2r\sqrt{\pi r}} \quad , \tag{5.20}$$

where r is the nugget radius. The initial equivalent Mode I SIF, $K_{I_{eq}}$, was defined as

$$K_{I_{eq}} = \sqrt{K_I^2 + \beta K_{II}^2} \quad , \tag{5.21}$$

in which β is an empirical material constant, which reflects the material's sensitivity to mode II loading. Experimental results from two or more different spot-weld specimen configurations are required to obtain β. Some of the specimen sets must involve only the mode I SIF (such as cross-tension or coach-peel configurations), and some other specimens must reflect only the effect of mode II or a combination of modes I and II SIFs. The parameter β was found such that the best correlation was achieved for equivalent stress intensities, $K_{I_{eq}}$, when plotted versus the fatigue life for all specimen configurations.

A geometrical correction factor, G, was defined to incorporate the effects of specimen and nugget size

$$G = \sqrt{\frac{t^2 W}{r^3}\left(\frac{9t^2}{4r^2} + 1\right)} \quad , \tag{5.22}$$

where t is the sheet thickness, and W is the specimen width. To account for the effect of load ratio, R, the general stress intensity parameter, K_i, was defined as

$$K_i = \frac{K_{I_{eq}}}{G}\sqrt{1 - R} \quad . \tag{5.23}$$

5.2.1.2 Fatigue modeling of Mg spot-welds

Swellam's model was evaluated by predicting the fatigue life for TS and CT magnesium spot-welds. Taking advantage of the simple specimen geometry, resultant loads at the spot-weld center were determined from hand calculations. The graphs in Figure 5.4 illustrate the fatigue life prediction results for the five specimen sets introduced in chapter 3. Figure 5.4(a) displays Swellam's damage parameter versus fatigue life. This diagram represents how successful the *master curve* is in correlating the experimental data. The master curve is usually considered as a fitted line to coupon-level data points in the plot of damage parameter versus fatigue life. The master curve in this graph is a bilinear trend line to the data points on a log-log scale, and is represented with a dashed line. As depicted in Figure 5.4(a), Swellam's model is not able to appropriately correlate the CT and TS experimental results. It should be noted that, as proposed in this model, SIFs were obtained from resultant forces and moments at the center of the spot-weld. For CT specimens, the resultant bending moment, M, and the corresponding SIF, K_{moment} , are zero. Therefore, the effect of bending moment, which is dominant for CT specimens, is neglected in this model. Figure 5.4(b) illustrates the predicted versus experimental fatigue life for spot-welded specimens. Diagonal dashed lines in this figure represent the factor of 2 bound lines, which are often considered as the criterion for fatigue models assessment. Since most of the data points fall outside these bound lines, especially the points corresponding to CT specimens, this model offers a poor fatigue life prediction. The capability of fatigue models in predicting life is usually quantified using the correlation coefficient, R^2 ($0 \leq R^2 \leq 1$), which is only 0.53 for this model. The low correlation coefficient affirms the conclusion that Swellam's model in this original form fails to predict the fatigue life of CT spot-weld specimens.

Swellam et al. later tried to resolve this issue [205]. Explicit equations were derived for K_i in terms of external loads and geometrical dimensions for different specimen configurations. In particular, for CT specimens, the bending compensation from the two ends was simply neglected.

Rather, the summation of bending moments from both ends was considered as the net bending moment at the nugget center. Also, the geometrical correction factor in this study was

$$G = \sqrt{\frac{t^2 W}{r^3}\left(\frac{36t^2}{4r^2} + 1\right)} \quad , \tag{5.24}$$

which is not the same as that in the previous work. Moreover, the K_i equation was modified to

$$K_i = \frac{K_{I_{eq}}}{G}\,(1-R)^{0.85} \quad . \tag{5.25}$$

to better account for the load ratio. Suppressing the effect of coupon deformation, for tensile-shear specimens we have $P = 0$, $Q = F$, and $M = Ft/2$ which yields

$$K_i = \frac{F}{2t\sqrt{\pi W(36t^2+4r^2)}}\sqrt{9t^2 + 4\beta r^2}\,(1-R)^{0.85} \quad . \tag{5.26}$$

Cross-tension specimens may be represented by $P = F$, $Q = 0$, and $M = F.e$ where e is the effective width of the CT coupons, *i.e.*, the distance between the two loading points. Therefore,

$$K_i = \frac{F}{2t\sqrt{\pi W(36t^2+4r^2)}}(2r + 3e)\,(1-R)^{0.85} \quad . \tag{5.27}$$

The results obtained from the modified form of Swellam's model are shown in Figure 5.5. Comparing the original and modified forms of Swellam's model demonstrates a clear improvement in correlation coefficient, which is attributed to incorporating the bending effect in CT specimens.

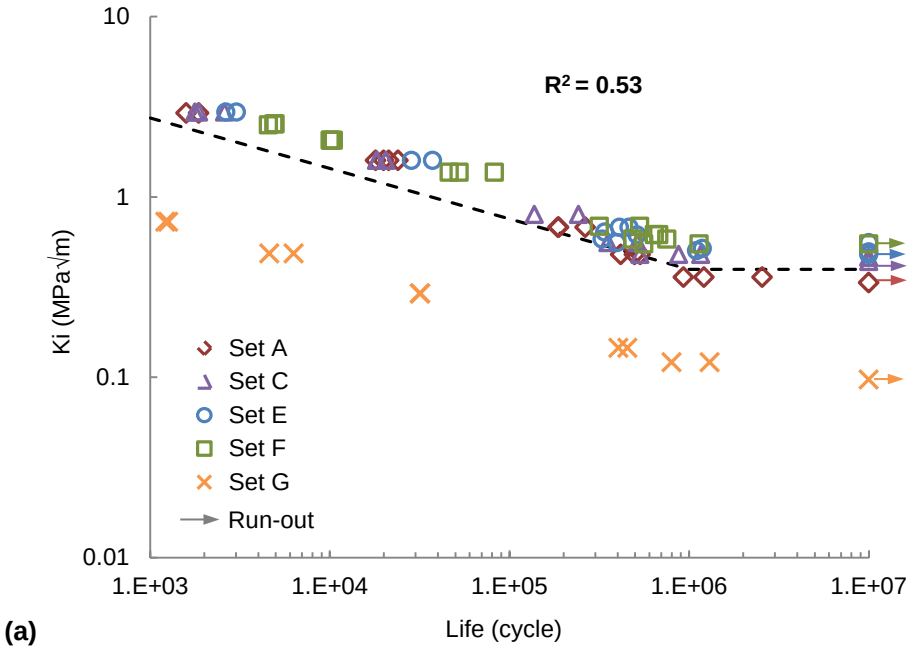

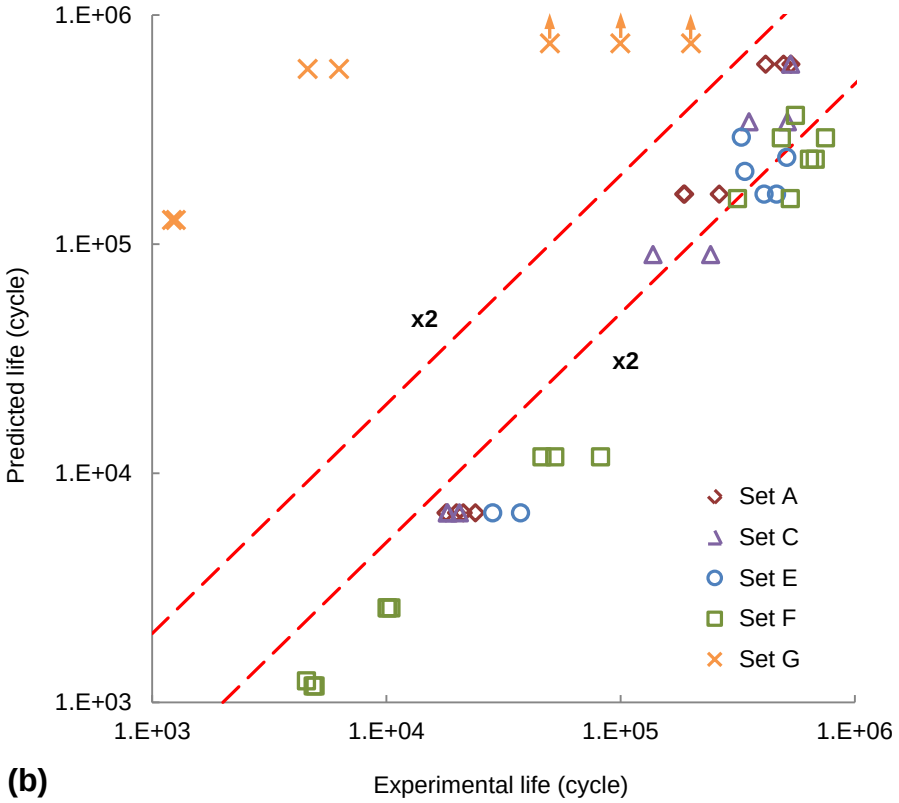

Figure 5.4: Original Swellam's model evaluation (a) stress intensity *vs.* fatigue life (b) predicted *vs.* experimental fatigue life

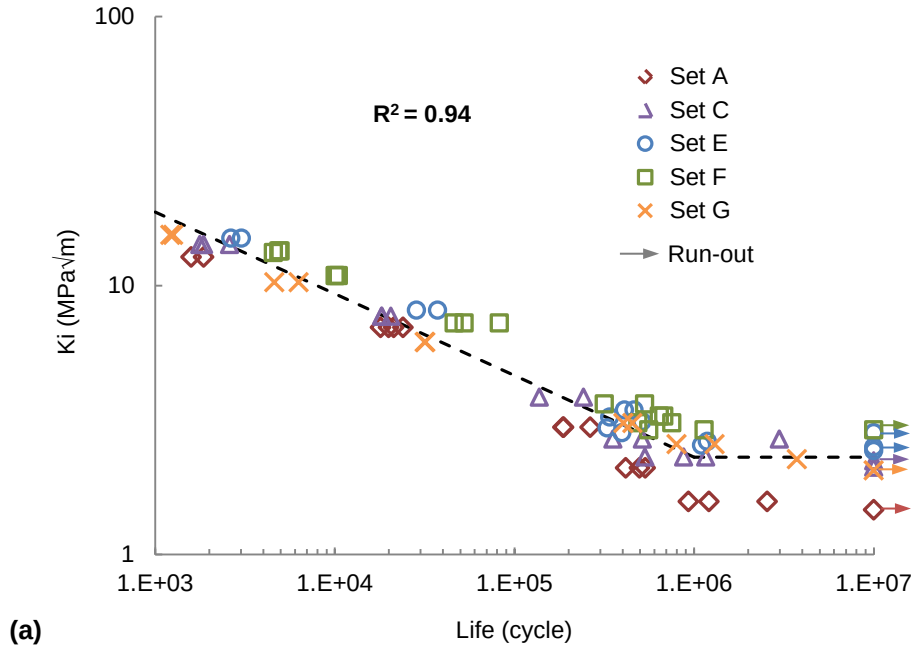

(a)

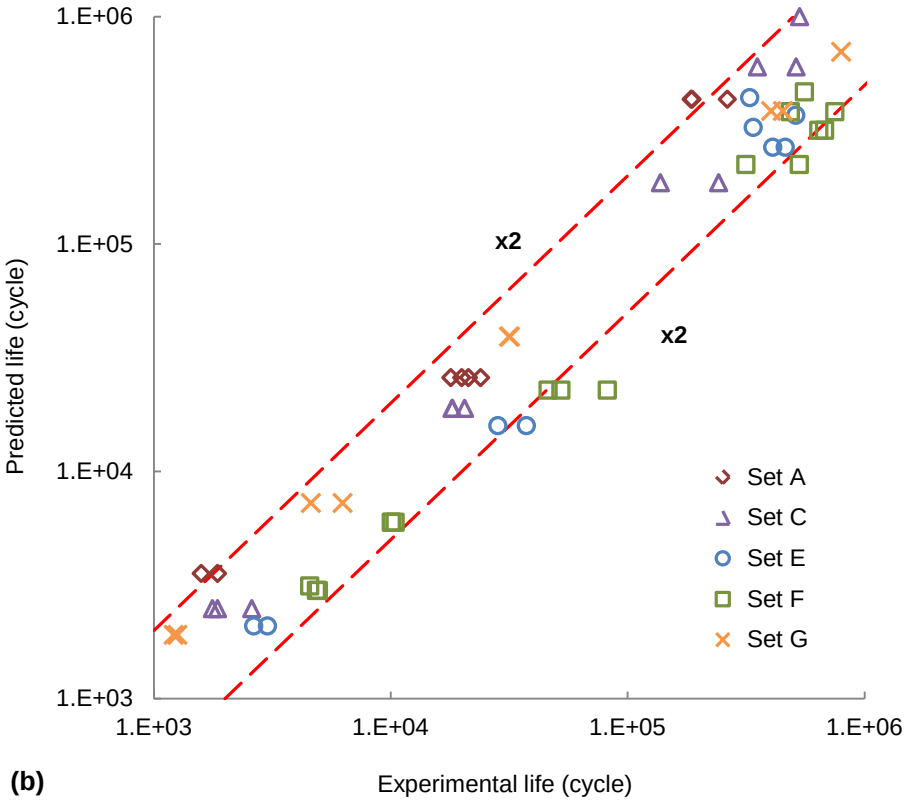

(b)

Figure 5.5: Modified Swellam's model evaluation (a) stress intensity vs. fatigue life (b) predicted vs. experimental fatigue life

5.2.2 Sheppard's Model

5.2.2.1 Introduction

Sheppard et al. in 1992 [134] developed a fatigue model for spot-welds based on the structural stress concept and assuming through-thickness cracking. Structural stress in this work was a function of membrane load and bending moment,

$$\Delta S_{ij} = \frac{\Delta P_{ij}}{\omega t_i} + 6\frac{\Delta M_{ij}}{t_i^2 W} \quad ; \quad i,j = 1, 2 \quad , \tag{5.28}$$

where ΔS_{ij} is the structural stress range, ΔP_{ij} and ΔM_{ij} are membrane load and bending moment ranges, respectively. ω is the effective coupon width and according to Wang et al. [206] was defined as $\pi d/3$, in which d is the nugget diameter. The subscript i represents the sheet (i =1 for the bottom sheet, and i =2 for the top sheet), and the subscript j represents the side (j =1 for the right side, and j =2 for the left side). Figure 5.6 illustrates the membrane forces and bending moments at the edges of a spot-weld.

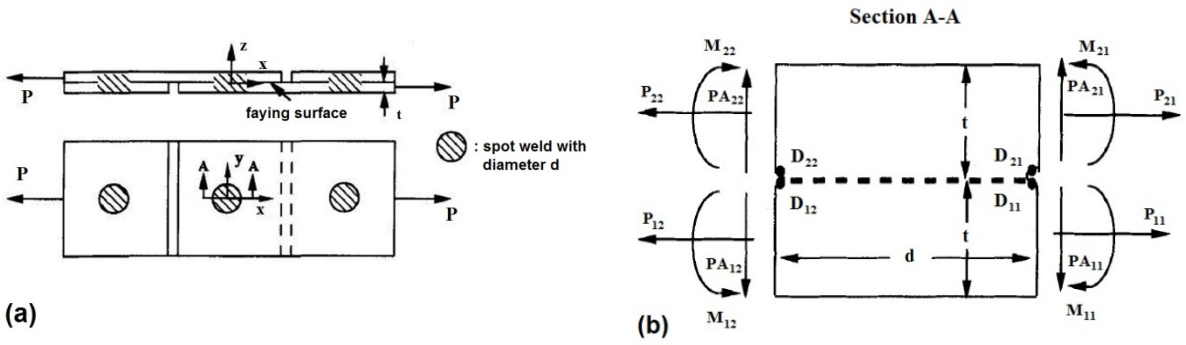

Figure 5.6: Forces and moments at a spot-weld nugget edge for Sheppard's structural stress calculation [134]

Forces and moments were determined from linear elastic FE simulations. As mentioned earlier, for FE models of spot-welds, sheets and spot-welds are modeled with shell and beam elements, respectively, to calculate the structural stress.

According to equation (5.28), four values were obtained for the structural stress range at each spot-weld. Maximum structural stress range,

$$\Delta S_{max} = max(\Delta S_{11}, \Delta S_{12}, \Delta S_{21}, \Delta S_{22}), \tag{5.29}$$

was used in Neuber's rule to estimate maximum local stress and strain ranges, *i.e.*, $\Delta\sigma_{max}$ and $\Delta\varepsilon_{max}$ (assuming cyclic Ramberg-Osgood behavior),

$$(K_f\ \Delta S_{max})^2/E\ =\ \Delta\sigma_{max}\ \Delta\varepsilon_{max}\quad , \tag{5.30}$$

$$\Delta\varepsilon_{max} = \Delta\sigma_{max}/E + 2(\Delta\sigma_{max}/2K')^{1/n'}\quad , \tag{5.31}$$

where K_f is the fatigue notch factor, E is the elastic modulus, K' is the cyclic strength coefficient, and n' is the cyclic strain hardening exponent. The effect of mean stress, σ_m, on the crack initiation process was accounted for in this model and was obtained from

$$\sigma_m\ = \sigma_{max} - 0.5\ \Delta\sigma_{max}\quad , \tag{5.32}$$

in which $\Delta\sigma_{max}$ was determined by solving equations (5.30) and (5.31), and σ_{max} was found from the following equations

$$(K_f\ \left[\max\left\{S_{ij_{peak}}\right\}\right] + \sigma_{rs})^2/E\ =\ \sigma_{max}\ \varepsilon_{max}\quad , \tag{5.33}$$

$$\varepsilon_{max} = \sigma_{max}/E + (\sigma_{max}/K)^{1/n}\quad , \tag{5.34}$$

where $S_{ij_{peak}} = \Delta S_{ij}/(1-R)$, R is the load ratio, σ_{rs} is the residual stress, K is the strength coefficient, and n is the strain hardening exponent. Crack initiation life and early growth, N_i, was found using the Smith-Watson-Topper's [135] formulation,

$$2N_i\ = \left[0.5\ \Delta\sigma_{max}/\left(\sigma_f' - \sigma_m\right)\right]^{1/b}\quad , \tag{5.35}$$

where σ_f' and b are the fatigue strength coefficient and fatigue strength exponent, respectively. σ_f' and b are material properties which theoretically correspond to the region where crack initiation occurs.

Residual stress, σ_{rs}, in the as-welded condition was assumed to be equal to the yield strength in the crack initiation region. The stress concentration factors reported by Radaj [207] and Kuang et al. [208] for tensile-shear specimens were adopted with an adjustment due to a different nominal stress definition.

Sheppard in 1993 [19] employed the structural stress concept to model crack propagation. The structural stress definition from equation (5.28) was utilized to find the SIF range,

$$\Delta K = \Delta K_T + \Delta K_B = f_1 \Delta S_T (\pi a)^{0.5} + f_2 \Delta S_B (\pi a)^{0.5} = f_1 \frac{\Delta P}{\omega t} (\pi a)^{0.5} + 6 f_2 \frac{\Delta M}{t^2 W} (\pi a)^{0.5} \quad , \tag{5.36}$$

where ΔK_T and ΔK_B are mode I SIF ranges for membrane force and bending moment, respectively. The crack depth is a, and f_1 and f_2 are geometry factors for membrane force and bending moment, respectively. ΔP and ΔM correspond to the maximum structural stress range, ΔS_{max}. Geometry factors were assumed to increase with crack growth according to

$$f_1 = c_1 + c_2 (a/t)^2 + c_3 (a/t)^4 \quad , \tag{5.37}$$

$$f_2 = c_4 + c_5 (a/t)^2 + c_6 (a/t)^4 \quad . \tag{5.38}$$

Coefficients in the above equations are constant and were estimated assuming a semi-elliptical crack propagating through the plate thickness, with a crack aspect ratio, a/c, between 0.33 and 1. Figure 5.7 displays a and c parameters for the semi-elliptical crack.

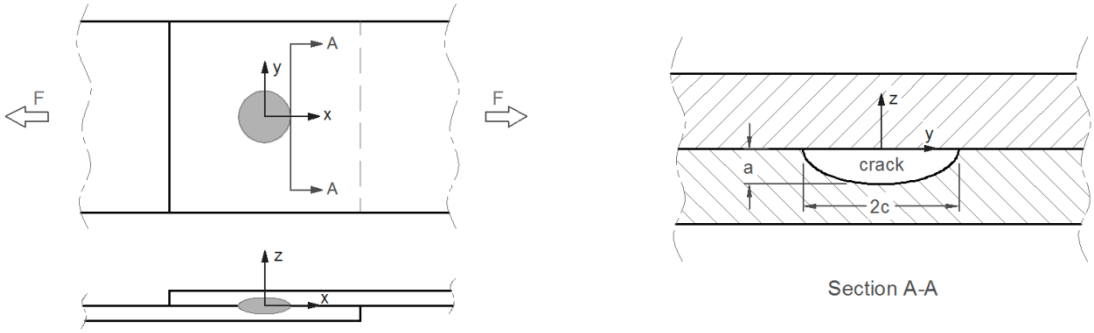

Figure 5.7: Illustration of semi-elliptical crack at the nugget edge [19]

Initial and final crack sizes were assumed to be a_i = 0.25 mm and $a_f = t$, respectively. Therefore, the relationship to find crack propagation life through Paris' equation was simplified to

$$N_p = \int_{a_i}^{a_f} \frac{da}{C(\Delta K)^m} = A_2(\Delta S_{max})^{-m} \tag{5.39}$$

where A_2 and m are material constants.

The structural stress definition was revised in 1996 [133] to modify the bending term and account for the axial force ΔP_{Ai}, as shown in Figure 5.6,

$$\Delta S_{ij} = \frac{\Delta P_{ij}}{\omega t_i} + 6\frac{\Delta M_{ij}^*}{t_i^2 W} + \frac{\Delta P_{Ai}}{t_i^2} \quad ; \quad i,j = 1, 2 \quad , \tag{5.40}$$

where ΔP_{Ai} is the axial or "cupping" force range, and ΔM_{ij}^* is the bending moment range, which was defined based on the difference between bending moments on opposite sides of the spot-weld. The moment, M^*, for bending along edge 1 according to Figure 5.8 was

$$M^* = (M_{4x} + M_{2x}) - (M_{3x} + M_{1x}) \quad . \tag{5.41}$$

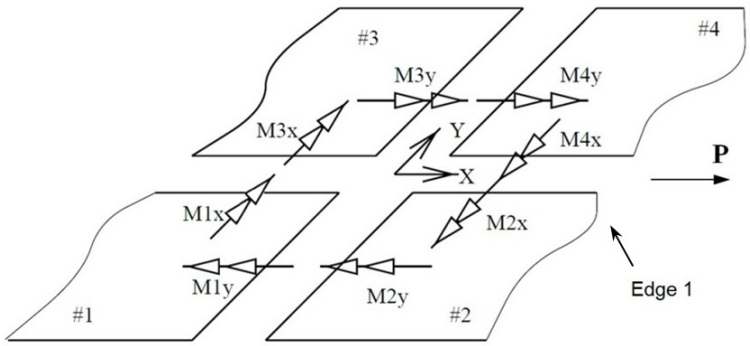

Figure 5.8: bending moments in elements surrounding the spot-weld in one sheet [209]

The bending and axial terms in the structural stress equation were further modified by Sheppard et al. in 2000 [209] to

$$\Delta S_{ij} = \frac{\Delta P_{ij}}{\omega t_i} + 6\frac{\Delta \widehat{M}_{ij}^*}{t_i^2 W} + 1.2\frac{\Delta P_{Ai}}{t_i^2} \quad ; \quad i,j = 1, 2 \quad . \tag{5.42}$$

The bending moment in this model was defined as

$$\widehat{M}^{*} = (M_{4x} + M_{2x}) - M_{avg} \quad , \tag{5.43}$$

where M_{avg} is the average of all positive nodal moments at elements adjacent to the spot-weld. The moments causing tension at the interface are considered as positive moments. Compared to equation (5.40), another refinement in this model is the change in coefficient for the axial stress from 1 to 1.2. This modification was made to account for the effect of boundary conditions on axial stress according to Young and Budynas [164]. This coefficient was found for the magnesium spot-welds investigated in the current study, and the values are listed in Table 5.1.

Table 5.1: axial stress coefficient in the Sheppard's model for magnesium spot-weld specimens

	Set A	Set C	Set E	Set F	Set G
Axial stress coefficient	1.20	1.05	0.95	1.13	1.40

In addition to deficiencies already mentioned in section 1.1.1, some further disadvantages restrict applicability of this model. The specimen width parameter, W, in the structural stress equation is not readily transferable to general applications, and determining this parameter requires some extra assumptions. Moreover, this model is able to explain only through-thickness cracking which is dominant mode of failure for magnesium spot-welds in moderate and high cycle regimes. However, experimental results on magnesium spot-welds (chapter 3) show that nugget failure is the predominant mode of failure in the LCF regime.

5.2.2.2 FE modeling

The loads and moments in the vicinity of spot-welds (ΔP_{ij}, ΔP_{Ai}, $\Delta \widehat{M}_{ij}^{*}$) in the current study were obtained through FE simulations. These variables are stored in nodal force (NFORC) output variables in ABAQUS 6.10 software. Note that the default setting for averaging element output at nodes has to be deactivated, so that the contribution of each element is represented correctly.

The sheets in Sheppard's model were represented with four-node linear shell elements, and the spot-weld was modeled with a two-node linear beam element. Similar to other structural stress approaches, elastic material properties are used in Sheppard's model; E=43 GPa and ν=0.35 for AZ31B-H24 magnesium alloy. Nonlinear geometry is recommended for a correct failure location prediction [139]. The FE models and boundary conditions for tensile-shear and cross-tension specimens are illustrated in Figure 5.9.

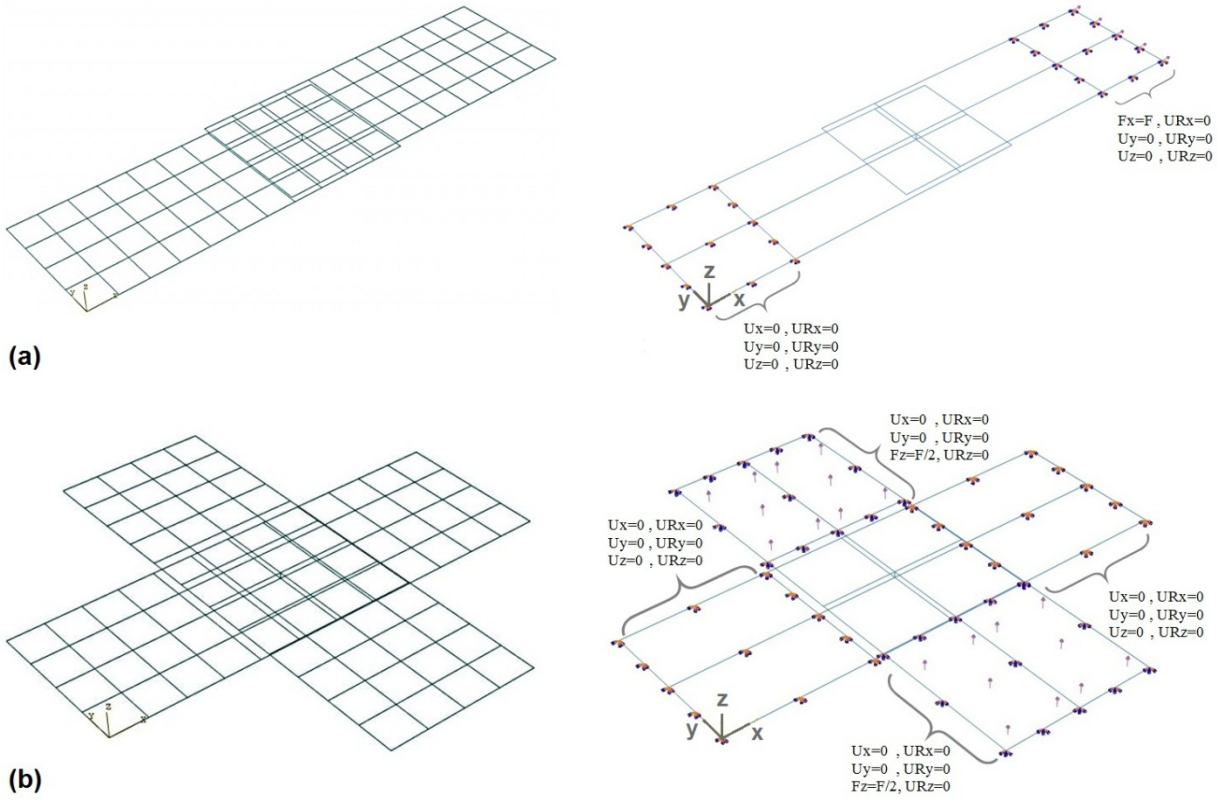

Figure 5.9: FE model of spot-weld specimens for Sheppard's model (a) TS specimen (b) CT specimen

5.2.2.3 Fatigue modeling of Mg spot-welds

Fatigue crack initiation life was not calculated for this model in this research because the stress concentration factor associated with Sheppard's nominal structural stress is not readily available for CT specimens. Therefore, only the crack propagation life results are presented in this section.

The maximum structural stress range for all experimental data points was calculated using the FE simulation results. The structural stress range was calculated employing equation (5.42) and using a coefficient for the axial stress term according to Table 5.1. Figure 5.10(a) displays results in terms of maximum structural stress range versus fatigue life. Because of a knee at about 10^6 cycles, a bilinear trend line was fitted on a log-log scale. This graph shows that Sheppard's model was successful in correlating experimental results from different specimen sets, with R^2=0.95. However, data points corresponding to the cross-tension specimens (set G) are shifted from the master curve, and the fatigue life is under-predicted. Figure 5.10(b) illustrates predicted versus experimental fatigue life utilizing Sheppard's model. This figure shows that almost all experimental data points corresponding to tensile-shear specimens (sets A-F) are located within the factor of 2 bound lines, while points for cross-tension specimens are outside these bound lines.

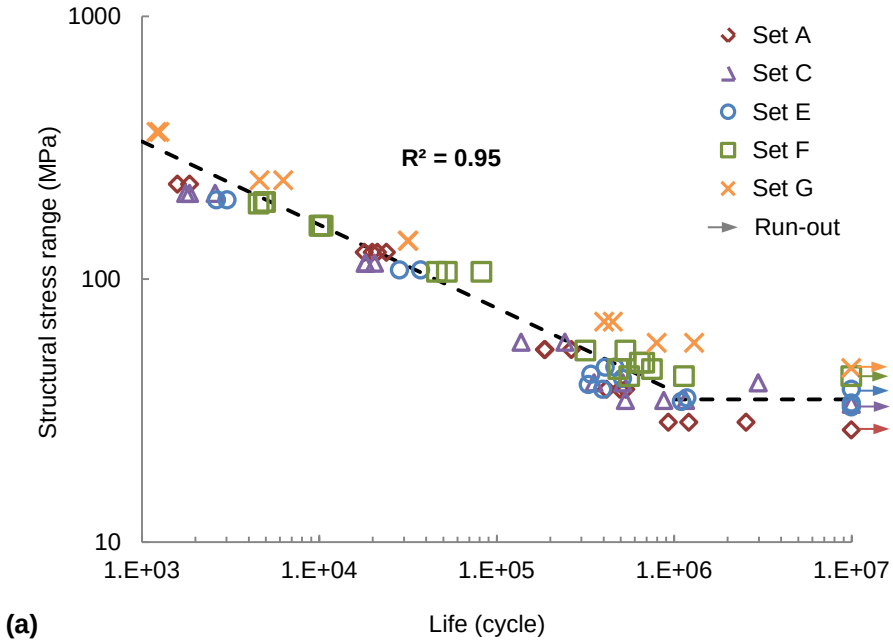

(a)

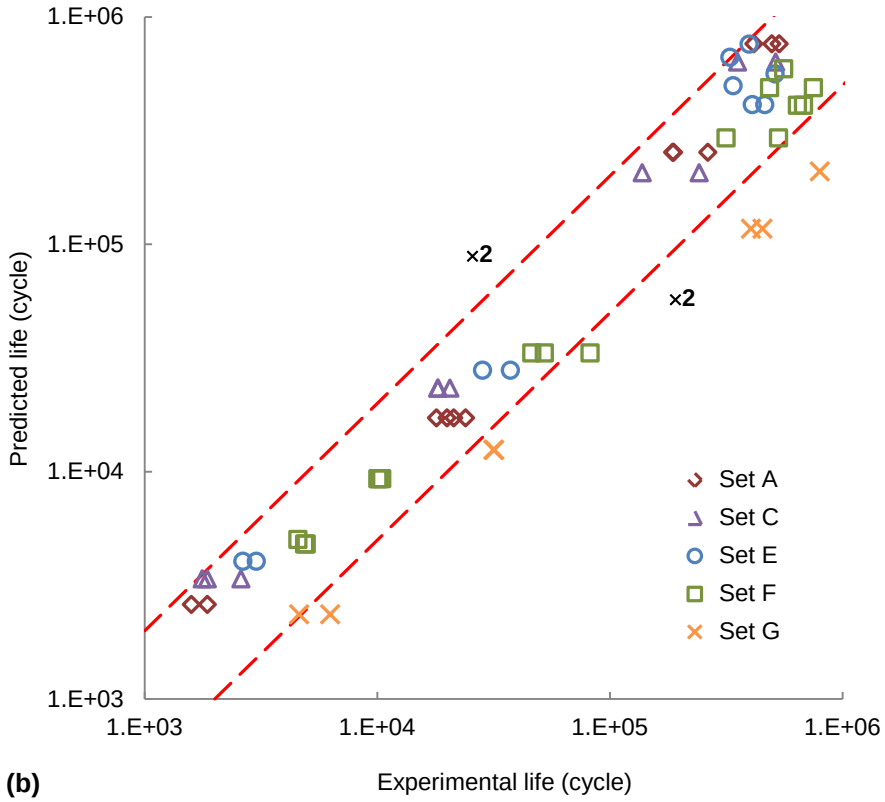

(b)

Figure 5.10: Sheppard's model evaluation (a) structural stress range *vs.* fatigue life (b) predicted *vs.* experimental fatigue life

5.2.3 Pan's Model

5.2.3.1 Introduction

Pan in 2000 [139] showed that Sheppard's model is capable of successfully predicting fatigue life of steel spot-welds, as long as the sheets being welded have the same thickness, but that the model fails for dissimilar thicknesses. To tackle this problem, Pan in 2002 [20] proposed a model based on the local strain approach. A detailed FE model of spot-weld specimens with a nominal radius at the nugget edge was employed in this model. The nominal radius was selected according to experimental observations of spot-weld cross-sections, Figure 5.1. The maximum principal strain range at the hot spot was used as the fatigue damage parameter. The hot spot was identified as the location with the maximum local principal strain at the end of the first reversal. Maximum principal strain range, according to Pan [20], is the difference in the principal strain at the end of the loading and unloading reversals.

5.2.3.2 FE modeling

Pan's model, similar to other local approaches, requires a detailed FE model to obtain a realistic approximation of stress and strain values at the hot spot. The FE model included details of the nugget root radius, which was found from experimental observation. The notch radius was obtained by sectioning spot-welds, and measuring the distance between the two sheets in the vicinity of the nugget. The notch radius in Pan's work was 0.076 mm for steel spot-welds [20]. Measurements indicate that the average notch radius for magnesium spot-welds in the current work is 0.10 mm, Figure 5.1(b).

The current FE model for a TS specimen is shown in Figure 5.11(a). Half of the tensile-shear specimen was modeled, taking advantage of a plane of symmetry. Eight-node linear brick elements with reduced integration were used in this model. Elastic properties of magnesium (E=43 GPa and

ν=0.35), along with the tensile stabilized cyclic stress-strain curve for AZ31B-H24 were used. The same material properties were assigned to the BM and the weld area, *i.e.*, HAZ and FZ, due to lack of suitable mechanical properties for the weld region. Moreover, the work by Pan [139] on HSLA steel showed that nonhomogeneous material properties had a minimal effect on principal strain distribution, nor on the hot spot location. The Mises criterion was employed as the yield function and kinematic hardening was used to represent the Bauschinger effect. Figure 5.11(b) illustrates the boundary conditions at the two ends, and on the plane of symmetry. All degrees of freedom (DOFs) were fixed in one end, and the other end was only free to move in the x-direction. The z-symmetry condition (Uz=0, URx=0, and URy=0) was applied to the plane of symmetry. Half of the load that was applied in the experiments was exerted due to the half model. Simulations were run for three steps to simulate three consecutive reversals, *i.e.*, loading, unloading, and reloading, while considering the effect of nonlinear geometry. The principal strain ranges at the hot spot were calculated for available experimental loads.

Figure 5.12(a) displays the FE model for a quarter CT specimen, which used two planes of symmetry. The notch radius, element type, and material properties were the same as the TS specimen model. The boundary conditions on the CT specimens, as illustrated in Figure 5.12(b), were applied such that the experimental conditions were simulated. All DOFs on one sheet were fixed within the gripping distance, and on the other sheet the translational DOF normal to the sheet was free, and the other DOFs were fixed. A quarter of the experimental load was applied uniformly on the moving end of the specimen, due to the quarter model. Two different symmetry boundary conditions (x-symmetry, and z-symmetry) were applied to the symmetry planes. Similar to the TS model, three loading steps were run for CT specimens to simulate one cycle. The results for Pan's model are presented and discussed in the next section.

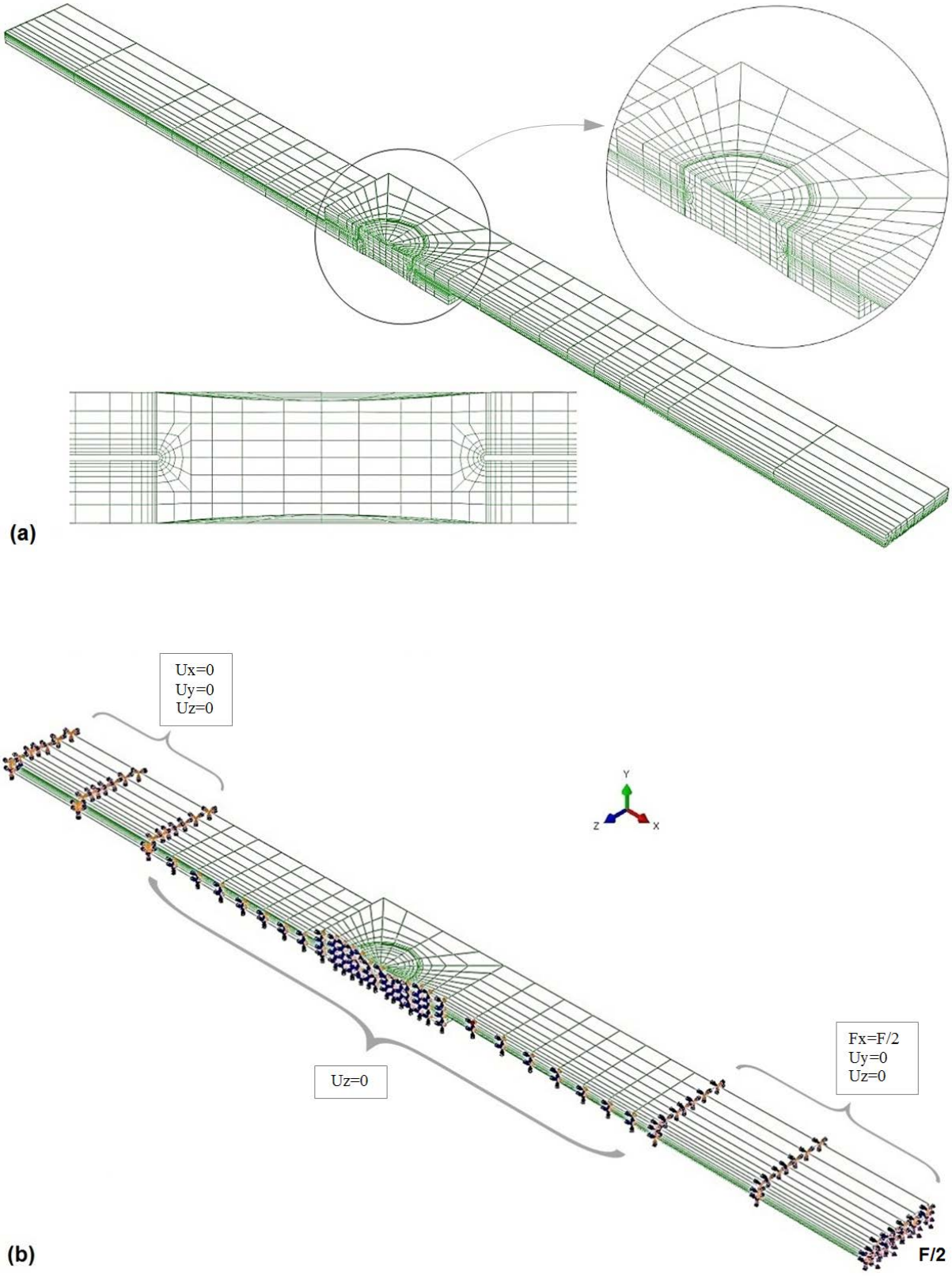

Figure 5.11: FE model of a TS specimen for Pan's model (a) FE model details (b) boundary conditions

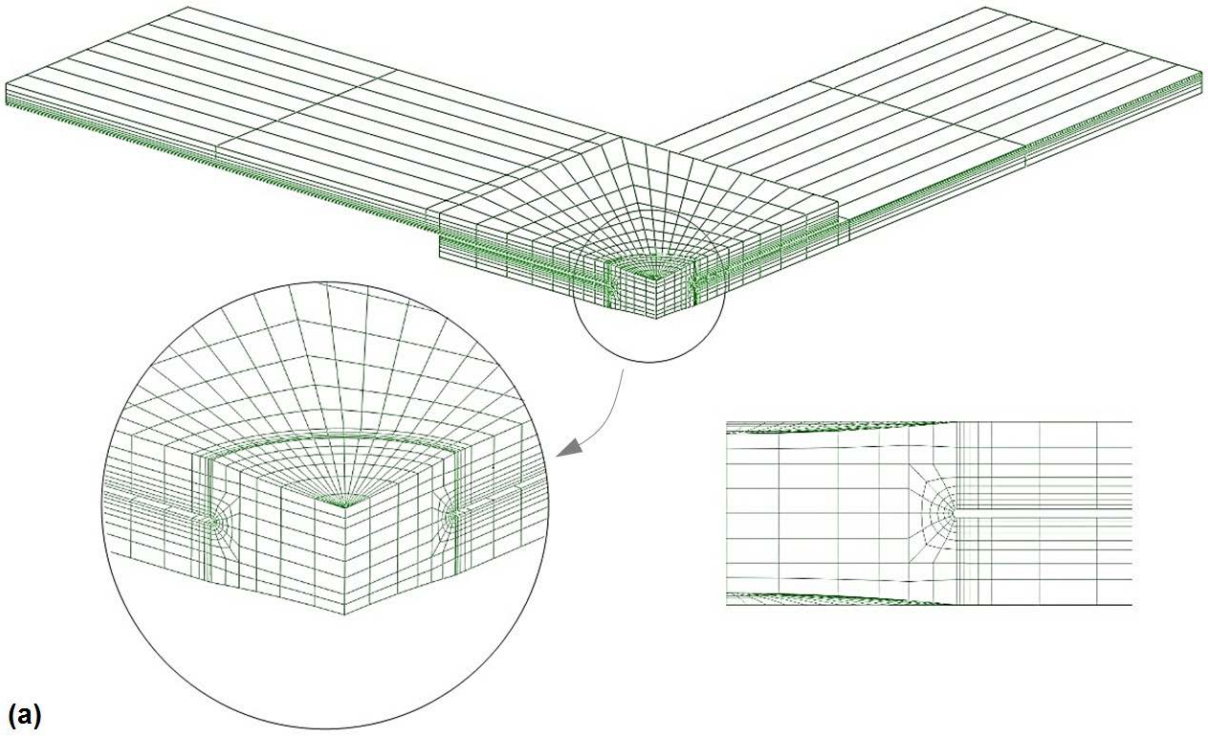

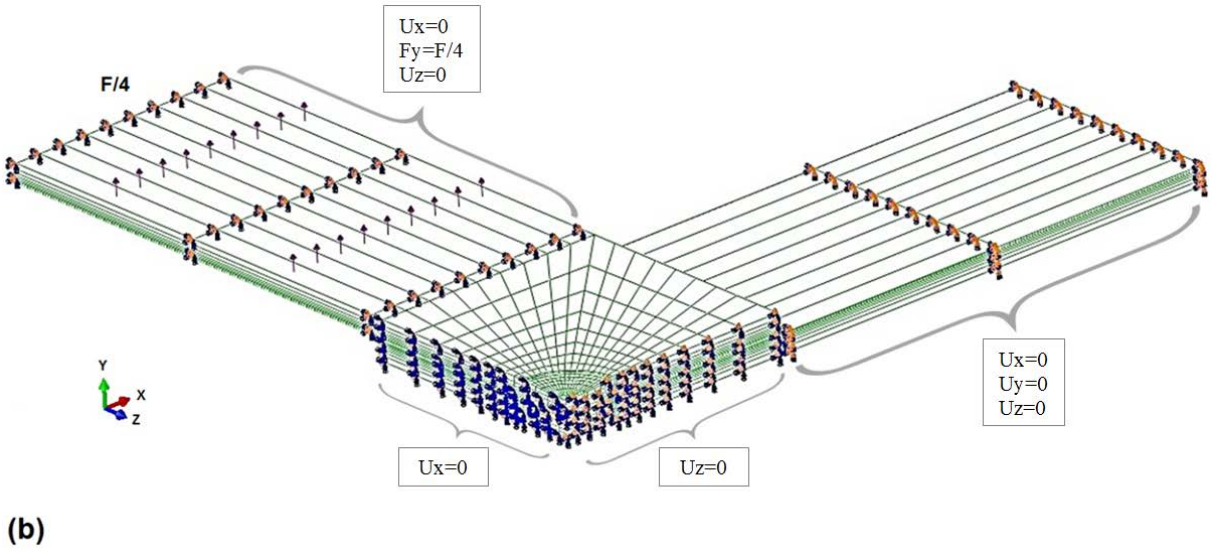

Figure 5.12: FE model of a CT specimen for Pan's model (a) FE model details (b) boundary conditions

5.2.3.3 Fatigue modeling of Mg spot-welds

The maximum principal strain range at the hot spot was obtained from FE simulation for all experimental data points. The principal strain range values were plotted versus fatigue life to obtain the master curve, Figure 5.13(a). Similar to Sheppard's model, a bilinear trend line was fitted to the data points, as a result of the sharp bend at a life of 10^6 cycles. This chart indicates that Pan's model is very successful in consolidating the experimental results for different specimen sets, with R^2=0.97. This figure also shows that the master curve after the knee rapidly tends to the endurance limit. Furthermore, it can be concluded that Pan's model is capable of providing a good correlation between the CT data points (set G) and the TS data points (sets A-F), in contrast to Swellam's and Sheppard's models. Figure 5.13(b) illustrates that almost all experimental data points, including the CT specimens, are located within the factor of 2 bound lines.

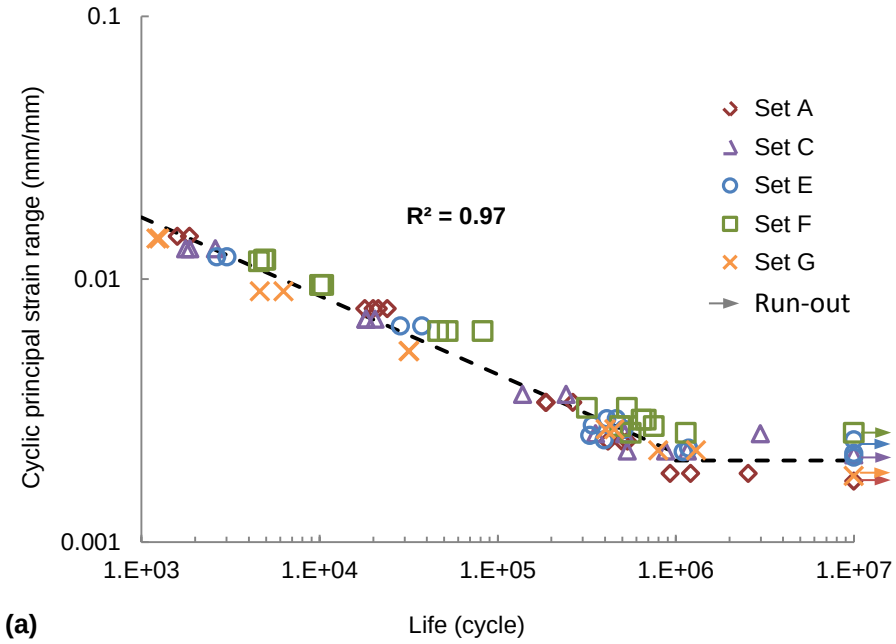

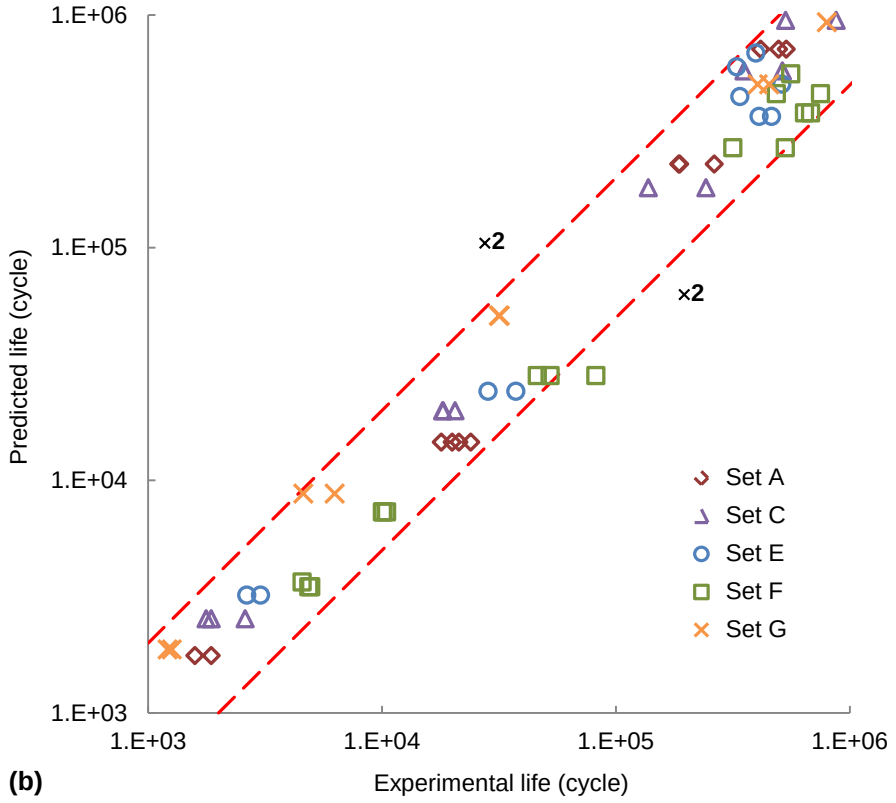

Figure 5.13: Pan's model evaluation (a) cyclic principal strain range *vs.* fatigue life (b) predicted *vs.* experimental fatigue life

5.2.4 Proposed modified Pan's Model

5.2.4.1 Introduction

As described in section 5.2.3, the Pan's original model uses the Mises yield function along with the kinematic hardening rule to simulate material behavior. Therefore, application of this model is only justifiable for materials with symmetric tension-compression hardening behavior, *e.g.*, steel and aluminum. HCP metals such as magnesium and titanium, which exhibit asymmetric hardening behavior, may not be modeled properly employing regular material models, as explained in chapter 4. To resolve this problem, Pan's model was re-applied using the UMAT developed herein (incorporating the Cazacu-Barlat yield function and combined isotropic-kinematic hardening rule), instead of the built-in Abaqus material model. The same FE models, loading steps, and boundary conditions as the original Pan's model were used to assess the modified Pan's model.

5.2.4.2 Fatigue modeling of Mg spot-welds

Figure 5.14(a) shows the maximum principal strain range at the hot spot versus fatigue life obtained utilizing the modified Pan's model. This graph demonstrates that, just like the original Pan's model, the modified form of this model is quite successful in correlating the experimental data points for different specimen sets, with R^2=0.97. Figure 5.14(b) illustrates that almost all the experimental data points, including those for CT specimens, are located within the factor of 2 bound lines. Comparing Figure 5.13 and Figure 5.14 reveals that incorporating asymmetric hardening behavior of magnesium did not improve the fatigue life prediction of magnesium spot-welds. This is attributed to a lack of comprehensive experimental data on spot-weld specimens; more various configurations of spot-weld specimens can make the contrast more obvious.

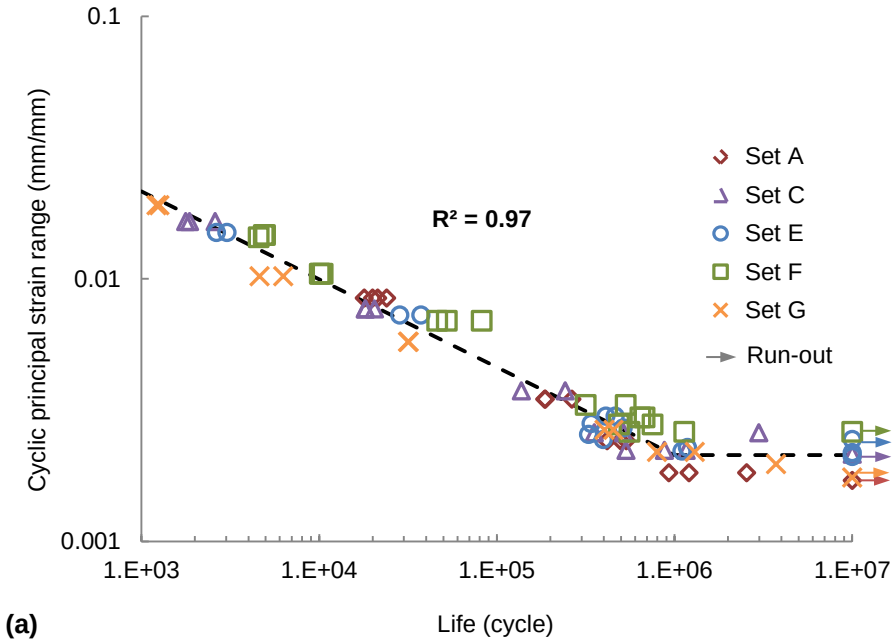

(a)

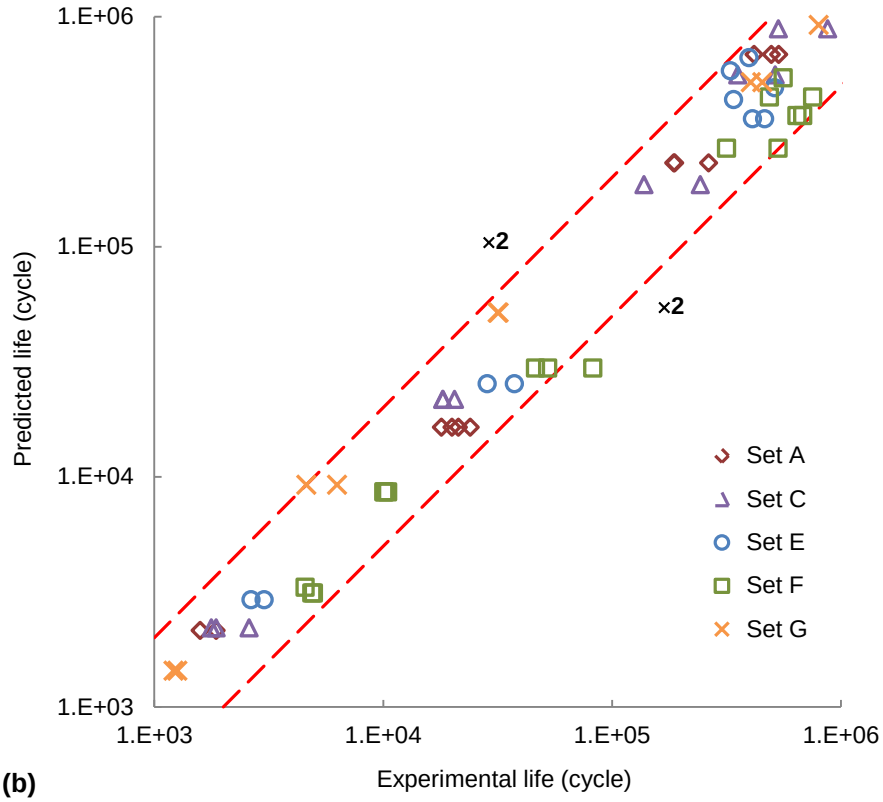

(b)

Figure 5.14: Modified Pan's model evaluation (a) cyclic principal strain range *vs.* fatigue life (b) predicted *vs.* experimental fatigue life

Also, shape of the hysteresis loops at the hot spot can contribute to the insignificant improvement. Figure 5.15(a) and Figure 5.15(b) present the stress-strain hysteresis response at the hot spot obtained from the symmetric and asymmetric hardening models, respectively. These graphs correspond to an experiment where a large load of 2000N was applied to a TS specimen. However, in the course of unloading and reloading reversals, no plastic deformation was predicted using the symmetric hardening model, and only a small hysteresis was predicted using the asymmetric material model. The reason for the minimal plasticity during unloading and reloading reversals is the positive R-ratio of 0.2, which is required for this specimen configuration to avoid buckling. Negative R-ratios, if possible, could make the difference clearer.

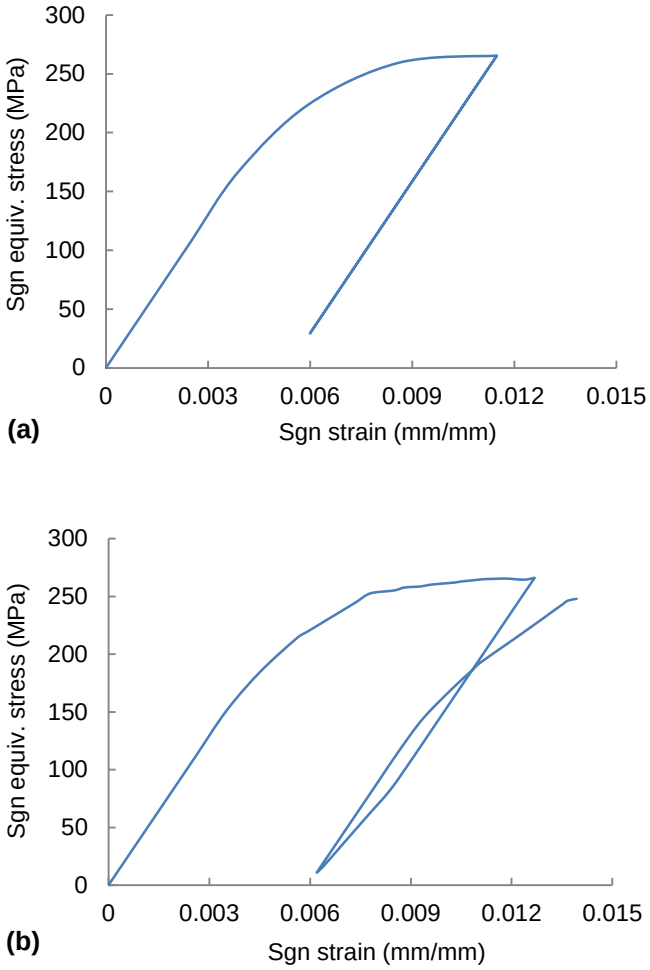

Figure 5.15: Stress-strain hysteresis response at the hot spot for a specimen set C under 2000N (a) symmetric material model (b) asymmetric material model (UMAT)

In other words, this figure demonstrates that available experimental data do not provide a situation where significant twinning/untwinning deformations occur. Therefore, the effect of asymmetric hardening behavior is not significant in the stress-strain response. Consequently, the contrast between the original and modified Pan's models is not obvious in terms of the fatigue life estimation.

Figure 5.16 illustrates the difference between symmetric and asymmetric hardening models under uniaxial fully-reversed strain-control condition, R=-1 and $\varepsilon_{amp} = 0.02$. The symmetric hardening model is kinematic hardening, and the asymmetric hardening model is the UMAT developed in the current study. Figure 5.16 shows that the symmetric material model does not follow the experimental hardening curves, and stress range and especially the hysteresis energy are significantly overestimated. The asymmetric hardening model (UMAT) closely follows the actual material behavior.

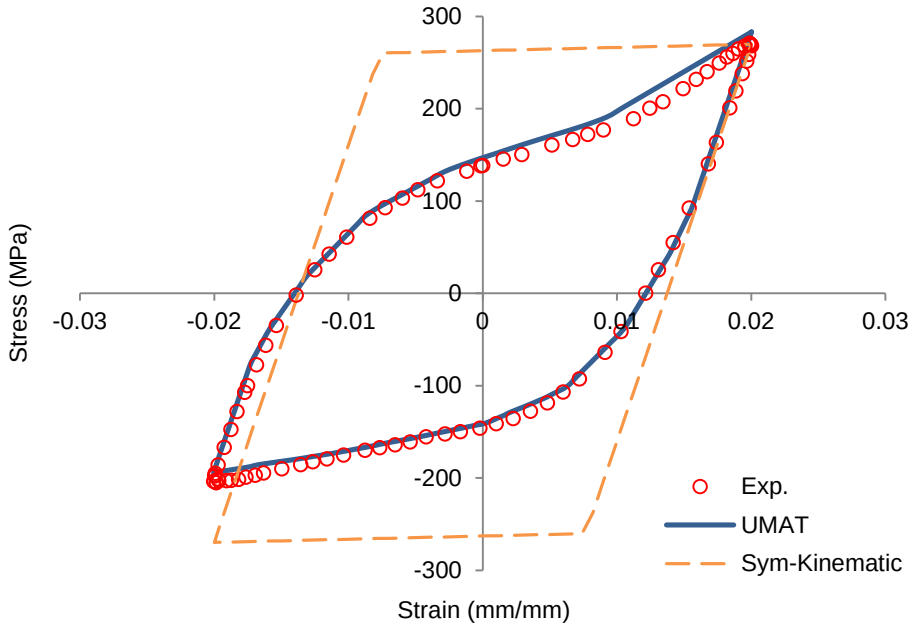

Figure 5.16: Effect of hardening model on the predicted material's behavior under a fully-reversed strain-control condition

5.3 Proposed Model

A number of commonly used fatigue models were evaluated in this chapter utilizing experimental data on magnesium spot-weld specimens. Some of these models were successful in generating a well-correlated master curve, at the coupon level. However, magnesium structure testing and simulation (see chapter 6) revealed that regular fatigue models, which do not account for asymmetric hardening behavior, are not able to predict the fatigue life nor the failure location. An energy-based fatigue model is proposed in this section which employs the asymmetric material model developed in chapter 4. The advantage of energy-based fatigue models over stress- and strain-based models is that energy is a scalar quantity. Therefore, the energy values corresponding to different axial and shear components of stress and strain tensors can be simply manipulated without the concern of dissimilar nature or direction. This approach has been applied to symmetric [210,211] and asymmetric [169,212,213] materials, and its accuracy has been verified. In the current research, an energy-based model is proposed for estimating the location and the life associated with fatigue crack initiation, rather than crack propagation or total fatigue failure process. This is because local stress/strain results at the hot spot are utilized for strain energy calculation. The propagation phase of the fatigue failure should be modeled using a fracture mechanics based model; this will be pursued as an extension to the current study.

5.3.1 Total Energy Model

5.3.1.1 Introduction

The material model which follows the actual behavior of wrought magnesium alloys is a requirement to obtain a realistic estimation of energy density. Energy density, as the damage parameter in the proposed model, includes the plastic energy density. The plastic energy dissipates in each cycle as a result of plastic deformation. To take the effect of mean stress into account, positive

elastic energy density is added to the plastic energy density. Moreover, the positive elastic energy term helps to distinguish the data points in the high cycle regime. To obtain the energy densities, a detailed FE model of the spot-weld specimen (the same as the one used in Pan's model) was utilized and the UMAT was linked to the simulation through the material properties. Because the stabilized cyclic behavior of magnesium was incorporated in the UMAT, and for the sake of minimizing computation time, the FE simulation was run for three reversals only, *i.e.*, loading, unloading, and reloading. Figure 5.17(a) schematically displays the signed equivalent (Cazacu-Barlat) stress versus signed total strain behavior at the spot-weld edge in the first three reversals. Signed equivalent stress and signed total strain were defined in chapter 4.

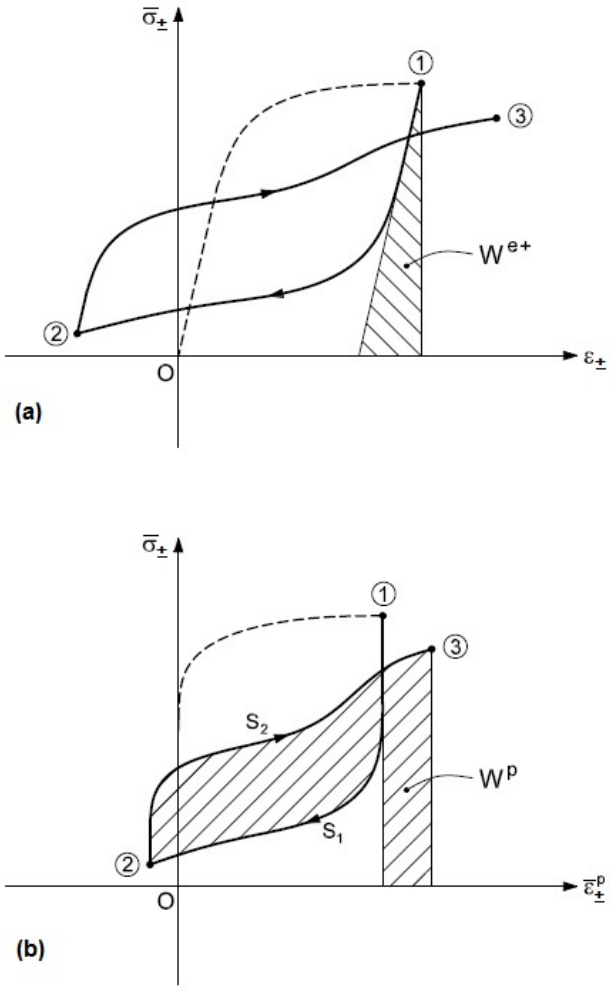

Figure 5.17: Schematic illustration of (a) positive elastic energy density and (b) plastic energy density

As depicted in this figure, the stress-strain response may constitute a non-closing hysteresis loop. The positive elastic energy density, W^{e+}, is defined as

$$W^{e+} = \frac{1}{2}\bar{\sigma}_{\pm①}\varepsilon^{e}_{\pm①} = \bar{\sigma}^{2}_{\pm①}/2E \quad , \tag{5.44}$$

where $\bar{\sigma}_{\pm①}$ and $\varepsilon^{e}_{\pm①}$ are signed equivalent stress and signed elastic strain at the end of the first reversal, respectively.

The plastic strain energy density accumulated in the unloading (S_1) and reloading (S_2) reversals is considered as the plastic energy density.

$$W^{p} = \int_{S_1} \bar{\sigma}_{\pm}\, d\bar{\varepsilon}^{p}_{\pm} + \int_{S_2} \bar{\sigma}_{\pm}\, d\bar{\varepsilon}^{p}_{\pm} \tag{5.45}$$

The hatched area in Figure 5.17(b) represents the plastic energy density, W^{p}. Note that Figure 5.17(b) is a plot of signed equivalent stress versus signed equivalent plastic strain.

Total energy density, which is the damage parameter, is the summation of the plastic energy and the positive elastic energy densities at the hot spot,

$$W^{t} = W^{e+} + W^{p} \quad . \tag{5.46}$$

The location with maximum signed equivalent plastic strain at the end of the first reversal is considered as the hot spot.

5.3.1.2 Fatigue modeling of Mg spot-welds

Total energy density, as defined in equation (5.46), was obtained at the spot-weld nugget edge from FE simulations for applied loads corresponding to the available experimental data points, chapter 3. The material model proposed in chapter 4 was employed to account for the asymmetric cyclic hardening behavior. The results obtained for total energy density were plotted with respect to crack initiation life, rather than the total fatigue life, as this model is intended to predict the fatigue crack initiation life. The definition of the crack initiation in this research, as well as the experimental results for crack initiation life, was presented in chapter 3. The total energy density if plotted against crack initiation life shows a knee at about an initiation life of 10^6 cycles, Figure 5.18(a). This graph indicates that the proposed model is successful in correlating experimental results for different specimen sets, with an R^2=0.96. Figure 5.18(b) illustrates that almost all experimental data points, including CT specimens, are located within the factor of 2 bound lines. However, the initiation life for CT specimens is slightly overestimated. This can be attributed to the criterion adopted for crack initiation, which has not been verified for CT specimens. Therefore, it can be concluded that the energy model is able to correlate the CT data points (set G) with TS data points (sets A-F). Comparing the R-squared value obtained from the energy method and the methods utilizing symmetric properties (Sheppard's and Pan's model) shows that incorporating the complex cyclic behavior of wrought magnesium alloys did not result in an improvement in the (initiation) life prediction. This implication, as stated in the section 5.2.4.2, is attributed to the lack of comprehensive experimental data on spot-welded specimens.

To demonstrate the contrast between symmetric and asymmetric material models, an automotive structure was simulated using the proposed model. The results were compared with experimental measurements as well as a simulation based on symmetric hardening model. The details about the structure and the simulations are presented in chapter 6.

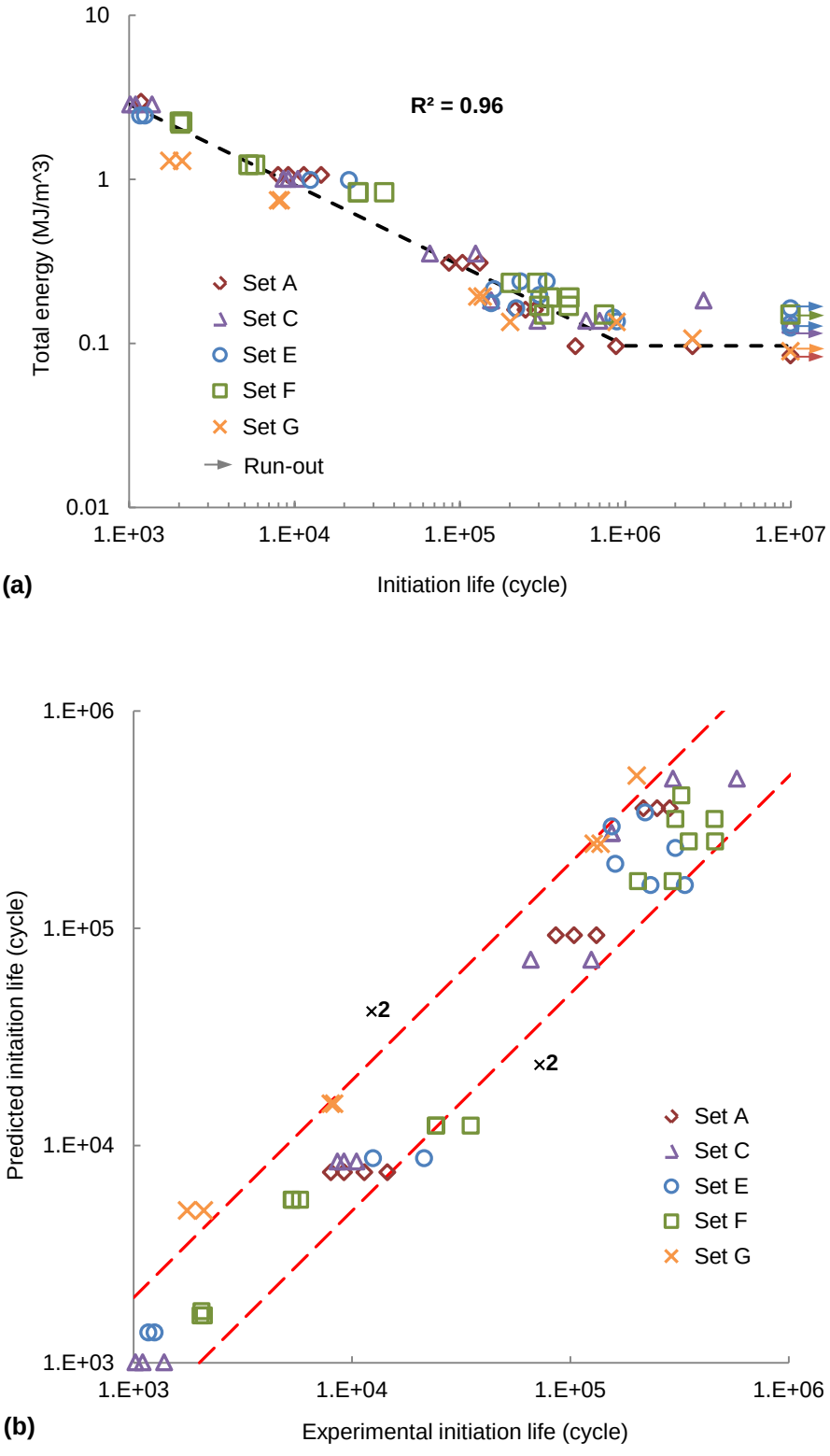

Figure 5.18: Energy model (a) total energy density *vs.* crack initiation life (b) predicted *vs.* experimental initiation life

5.4 Summary

In this chapter, available models for predicting the fatigue life of spot-welds were categorized into three major groups: fracture mechanics, structural stress, and local strain approaches. The fracture mechanics approach considers the spot-weld as a crack-like slit by neglecting the spot-weld root radius. This assumption is often justified due to the insignificant effect of BM strength on the fatigue strength of spot-welds. The fracture mechanics approach considers a measure of stress intensity factor or J-integral as the fatigue damage parameter, and relates this parameter to the fatigue life or the crack growth rate. In the structural stress approach, it is assumed that structural stress (directly or indirectly) controls the fatigue failure. Structural stress is a linearly distributed stress over the thickness, obtained by neglecting the effect of stress concentration. Structural stress reflects the effect of forces and moments at the spot-weld center or edge through different theories and assumptions. The local strain approach, in contrast to the fracture mechanics approach, considers a spot-weld as a blunt notch with a finite radius. A measure of local strain at the hot spot is considered as the damage parameter.

The most common fatigue models from each approach were introduced and advantages and shortcomings associated with each model were introduced. To evaluate available fatigue models for magnesium spot-welds, the models developed by Swellam, Sheppard, and Pan were selected from the fracture mechanics, structural stress, and local strain approaches, respectively.

A fatigue model was proposed for predicting the location and the life associated with fatigue crack initiation. This model was based on local strain energy, which was found from FE simulations using the UMAT. Total energy was defined as the summation of plastic and positive elastic strain energies, which were calculated from the stress–strain response. Total energy at the hot spot was considered as the fatigue damage parameter. The hot spot was identified as the location with maximum signed equivalent plastic strain at the end of the first loading reversal.

The selected available models as well as the proposed model were evaluated by examining the capability to correlate experimental fatigue data for different spot-welded specimens. It was shown that Swellam's model in its original form was unsuccessful in correlating the experimental data for TS and CT spot-weld specimens. This failure was attributed to neglecting the effect of bending moment on CT specimens. A modified form of Swellam's model and other investigated models were able to successfully correlate the experimental results.

Chapter 6

Automotive Application

This chapter puts together the material properties presented in chapter 3, material model developed in chapter 4, and the fatigue model proposed in chapter 5, to predict the fatigue failure location and life for an automotive structure.

The chapter starts with an introduction to the structure. Because a new joining process was utilized in this structure, the process is briefly introduced. Using the fatigue damage parameter proposed in this research, master curves are obtained through specimen-level analyses. FE modeling of the structure is explained. Simulation results under different cyclic load cases are compared with experimental measurements and the performance of the proposed model is discussed.

6.1 Introduction

6.1.1 Demo-structure

As mentioned in chapter 1, this research was performed as a part of the MFERD project. A structure was designed and manufactured in this project to evaluate the performance of a magnesium front-end structure for automobiles and to verify different simulations. The structure is called the "*Demo-structure*" and consists of three components, which are made of three different magnesium alloys. The components include the upper rail, lower rail, and shock tower, and are made of AZ31B sheet, AM30 extrusion, and AM60B cast Mg alloys, respectively.

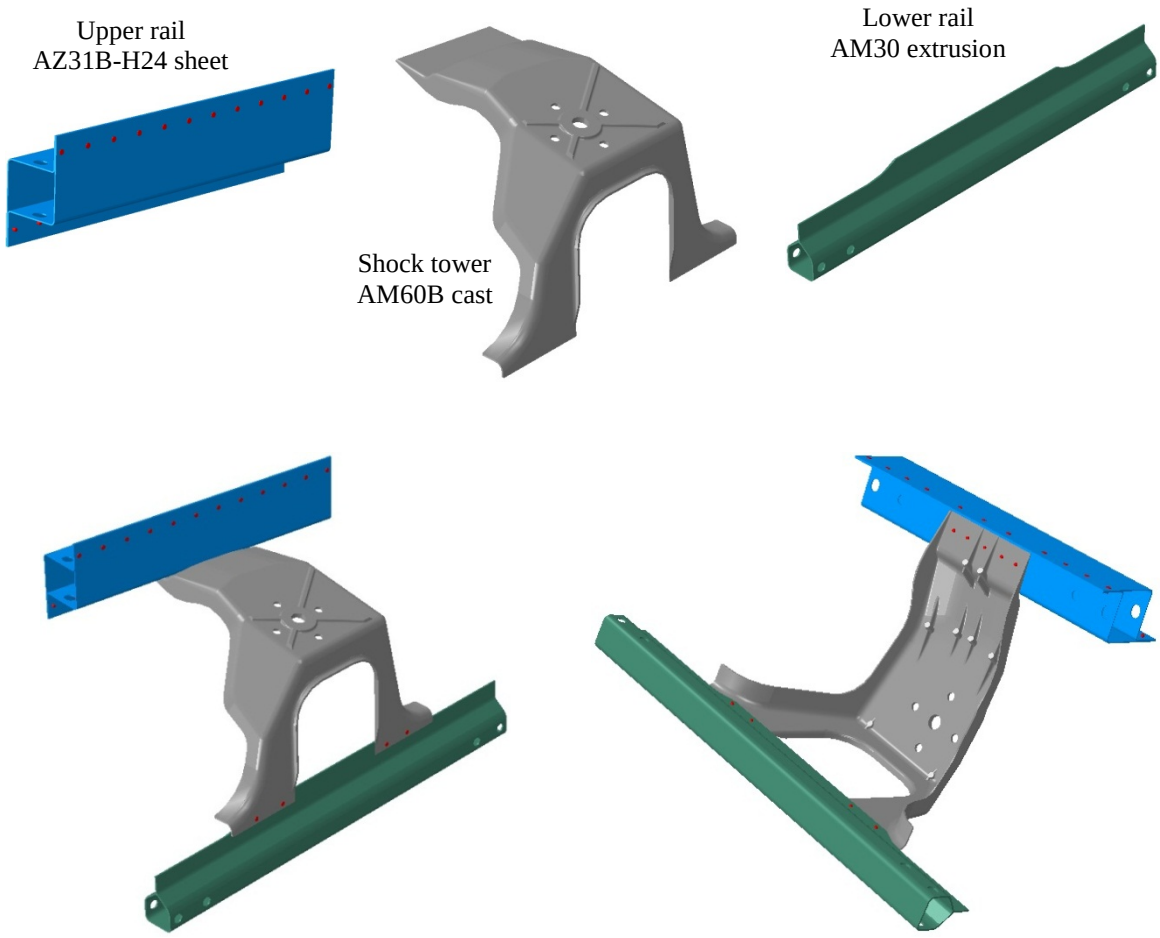

Figure 6.1: Illustration of components and assembly of the Demo-structure

Figure 6.1 shows the components and assembly of the Demo-structure and Figure 6.2 shows a number of the manufactured Demo-structures, ready for testing. The tests that were performed on the Demo-structures included, but were not limited to, cyclic loading.

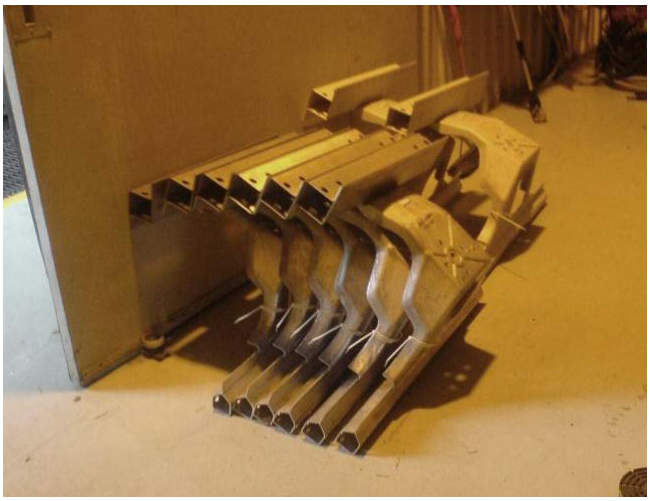

Figure 6.2: Manufactured Demo-structures

The joining process for assembling the Demo-structure was a modified form of self-pierce riveting. This joining technique is briefly introduced in the next section.

6.1.2 Self-Pierce Riveting

The self-pierce riveting (SPR) technique was introduced in the 1960s, but was not promoted until twenty years ago [214]. SPR has primarily targeted lightweight materials, such as aluminum and magnesium [214,215], but can be used for steel structures as well. Several automobile manufacturers apply the SPR process in the body assembly line to join aluminum parts [216-218].

Compared to conventional joining techniques, SPR offers a number of advantages and suffers from some disadvantages. Applicability to dissimilar material joining and multilayer stacks, superior fatigue strength, and ease of automation are among the advantages of this method of joining. On the other hand, the shortcomings of SPR include the requirement to access both sides of the workpieces, and its unsuitability for brittle materials [214,219].

SPR is a cold forming process to join two or more workpieces by driving a semi-tubular rivet through the top sheet and partial piercing the bottom sheet. As its name suggests, SPR does not require pre-drilled holes in the components to be joined. Therefore, precautions for precise aligning the workpieces with each other and with the riveting machine are eliminated.

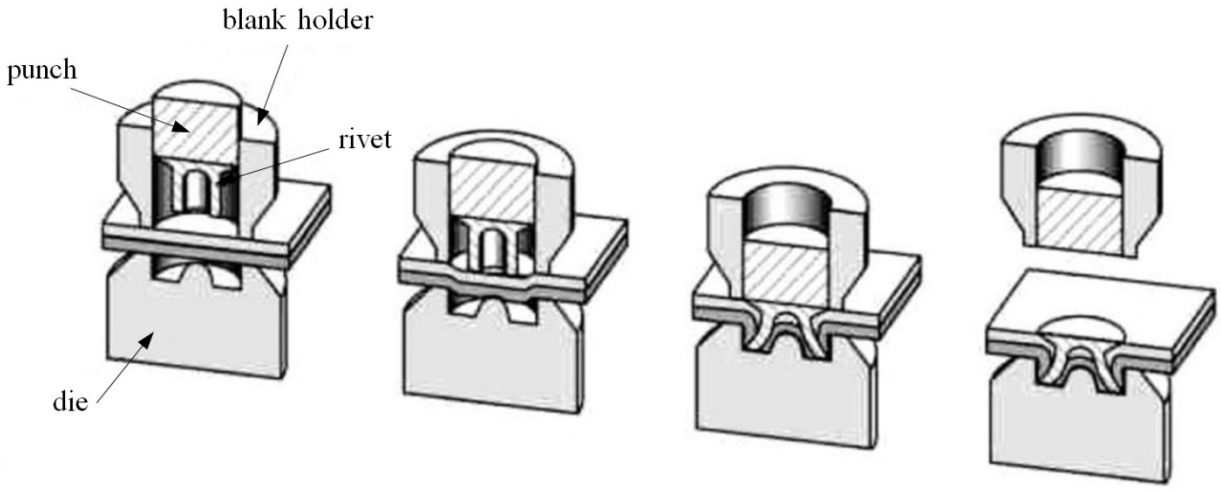

Figure 6.3: Self-pierce riveting process [220]

As shown in Figure 6.3, the SPR process is performed in four steps [214]. In the first step, the blank holder moves toward a small die and clamps the sheets and the punch pushes the rivet to contact the upper surface of the top sheet. In the second step, the rivet is forced to deform the top and bottom sheets. In the next step, the rivet pierces through the top sheet and partially through the bottom sheet, and flares into the bottom sheet following the shape of the die. Finally, the blank holder and punch retract after the punch reaches predetermined values of load or stroke [214].

Localized and severe plastic deformation, especially in the bottom sheet, is a challenge in the SPR joining method. This feature may cause cracking in the bottom sheet if the material does not have the required ductility. Magnesium, as mentioned in chapter 2, has poor ductility and formability at room temperature due to the hexagonal lattice structure and limited slip systems. As a result, SPR generally causes cracking in magnesium alloys [221]. At elevated temperatures additional slip systems are activated [52,64], which results in enhanced formability. The work by Durandet et al.

[221] has shown that a laser beam can provide enough heat at the joint location prior to SPR, to make a crack-free joint in AZ31 magnesium alloy. This process is called "*laser assisted self-pierce riveting*" or LSPR, which was employed for joining the components of the Demo-structure.

6.2 Material Properties and Modeling

6.2.1 Material Properties

As stated earlier in this chapter, Demo-structures were made of three magnesium alloys: AZ31B, AM30, and AM60B. Therefore, simulation of the Demo-structure requires the mechanical behavior for each of these materials. The behavior for AZ31B was obtained from experiments performed by the author, and reported in chapter 3. The uniaxial stress-strain curves for AM30 and AM60B were taken from the literature [222,223]. AM30, due to the extrusion manufacturing process, possesses highly textured microstructure, which results in directional behavior. In contrast, AM60B cast alloy has a randomly oriented crystal structure which results in isotropic behavior. Figure 6.4 illustrates the monotonic behavior of textured alloys, *i.e.*, AZ31B and AM30, in different directions, as well as the behavior of non-textured AM60B alloy under uniaxial loading. RD, TD, and ED in this figure represent the rolling, transverse, and extrusion directions, respectively.

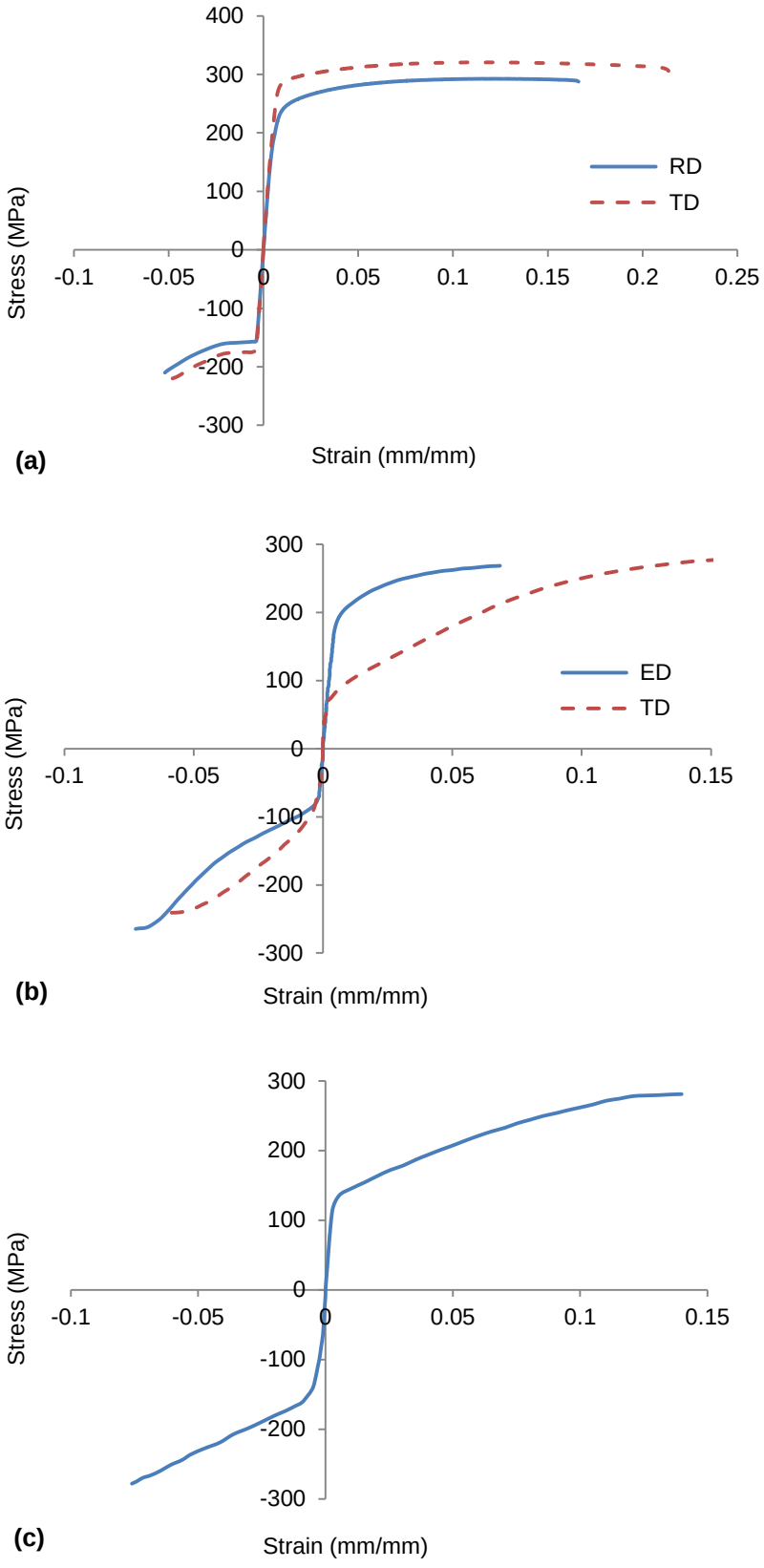

Figure 6.4: Monotonic stress-strain curves for (a) AZ31B, (b) AM30 [222], and (c) AM60B [223]

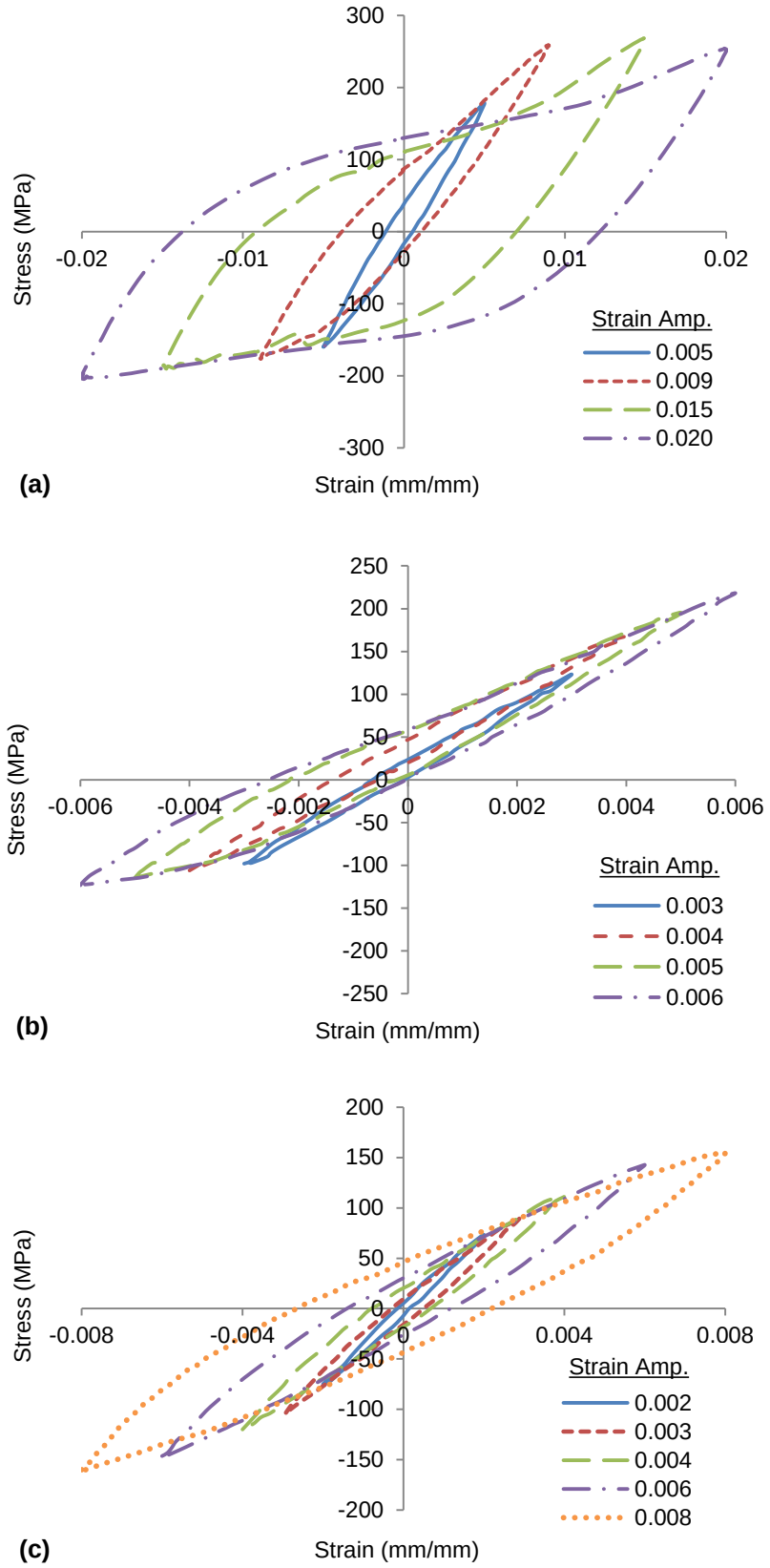

Figure 6.5: Stabilized cyclic hysteresis curves for (a) AZ31B, (b) AM30 [224], and (c) AM60B [225]

The fatigue behavior for AZ31B was obtained as part of the experimental work in the current study. The behavior for AM30 and AM60B were obtained from the literature [224,225]. Figure 6.5 displays the stabilized cyclic stress-strain hysteresis for these alloys for different strain amplitudes. The strain-life curves for these alloys under fully-reversed strain-control testing conditions are shown in Figure 6.6. The fatigue properties illustrated in these figures correspond to RD for AZ31B, and ED for AM30 magnesium alloys.

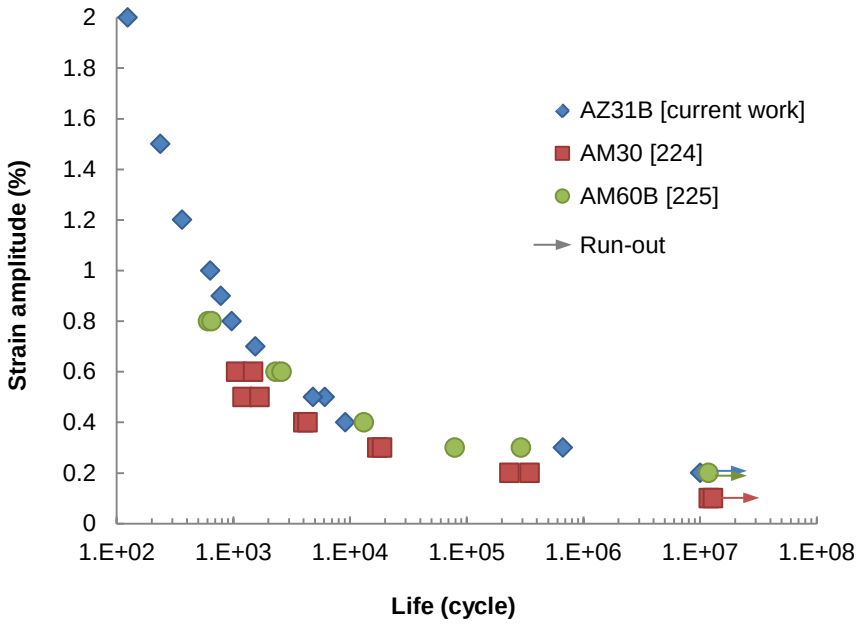

Figure 6.6: Fully-reversed strain-life curve for different magnesium alloys

The rivets are made of steel with unknown monotonic and cyclic properties. Therefore, elastic steel properties, *i.e.*, E=210 GPa and ν=0.3 were used for the simulations.

6.2.2 Material Modeling

The stress-strain behavior for AZ31B sheet under different loading conditions was obtained from the material model developed in this research, and the results were presented and discussed in chapter 4. This section demonstrates how the material model performs for AM30 extrusion and

AM60B cast alloys. Figure 6.7 compares the results obtained from the material model (UMAT) with experimental results for AM30. This figure illustrates the results for monotonic uniaxial tension and uniaxial compression as well as cyclic loading for two different strain amplitudes.

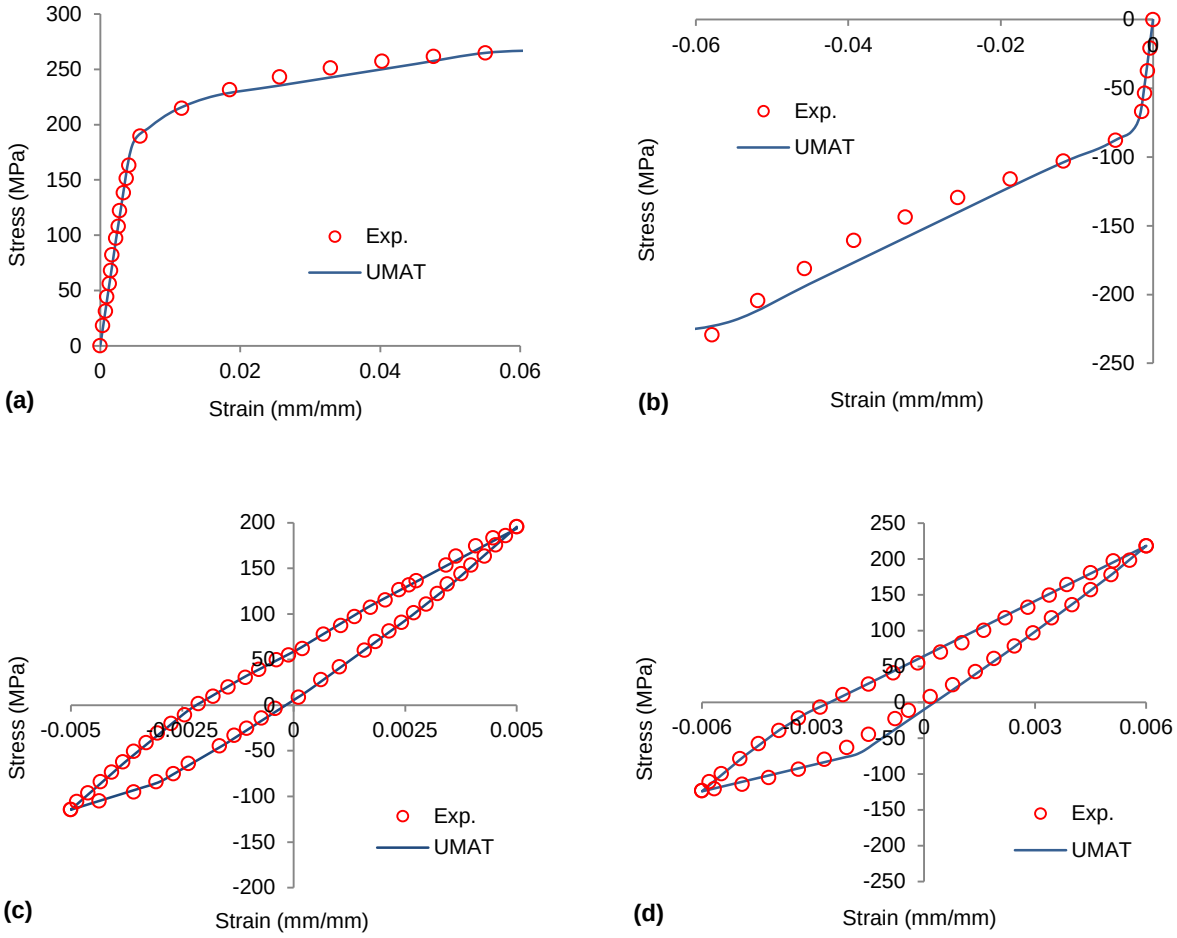

Figure 6.7: Stress-Strain response for AM30 in ED (a) monotonic tension, (b) monotonic compression, (c) cyclic with ε_{amp} = 0.5%, (d) cyclic with ε_{amp} = 0.6%

According to Figure 6.4 and Figure 6.5, the monotonic and cyclic behavior of AM60B magnesium alloy is approximately symmetric. Therefore, available hardening models in the Abaqus/CAE software were examined before using the material model developed in this thesis. To obtain the best fit to experimental results, combined isotropic-kinematic hardening models were selected, because they provide more flexibility than separate isotropic and kinematic hardening

models to adjust to the experimental flow curves. The combined hardening models available in Abaqus/CAE are "*stabilized*" or "*half-cycle*" models. The stabilized model predicts hardening behavior based on the stabilized response of the material under a fully reversed cyclic loading in the tension reversal, and applies the same trend to the compression reversal. The half-cycle hardening model is based on the stress-strain data from the first reversal of the uniaxial tension or compression loading [191]. These models, as well as the material model (UMAT) developed in this thesis, are compared with experimental cyclic behavior of AM60B. Figure 6.8 displays the effect of hardening models on stress-strain results for a single element model under uniaxial loading with ε_{amp} = 0.6%.

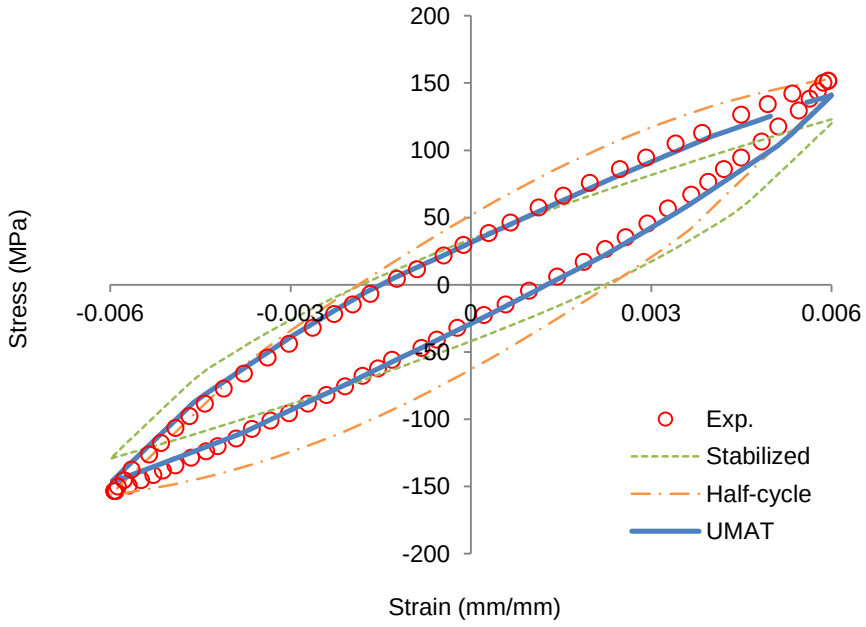

Figure 6.8: Comparing different hardening models for cyclic behavior of AM60B for ε_{amp} = 0.6%

According to the energy approach for fatigue life estimation, the shape of the hysteresis loop (plastic energy) and the value of the peak stress (positive elastic energy) are key factors to reliably calculate total energy. As depicted in this figure, the UMAT provides the best fit to the experimental behavior. Therefore, the proposed material model was used for AM60B cast magnesium alloy.

Figure 6.9 illustrates the performance of the UMAT in following monotonic uniaxial tension and compression, as well as two cyclic loading with different strain amplitudes, for AM60B.

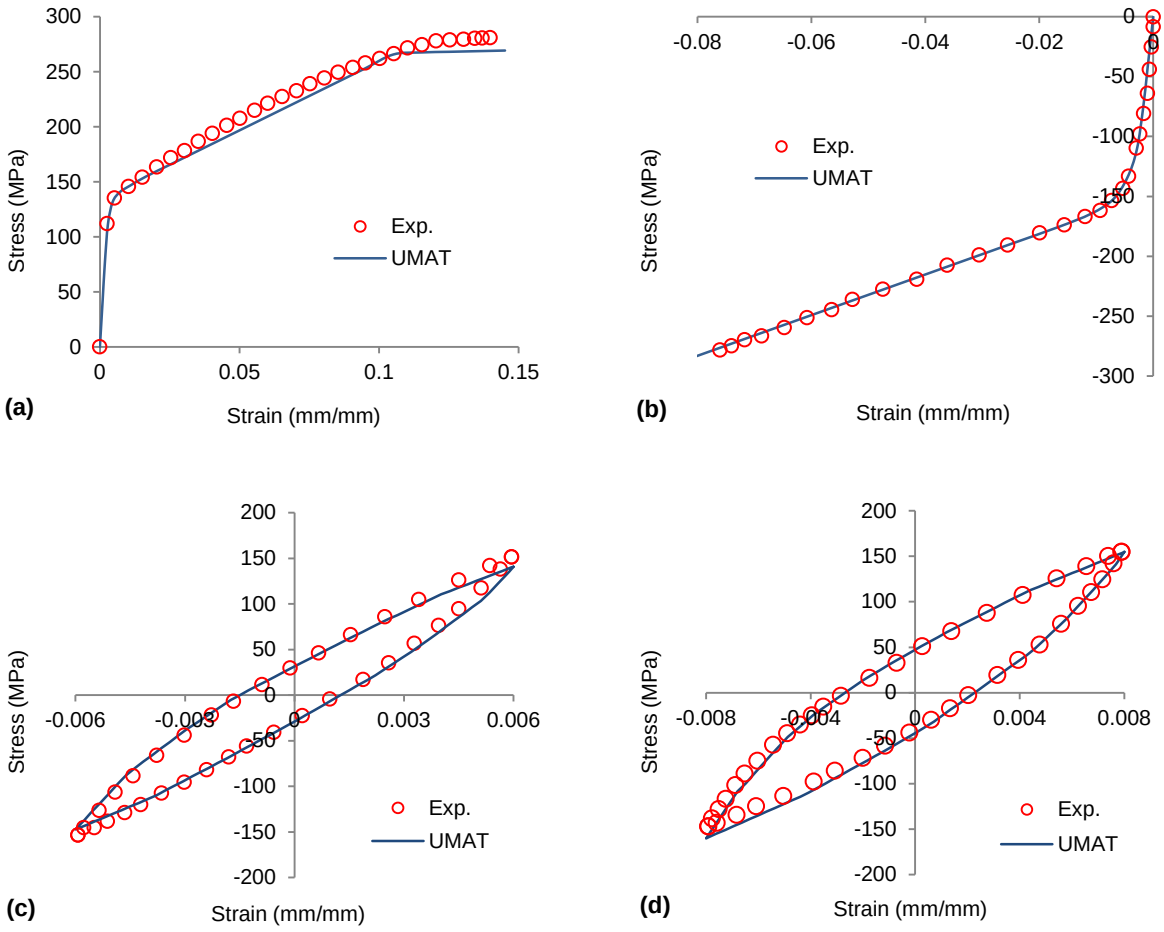

Figure 6.9: Stress-Strain response for AM60B (a) monotonic tension, (b) monotonic compression, (c) cyclic with ε_{amp} = 0.6%, and (d) cyclic with ε_{amp} = 0.8%

Based on the results presented in this section, it can be concluded that, similar to AZ31B, the UMAT is able to successfully regenerate the behavior of AM30 and AM60B magnesium alloys. In the next step, total energy was calculated for each experimental data point plotted in Figure 6.6, using the method introduced in chapter 5.

To find the total energy, a single element model was considered, appropriate cyclic properties were assigned, and the same uniaxial strain amplitude as the experiment was applied.

Figure 6.10 shows the total energy results plotted versus the fatigue life for different magnesium alloys.

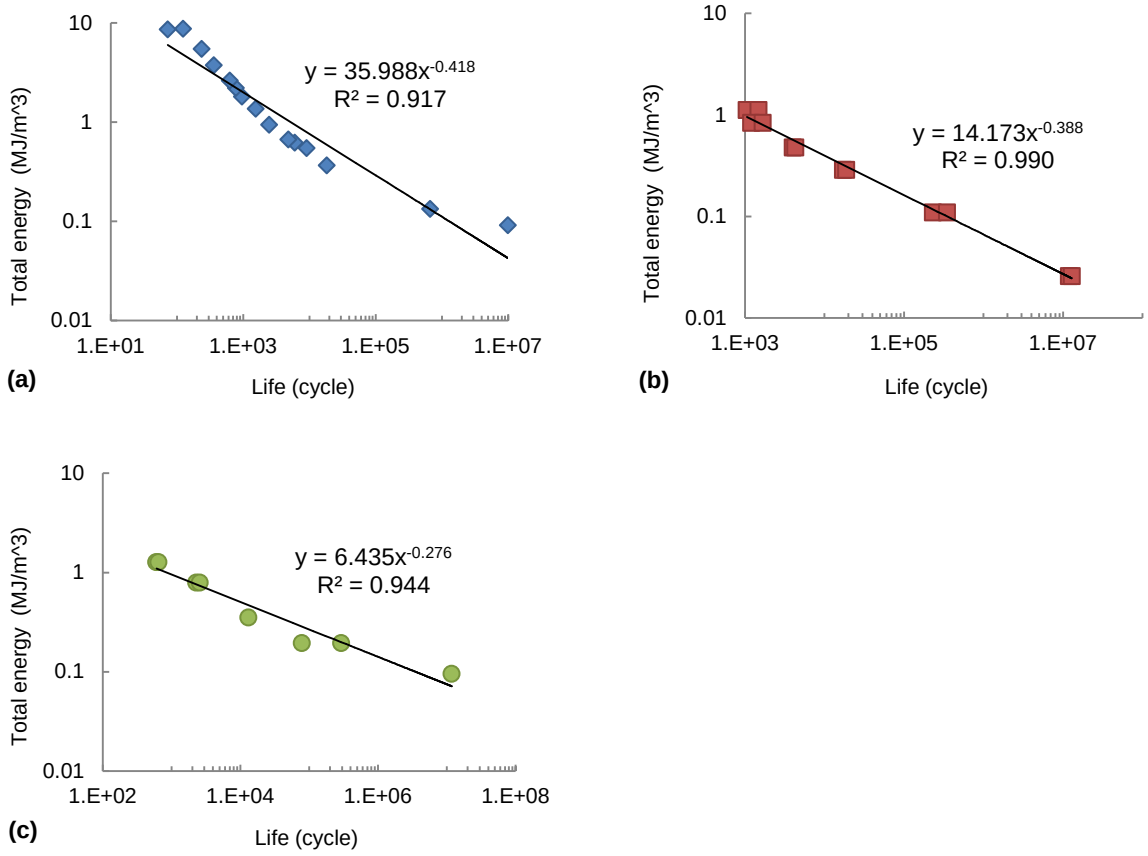

Figure 6.10: Energy-life curves for (a) AZ31B, (b) AM30, and (c) AM60B

Therefore, the energy-life equation is considered as

$$N_f = P.W^{t^q} \quad , \tag{6.1}$$

where N_f is the fatigue life, and W^t is the total energy. P and q are material constants which were obtained for the investigated magnesium alloys using the trend line equations in Figure 6.10. The material constants for the energy-life equation are presented in Table 6.1.

Table 6.1: Constants of the energy-life equation for different magnesium alloys

	AZ31B	AM30	AM60B
P	5257	925	844
q	-2.391	-2.576	-3.619

6.3 LSPR Specimen

6.3.1 Specimen Preparation and Testing

Before fabricating the Demo-structure, the LSPR process was attempted on specimens with different stack-ups of Mg alloys to determine the process parameters, such as rivet geometry and laser power, and also to measure ultimate load and fatigue strength. Five sets of LSPR specimens were produced in tensile-shear configuration with the geometry shown in Figure 6.11, and the material combinations listed in Table 6.2. Note that all the experimental work on LSPR specimens, including preparation and testing, were performed by various contractors for the US Automotive Materials Partnership (USAMP).

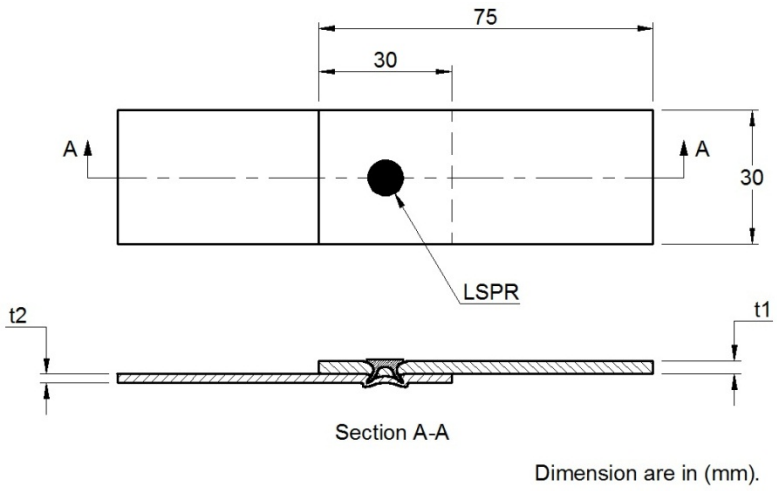

Figure 6.11: LSPR specimen geometry [226]

Table 6.2: LSPR specimen stack composition [226]

Specimen	Top sheet	Bottom sheet
AM30-AM60B	AM30 (2.5 mm)	AM60B (2 mm)
AM60B-AM30	AM60B (2 mm)	AM30 (2.5 mm)
AM60B-AZ31B	AM60B (2 mm)	AZ31B (2 mm)
AZ31B-AM60B	AZ31B (2 mm)	AM60B (2 mm)
AZ31B-AZ31B	AZ31B (2 mm)	AZ31B (2 mm)

The materials used in the specimens are AZ31B sheet, AM30 extrusion, and AM60B cast Mg alloys with 2 mm, 2.5 mm, and 2 mm thicknesses, respectively. It should be noted that the top sheet and the bottom sheet (in Table 6.2) are specified according to the direction of LSPR insertion.

A number of specimens were tested under monotonic loading and the results for the average ultimate static load are shown in Table 6.3 [226].

Table 6.3: Monotonic test results for different LSPR specimens [226]

Specimen	Ultimate tensile-shear load (kN)
AM30-AM60B	3.4
AM60B-AM30	5.2
AM60B-AZ31B	5.2
AZ31B-AM60B	4.7
AZ31B-AZ31B	5.5

Fatigue tests were performed on the same specimen sets, under load-control with a load ratio R=0.1. The load-life results are plotted in Figure 6.12.

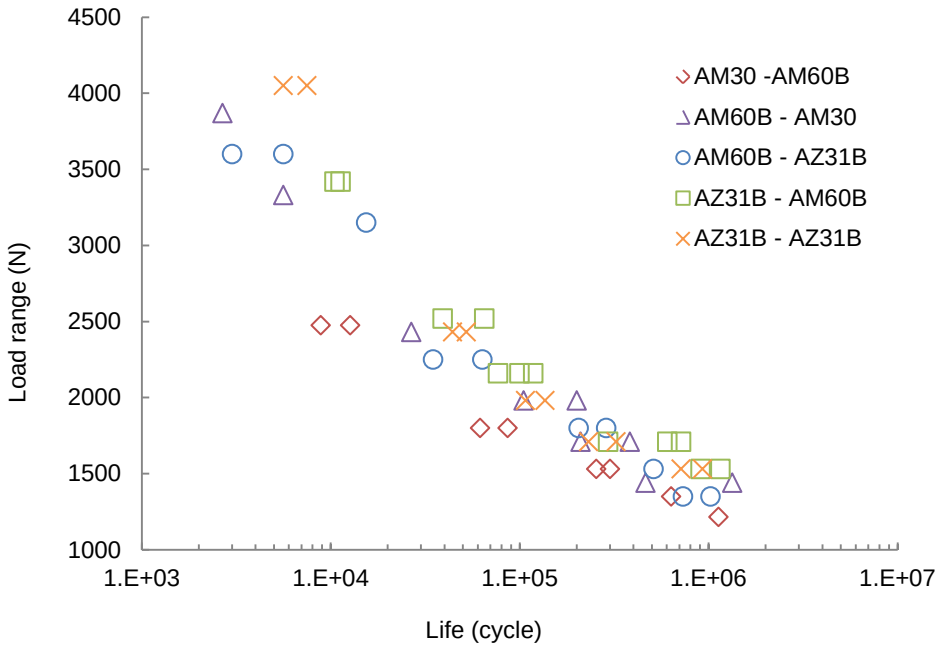

Figure 6.12: Fatigue test results for different LSPR specimens [226]

6.3.2 FE Modeling

The LSPR specimens listed in Table 6.2, and with the geometry depicted in Figure 6.11, were modeled in the commercial FE software Abaqus/CAE 6.10. Five FE models with three different geometries were generated according to the different thickness combinations. Taking advantage of the plane of symmetry, half of each specimen was considered for FE modeling. Eight-node linear brick elements with reduced integration and enhanced hourglass control (C3D8R elements) were employed. Figure 6.13 displays the FE half-model with details around the LSPR, for the three models with different sheet thickness combinations. According to Table 6.2, appropriate fatigue properties were assigned to the top and bottom magnesium sheets, and elastic properties for steel were used for the rivets.

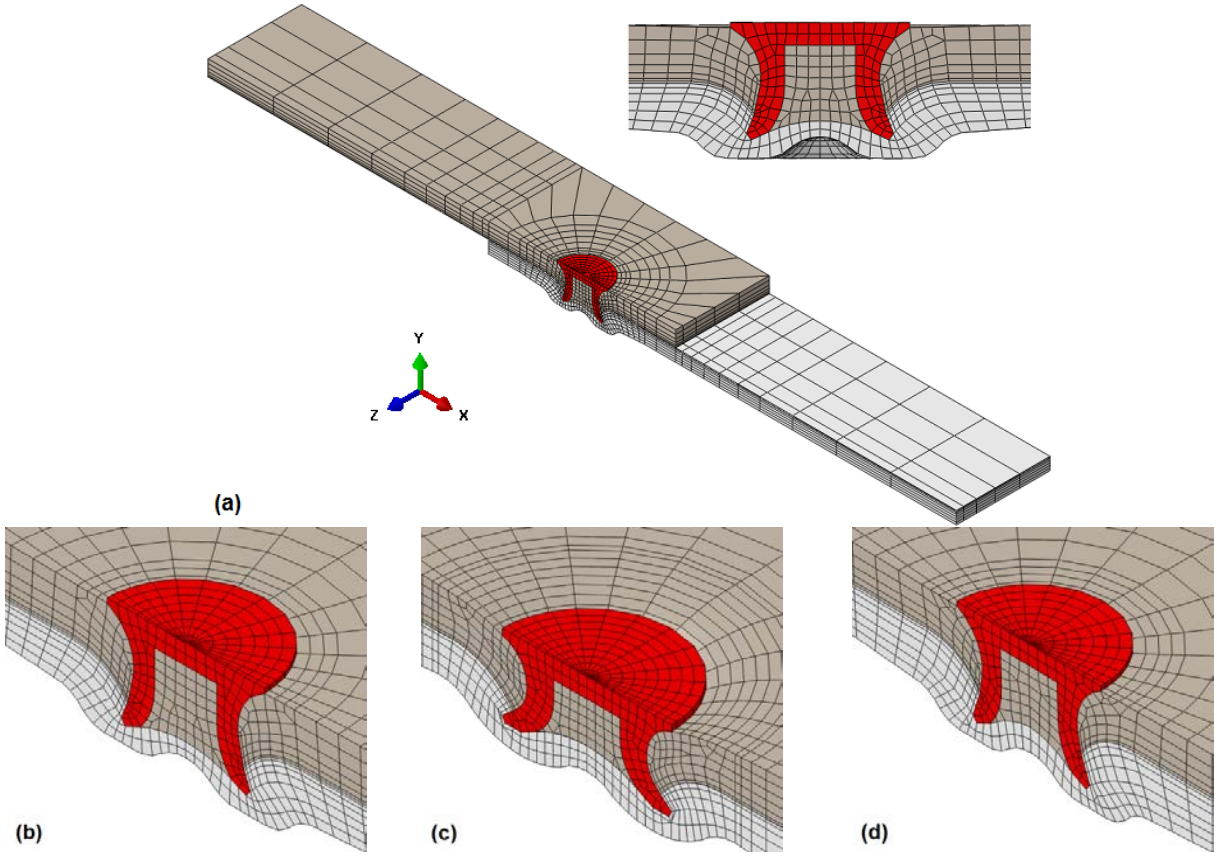

Figure 6.13: FE model for LSPR specimens (a) overal view of the half model (b) 2.5mm (top thickness) × 2mm (bottom thickness) (c) 2mm × 2mm (d) 2mm × 2.5mm

Boundary conditions included the end conditions, and the symmetry condition on the plane of symmetry. The end condition at one side was fixed displacement in all directions, and in the other end was fixed lateral displacements with free displacement in the axial direction with a force applied in this direction. The boundary condition on the plane of symmetry is zero displacement normal to the plane and zero rotations in the other two directions. The boundary conditions for the LSPR specimens are shown in Figure 6.14.

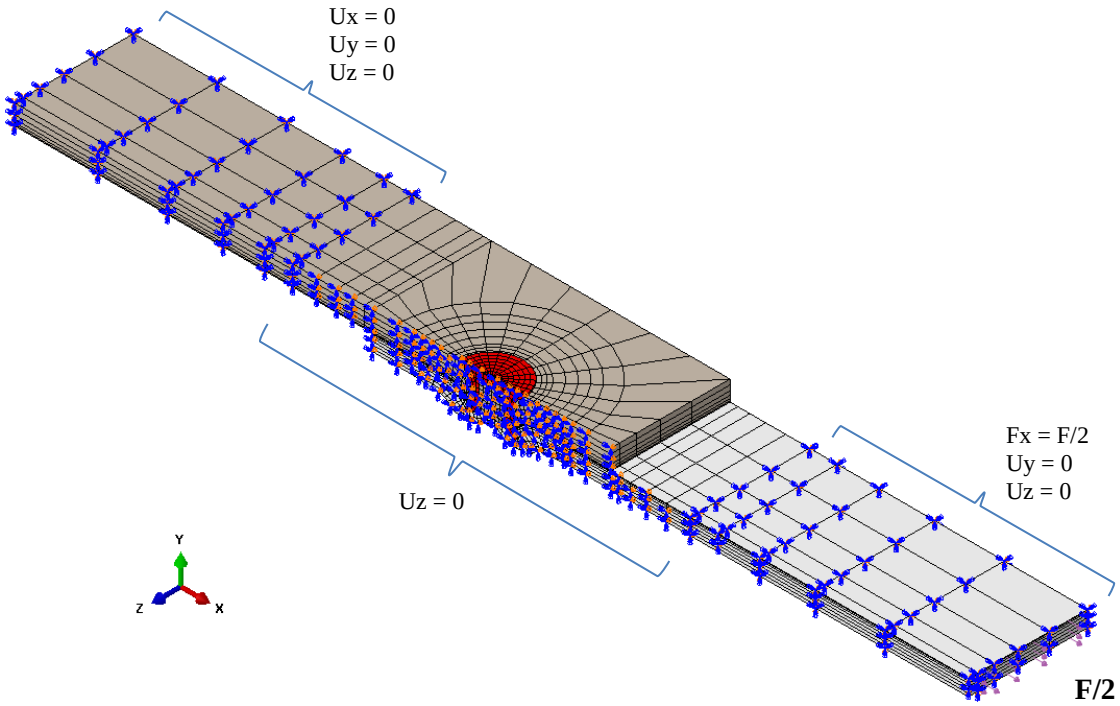

Figure 6.14: Boundary conditions for the half FE model of the LSPR specimens

FE modeling of the LSPR specimens was performed by Mi Chengji, a visiting PhD student to Waterloo, from Hunan University in China.

6.3.3 Simulation Results and Discussion

FE simulations for LSPR specimens were run in three steps which represent three consecutive reversals: loading, unloading, and reloading. Because the SPR geometry is not symmetric in the top and bottom sheets, the deformation and stress and strain distributions are different between the sheets. Figure 6.15 shows the deformation on the signed equivalent plastic strain contour. As explained in

chapter 4, the signed equivalent plastic strain is a state variable defined in the UMAT which distinguishes the tension/compression status of integration points using positive/negative signs. As shown in Figure 6.15(a), the top and bottom sheets intersect on one side of the rivet (left side in the figure) due to asymmetric deformation. To avoid intersection and obtain more realistic distributions for stress and strain at the hot spot, contact interaction was defined between the sheets in the FE model. The deformed shape and the signed equivalent plastic strain contour for the model with contact are displayed in Figure 6.15(b). Because of the significant effect of the contact on the equivalent plastic strain, the model with contact was considered for strain energy and fatigue life calculations.

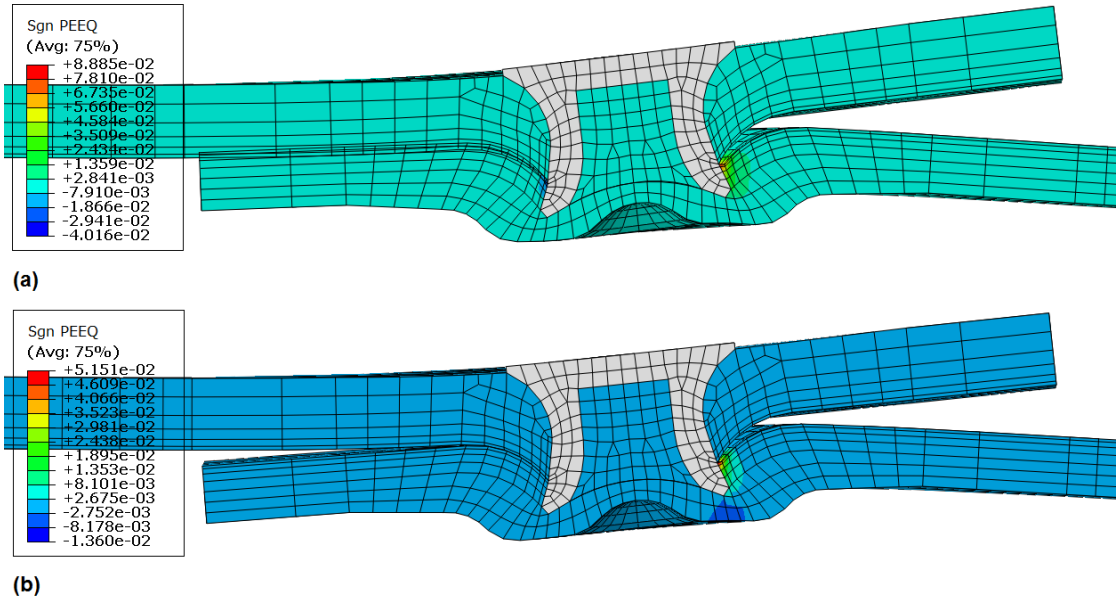

Figure 6.15: Signed equivalent plastic strain contour on deformed shape for AM30-AM60B specimen under a load range = 1800N in models (a) without contact and (b) with contact

Total strain energy at the hot spot was considered as the fatigue damage parameter in this study. Hot spot was considered as the location with the maximum equivalent plastic strain at the end of the first reversal. Therefore, to obtain the total strain energy for each experimental data point, half of the corresponding load was applied to the half model and the hot spot was identified. Total strain energy was calculated for the hot spot according to the method introduced in chapter 5.

The experimental data points plotted in Figure 6.12 were simulated by applying the corresponding cyclic load (knowing the load range from the figure and R-ratio=0.1). The graphs shown in Figure 6.16 were obtained for the different LSPR specimen sets.

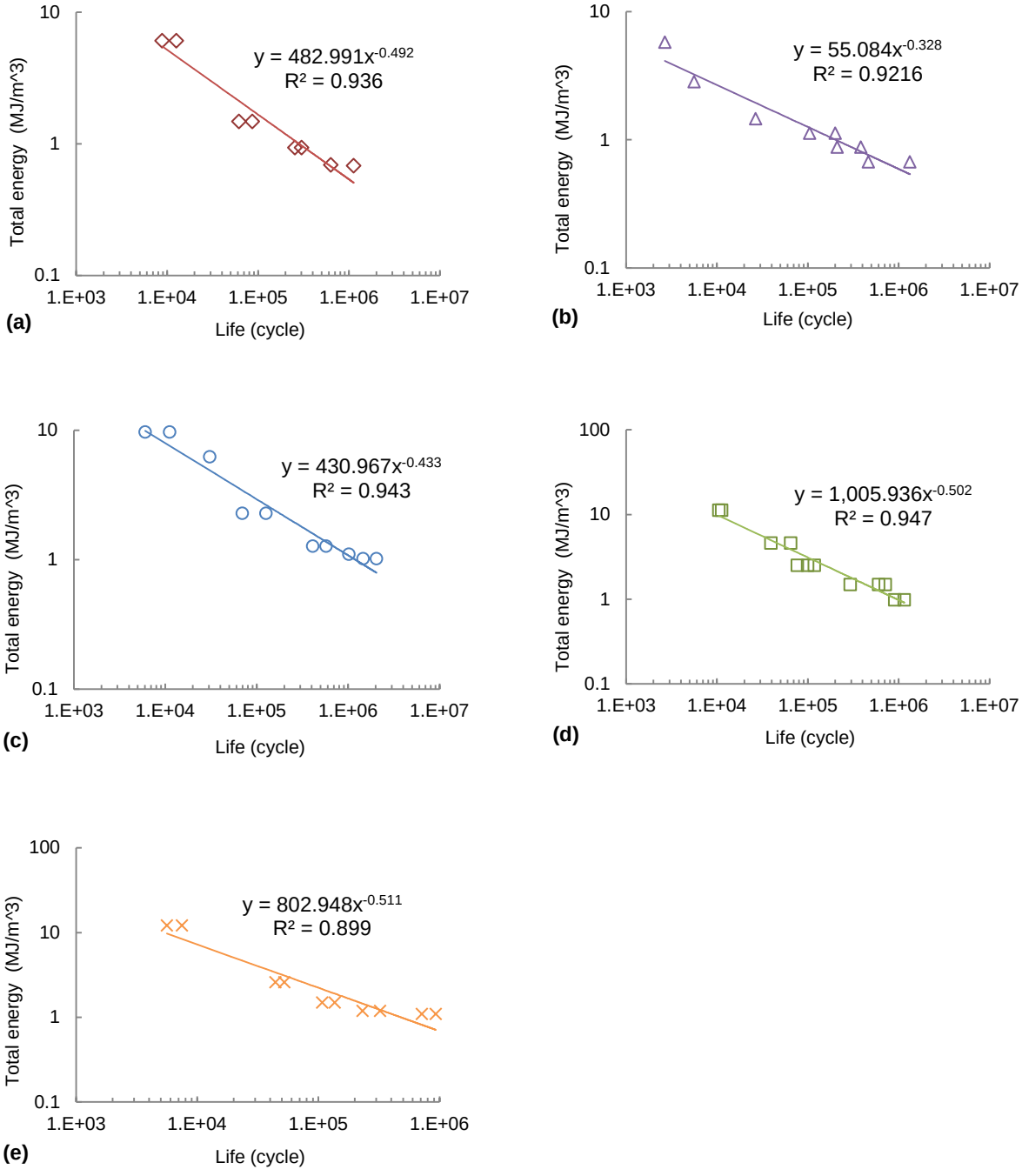

Figure 6.16: Energy-life curves for LSPR specimens
(a) AM30-AM60B, (b) AM60B-AM30, (c) AM60B-AZ31B, (d) AZ31B-AM60B, and (e) AZ31B-AZ31B

The material constants for the energy-life relationship, equation (6.1), were obtained and shown in Table 6.4.

Table 6.4: Constants of the energy-life equation for different LSPR specimens

	AM30-AM60B	AM60B-AM30	AM60B-AZ31B	AZ31B-AM60B	AZ31B-AZ31B
P	283,184	202,538	600,424	956,669	479,112
q	-2.031	-3.048	-2.308	-1.992	-1.956

These constants correspond to the area around the rivet, as materials behave differently in this region than the base metal due to the residual stress induced during the SPR joining process.

6.4 Demo-structure

6.4.1 FE Modeling

A three-dimensional geometry model for the Demo-structure was available through the USAMP. Detailed geometry for the riveted areas as well as a FE model for the Demo-structure were generated by Mi Chengji, a visiting PhD student from Hunan University in China. To expedite the mesh generation phase, the riveted areas were partitioned from the whole assembly. Figure 6.17 displays the SPR joint regions partitioned between different parts.

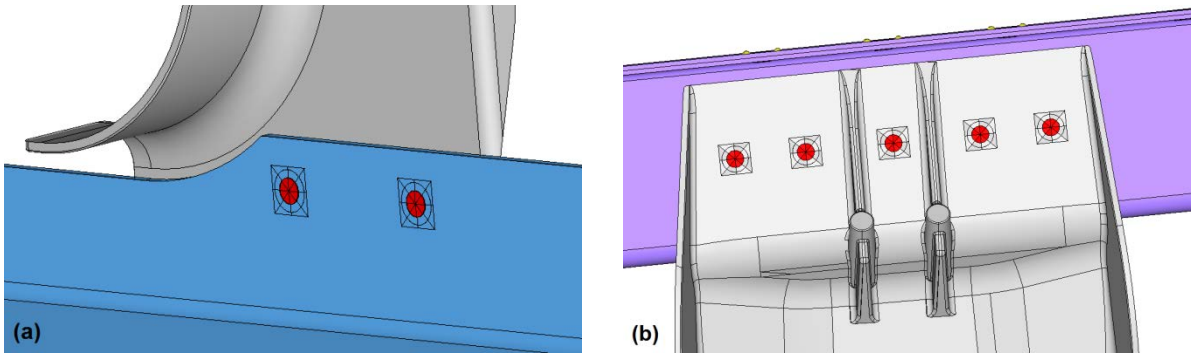

Figure 6.17: Partitioned SPR joints in the Demo-structure
(a) lower rail-shock tower joints (b) shock tower-upper rail joints

Owing to four planes of symmetry in each partitioned square (shown in Figure 6.17), only one-eighth of each SPR joint was considered for FE modeling, which then was reflected to form the whole joint. Figure 6.18 illustrates the detailed FE model for a sample SPR joint. Eventually, the FE model generated for one rivet was copied to other locations with the same stack conditions. As shown in this figure, mapped meshes were generated in SPR joint regions with gradual refinement toward the interface. The fine mesh around rivets, which are stress concentration sites, helps to capture stress and strain distributions more accurately.

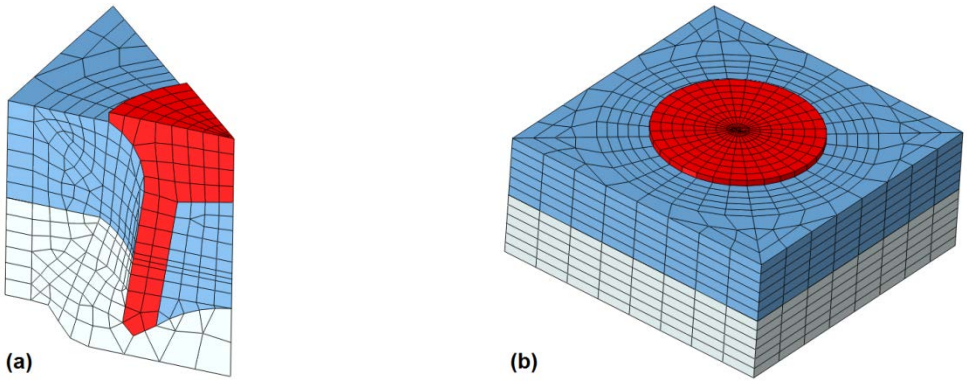

Figure 6.18: FE model for a sample SPR joint (a) one-eighths model (b) whole model

The meshing technique for other regions of the Demo-structure was free mesh, due to the complex geometry. Figure 6.19 shows the FE model of the Demo-structure with details around different SPR joints. Eight-node linear brick elements with reduced integration and enhanced hourglass control (C3D8R) along with 4-node linear tetrahedron elements (C3D4) were employed. Contact interaction was defined between matching surfaces to avoid intersection of different parts.

To save computation time, a simplified model was also generated. In this model, the SPR joints in the upper rail were ignored and the two sheets forming the upper rail were merged together. A detailed FE model in the other SPR joints was maintained. This simplification was decided after several preliminary simulations, which indicated that these joints were not critical in any loading condition of interest.

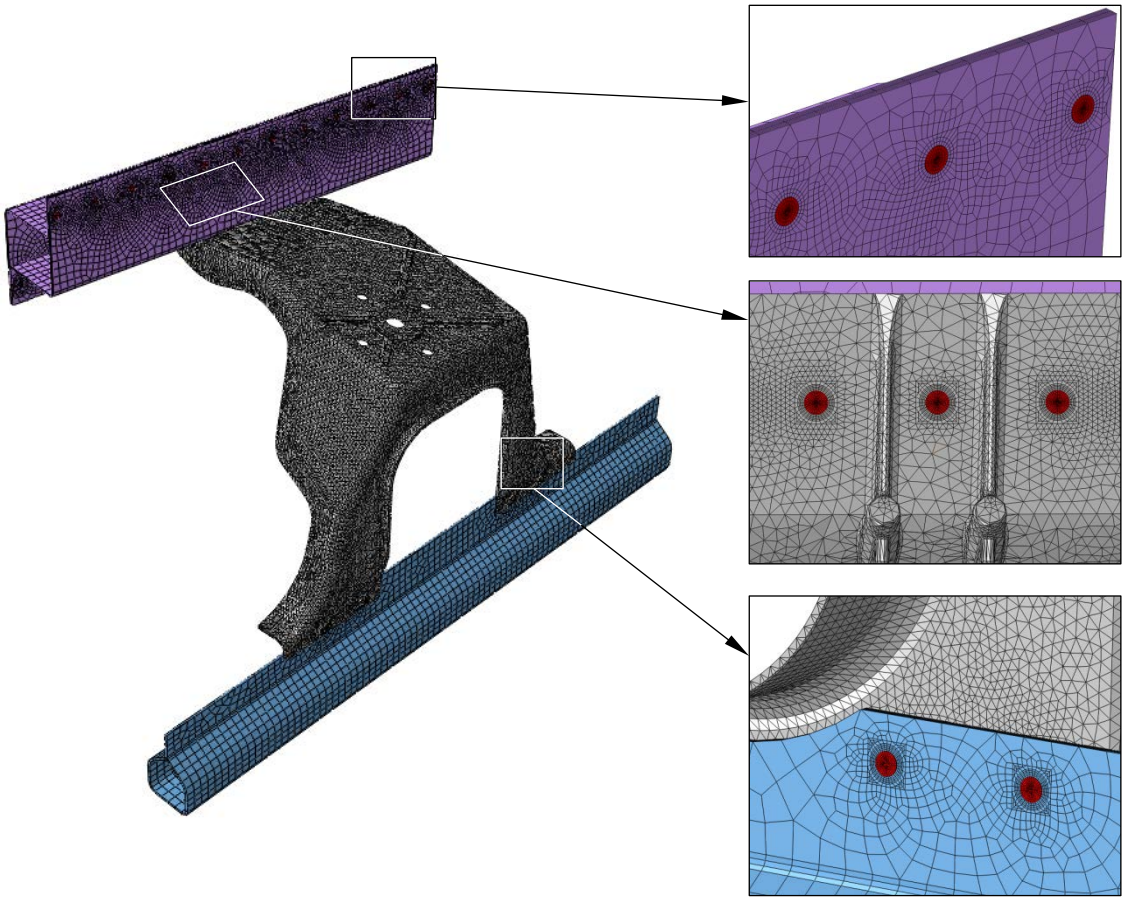

Figure 6.19: FE model of the Demo-structure

The cyclic material model developed in this thesis for magnesium alloys, Figure 6.5, was utilized for all fatigue simulations. Elastic properties for steel were used for the rivets. The user material model subroutine (UMAT) was slightly modified to calculate the strain energy and fatigue life at all integration points. The material constants for the energy-life equation obtained in the previous section for base metal (Table 6.1) and SPR joints (Table 6.4) were assigned to the corresponding regions, Figure 6.20.

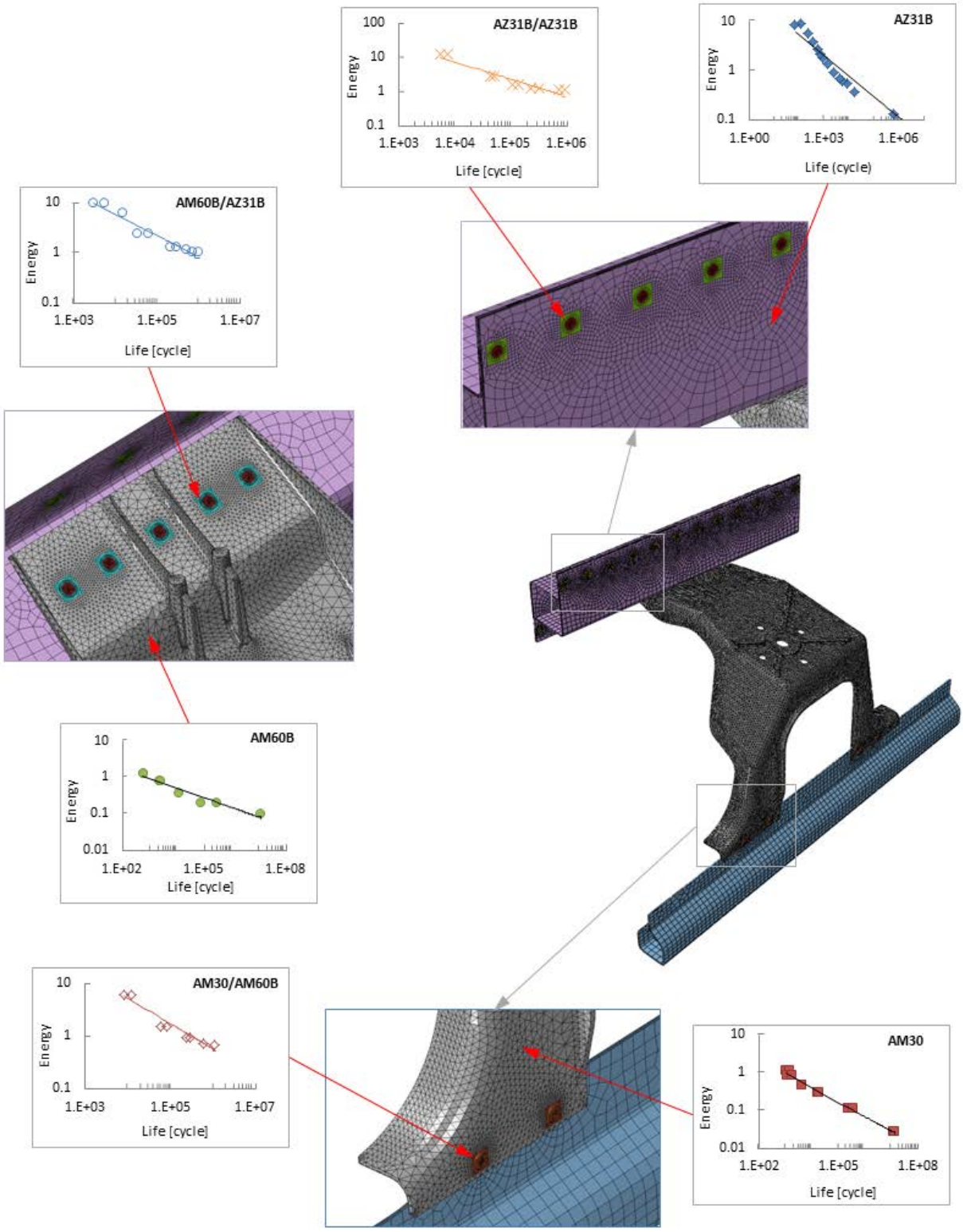

Figure 6.20: Fatigue property assignment to different regions of the Demo-structure

Boundary conditions included constraints on the ends of the upper and lower rails. Due to the special test setup and fixtures, the constraints were applied as shown in Figure 6.21.

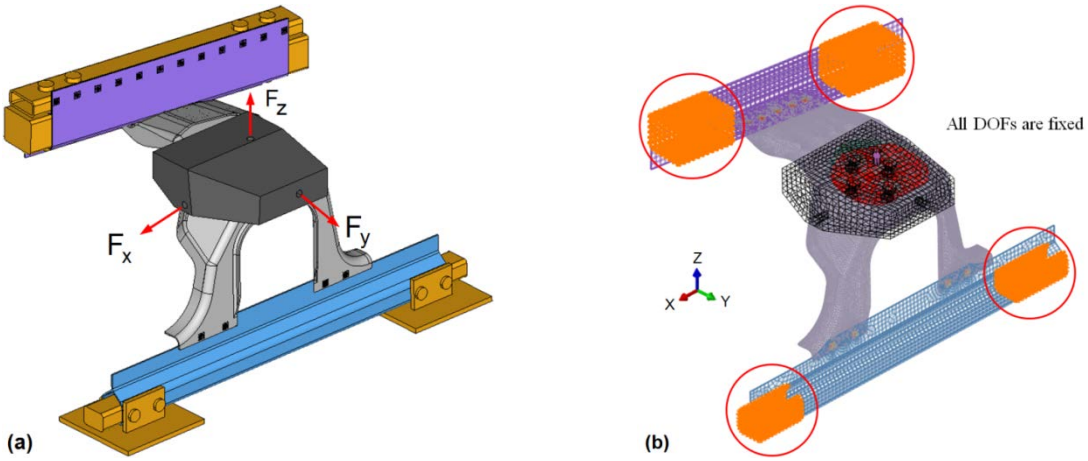

Figure 6.21: Application of loading and boundary conditions to the Demo-structure (a) testing fixture geometry and loading, and (b) boundary conditions in the FE model

Loading the actual structure was performed through a block which was attached to the tower with four bolts. The loading block provided three holes in x, y, and z directions to facilitate; the loading block and corresponding forces are illustrated in Figure 6.21.

6.4.2 Simulation Results and Discussion

A number of Demo-structures were tested under constant amplitude loading in different directions. The Demo-structure was simulated under the same loading conditions by USCAR [227] (method A) and using the fatigue model developed in the present work (method B). The features associated with these methods are compared in Table 6.5.

Table 6.5: Comparison between different simulation methods of the Demo-structure

Feature	Method A	Method B
Component geometry	detailed	detailed
SPR joint geometry	not modeled	detailed
Material model	symmetric	asymmetric
Damage Parameter	Mises stress	strain energy

As stated in this table, detailed geometry for all components was considered in both models. However, for method A the upper and lower rails were modeled with shell elements and the SPR joints were represented by tie connections between nodes of matching components, Figure 6.22.

A more detailed representation was considered for method B as discussed above.

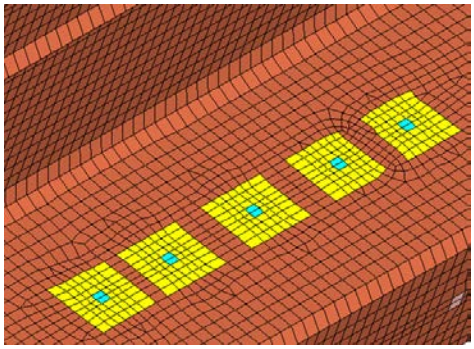

Figure 6.22: FE model for SPR joints for method A [227]

For method A, symmetric hardening behavior was assumed and the Mises equivalent stress was considered as the fatigue damage parameter. Method A was used to predict the failure location and the ***total*** fatigue life [227]. For method B, the asymmetric material model developed in chapter 4 was used along with the energy model proposed in chapter 5. Method B was used to predict the location and the fatigue ***initiation*** life. To refer to different SPRs in the Demo-structure, the SPRs are numbered according to Figure 6.23.

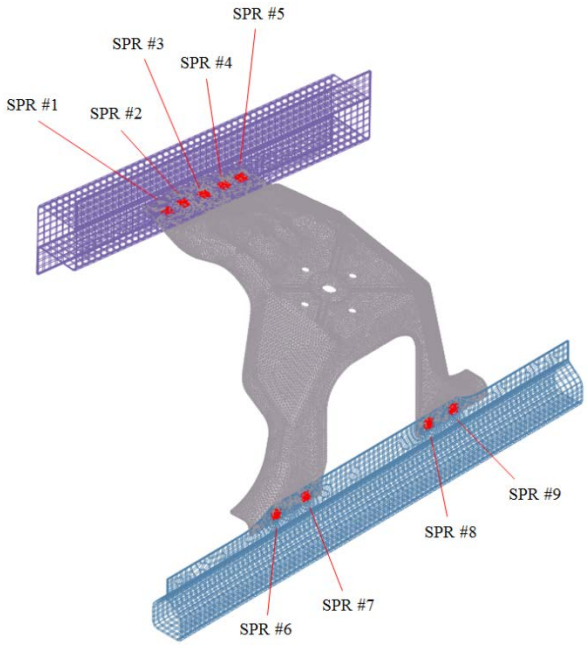

Figure 6.23: Numbering SPRs in the Demo-structure

In the following sections, the results obtained from the two simulation methods are compared with experimental measurements under different cyclic loading conditions.

6.4.2.1 Cyclic loading in x-direction

Fatigue testing in the x-direction, Figure 6.21, was performed on four Demo-structures. The tests were conducted with constant amplitude loading with a maximum load, F_{max}= 4 kN, and a load ratio, R=0. The experimental results are summarized in Table 6.6.

Table 6.6: Experimental results for fatigue testing of the Demo-structure in the x-direction [228]

No.	Failure location	Loading cycle	Descriptions
1	SPR #9	253,481	-
2	SPR #9	283,012	-
3	SPR #9	676,579	crack length = 45 mm
4	no failure	1,000,000	test stopped with no observable crack

Figure 6.24 displays the cracks observed at SPR#9 in the Demo-structures, under cyclic loading in the x-direction.

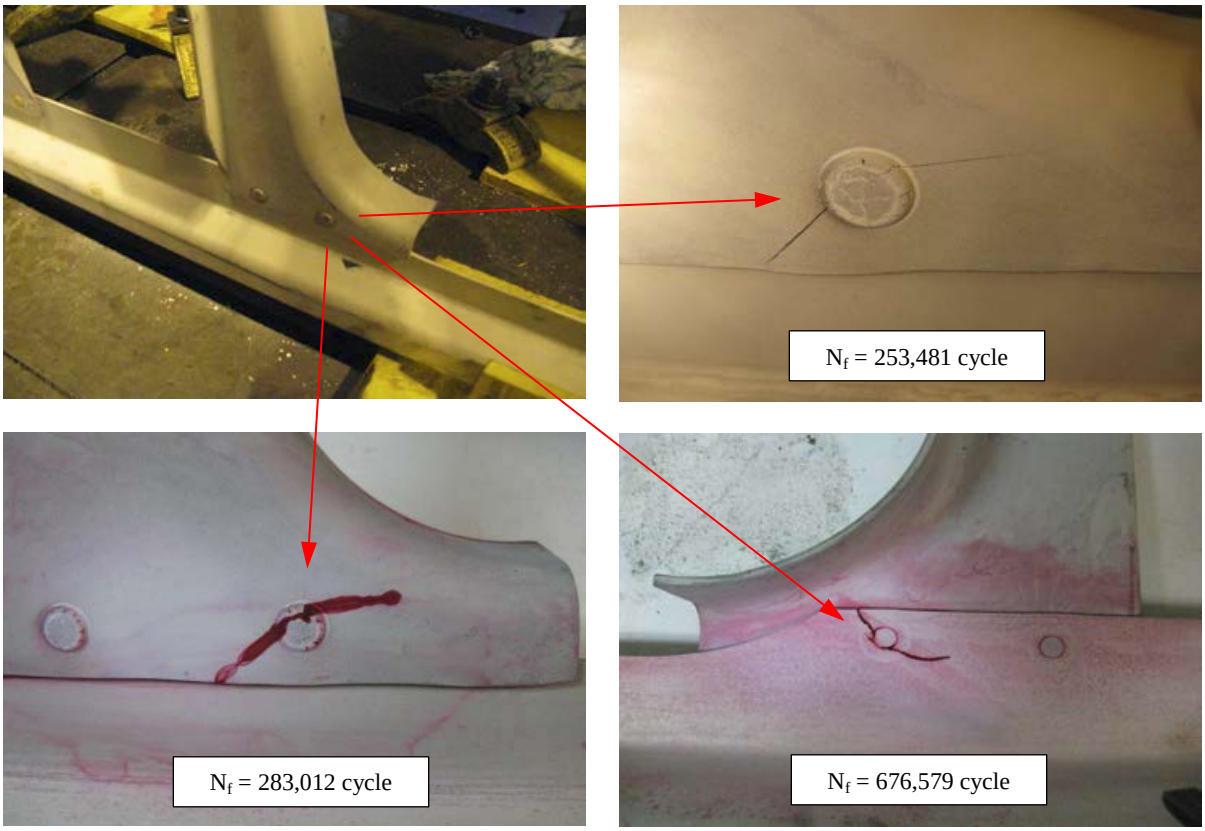

Figure 6.24: Fatigue failure in the three Demo-structures for loading in the x-direction [228]

The results obtained from simulation methods A and B are given in Table 6.7.

Table 6.7: Simulation results for fatigue testing of the Demo-structure in the x-direction

Simulation	Failure location	Life (cycle)
Method A [228]	SPR #6	3,727
Method B	SPR #9	50,540

Figure 6.25 shows the fatigue life distribution in the Demo-structure predicted using method B, with a focus on the different SPRs.

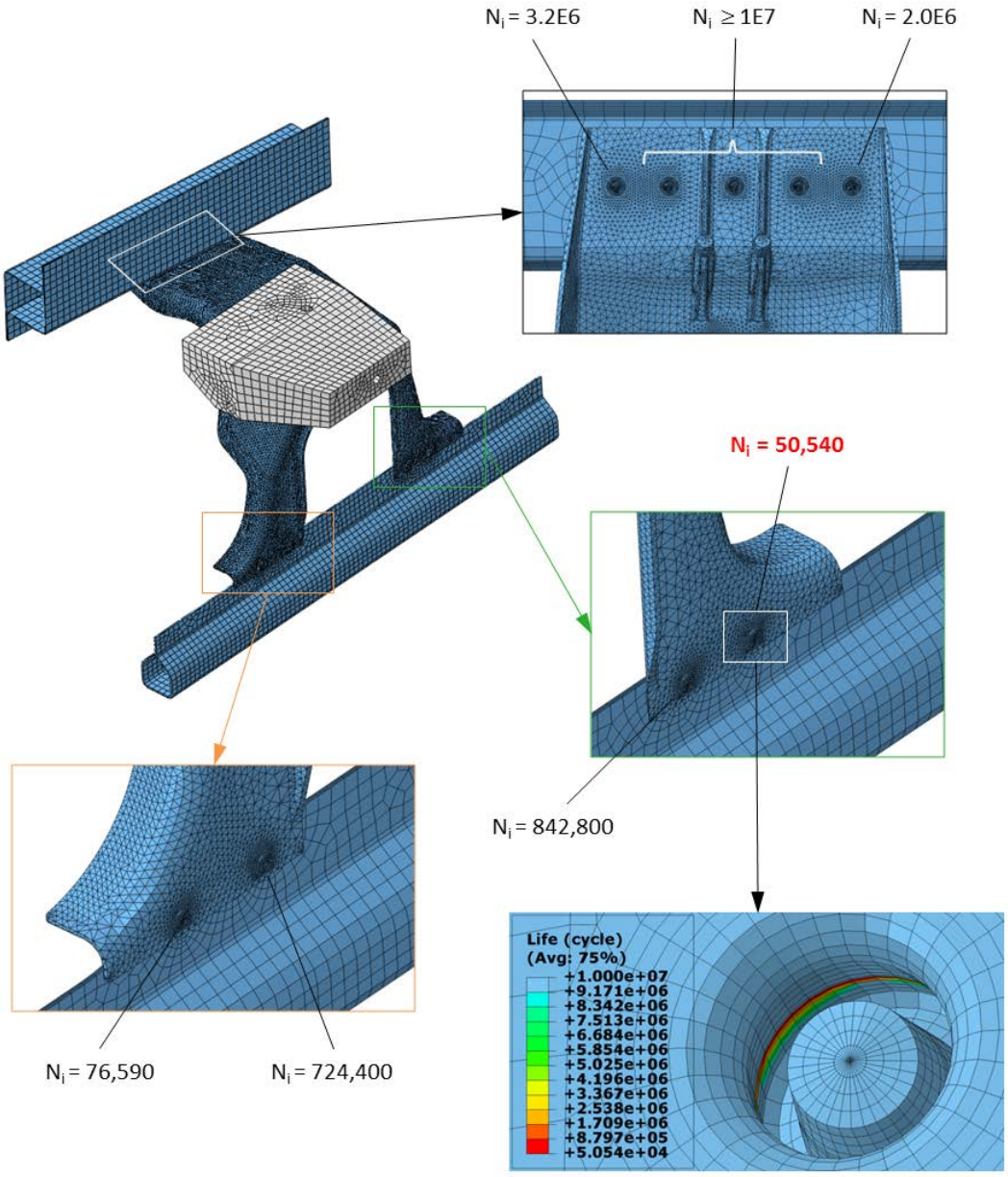

Figure 6.25: Distribution of the crack initiation life obtained from method B for loading in the x-direction

Comparing the results obtained from the two simulation methods with experimental measurements reveals that method B was able to predict the correct location of failure, but method A was not. Both methods are conservative, but method A significantly underestimates the total fatigue life. It should also be noted when comparing the life obtained from method B with the experimental life, that method B calculates only the crack initiation life, while the experimental life corresponds to a crack which has propagated to a finite length. As discussed in chapter 5, the proposed damage parameter is based on total energy, which is calculated using stress/strain results at the notch root. Therefore, the energy is independent of crack length and can only account for crack initiation life. Crack propagation phase must be dealt with separately, using a fracture mechanics based model.

According to Table 6.5, there were two main differences between the simulation methods A and B: the SPR joints geometry and the material/fatigue model. To investigate which factor contributed to the different predictions, another simulation was run. In this simulation, the FE model was the same as that in method B, including the SPR details; the material properties were stabilized cyclic behavior of the participating Mg alloys, Figure 6.5, in tension reversals. The stabilized combined hardening rule built-in Abaqus/CAE 6.10 was adopted in the new simulation and Mises equivalent stress was used as the damage parameter. The same boundary conditions and loading in the x-direction were applied. The failure location in this simulation, similar to method A, was incorrectly predicted at SPR #6. This study showed that the proposed material and fatigue models significantly contributed to the correct prediction of failure location in method B. Furthermore, the effects of the proposed material and fatigue models were decomposed. To do this, the simulation with asymmetric material model was considered along with Mises stress as the damage parameter. In this simulation, SPR#6 was the location for maximum equivalent Mises stress and the predicted failure location. This analysis demonstrated that asymmetric material model alone does not result in correct predictions. Also, this study suggests that stress-based fatigue models are not effective for structures composed of dissimilar materials.

6.4.2.2 Cyclic loading in y-direction

Only one Demo-structure was tested under constant amplitude cyclic loading in the y-direction. The test was performed with a maximum load, F_{max}= 4 kN, and a load ratio, R=0. To force failure to occur at the shock tower to upper rail interface, four out of five SPRs were drilled out for fatigue testing in the y-direction. The FE models for methods A and B simulations were modified accordingly. Figure 6.26 displays the removed SPR joints at the connection between the shock tower and the upper rail.

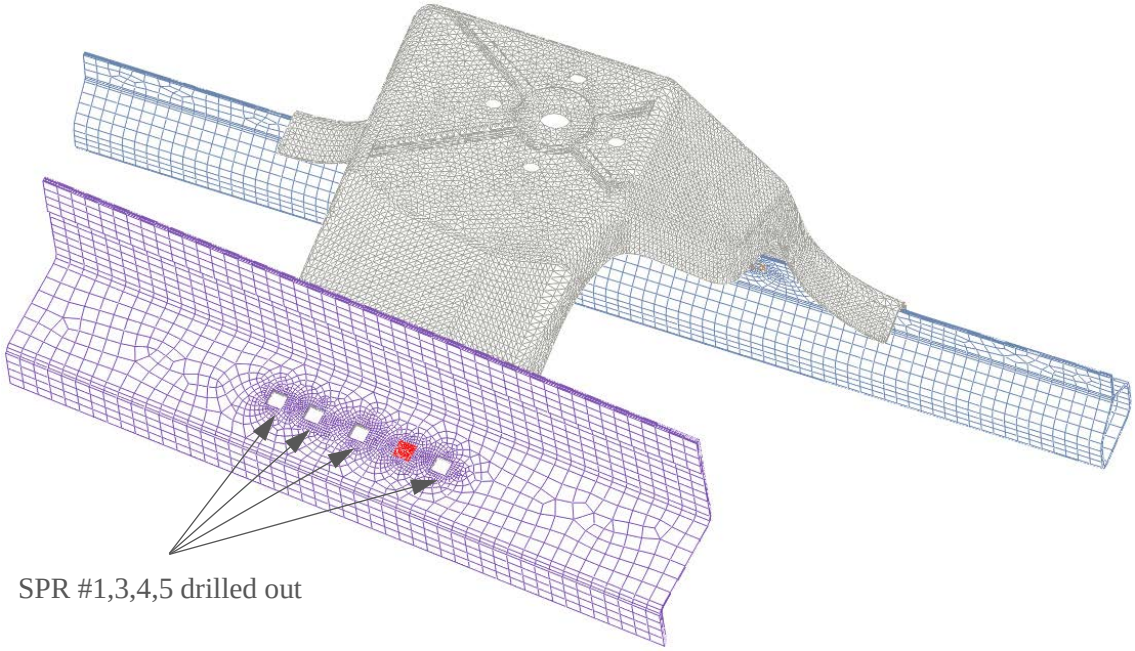

Figure 6.26: Configuration of SPR joint for fatigue testing in the y-direction

The experimental results are shown in Table 6.8 [228].

Table 6.8: Experimental results for fatigue testing of the Demo-structure in the y-direction [228]

No.	Failure location	Loading cycle	Descriptions
1	SPR #2	514,343	crack length = 20 mm

Figure 6.27 displays the failure in SPR#2 for fatigue testing in the y-direction.

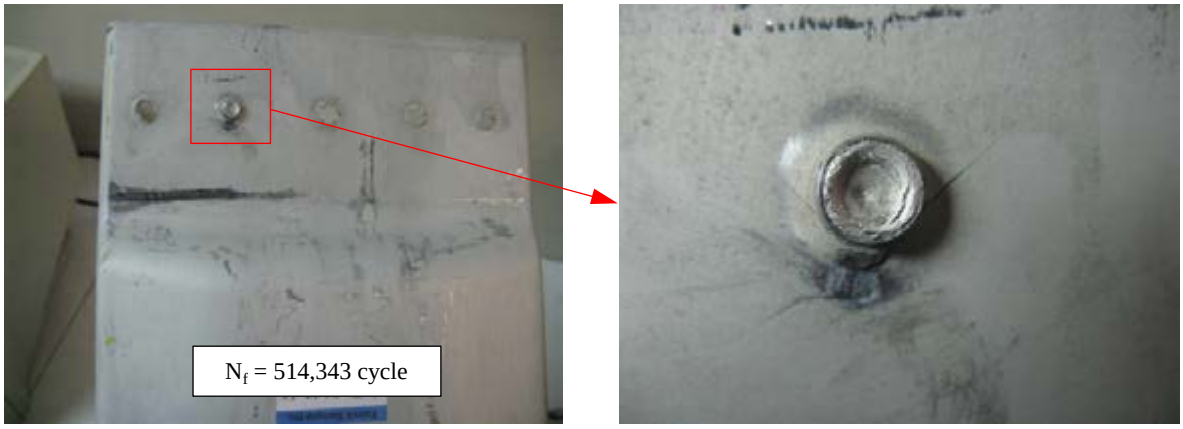

Figure 6.27: Experimental failure in SPR#2 for cyclic loading in the y-direction [228]

The results obtained from simulation methods A and B are given in Table 6.9.

Table 6.9: Simulation results for fatigue testing of the Demo-structure in the y-direction

Simulation	Failure location	Life (cycle)
Method A [228]	SPR #2	4,056
Method B	SPR #2	71,770

According to Table 6.8 and Table 6.9, both methods A and B predicted the correct failure location. Similar to the results in the x-direction, method A underestimates the life for cyclic loading in the y-direction by two orders of magnitude. The fatigue life predicted by method B is closer but still less than the experimental life. As stated earlier, method B predicts crack initiation life, rather than the total life. Figure 6.28 depicts the distribution of fatigue life in different SPRs of the Demo-structure for cyclic loading in the y-direction.

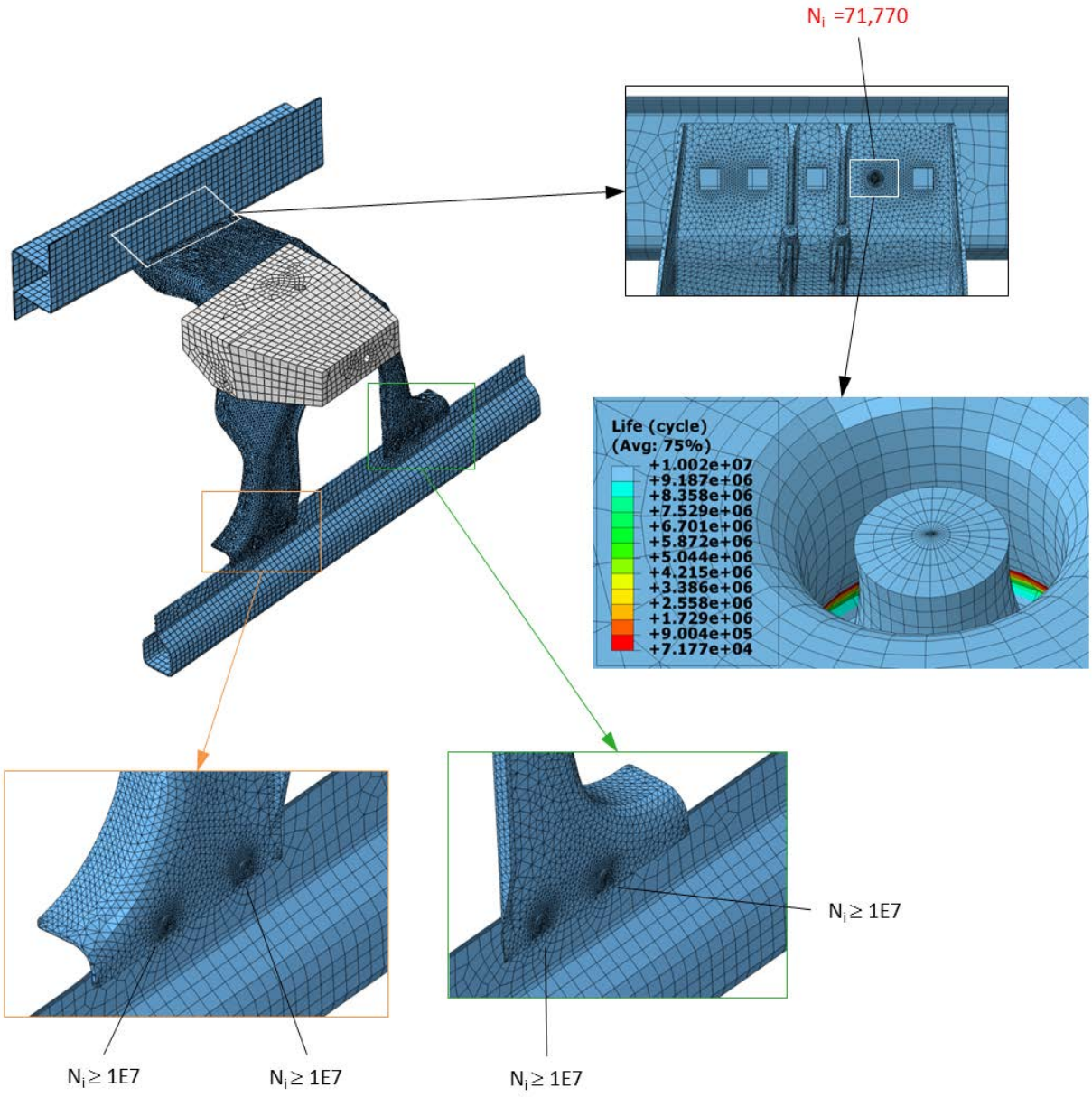

Figure 6.28: Distribution of the crack initiation life obtained from method B for loading in the y-direction

6.4.2.3 Cyclic loading in z-direction

A number of Demo-structures were tested in the z-direction with different constant load amplitudes. However, in most cases fatigue failure occurred where the loading block was attached to the shock tower. The test with a maximum load, F_{max}=7.26 kN, and a load ratio, R=0, was one of the only runs where failure happened away from the attachment area. Therefore, only this load case was considered for simulation. The experimental results from this test are given in Table 6.10 [228].

Table 6.10: Experimental results for fatigue testing of the Demo-structure in z-direction [228]

No.	Failure location	Loading cycle	Descriptions
1	shock tower leg radius	61,137	crack length = 45 mm

Figure 6.29 displays the fatigue crack in the shock tower for loading in the z-direction.

Figure 6.29: Fatigue cracking in the shock tower leg for loading in the z-direction

Table 6.11 summarizes the results obtained from simulation methods A and B.

Table 6.11: Simulation results for fatigue testing of the Demo-structure in the z-direction

Simulation	Failure location	Life (cycle)
Method A [228]	SPR #6	25,905
Method B	SPR #6	32,960

Neither simulation methods predicted the correct failure location. Therefore, the predicted fatigue lives are not comparable to the life obtained from the test. A few factors can contribute to the different failure locations. First, the repeatability of the experimental results is questioned since this test was not duplicated. Also, in the method B simulation the cyclic properties of AM60B cast alloy,

from which the shock tower was fabricated, was based on data available in the literature. Because the properties of cast alloys are quite variable and controlled by the manufacturing process, it is important to use properties associated with the same process parameters, and preferably with the same cast component. Furthermore, even in a specific cast component the material properties can be inconsistent in different regions as a result of dissimilar flow of metal, porosity, *etc*.

Figure 6.30 depicts the distribution of crack initiation life in different SPRs for the Demo-structure for cyclic loading in the z-direction.

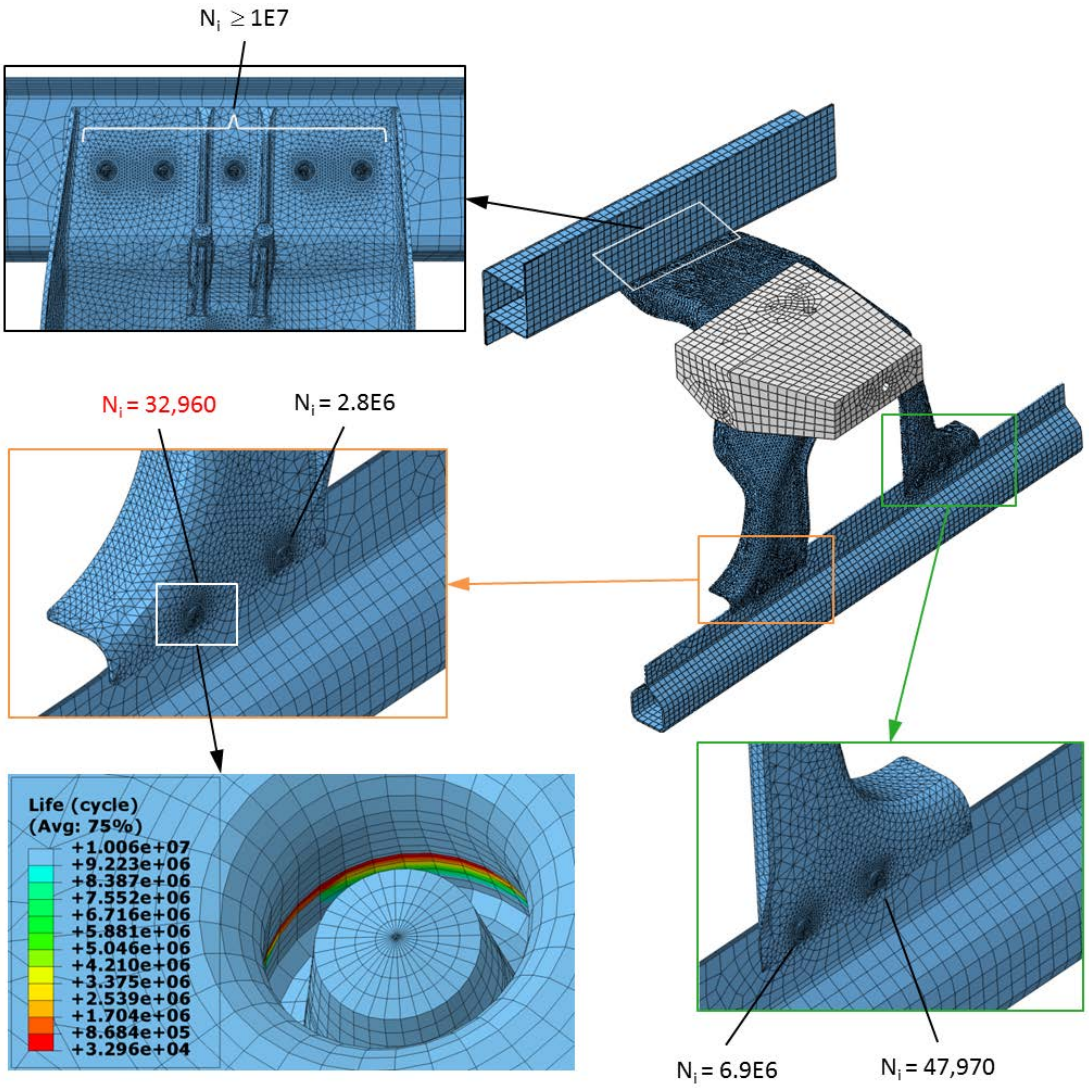

Figure 6.30: Distribution of crack initiation life obtained from method B for loading in the z-direction

6.5 Summary

The developed material model implemented in the UMAT, and the proposed fatigue model, were employed to predict the crack initiation life and location in an automotive structure. The structure, the so-called "*Demo-structure*", was designed and manufactured within the magnesium front end research and development (MFERD) project. The Demo-structure was composed of three components, which were made of different Mg alloys. The components include the upper rail, lower rail, and shock tower, manufactured from AZ31B sheet, AM30 extrusion, and AM60B cast Mg alloys, respectively. The joining process for assembling the Demo-structure was a modified form of self-pierce riveting called laser assisted self-pierce riveting (LSPR).

Material properties for AM30 and AM60B magnesium alloys were obtained from the literature. While the cyclic behavior of AM30 was quite asymmetric, AM60B cast alloy did not show strong asymmetry in unloading and reloading reversals. Therefore, available material models in Abaqus, which assume symmetric hardening, were used for AM30. It was demonstrated that none of these models could properly follow the experimental cyclic behavior. Therefore, the cyclic behavior for all the three participating alloys was input into the UMAT. It was shown that the UMAT could successfully duplicate the experimental stress-strain behavior of these alloys under different cyclic loading conditions. The experimental strain-life curves for the three alloys were converted to energy-life curves according to the proposed definition of total energy.

Five LSPR specimen sets were prepared with different Mg alloy combinations and tested under cyclic loading. LSPR specimen preparation and testing was performed by USAMP, through which the load-life experimental data was provided. FE simulations were performed on the LSPR specimens, and fatigue simulated using the UMAT to convert the load-life data to energy-life curves. Energy-life constants were obtained for different BM and LSPR specimens. The UMAT was slightly modified to incorporate the energy-life constants for the fatigue life calculations.

A number of constant amplitude fatigue tests were performed by USAMP on the Demo-structure, with uniaxial loading applied in the x, y, and z directions. These tests were simulated by applying the same loading and proper boundary conditions to simulate the experimental test setup. The UMAT was utilized in the simulations to account for asymmetric hardening behavior. The results obtained from these simulations were compared with the experimental data and another simulation provided by USAMP, which assumed symmetric material properties for the Mg alloys.

Comparing the simulation results for fatigue testing in the x-direction, showed that the symmetric simulation (USAMP) could not predict the failure location correctly; however, the asymmetric simulation from the current work was successful. Furthermore, the fatigue life from the asymmetric simulation was closer to but still less than the experimental life. A similar situation was observed for fatigue life estimation for loading in the y-direction. Considering that the life obtained from the asymmetric simulation corresponds to crack initiation life, it can be concluded that the asymmetric simulation provide more promising results than the symmetric simulation. For loading in the z-direction, the failure location was not predicted correctly by either the symmetric or asymmetric simulations. One likely reason for the discrepancy was the inconsistent material properties anticipated for the case of AM60B material.

The main differences between the symmetric and asymmetric simulations (methods A and B) were simplified/detail FE model and different material/fatigue models. Some studies were performed to identify the contribution of each factor. A simulation with the detail FE model, symmetric material model, and stress-based fatigue model was run. This simulation was unsuccessful to predict the correct failure location. It was concluded that the proposed material and fatigue models significantly contributed to correct prediction of the failure location in method B. To investigate the effect of the asymmetric material model and the proposed damage parameter, the simulation with asymmetric material model was considered. Assuming Mises equivalent stress as the damage parameter, the failure location was not correctly predicted. This study showed that considering the hardening asymmetry is not sufficient for an effective fatigue model. This investigation also implied that stress-based damage parameters are not applicable to structures with dissimilar materials.

Chapter 7

Conclusions and Future Work

This chapter presents a brief review of the contributions made in this research, and summarizes the major findings regarding application of magnesium spot-welds. These findings may be of interest to the automotive industry. Recommendations for future work are given at the end of this chapter.

7.1 Summary of Contributions

The contributions of this research work are presented in this section in the same order they appeared in the thesis.

1. Fatigue characterization of AZ31B spot-welds

Many researchers have characterized magnesium spot-welds from microstructural and static strength perspectives. However, very limited studies have been performed on fatigue characterization of magnesium spot-welds. The present research provided the following specific new contributions that were not available before:

- Fatigue test results for different configurations, *i.e.*, tensile-shear (TS) and cross-tension (CT) and various nugget sizes of AZ31B spot-welded specimens.

- Measurement of fatigue crack initiation life for spot-welded specimens and discussion of the effect of specimen configuration and cyclic load level on the ratio of crack initiation to total fatigue life.

- Effect of cyclic loading on microstructure and hardness in the weld area, as well as fatigue crack initiation location and propagation path.

2. Cyclic plasticity modeling of metals with asymmetric hardening

Several continuum-based plasticity models are available in the literature. However, the current research developed the first continuum-based cyclic plasticity constitutive model for metals with tension-compression asymmetric hardening behavior. The contributions in this part of the current research can be summarized as follows:

- Existing asymmetric material models were proposed for metal forming applications; therefore, material behavior in the first loading/unloading reversals was of interest. The present thesis focused on stabilized cyclic behavior of asymmetric materials.

- Available asymmetric models are not technically appropriate for wrought magnesium alloys, especially where reverse yielding occurs; they use either a symmetric yield function, or an asymmetric yield function for pressure sensitive materials, or an asymmetric yield function for pressure insensitive materials but with an isotropic hardening rule. The present study proposed the first plasticity model that uses an asymmetric yield function for pressure independent materials, coupled with a combined hardening rule. The asymmetric yield criterion was adopted to account for yield asymmetry. Using a pressure insensitive yield function makes the model applicable to more metals, including magnesium. A combined isotropic-kinematic hardening rule was employed to account for the Bauschinger effect. Specifying the importance of each of these factors requires more research. For instance, bi-axial cyclic tests need to be performed to examine how much improvement was achieved by adopting an asymmetric yield function.

- Another unique feature of the proposed model is it was developed for a general stress state, rather than the plane-stress condition, which was assumed in all existing asymmetric models.

It should also be mentioned that several asymmetric models are available which account for material anisotropy. However, to simplify the implementation, anisotropy was suppressed in the proposed model. This simplification was performed according to some literature which showed that anisotropy in the cyclic behavior of AZ31 is not as pronounced as the yield asymmetry.

3. Material model implementation and verification

To make use of the proposed cyclic plasticity model in solving real-life problems, a procedure was developed for numerical implementation and the corresponding programming logic was

detailed in a flowchart. The model was implemented in a user material (UMAT) subroutine to be used with Abaqus/Standard. The validity of the model and its numerical implementation was verified for a single element model by comparing the simulation and experimental results for different loading scenarios. The proposed material model was also verified by comparing the UMAT results with available solutions based on an alternative approach for one- and two-dimensional problems, which itself had been separately verified.

4. Fatigue model assessment

For the first time, the present research assessed a number of available fatigue models for predicting fatigue life of magnesium spot-welds. The existing fatigue models were classified into three groups: fracture mechanics, structural stress, and local strain approaches. One reference model from each approach was selected for the evaluation. A new fatigue model based on strain energy was proposed in the current study. The reference models as well as the proposed model were assessed by comparing the predicted and experimental fatigue lives for different Mg spot-welded specimens. Considering the asymmetric hardening behavior of wrought magnesium alloys in an existing model and in the new model did not improve the fatigue life prediction. This was attributed to the limited experimental data on spot-welded specimens.

5. “Large-scale” verification of material/fatigue model

In the present thesis the proposed material model and fatigue damage parameter were verified by analyzing a real-life problem from the automotive industry. The structure was manufactured and fatigue tested by the US Automotive Materials Partnership (USAMP). The results obtained from the proposed asymmetric model were compared with available symmetric simulation results and experimental data. This comparison showed that the proposed asymmetric model was more successful in terms of predicting the fatigue failure location and crack initiation life. For instance,

for a load case, the symmetric model did not predict the failure location correctly, and the fatigue life was underestimated by two orders of magnitude. Asymmetric model, for the same load case, predicted the failure location successfully, and the ***crack initiation life*** was one order of magnitude less than the experimental ***total life***.

It should be mentioned that the more reliable fatigue model was obtained at the cost of generating a detailed FE model and more intense computation. To apply the proposed model, the FE model must include details of the joints and any other stress concentration areas, which is often possible only with 3D solid elements. Generating such a FE model is more time consuming than a simplified model using 2D shell elements, which is all that is required for some existing models. The total degree of freedom in such a detailed model with solid elements is significantly more than that in a simplified model, which causes higher computation time.

The asymmetric cyclic plasticity model developed in the current research was used as the material model in the proposed fatigue model. The procedure implemented in the proposed material model is more complex than available symmetric material models in FE packages. Therefore, the asymmetric material model further adds to the computation time. The contribution of the asymmetric material model to computation time is more pronounced when analyzing smooth structures with minimal stress concentration areas. In structures with highly concentrated stresses/strains (such as the structure investigated in this study) plasticity is localized at these stress concentration sites and the effect of the asymmetric material model is limited to small regions. Consequently, the proposed asymmetric material model is recommended to be applied in fatigue problems where the critical component/structure is made of metals with significant asymmetric hardening behavior. Also, employing the proposed material model is suggested where a high cyclic load is applied to the structure and significant plastic deformation is evident, *i.e.*, low cycle fatigue.

7.2 Conclusions

Through this research the following conclusions were made:

1. Within the scope of the experimental work performed in this study, magnesium spot-welds exhibit a substantially uniform hardness distribution in the base metal, AZ31B-H24, and the weld area. This observation for magnesium spot-welds is in contrast to steel and aluminum.

2. Monotonic behavior of AZ31B-H24 is asymmetric under in-plane tension and compression. This behavior is attributed to the textured microstructure and different plastic deformation mechanisms. Hardening curve under in-plane tension is concave-down as a result of the slip deformation mode. However, the flow curve under in-plane compression has a concave-up shape, due to twinning plastic deformation. Furthermore, the base metal shows distinct hardening behavior in rolling and transverse directions, *i.e.*, in-plane anisotropy, as a result of different basal textures.

3. Monotonic loading results in different failure modes in TS and CT spot-welded specimens of AZ31B-H24. TS specimens fail in interfacial and partially-interfacial modes, and CT specimens fail in button-pullout and coupon failure modes. Similar to steel and aluminum, ultimate tensile shear load for magnesium spot-welds is linearly related to nugget diameter.

4. An unusual asymmetric shape of the hysteresis loop is the key feature of the cyclic behavior of the base metal, which was more pronounced at high strain amplitudes. This behavior is related to twinning and untwinning deformation mechanisms in unloading and reloading reversals, respectively. An aspect of the strain-life curve for the base metal is a kink at strain amplitude above which the cyclic hysteresis loop becomes asymmetric, *i.e.*, twin and untwin deformations become evident.

5. Fatigue failure modes in TS spot-welded specimens include interfacial, partially-interfacial, and coupon failure, while CT specimens fail only in the button-pullout mode. Fatigue strength of TS specimens is essentially independent of spot-weld nugget size.

6. Within the testing condition in this study, fatigue crack initiation location for AZ31B spot-welded specimens depends on the cyclic load level. Under high cyclic loading, cracks initiate close to the nugget edge; decreasing the cyclic load causes the cracks to initiate farther from the nugget. In run-out specimens no crack is nucleated. Crack initiation life was calculated in this research based on a 5% increase in non-dimensional compliance. For the cases that total fatigue life is less than one million cycles, crack initiation lives for TS and CT specimens is around 50% and 30% of the total life, respectively. This fraction increases at higher lives.

7. Preliminary comparative studies were performed in this study between magnesium, aluminum and steel spot-welds from static and fatigue points of view. Static and fatigue strengths were characterized in terms of static overload capacity and cyclic load range, respectively. According to this comparison, the static and fatigue strengths of magnesium TS spot-welds are comparable with those of aluminum, but are significantly less than those of steel. More work is required to ensure that this is a general result. For instance, the fatigue strength of spot-welded joints in different configurations should be compared. Also, fatigue strength of dissimilar joints should be studied. The potential for fatigue life improvement for magnesium spot welds was not investigated; this should be further studied.

8. A continuum-based constitutive model was developed, implemented, and verified to model the asymmetric hardening behavior of wrought magnesium alloys under cyclic loading. The Cazacu-Barlat yield function along with associated flow rule and a combined hardening model were used in this model. The algorithm for numerical implementation of the proposed model was presented. The numerical formulation was implemented into a user material (UMAT) subroutine to run with the commercial finite element program, Abaqus/Standard. It was demonstrated that the material model

implemented in the UMAT follows the experimental asymmetric material behavior under different loading conditions.

9. The proposed constitutive model was verified by solving two problems with available solutions. The available solutions used as a benchmark were based on variable material property (VMP) method, the accuracy of which has been already validated. The results obtained from the UMAT and VMP methods showed good agreement for both problems.

10. Several available fatigue models based on different approaches were evaluated by examining the capability to correlate experimental fatigue data for different spot-welded specimens. It was shown that Swellam's model in its original form is unsuccessful in correlating the experimental data for TS and CT specimens. This failure is attributed to neglecting the effect of bending moment on CT specimens. A modified form of Swellam's model and other investigated models were able to successfully correlate the experimental results.

11. A fatigue model was proposed for predicting the location and the life associated with fatigue crack initiation. This model was based on local strain energy, which was calculated from finite element simulations using the UMAT. Strain energy at the hot spot was considered as the fatigue damage parameter. The hot spot was identified as the location with maximum signed equivalent plastic strain at the end of the first loading reversal.

12. The proposed fatigue model, which accounts for asymmetric cyclic hardening behavior, when applied to available spot-weld experimental results, was as successful as available models which assume symmetric hardening behavior. This was attributed to lack of experimental data which was limited to TS and CT specimens in the present research. Moreover, positive R-ratio, which was enforced by the specimen geometries, contributed to the insignificant enhancement.

13. Ignoring asymmetric hardening behavior of wrought magnesium alloys resulted in unreliable fatigue predictions for the structure studied in this research. Considering the asymmetric hardening

behavior and using an energy-based damage parameter has been shown to improve the prediction of the failure location and life. Separating these two effects would require extra studies.

14. Stress-based fatigue models were not effective for the investigated structure made of dissimilar metals, especially where plasticity was involved; rather, energy-based models were more reliable.

7.3 Recommendations and Future Work

As a result of the studies performed in the current research, the following future research is recommended.

1. To make a better comparison between magnesium, aluminum and steel spot-welds, it is suggested to perform fatigue studies on dissimilar spot-welded joints. In the present work, comparisons were based on $d/\sqrt{t}$ (d: nugget diameter, t: sheet thickness). This was the most convenient basis for comparison. However, it would be better to determine the optimum spot-weld parameters (including post-weld processes) for each material prior to making these comparisons.

2. The criterion for fatigue crack initiation in the present work was a 5% increase in compliance. More work is required to correlate this criterion with other initiation criteria, such as 5-10 average grains. This would require interrupting fatigue tests, sectioning specimens, and inspecting for crack initiation. To the best of author's knowledge, this study has not been completed. This verification will be more important if the current fatigue model is extended to include crack propagation, as suggested below.

3. The proposed fatigue model uses local energy at the hot spot as the damage parameter. This model can only account for fatigue crack initiation. Predicting the total fatigue life requires accounting for the crack propagation life. It is suggested to study the crack growth process in

magnesium spot-welds, and develop a model based on fracture mechanics for predicting the crack propagation life.

4. The accuracy of the yield function and the hardening rule utilized in this study should be further verified with biaxial testing of AZ31B sheet.

5. The superior predictions of the proposed fatigue model over conventional models may arise from the asymmetric material model, and/or the energy-based damage parameter. To decompose the effects of these two factors and possibly simplify the proposed model, one should examine a symmetric material model along with a strain- or energy-based damage parameter.

Appendix A

Flow rule associated with the Cazacu-Barlat yield function

The equivalent stress that corresponds to the Cazacu-Barlat yield criterion is

$$\bar{\sigma} = A\left[(J_2)^{3/2} - C\,J_3\right]^{\frac{1}{3}} \quad , \tag{A.1}$$

where, A is a constant, $J_2 = \frac{1}{2}tr(\boldsymbol{S}^2)$, and $J_3 = \frac{1}{3}tr(\boldsymbol{S}^3)$ are the second and third invariants of deviatoric stress tensor, $\boldsymbol{S}$.

The constant A and invariants J_2 and J_3 for isotropic materials are

$$A = 3\left(3^{3/2} - 2c\right)^{-1/3} \quad , \tag{A.2}$$

$$J_2 = \frac{1}{3}\left(\sigma_x^2 + \sigma_y^2 + \sigma_z^2 - \sigma_x\sigma_y - \sigma_y\sigma_z - \sigma_x\sigma_z\right) + \tau_{xy}^2 + \tau_{yz}^2 + \tau_{xz}^2 \quad , \tag{A.3}$$

$$\begin{aligned} J_3 = \frac{1}{27}\big(&2\sigma_x^3 + 2\sigma_y^3 + 2\sigma_z^3 - 3\sigma_x^2\sigma_y - 3\sigma_y^2\sigma_x - 3\sigma_y^2\sigma_z - 3\sigma_z^2\sigma_y - \\ &3\sigma_x^2\sigma_z - 3\sigma_z^2\sigma_x + 12\sigma_x\sigma_y\sigma_z\big) + \frac{1}{3}\big[\left(\sigma_x + \sigma_y - 2\sigma_z\right)\tau_{xy}^2 + \left(-2\sigma_x + \sigma_y + \right. \\ &\left.\sigma_z\right)\tau_{yz}^2 + \left(\sigma_x - 2\sigma_y + \sigma_z\right)\tau_{xz}^2\big] + 2\tau_{xy}\tau_{yz}\tau_{xz} \quad . \end{aligned} \tag{A.4}$$

Applying the chain rule

$$\frac{\partial\bar{\sigma}}{\partial\sigma_{ij}} = \frac{\partial\bar{\sigma}}{\partial J_2}\frac{\partial J_2}{\partial\sigma_{ij}} + \frac{\partial\bar{\sigma}}{\partial J_3}\frac{\partial J_3}{\partial\sigma_{ij}} \quad , \tag{A.5}$$

where

$$\frac{\partial\bar{\sigma}}{\partial J_2} = \frac{A^3 J_2^{1/2}}{2\bar{\sigma}^2} \quad , \tag{A.6}$$

$$\frac{\partial\bar{\sigma}}{\partial J_3} = -\frac{C}{3}\frac{A^3}{\bar{\sigma}^2} \quad , \tag{A.7}$$

and other partial derivatives in equation (A.5) are simply obtained from equations (A.3) and (A.4).

Appendix B

Flowchart for numerical implementation of the two-surface plasticity

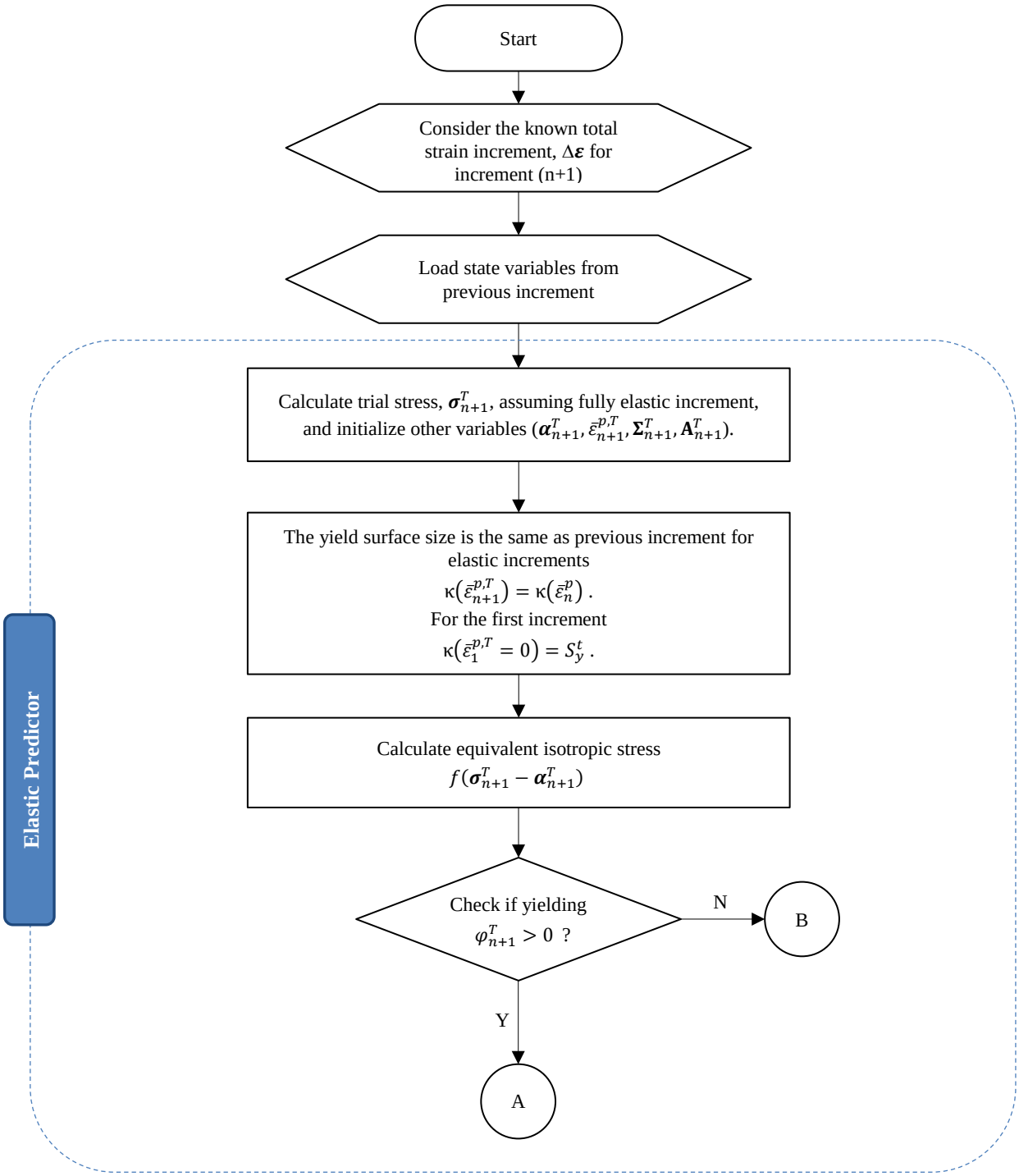

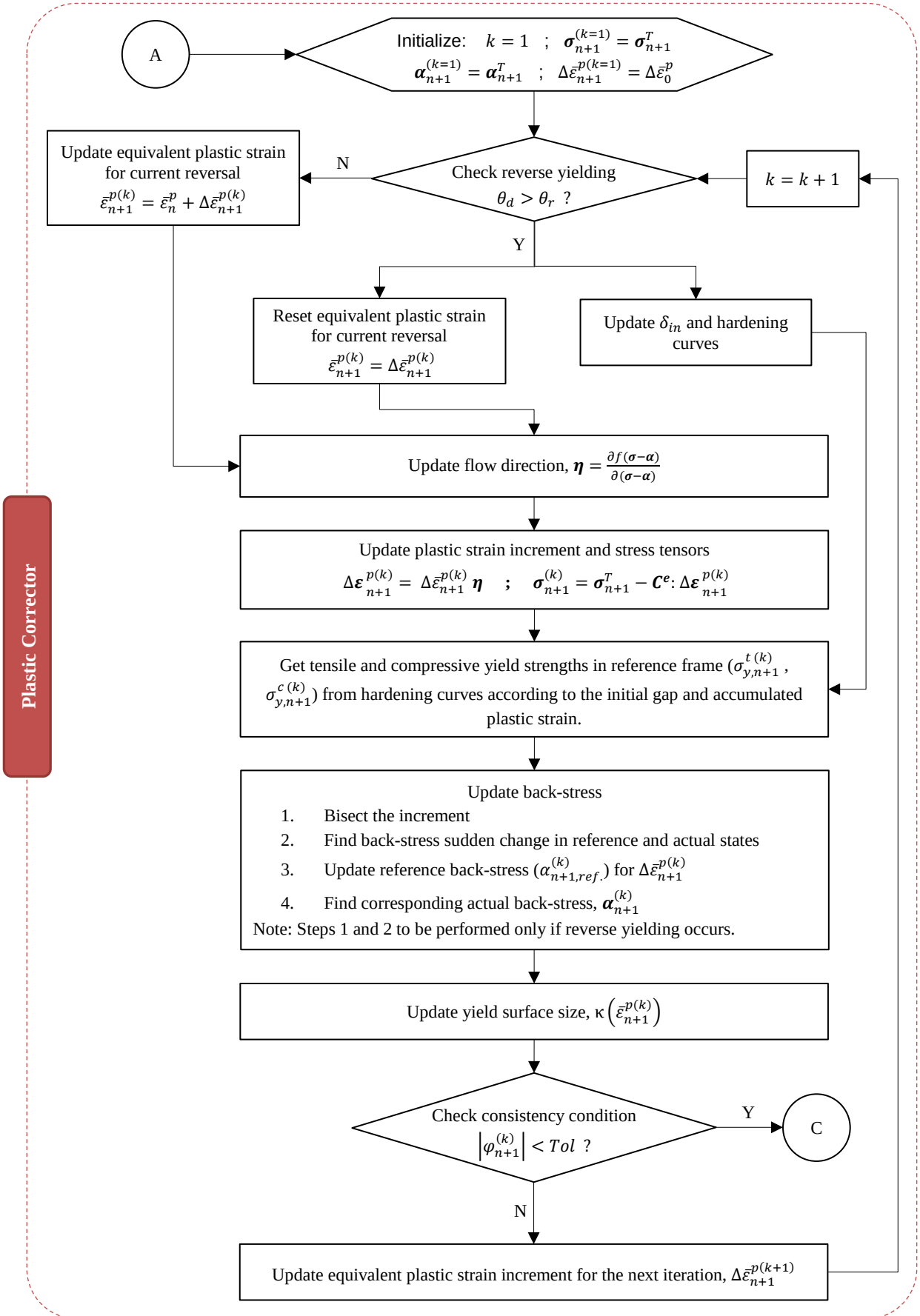
Plastic Corrector
A
Initialize: $k = 1$; $\boldsymbol{\sigma}_{n+1}^{(k=1)} = \boldsymbol{\sigma}_{n+1}^{T}$
$\boldsymbol{\alpha}_{n+1}^{(k=1)} = \boldsymbol{\alpha}_{n+1}^{T}$; $\Delta\bar{\varepsilon}_{n+1}^{p(k=1)} = \Delta\bar{\varepsilon}_{0}^{p}$
Check reverse yielding
$\theta_d > \theta_r$?
N
Update equivalent plastic strain for current reversal
$\bar{\varepsilon}_{n+1}^{p(k)} = \bar{\varepsilon}_{n}^{p} + \Delta\bar{\varepsilon}_{n+1}^{p(k)}$
$k = k + 1$
Y
Reset equivalent plastic strain for current reversal
$\bar{\varepsilon}_{n+1}^{p(k)} = \Delta\bar{\varepsilon}_{n+1}^{p(k)}$
Update δ_{in} and hardening curves
Update flow direction, $\boldsymbol{\eta} = \frac{\partial f(\boldsymbol{\sigma}-\boldsymbol{\alpha})}{\partial(\boldsymbol{\sigma}-\boldsymbol{\alpha})}$
Update plastic strain increment and stress tensors
$\Delta\boldsymbol{\varepsilon}_{n+1}^{p(k)} = \Delta\bar{\varepsilon}_{n+1}^{p(k)}\,\boldsymbol{\eta}$; $\boldsymbol{\sigma}_{n+1}^{(k)} = \boldsymbol{\sigma}_{n+1}^{T} - \boldsymbol{C}^{e}\colon\Delta\boldsymbol{\varepsilon}_{n+1}^{p(k)}$
Get tensile and compressive yield strengths in reference frame ($\sigma_{y,n+1}^{t\,(k)}$, $\sigma_{y,n+1}^{c\,(k)}$) from hardening curves according to the initial gap and accumulated plastic strain.
Update back-stress
1. Bisect the increment
2. Find back-stress sudden change in reference and actual states
3. Update reference back-stress ($\alpha_{n+1,ref.}^{(k)}$) for $\Delta\bar{\varepsilon}_{n+1}^{p(k)}$
4. Find corresponding actual back-stress, $\boldsymbol{\alpha}_{n+1}^{(k)}$
Note: Steps 1 and 2 to be performed only if reverse yielding occurs.
Update yield surface size, $\kappa\left(\bar{\varepsilon}_{n+1}^{p(k)}\right)$
Check consistency condition
$\left|\varphi_{n+1}^{(k)}\right| < Tol$?
Y
C
N
Update equivalent plastic strain increment for the next iteration, $\Delta\bar{\varepsilon}_{n+1}^{p(k+1)}$

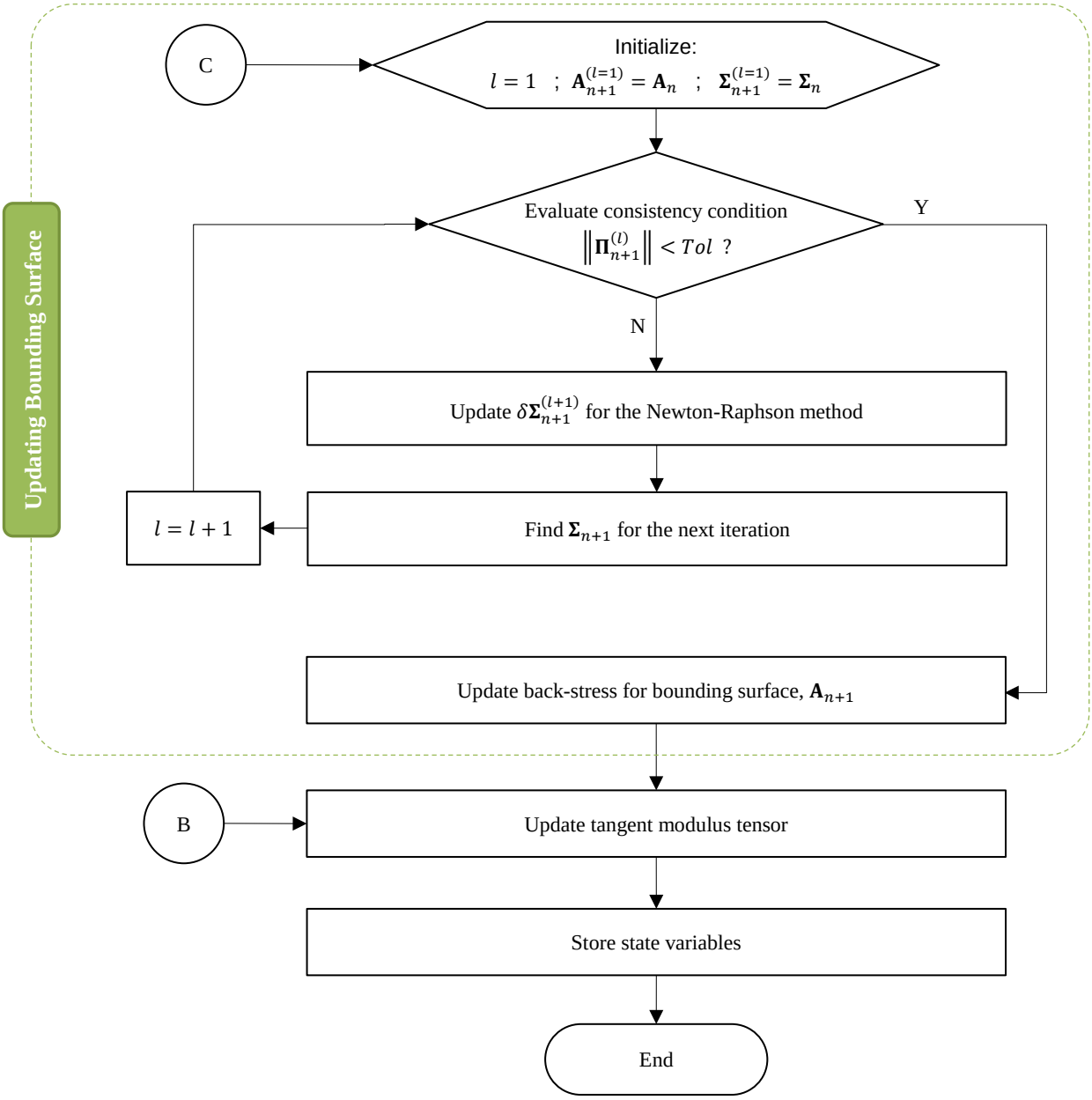

Figure B.1: Flowchart for numerical implementation of the two-surface plasticity model

References

[1] D. Radaj, *Design and Analysis of Fatigue Resistant Welded Structures*, Abington, Cambridge: Woodhead Publishing Ltd., 1990.

[2] W. Miller, L. Zhuang, J. Bottema, A.J. Wittebrood, P. De Smet, A. Haszler, and A. Vieregge, *Recent Development in Aluminium Alloys for the Automotive Industry*, Materials Science and Engineering: A (2000), 280(1): p. 37-49.

[3] J. Al Bin Mousa, *Multiaxial Fatigue Characterization and Modeling of AZ31B Magnesium Extrusion*, Ph.D thesis, University of Waterloo, 2011.

[4] H. Friedrich and S. Schumann, *Research for a "New Age of Magnesium" in the Automotive Industry*, Journal of Materials Processing Technology (2001), 117(3): p. 276-281.

[5] M.K. Kulekci, *Magnesium and Its Alloys Applications in Automotive Industry*, International Journal of Advanced Manufacturing Technology (2008), 39(9-10): p. 851-865.

[6] W. Chen, P. Ackerson, and P. Molian, *CO2 Laser Welding of Galvanized Steel Sheets using Vent Holes*, Materials & Design (2009), 30(2): p. 245-251.

[7] S. Aslanlar, A. Ogur, U. Ozsarac, and E. Ilan, *Welding Time Effect on Mechanical Properties of Automotive Sheets in Electrical Resistance Spot Welding*, Materials & Design (2008), 29(7): p. 1427-1431.

[8] J.C. Ion, *Laser Beam Welding of Wrought Aluminium Alloys*, Science and Technology of Welding and Joining (2000), 5(5): p. 265-276.

[9] H. Aydin, A. Bayram, A. Uguz, and K.S. Akay, *Tensile Properties of Friction Stir Welded Joints of 2024 Aluminum Alloys in Different Heat-treated-state*, Materials & Design (2009), 30(6): p. 2211-2221.

[10] X. Cao, M. Jahazi, J.P. Immarigeon, and W. Wallace, *A Review of Laser Welding Techniques for Magnesium Alloys*, Journal of Materials Processing Technology (2006), 171(2): p. 188-204.

[11] L.K. Pan, C.C. Wang, Y.C. Hsiao, and K.C. Ho, *Optimization of Nd: YAG Laser Welding onto Magnesium Alloy via Taguchi Analysis*, Optics & Laser Technology (2005), 37(1): p. 33-42.

[12] C.T. Chi, C.G. Chao, T.F. Liu, and C.C. Wang, *A Study of Weldability and Fracture Modes in Electron Beam Weldments of AZ Series Magnesium Alloys*, Materials Science and Engineering: A (2006), 435: p. 672-680.

[13] A. Munitz, C. Cotler, H. Shaham, and G. Kohn, *Electron Beam Welding of Magnesium AZ91D Plates*, Welding Journal (2000), 79(7): p. 202s-208s.

[14] L. Commin, M. Dumont, J.E. Masse, and L. Barrallier, *Friction Stir Welding of AZ31 Magnesium Alloy Rolled Sheets: Influence of Processing Parameters*, Acta Materialia (2009), 57(2): p. 326-334.

[15] J.A. Esparza, W.C. Davis, E.A. Trillo, and L.E. Murr, *Friction-stir Welding of Magnesium Alloy AZ31B,* Journal of Materials Science Letters (2002), 21(12): p. 917-920.

[16] R.W. Rathbun, D.K. Matlock, and J.G. Speer, *Fatigue Behavior of Spot Welded High-Strength Sheet Steels,* Welding Journal (2003), 82(8): p. 207s-218s.

[17] D.J. Radakovic and M. Tumuluru, *Predicting Resistance Spot Weld Failure Modes in Shear Tension Tests of Advanced High-Strength Automotive Steels,* Welding Journal (2008), 87(4): p. 96s-105s.

[18] M.H. Swellam, P. Kurath, and F.V. Lawrence, *Electric-Potential-Drop Studies of Fatigue Crack Development in Tensile-Shear Spot Welds,* Advances in Fatigue Lifetime Predictive Techniques (1992), 1122: p. 383-401.

[19] S.D. Sheppard, *Estimation of Fatigue Propagation Life in Resistance Spot Welds,* in *Advances in Fatigue Lifetime Predictive Techniques: Second Volume*, ASTM STP 1211, (1993): p. 169-185.

[20] N. Pan and S. Sheppard, *Spot Welds Fatigue Life Prediction With Cyclic Strain Range,* International Journal of Fatigue (2002), 24(5): p. 519-528.

[21] H.E. Friedrich and B.L. Mordike, *Magnesium Technology: Metallurgy, Design Data, Applications*, Springer, 2006.

[22] B. Mordike and T. Ebert, *Magnesium: Properties—Applications—Potential,* Materials Science and Engineering: A (2001), 302(1): p. 37-45.

[23] M. Gupta and N.M.L. Sharon, *Magnesium, Magnesium Alloys, and Magnesium Composites,* Wiley, 2011.

[24] M.M. Avedesian and H. Baker, *ASM Specialty Handbook: Magnesium and Magnesium Alloys,* Asm International, 1999.

[25] E.F. Emley, *Principles of Magnesium Technology*, Oxford Pergamon Press Inc., 1966.

[26] C.S. Roberts, *Magnesium and Its Alloys*, Wiley, 1960.

[27] I. Polmear, *Light Alloys: from Traditional Alloys to Nanocrystals*, Butterworth-Heinemann, 2006.

[28] R.W.K. Honeycombe, *The Plastic Deformation of Metals*, New York: St. Martin's Press, 1975.

[29] D.C. Stouffer and L.T. Dame, *Inelastic Deformation of Metals: Models, Mechanical Properties, and Metallurgy*, John Wiley & Sons, 1996.

[30] Z.X. Guo, *The Deformation and Processing of Structural Materials*, Woodhead Pub Limited, 2005.

[31] R.W. Hertzberg, *Deformation and Fracture Mechanics of Engineering Materials*, New York: Wiley, 1996.

[32] W.F. Hosford and R.M. Caddell, *Metal Forming: Mechanics and Metallurgy*, Cambridge University Press, 2011.

[33] W.D. Callister and D.G. Rethwisch, *Materials Science and Engineering: An Introduction*, New York: Wiley, 2007.

[34] A. Staroselsky and L. Anand, *A Constitutive Model for HCP Materials Deforming by Slip and Twinning: Application to Magnesium Alloy AZ31B*, International Journal of Plasticity (2003), 19(10): p. 1843-1864.

[35] ASTM, B951-11, *Standard Practice for Codification of Unalloyed Magnesium and Magnesium-Alloys, Cast and Wrought*, 2011.

[36] ASTM, B296, *Standard Practice for Temper Designations of Magnesium Alloys, Cast and Wrought*, 2008.

[37] F. Campbell, *Joining: Understanding the Basics*, ASM International, 2011.

[38] M. Jackson, *Welding Methods and Metallurgy*, London: Charles Griffin Ltd., 1967.

[39] M.f. Dummies. *What is Spot Welding?* 2011 [cited 2013 April 23]; Available from: http://metallurgyfordummies.com/what-is-spot-welding/.

[40] R.A. Lindberg and N.R. Braton, *Welding and other Joining Processes*, Boston: Allyn and Bacon, 1976.

[41] Y.J. Chao, *Ultimate Strength and Failure Mechanism of Resistance Spot Weld Subjected to Tensile, Shear, or Combined Tensile/Shear Loads*, Journal of Engineering Materials and Technology (2003), 125(2): p. 125-132.

[42] H. Cary, *Modern Welding Technology*, 4th Ed., New Jersey: Prentice Hall, 1998.

[43] M. Salem, *Control and Power Supply for Resistance Spot Welding (RSW)*, Ph.D thesis, University of Western Ontario, 2011.

[44] W. Li, E. Feng, D. Cerjanec, and G.A. Grzadzinski, *Energy Consumption in AC and MFDC Resistance Spot Welding*, in *Sheet Metal Welding Conference XI*, Sterling Heights, Michigan (2004).

[45] B. Brown, *A Comparison of AC and DC Resistance Welding of Automotive Steels*, Welding Journal (1987), 66(1): p. 18-23.

[46] L. Liu, *Welding and Joining of Magnesium Alloys*, Woodhead Pub Ltd. , 2010.

[47] AWS, D17.2/D17.2M, *Specification for Resistance Welding for Aerospace Applications*, 2007.

[48] S. Zhou, L. Liu, J.P. Jung, M.Y. Lee, and Y.N. Zhou, *Effects of Welding Parameters and Surface Pretreatments on Resistance Spot Welding of AZ31B Mg Alloy*, Metals and Materials International (2010), 16(6): p. 967-974.

[49] E. Del Vecchio, *Resistance Welding Manual*, Resistance welder manufacturers' association, 1956.

[50] C. Bettles and M. Gibson, *Current Wrought Magnesium Alloys: Strengths and Weaknesses,* JOM Journal of the Minerals, Metals and Materials Society (2005), 57(5): p. 46-49.

[51] O. Duygulu and S.R. Agnew, *The Effect of Temperature and Strain Rate on the Tensile Properties of Textured Magnesium Alloy AZ31B Sheet,* Magnesium Technology (2003), 237: p. 242.

[52] X. Lou, M. Li, R. Boger, S. Agnew, and R. Wagoner, *Hardening Evolution of AZ31B Mg Sheet,* International Journal of Plasticity (2007), 23(1): p. 44-86.

[53] Z. Keshavarz and M.R. Barnett, *EBSD Analysis of Deformation Modes in Mg–3Al–1Zn,* Scripta Materialia (2006), 55(10): p. 915-918.

[54] R. Mises, *Mechanik der Plastischen Formänderung von Kristallen,* Journal of Applied Mathematics and Mechanics/Zeitschrift für Angewandte Mathematik und Mechanik (1928), 8(3): p. 161-185.

[55] S.G.I. Taylor, *Plastic Strain in Metals,* Journal of the Institute of Metals (1938), 62: p. 307-324.

[56] U. Kocks and D. Westlake, *The Importance of Twinning for the Ductility of CPH Polycrystals,* Transactions of the Metallurgical Society of AIME (1967), 239(7): p. 1107-1109.

[57] D. Brown, S. Agnew, M. Bourke, T. Holden, S. Vogel, and C. Tomé, *Internal Strain and Texture Evolution during Deformation Twinning in Magnesium,* Materials Science and Engineering: A (2005), 399(1): p. 1-12.

[58] S. Kleiner and P. Uggowitzer, *Mechanical Anisotropy of Extruded Mg–6% Al–1% Zn Alloy,* Materials Science and Engineering: A (2004), 379(1): p. 258-263.

[59] A. Jain, O. Duygulu, D. Brown, C. Tomé, and S. Agnew, *Grain Size Effects on the Tensile Properties and Deformation Mechanisms of a Magnesium Alloy, AZ31B, Sheet,* Materials Science and Engineering: A (2008), 486(1): p. 545-555.

[60] M.R. Barnett, *Twinning and the Ductility of Magnesium Alloys, Part I: "Tension" Twins,* Materials Science and Engineering: A (2007), 464(1): p. 1-7.

[61] Y. Wang and J. Huang, *The Role of Twinning and Untwinning in Yielding Behavior in Hot-Extruded Mg–Al–Zn Alloy,* Acta Materialia (2007), 55(3): p. 897-905.

[62] L. Wu, A. Jain, D. Brown, G. Stoica, S. Agnew, B. Clausen, D. Fielden, and P. Liaw, *Twinning–Detwinning Behavior during the Strain-Controlled Low-Cycle Fatigue Testing of a Wrought Magnesium Alloy, ZK60A,* Acta Materialia (2008), 56(4): p. 688-695.

[63] S.R. Agnew and Ö. Duygulu, *Plastic Anisotropy and the Role of Non-basal Slip in Magnesium Alloy AZ31B,* International Journal of Plasticity (2005), 21(6): p. 1161-1193.

[64] E. Yukutake, J. Kaneko, and M. Sugamata, *Anisotropy and Non-Uniformity in Plastic Behavior of AZ31 Magnesium Alloy Plates,* Materials Transactions (2003), 44(4): p. 452-457.

[65] S.H. Park, S.G. Hong, W. Bang, and C.S. Lee, *Effect of Anisotropy on the Low-Cycle Fatigue Behavior of Rolled AZ31 Magnesium Alloy*, Materials Science and Engineering: A (2010), 527(3): p. 417-423.

[66] F. Lv, F. Yang, Q. Duan, Y. Yang, S. Wu, S. Li, and Z. Zhang, *Fatigue Properties of Rolled Magnesium Alloy (AZ31) Sheet: Influence of Specimen Orientation*, International Journal of Fatigue (2011), 33(5): p. 672-682.

[67] D.W. Brown, A. Jain, S.R. Agnew, and B. Clausen, *Twinning and Detwinning during Cyclic Deformation of Mg Alloy AZ31B*, Materials science forum (2007), 539-543(4): p. 3407-3413.

[68] L. Wu, S. Agnew, Y. Ren, D. Brown, B. Clausen, G. Stoica, H. Wenk, and P. Liaw, *The Effects of Texture and Extension Twinning on the Low-Cycle Fatigue Behavior of a Rolled Magnesium Alloy, AZ31B*, Materials Science and Engineering: A (2010), 527(26): p. 7057-7067.

[69] X. Lin and D. Chen, *Strain Controlled Cyclic Deformation Behavior of an Extruded Magnesium Alloy*, Materials Science and Engineering: A (2008), 496(1): p. 106-113.

[70] J. Bauschinger, *On the Change of the Elastic Limit and the Strength of Iron and Steel, by Drawing out, by Heating and Cooling, and by Repetition of Loading (Summary)*, Minutes of Proceedings of the Institution of Civil Engineers with Other Selected and Abstracted Papers (1886), 87: p. 463.

[71] H. Margolin, F. Hazaveh, and H. Yaguchi, *The Grain Boundary Contribution to the Bauschinger Effect*, Scripta Metallurgica (1978), 12(12): p. 1141-1145.

[72] T. Hasegawa, T. Yakou, and U. Kocks, *Forward and Reverse Rearrangements of Dislocations in Tangled Walls*, Materials Science and Engineering (1986), 81: p. 189-199.

[73] I. Karaman, H. Sehitoglu, Y.I. Chumlyakov, I. Kireeva, and H.J. Maier, *The Effect of Twinning and Slip on the Bauschinger Effect of Hadfield Steel Single Crystals*, Metallurgical and Materials Transactions A (2001), 32(3): p. 695-706.

[74] S. Begum, D. Chen, S. Xu, and A.A. Luo, *Low Cycle Fatigue Properties of an Extruded AZ31 Magnesium Alloy*, International Journal of Fatigue (2009), 31(4): p. 726-735.

[75] L. Liu, S.Q. Zhou, Y.H. Tian, J.C. Feng, J.P. Jung, and Y.N. Zhou, *Effects of Surface Conditions on Resistance Spot Welding of Mg Alloy AZ31*, Science and Technology of Welding and Joining (2009), 14(4): p. 356-361.

[76] B. Lang, D.Q. Sun, G.Z. Li, and X.F. Qin, *Effects of Welding Parameters on Microstructure and Mechanical Properties of Resistance Spot Welded Magnesium Alloy Joints*, Science and Technology of Welding and Joining (2008), 13(8): p. 698-704.

[77] H. Liu, M.G. Wang, X.Q. Zhang, and W. Dong, *Effect of Electrode Tip Shape on Strength and Microstructure in Resistance Spot Welding of AZ31B Magnesium Alloy*, Advanced Materials Research (2011), 239: p. 2528-2532.

[78] J.C. Feng, Y.R. Wang, and Z.D. Zhang, *Nugget Growth Characteristic for AZ31B Magnesium Alloy during Resistance Spot Welding*, Science and Technology of Welding and Joining (2006), 11(2): p. 154-162.

[79] W. Xu, D. Chen, L. Liu, H. Mori, and Y. Zhou, *Microstructure and Mechanical Properties of Weld-Bonded and Resistance Spot Welded Magnesium-to-Steel Dissimilar Joints,* Materials Science and Engineering: A (2012), 537: p. 11-24.

[80] V. Patel, S. Bhole, and D. Chen, *Improving Weld Strength of Magnesium to Aluminium Dissimilar Joints via tin Interlayer During Ultrasonic Spot Welding,* Science and Technology of Welding & Joining (2012), 17(5): p. 342-347.

[81] D.Q. Sun, B. Lang, D.X. Sun, and J.B. Li, *Microstructures and Mechanical Properties of Resistance Spot Welded Magnesium Alloy Joints,* Materials Science and Engineering: A (2007), 460: p. 494-498.

[82] B. Lang, D.Q. Sun, Z.Z. Xuan, and X.F. Qin, *Hot Cracking of Resistance Spot Welded Magnesium Alloy,* ISIJ International (2008), 48(1): p. 77-82.

[83] L. Xiao, L. Liu, D. Chen, S. Esmaeili, and Y. Zhou, *Resistance Spot Weld Fatigue Behavior and Dislocation Substructures in Two Different Heats of AZ31 Magnesium Alloy,* Materials Science and Engineering: A (2011), 529: p. 81-87.

[84] N.K. Babu, S. Brauser, M. Rethmeier, and C. Cross, *Characterization of Microstructure and Deformation Behaviour of Resistance Spot Welded AZ31 Magnesium Alloy,* Materials Science and Engineering: A (2012), 549: p. 149-156.

[85] L. Xiao, L. Liu, Y. Zhou, and S. Esmaeili, *Resistance-Spot-Welded AZ31 Magnesium Alloys: Part I. Dependence of Fusion Zone Microstructures on Second-Phase Particles,* Metallurgical and Materials Transactions A (2010), 41(6): p. 1511-1522.

[86] AWS, D8.9M, *Recommended Practices for Test Methods for Evaluating the Resistance Spot Welding Behavior of Automotive Sheet Steel Materials,* 2002.

[87] L. Liu, L. Xiao, J. Feng, Y. Tian, S. Zhou, and Y. Zhou, *Resistance Spot Welded AZ31 Magnesium Alloys, Part II: Effects of Welding Current on Microstructure and Mechanical Properties,* Metallurgical and Materials Transactions A (2010), 41(10): p. 2642-2650.

[88] M. Pouranvari, H. Asgari, S. Mosavizadch, P. Marashi, and M. Goodarzi, *Effect of Weld Nugget Size on Overload Failure Mode of Resistance Spot Welds,* Science and Technology of Welding & Joining (2007), 12(3): p. 217-225.

[89] M.E. Nixon, O. Cazacu, and R.A. Lebensohn, *Anisotropic Response of High-Purity α-Titanium: Experimental Characterization and Constitutive Modeling,* International Journal of Plasticity (2010), 26(4): p. 516-532.

[90] M.G. Lee, R. Wagoner, J. Lee, K. Chung, and H. Kim, *Constitutive Modeling for Anisotropic/Asymmetric Hardening Behavior of Magnesium Alloy Sheets,* International Journal of Plasticity (2008), 24(4): p. 545-582.

[91] D.C. Drucker, *A Definition of Stable Inelastic Material,* Journal of Applied Mechanics (1957), 26(1): p. 101-106.

[92] J.J. Skrzypek and R.B. Hetnarski, *Plasticity and Creep: Theory, Examples, and Problems,* CRC Press, 1993.

[93] A.S. Khan and S. Huang, *Continuum Theory of Plasticity,* Wiley-Interscience, 1995.

[94] H.E. Tresca, *Mémoires sur l'écoulement des corps solides*, Imprimerie impériale, 1869.

[95] R. von Mises, *Mechanik der Festen Körper im Plastisch Deformablen Zustand,* Göttin. Nachr. Math. Phys (1913), 1: p. 582-592.

[96] D.C. Drucker, *The Relation of Experiments to Mathematical Theories of Plasticity,* Journal of Applied Mechanics (1948), 16: p. 349-357.

[97] R. Hill, *A Theory of the Yielding and Plastic Flow of Anisotropic Metals,* Proceedings of the Royal Society of London: Series A (1948), 193(1033): p. 281-297.

[98] A. Karafillis and M. Boyce, *A General Anisotropic Yield Criterion Using Bounds and a Transformation Weighting Tensor,* Journal of the Mechanics and Physics of Solids (1993), 41(12): p. 1859-1886.

[99] W. Hosford, *A Generalized Isotropic Yield Criterion,* Journal of Applied Mechanics (1972), 39: p. 607-609.

[100] R. Hill, *Constitutive Modelling of Orthotropic Plasticity in Sheet Metals*, Journal of the Mechanics and Physics of Solids (1990), 38(3): p. 405-417.

[101] F. Barlat, R.C. Becker, Y. Hayashida, Y. Maeda, M. Yanagawa, K. Chung, J.C. Brem, D.J. Lege, K. Matsui, S.J. Murtha, and S. Hattori, *Yielding Description for Solution Strengthened Aluminum Alloys,* International Journal of Plasticity (1997), 13(4): p. 385-401.

[102] O. Cazacu and F. Barlat, *Application of the Theory of Representation to Describe Yielding of Anisotropic Aluminum Alloys,* International Journal of Engineering Science (2003), 41(12): p. 1367-1385.

[103] W. Hosford, *Texture Strengthening,* Metals Engineering Quarterly (1966), 6(4): p. 13-19.

[104] O. Cazacu and F. Barlat, *A Criterion for Description of Anisotropy and Yield Differential Effects in Pressure-Insensitive Metals,* International Journal of Plasticity (2004), 20(11): p. 2027-2045.

[105] S. Graff, D. Steglich, and W. Brocks, *Forming of Magnesium–Crystal Plasticity and Plastic Potentials,* Advanced Engineering Materials (2007), 9(9): p. 803-806.

[106] O. Cazacu, B. Plunkett, and F. Barlat, *Orthotropic Yield Criterion for Hexagonal Closed Packed Metals,* International Journal of Plasticity (2006), 22(7): p. 1171-1194.

[107] R. Hill, *The Mathematical Theory of Plasticity*, London: Oxford University Press, 1950.

[108] M. Li, *Constitutive Modeling of Slip, Twinning, and Untwinning in AZ31B Magnesium,* Ph.D thesis, The Ohio State University, 2006.

[109] W. Prager, *A New Method of Analyzing Stresses and Strains in Work-Hardening Plastic Solids,* Journal of Applied Mechanics (1956), 23: p. 493-496.

[110] H. Ziegler, *A Modification of Prager's Hardening Rule,* Quarternery Applied Mathematics (1959), 17: p. 55-65.

[111] M.G. Lee, D. Kim, C. Kim, M. Wenner, R. Wagoner, and K. Chung, *A Practical Two-surface Plasticity Model and its Application to Spring-Back Prediction*, International Journal of Plasticity (2007), 23(7): p. 1189-1212.

[112] C. Frederick and P. Armstrong, *A Mathematical Representation of the Multiaxial Bauschinger Effect*, Materials at High Temperatures (1966), 24(1): p. 1-26.

[113] J. Chaboche, *Time-independent Constitutive Theories for Cyclic Plasticity*, International Journal of Plasticity (1986), 2(2): p. 149-188.

[114] Z. Mroz, *On the Description of Anisotropic Workhardening*, Journal of the Mechanics and Physics of Solids (1967), 15(3): p. 163-175.

[115] Y. Garud, *A New Approach to the Evaluation of Fatigue under Multiaxial Loadings*, Journal of Engineering Materials and Technology (1981), 103(2): p. 118-125.

[116] R. Krieg, *A Practical Two Surface Plasticity Theory*, Journal of Applied Mechanics (1975), 42: p. 641-646.

[117] Y. Dafalias and E. Popov, *Plastic Internal Variables Formalism of Cyclic Plasticity*, Journal of Applied Mechanics (1976), 43: p. 645-651.

[118] T. Hassan and S. Kyriakides, *Ratcheting of Cyclically Hardening and Softening Materials: I. Uniaxial Behavior*, International Journal of Plasticity (1994), 10(2): p. 149-184.

[119] J. Chaboche, *A Review of some Plasticity and Viscoplasticity Constitutive Theories*, International Journal of Plasticity (2008), 24(10): p. 1642-1693.

[120] M. Li, X. Lou, J. Kim, and R. Wagoner, *An Efficient Constitutive Model for Room-temperature, Low-rate Plasticity of Annealed Mg AZ31B Sheet*, International Journal of Plasticity (2010), 26(6): p. 820-858.

[121] J. Kim, H. Ryou, D. Kim, W. Lee, S.H. Hong, and K. Chung, *Constitutive Law for AZ31B Mg Alloy Sheets and Finite Element Simulation for Three-point Bending*, International Journal of Mechanical Sciences (2008), 50(10): p. 1510-1518.

[122] J.H. Kim, M.G. Lee, H. Ryou, K. Chung, J.R. Youn, and T.J. Kang, *Development of Nonlinear Constitutive Laws for Anisotropic and Asymmetric Fiber Reinforced Composites*, Polymer Composites (2008), 29(2): p. 216-228.

[123] B. Plunkett, R. Lebensohn, O. Cazacu, and F. Barlat, *Anisotropic Yield Function of Hexagonal Materials taking into account Texture Development and Anisotropic Hardening*, Acta Materialia (2006), 54(16): p. 4159-4169.

[124] J. Cooper and R. Smith, *Fatigue Crack Propagation at Spot Welds*, Metal Construction (1986), 18(6): p. 383-386.

[125] J.L. Overbeeke and J. Draisma, *Influence of Stress Relieving on Fatigue of Heavy-Duty Spot Welded Lap Joints*, Metal Construction (1978), 10(9): p. 433-434.

[126] B. Pollard, *Fatigue Strength of Spot Welds in Titanium-Bearing HSLA Steels*, in *SAE International Congress and Exposition*, Detroit, Michigan, United States, SAE Technical Paper: 820284, 1982.

[127] L.P. Pook, *Fracture Mechanics Analysis of the Fatigue Behaviour of Spot Welds,* International Journal of Fracture (1975), 11(1): p. 173-176.

[128] H. Tada, P.C. Paris, and G.R. Irwin, *The Stress Analysis of Cracks Handbook,* New York: ASME press, 2000.

[129] J.A. Newman and N.E. Dowling, *A Crack Growth Approach to Life Prediction of Spot-Welded Lap Joints,* Fatigue & Fracture of Engineering Materials & Structures (1998), 21(9): p. 1123-1132.

[130] D. Radaj, C. Sonsino, and W. Fricke, *Fatigue Assessment of Welded Joints by Local Approaches*, Cambridge, England: Woodhead Publishing Ltd., 2006.

[131] D. Radaj, *Stress Singularity, Notch Stress and Structural Stress at Spot-Welded Joints,* Engineering Fracture Mechanics (1989), 34(2): p. 495-506.

[132] A. Rupp, K. Storzel, and V. Grubisic, *Computer Aided Dimensioning of Spot-Welded Automotive Structures*, in *SAE International Congress & Exposition*, Detroit, Michigan, United States, SAE Technical Paper: 950711, 1995.

[133] S.D. Sheppard, *Further Refinement of a Methodology for Fatigue Life Estimation in Resistance Spot Weld Connections,* in *Advances in Fatigue Lifetime Predictive Techniques: Third Volume,* ASTM STP 1292, (1996): p. 265-282.

[134] S.D. Sheppard and M. Strange, *Fatigue Life Estimation in Resistance Spot Welds: Initiation and Early Growth Phase,* Fatigue & Fracture of Engineering Materials & Structures (1992), 15(6): p. 531-549.

[135] K.N. Smith, T. Topper, and P. Watson, *A Stress-Strain Function for the Fatigue of Metals(Stress-Strain Function for Metal Fatigue Including Mean Stress Effect),* Journal of Materials (1970), 5: p. 767-778.

[136] H. Neuber, *Theory of Stress Concentration for Shear-Strained Prismatical Bodies with Arbitrary Nonlinear Stress-Strain Law,* Journal of Applied Mechanics (1961), 28: p. 544-550.

[137] H.L. Oh, *Fatigue-Life Prediction for Spotweld using Neubers Rule*, in *Design of fatigue and fracture resistance structures,* ASTM STP 761, (1982): p. 296–309.

[138] J. Morrow and F. Tuler, *Low Cycle Fatigue Evaluation of Inconel 713 C and Waspaloy,* Journal of Basic Engineering (1965), 87(2): p. 275-289.

[139] N. Pan, *Fatigue Life Study of Spot Welds,* Ph.D thesis, Stanford University, 2000.

[140] ASTM, E8/E8M-11, *Standard Test Methods for Tension Testing of Metallic Materials,* 2011.

[141] ASTM, E606-04, *Standard Practice for Strain-Controlled Fatigue Testing,* 2004.

[142] X. Long and S.K. Khanna, *Fatigue Properties and Failure Characterization of Spot Welded High Strength Steel Sheet,* International Journal of Fatigue (2007), 29(5): p. 879-886.

[143] J. Bonnen, H. Agrawal, M. Amaya, R. Iyengar, H. Kang, A. Khosrovaneh, T. Link, M. Shih, M. Walp, and B. Yan, *Fatigue of Advanced High Strength Steel Spot Welds,* in *SAE World*

Congress & Exhibition, Detroit, Michigan, United States, SAE Technical Paper: 2006-01-0978, 2006.

[144] S. Zuniga and S.D. Sheppard, *Resistance Spot Weld Failure Loads and Modes in Overload Conditions,* in *Fatigue and Fracture Mechanics: 27th Volume*, ASTM STP 1296, (1997): p. 469-489.

[145] Z. Yang, J. Li, J. Zhang, G. Lorimer, and J. Robson, *Review on Research and Development of Magnesium Alloys,* Acta Metallurgica Sinica (English Letters) (2008), 21(5): p. 313-328.

[146] RWMA, *Resistance Welding Manual*, 4'th Ed., Bridgeport, NJ, USA: George H Bauchanan, 2003.

[147] J. Chen, T. Liu, L. Lu, Y. Zhang, and W. Zeng, *Microstructure and Mechanical Property of Rolled-weld Magnesium Alloy AZ31,* Materials & Design (2012), 36: p. 577-583.

[148] ASTM, E384-99, *Standard Test Method for Microindentation Hardness of Materials,* 1999.

[149] C. Ma, D.L. Chen, S.D. Bhole, G. Boudreau, A. Lee, and E. Biro, *Microstructure and Fracture Characteristics of Spot-Welded DP600 Steel,* Materials Science and Engineering: A (2008), 485(1): p. 334-346.

[150] A.M. Pereira, J.M. Ferreira, A. Loureiro, J.D.M. Costa, and P.J. Bartolo, *Effect of Process Parameters on the Strength of Resistance Spot Welds in 6082-T6 Aluminium Alloy,* Materials & Design (2010), 31(5): p. 2454-2463.

[151] M. Gharghouri, G. Weatherly, J. Embury, and J. Root, *Study of the Mechanical Properties of Mg-7.7 at.% Al by in-situ Neutron Diffraction,* Philosophical Magazine A (1999), 79(7): p. 1671-1695.

[152] J. Koike and R. Ohyama, *Geometrical Criterion for the Activation of Prismatic Slip in AZ61 Mg Alloy Sheets Deformed at Room Temperature,* Acta Materialia (2005), 53(7): p. 1963-1972.

[153] F. Kaiser, D. Letzig, J. Bohlen, A. Styczynski, C. Hartig, and K.U. Kainer, *Anisotropic Properties of Magnesium Sheet AZ31,* Materials Science Forum (2003), 419-422: p. 315-320.

[154] F. Lv, F. Yang, Q. Duan, T. Luo, Y. Yang, S. Li, and Z. Zhang, *Tensile and Low-cycle Fatigue Properties of Mg–2.8% Al–1.1% Zn–0.4% Mn Alloy along the Transverse and Rolling Directions,* Scripta Materialia (2009), 61(9): p. 887-890.

[155] N. Afrin, D. Chen, X. Cao, and M. Jahazi, *Strain Hardening Behavior of a Friction Stir Welded Magnesium Alloy,* Scripta Materialia (2007), 57(11): p. 1004-1007.

[156] H.Y. Wu and F.Z. Lin, *Mechanical Properties and Strain-Hardening Behavior of Mg Alloy AZ31B-H24 Thin Sheet,* Materials Science and Engineering: A (2010), 527(4): p. 1194-1199.

[157] L.F. Yang, L. Yi, and C. Guo, *Influence of Pressure Amplitude on Formability in Pulsating Hydro-Bugling of AZ31B Magnesium Alloy Sheet,* Applied Mechanics and Materials (2012), 128: p. 397-402.

[158] R. Boger, R. Wagoner, F. Barlat, M. Lee, and K. Chung, *Continuous, Large Strain, Tension/Compression Testing of Sheet Material,* International Journal of Plasticity (2005), 21(12): p. 2319-2343.

[159] S.C. Choi, H.Y. Kim, S.M. Hong, Y.S. Shin, G.H. Lee, and H.J. Kim, *Evaluation and Prediction of the Forming Limit of AZ31B Magnesium Alloy Sheets in a Cross-shaped Cup Deep Drawing Process,* Metals and Materials International (2009), 15(4): p. 575-584.

[160] A. Gean, S.A. Westgate, J.C. Kucza, and J.C. Ehrstrom, *Static and Fatigue Behavior of Spot-welded 5182-0 Aluminum Alloy Sheet,* Welding Journal (1999), 78(3): p. 80s-86s.

[161] M. Ghorbani and A. Assempour, *The Influence of Weld Current and Time on the Properties of Spot Welds in 5754 Aluminum Alloy Sheet*, in *SAE World Congress & Exhibition*, Detroit, Michigan, United States, SAE Technical Paper: 2002-01-0387, 2002.

[162] A. De, O. Gupta, and L. Dorn, *An Experimental Study of Resistance Spot Welding in 1 mm Thick Sheet of Low Carbon Steel,* Proceedings of the Institution of Mechanical Engineers, Part B: Journal of Engineering Manufacture (1996), 210(4): p. 341-347.

[163] H.J. Cho, J.Y. Lee, and H.K. Yi, *Study on the Spot Weldability of Aluminum Alloy Sheets for Autobody*, in *Eighth International Pacific Conference on Automotive Engineering*, Yokohama, Japan, JSAE Technical Paper: 9531408, 1995.

[164] W.C. Young and R.G. Budynas, *Roark's Formulas for Stress and Strain*, New York: McGraw-Hill, 2002.

[165] D. Afshari, M. Sedighi, Z. Barsoum, and R.L. Peng, *An approach in prediction of failure in resistance spot welded aluminum 6061-T6 under quasi-static tensile test*, Proceedings of the Institution of Mechanical Engineers, Part B: Journal of Engineering Manufacture (2012), 226(6): p. 1026-1032.

[166] M. Pouranvari, *Failure Mode Transition in Similar and Dissimilar Resistance Spot Welds of HSLA and Low Carbon Steels,* Canadian Metallurgical Quarterly (2012), 51(1): p. 67-74.

[167] M.D. Tumuluru, *A Comparative Examination of the Resistance Spot Welding Behavior of Two Advanced High Strength Steels*, in *SAE World Congress & Exhibition*, Detroit, Michigan, United States, SAE Technical Paper: 2006-01-1214, 2006.

[168] H. Lee, N. Kim, and T.S. Lee, *Overload Failure Curve and Fatigue Behavior of Spot-Welded Specimens,* Engineering Fracture Mechanics (2005), 72(8): p. 1203-1221.

[169] J. Albinmousa, H. Jahed, and S. Lambert, *Cyclic Behaviour of Wrought Magnesium Alloy under Multiaxial Load,* International Journal of Fatigue (2011), 33(8): p. 1127–1139.

[170] S. Hasegawa, Y. Tsuchida, H. Yano, and M. Matsui, *Evaluation of Low Cycle Fatigue Life in AZ31 Magnesium Alloy*, International Journal of Fatigue (2007), 29(9): p. 1839-1845.

[171] Q. Li, Q. Yu, J. Zhang, and Y. Jiang, *Effect of Strain Amplitude on Tension-compression Fatigue Behavior of Extruded Mg6Al1ZnA Magnesium Alloy,* Scripta Materialia (2010), 62(10): p. 778-781.

[172] Y. Xiong, Q. Yu, and Y. Jiang, *Multiaxial Fatigue of Extruded AZ31B Magnesium Alloy,* Materials Science and Engineering: A (2012), 546: p. 119–128.

[173] M. Vural, A. Akkus, and B. Eryurek, *Effect of Welding Nugget Diameter on the Fatigue Strength of the Resistance Spot Welded Joints of Different Steel Sheets*, Journal of Materials Processing Technology (2006), 176(1): p. 127-132.

[174] B.H. Chang, D. Du, B. Sui, Y. Zhou, Z. Wang, and F. Heidarzadeh, *Effect of Forging Force on Fatigue Behavior of Spot Welded Joints of Aluminum Alloy 5182*, Journal of Manufacturing Science and Engineering (2007), 129(1): p. 95-100.

[175] Y. Uematsu and K. Tokaji, *Comparison of Fatigue Behaviour Between Resistance Spot and Friction Stir Spot Welded Aluminium Alloy Sheets*, Science and Technology of Welding and Joining (2009), 14(1): p. 62-71.

[176] R.I. Stephens, A. Fatemi, R.R. Stephens, and H.O. Fuchs, *Metal Fatigue in Engineering*, Second Ed., New York: John Willey & Sons, 2001.

[177] L.P. Pook, *Metal Fatigue: What It Is, Why It Matters*, Springer, 2007.

[178] J.C. McMahon and F.V. Lawrence, *Fatigue Crack Initiation and Early Growth in Tensile-Shear Spot Weldments*, University of Illinois at Urbana-Champaign, Report No. 131, 1986.

[179] F.G. Hamel and J. Masounave, *The Fatigue Behaviour of HSLA non-load Carrying Spot Welded Joints*, Canadian Metallurgical Quarterly (1990), 29(4): p. 313-318.

[180] Ford Motor Company, *Fatigue Testing Procedure for Fusion Welded Coupons*, 2007.

[181] J. McMahon, G. Smith, and F. Lawrence, *Fatigue Crack Initiation and Growth in Tensile-Shear Spot Weldments*, in *Fatigue and Fracture Testing of Weldments*, ASTM STP 1058, (1990): p. 47-77.

[182] W. Chen and D. Han, *Plasticity for Structural Engineers*, New York: Springer, 1988.

[183] J.E. Shigley, C.R. Mischke, R.G. Budynas, X. Liu, and Z. Gao, *Mechanical Engineering Design*, Eighth Ed., New York: McGraw-Hill, 2006.

[184] Wikipedia. *Von Mises Yield Criterion*. May 12, 2012 [cited 2012 June 16]; Available from: http://en.wikipedia.org/wiki/Von_Mises_yield_criterion#cite_note-0.

[185] R.O. Davis and A.P.S. Selvadurai, *Plasticity and Geomechanics*, Cambridge University Press, 2002.

[186] W. Prager, *The Theory of Plasticity: A Survey of Recent Achievements*, Proceedings of the Institution of Mechanical Engineers (1955), 169(1): p. 41-57.

[187] R.T. Shield and H. Ziegler, *On Prager's Hardening Rule*, Zeitschrift für Angewandte Mathematik und Physik (1958), 9(3): p. 260-276.

[188] W. Prager, *Recent Developments in the Mathematical Theory of Plasticity*, Journal of Applied Physics (1949), 20(3): p. 235-241.

[189] A. Abel, *Historical Perspectives and Some of the Main Features of the Bauschinger Effect*, in *Materials Forum*: Institute of Metals and Materials Australasia (1987), 10(1): p. 11-26.

[190] P. Partridge, *Cyclic Twinning in Fatigued Close-Packed Hexagonal Metals,* Philosophical Magazine (1965), 12(119): p. 1043-1054.

[191] Abaqus, *User's Manual for Version 6.10-EF1,* Dassault Systemes Simulia Corp., Providence, RI, USA, 2010.

[192] F. Barlat, J. Brem, J. Yoon, K. Chung, R. Dick, D. Lege, F. Pourboghrat, S.H. Choi, and E. Chu, *Plane Stress Yield Function for Aluminum Alloy Sheets—Part 1: Theory,* International Journal of Plasticity (2003), 19(9): p. 1297-1319.

[193] E. Kalateh Molaei, *Asymmetric Elastic-Plastic Solution and its Application in Numerical Analysis of the Effect of Cold Spray on Fatigue of AZ31B,* Masters' thesis, Iran University of Science and Technology, 2012.

[194] M. Khayamian, *An Axisymmetric Elastoplastic Model for Wrought Magnesium Alloys,* Masters' thesis, Iran University of Science and Technology, 2012.

[195] H. Jahed, R. Sethuraman, and R. Dubey, *A Variable Material Property Approach for Solving Elastic-Plastic Problems,* International journal of pressure vessels and piping (1997), 71(3): p. 285-291.

[196] H. Jahed and R. Dubey, *An Axisymmetric Method of Elastic-Plastic Analysis Capable of Predicting Residual Stress Field,* Journal of pressure vessel technology (1997), 119(3): p. 264-273.

[197] N.E. Frost, K.J. Marsh, and L.P. Pook, *Metal Fatigue*, New York: DoverPublications, 1999.

[198] J.A. Davidson and E.J. Imhof, *A Fracture-Mechanics and System-Stiffness Approach to Fatigue Performance of Spot-Welded Sheet Steels*, in *SAE International Congress and Exposition*, Detroit, Michigan, United States, SAE Technical Paper: 830034, 1983.

[199] M. Barsom John and T. Rolfe Stanley, *Fracture & Fatigue Control in Structures–Application of Fracture Mechanics,* New Jersey: Prentice Hall, 1987.

[200] P.C. Wang and K.W. Ewing, *Fracture Mechanics Analysis of Fatigue Resistance of Spot Welded Coach-Peel Joints,* Fatigue & Fracture of Engineering Materials & Structures (1991), 14(9): p. 915-930.

[201] J.F. Cooper and R.A. Smith, *The Measurement of Fatigue Cracks at Spot-welds,* International Journal of Fatigue (1985), 7(3): p. 137-140.

[202] L.P. Pook, *Approximate Stress Intensity Factors for Spot and Similar Welds*, National Engineering Laboratory, UK, Report No. 588, 1975.

[203] S.C. Zhang, *Stress Intensities at Spot Welds,* International Journal of Fracture (1997), 88(2): p. 167-185.

[204] S.B. Behravesh, H. Jahed, and S. Lambert, *Characterization of Magnesium Spot Welds under Tensile and Cyclic Loadings,* Materials & Design (2011), 32(10): p. 4890-4900.

[205] M.H. Swellam, G. Banas, and F.V. Lawrence, *A Fatigue Design Parameter for Spot Welds,* Fatigue & Fracture of Engineering Materials & Structures (1994), 17(10): p. 1197-1204.

[206] P.C. Wang, H.T. Corten, and F.V. Lawrence, *A Fatigue Life Prediction Method for Tensile-Shear Spot Welds*, in *SAE International Congress and Exposition*, Detroit, Michigan, United States, SAE Technical Paper: 850370, 1985.

[207] D. Radaj, *Hot Spot Stress Concept for Spot-Welded Joints*, in *Structural Design and Crashworthiness of Automobiles*, New York: Springer-Verlag, (1987): p. 149-170.

[208] J.H. Kuang and A.H. Liu, *A Study of the Stress Concentration Factor on Spot Welds*, Welding Journal (1990), 69(12): p. 468s-474s.

[209] S. Sheppard, N. Pan, Z. Bai, and Y.C. Sheu, *Refinement and Verification of the Structural Stress Method for Fatigue Life Prediction of Resistance Spot Welds Under Variable Amplitude Loads*, in *International Body Engineering Conference & Exposition*, Detroit, Michigan, United States, SAE Technical Paper: 2000-01-2727, 2000.

[210] J. Park and D. Nelson, *Evaluation of an Energy-Based Approach and a Critical Plane Approach for Predicting Constant Amplitude Multiaxial Fatigue Life*, International Journal of Fatigue (2000), 22(1): p. 23-39.

[211] K.O. Lee, S.G. Hong, and S.B. Lee, *A New Energy-based Fatigue Damage Parameter in life Prediction of High-temperature Structural Materials*, Materials Science and Engineering: A (2008), 496(1): p. 471-477.

[212] S. Kwon, K. Song, K. Shin, and S. Kwun, *Low Cycle Fatigue Properties and an Energy-based Approach for As-extruded AZ31 Magnesium Alloy*, Metals and Materials International (2011), 17(2): p. 207-213.

[213] S.H. Park, S.G. Hong, B.H. Lee, and C.S. Lee, *Fatigue Life Prediction of Rolled AZ31 Magnesium Alloy using an Energy-Based Model*, International Journal of Modern Physics B (2008), 22(31-32): p. 5503-5508.

[214] X. He, I. Pearson, and K. Young, *Self-pierce Riveting for Sheet Materials: State of the Art*, Journal of Materials Processing Technology (2008), 199(1): p. 27-36.

[215] M. Fu and P.K. Mallick, *Effect of Process Variables on the Static and Fatigue Properties of Self-Piercing Riveted Joints in Aluminum Alloy 5754*, in *SAE World Congress*, Detroit, Michigan, United States, SAE Technical Paper: 2001-01-0825, 2001.

[216] A. Kochan, *Audi Moves Forward with All-Aluminium Cars*, Assembly Automation (2000), 20(2): p. 132-135.

[217] J. Mortimer, *Jaguar uses Castings, Extrusions to Reduce Parts Count in New Sports Car*, Assembly Automation (2006), 26(2): p. 115-120.

[218] M. LaPensee, *Self-Pierce Riveting Technology: A Joining Solution for Light Metals*, Light Metal Age (2003), 61(9-10): p. 32-35.

[219] T.A. Barnes and I.R. Pashby, *Joining Techniques for Aluminium Spaceframes Used in Automobiles: Part I — Solid and Liquid Phase Welding*, Journal of Materials Processing Technology (2000), 99(1): p. 62-71.

[220] N.H. Hoang, R. Porcaro, M. Langseth, and A.G. Hanssen, *Self-piercing Riveting Connections using Aluminium Rivets*, International Journal of Solids and Structures (2010), 47(3): p. 427-439.

[221] Y. Durandet, R. Deam, A. Beer, W. Song, and S. Blacket, *Laser Assisted Self-pierce Riveting of AZ31 Magnesium Alloy Strips*, Materials & Design (2010), 31: p. S13-S16.

[222] S. Xu, W. Tyson, G. Shen, R. Eagleson, and A. Balmy, *Uniaxial Deformation, Charpy and Fracture Toughness Testing of Extruded Magnesium Alloy AM30*, in *SAE World Congress & Exposition*, Detroit, Michigan, United States, SAE Technical Paper: 2010-01-0406, 2010.

[223] D.A. Wagner, S. Logan, K. Wang, and T. Skszek, *FEA Predictions and Test Results from Magnesium Beams in Bending and Axial Compression*, in *SAE World Congress & Exhibition*, Detroit, Michigan, United States, SAE Technical Paper: 2010-01-0405, 2010.

[224] S. Begum, D. Chen, S. Xu, and A.A. Luo, *Strain-controlled Low-cycle Fatigue Properties of a Newly Developed Extruded Magnesium Alloy*, Metallurgical and Materials Transactions A (2008), 39(12): p. 3014-3026.

[225] H.A. Patel, N. Rashidi, D.L. Chen, S.D. Bhole, and A.A. Luo, *Cyclic Deformation Behavior of a Super-Vacuum Die Cast Magnesium Alloy*, Materials Science and Engineering: A (2012), 546: p. 72-81.

[226] Magnesium Front End Research & Development (MFERD), *United States Annual Progress Report - Task 2.3 Fatigue & Durability*, 2011.

[227] Cosma International, *USCAR – Phase 2: Method for Modeling and Analyzing Magnesium Joints*, 2012.

[228] Cosma Engineering, *Test Report for USAMP AMD904 Task 2.0.2 Cosma Tests*, 2012.